

**CHARACTERIZATION OF THE PHASE BEHAVIOR OF
SUPERSATURATED SOLUTIONS IN SIMULATED AND ASPIRATED
HUMAN FLUIDS**

by

Ahmed Elkhabaz

A Dissertation

Submitted to the Faculty of Purdue University

In Partial Fulfillment of the Requirements for the degree of

Doctor of Philosophy



Department of Industrial and Physical Pharmacy

West Lafayette, Indiana

December 2019

THE PURDUE UNIVERSITY GRADUATE SCHOOL
STATEMENT OF COMMITTEE APPROVAL

Dr. Lynne S. Taylor, Chair

Department of Industrial and Physical Pharmacy

Dr. Garth J. Simpson

Department of Chemistry

Dr. Gregory T. Knipp

Department of Industrial and Physical Pharmacy

Dr. Qi (Tony) Zhou

Department of Industrial and Physical Pharmacy

Approved by:

Dr. Rodolfo Pinal

Head of the Graduate Program

To my parents

ACKNOWLEDGMENTS

I would like to thank, first and foremost, my advisor Dr. Lynne S. Taylor for her constant mentorship, support and guidance during these years. Her dedication and passion for research is truly inspirational and have helped me grow as a researcher and as an individual. I am very fortunate to have the opportunity to work in her group.

I am very thankful to my committee members, Dr. Gregory T. Knipp, Dr. Qi (Tony) Zhou, and Dr. Garth J. Simpson, for their guidance and service.

This research would not have been possible without the contributions of our collaborators at Purdue University and KU Leuven. I am grateful to Dr. Garth J. Simpson and Sreya Sarkar for their collaborative work and discussions. I am indebted to Dr. Patrick Augustijns and his group in Belgium for providing us with the aspirated intestinal fluids and establishing a fruitful collaboration. All financial support from the National Science Foundation, Bilsland Dissertation Fellowship and the department of Industrial and Physical Pharmacy is duly acknowledged.

I am grateful to all present and former colleagues of Taylor lab for all the work/fun moments we shared together. I would like to thank Matthew Jackson and Niraj Trasi for their guidance during my early stages as a graduate student. I am very grateful to my friend and colleague Laura Mosquera-Giraldo for all the help, discussions and good memories. My sincere gratitude to Dana Moseson for her help and support in working with electron microscopy. Special thanks to Chailu Que, Clara Correa Soto, Siddhi Hate, Jennifer Lu, Sugandha Saboo, Anura Indulkar and Naila Mugheirbi for their collaboration and friendship.

Lastly, I am deeply thankful to my family and friends, here at Purdue and in Egypt. I owe everything to my parents and my brother. I am eternally grateful for all the unconditional love, motivation and support they provided me.

TABLE OF CONTENTS

LIST OF TABLES.....	9
LIST OF FIGURES	10
ABSTRACT.....	16
CHAPTER 1. INTRODUCTION	17
1.1 Research significance, specific aims and hypotheses	17
1.2 Background	21
1.2.1 Crystalline versus amorphous solids	21
1.2.2 Thermodynamics of the amorphous state	22
1.2.3 Mixing energy and solubilization	23
1.2.4 The amorphous solubility advantage	24
1.2.5 Supersaturation	25
1.2.6 Crystallization.....	26
Nucleation	26
Crystal Growth	28
1.2.7 Liquid-liquid phase separation	29
1.2.8 Phase-boundaries of supersaturated solutions	30
1.2.9 Dissolution of ASDs	31
1.2.10 Routes of crystallization during dissolution of ASDs	32
CHAPTER 2. VARIATION IN SUPERSATURATION AND PHASE BEHAVIOR OF EZETIMIBE AMORPHOUS SOLID DISPERSIONS UPON DISSOLUTION IN DIFFERENT BIORELEVANT MEDIA	35
2.1 Abstract.....	35
2.2 Introduction.....	36
2.3 Materials	38
2.4 Methods.....	39
2.4.1 Equilibrium solubility experiments of ezetimibe in different media.....	39
2.4.2 Liquid-liquid phase separation (LLPS) onset determination using ultraviolet (UV) spectroscopy	40
2.4.3 Nucleation induction time experiments using UV spectroscopy.....	40

2.4.4 Preparation of ezetimibe bulk ASDs	40
2.4.5 Dissolution studies of ezetimibe ASDs	41
2.4.6 Polarized light microscopy and powder X-ray diffraction (PXRD) for evaluation of ezetimibe suspended ASDs.....	41
2.4.7 Detection of crystallization during dissolution of ezetimibe ASDs using SHG microscopy.....	42
2.5 Results.....	43
2.5.1 Equilibrium solubility experiments of ezetimibe in different media.....	43
2.5.2 LLPS onset determination using UV spectroscopy	43
2.5.3 Nucleation induction time experiments using UV spectroscopy.....	44
2.5.4 Characterization of ezetimibe ASDs dissolution in different media	46
2.6 Discussion	58
2.7 Conclusions.....	65
CHAPTER 3. CHARACTERIZATION OF PHASE TRANSFORMATIONS FOR AMORPHOUS SOLID DISPERSIONS OF A WEAKLY BASIC DRUG UPON DISSOLUTION IN BIORELEVANT MEDIA	66
3.1 Abstract	66
3.2 Introduction.....	67
3.3 Materials	70
3.4 Methods.....	71
3.4.1 Equilibrium solubility measurements	71
3.4.2 UV/Vis extinction measurements	71
3.4.3 Fluorescence spectroscopy measurements	71
3.4.4 Preparation of posaconazole ASDs	72
3.4.5 Dissolution studies.....	72
3.4.6 Nanoparticle tracking analysis (NTA) and powder x-ray diffraction (PXRD)	74
3.4.7 Second harmonic generation (SHG) and two-photon excitation ultraviolet fluorescence (TPE-UVF) microscopy	75
3.5 Results.....	76
3.5.1 Equilibrium solubility measurements	76
3.5.2 UV/Vis extinction measurements	76

3.5.3	Fluorescence spectroscopy measurements	77
3.5.4	Dissolution studies of posaconazole ASDs and tablets	79
3.5.5	Characterization of posaconazole ASDs and tablet powder dissolution	81
3.6	Discussion.....	87
3.7	Conclusions.....	94
CHAPTER 4. INTERPLAY OF SUPERSATURATION AND SOLUBILIZATION: LACK OR CORRELATION BETWEEN CONCENTRATION-BASED SUPERSATURATION MEASUREMENTS AND MEMBRANE TRANSPORT RATES IN SIMULATED AND ASPIRATED HUMAN FLUIDS		95
4.1	Abstract	95
4.2	Introduction.....	95
4.3	Materials	99
4.4	Methods.....	100
4.4.1	Media selection and preparation	100
4.4.2	Sampling and handling of FaHIF	100
4.4.3	Crystalline solubility measurements.....	101
4.4.4	Amorphous solubility measurements	102
4.4.5	Confirmation of amorphous solubility and formation of LLPS nanodroplets by fluorescence spectroscopy and scanning electron microscopy (SEM).....	102
4.4.6	Diffusion cell experiments.....	103
4.5	Results.....	104
4.5.1	Crystalline solubility measurements.....	104
4.5.2	Amorphous solubility measurements	104
4.5.3	Supersaturation determination by diffusive flux measurements	107
4.6	Discussion	111
4.7	Conclusion	118
CHAPTER 5. IMPACT OF SIMULATED AND ASPIRATED MEDIA ON CRYSTALLIZATION KINETICS OF ATAZANAVIR AND POSACONAZOLE SUPERSATURATED SOLUTIONS		120
5.1	Abstract	120
5.2	Introduction.....	120

5.3 Materials	122
5.4 Methods.....	123
5.4.1 Preparation of test media	123
5.4.2 Sampling and handling of FaHIF samples.....	124
5.4.3 Crystalline and amorphous solubilities of atazanavir and posaconazole in FaHIF .	125
5.4.4 Nucleation induction time experiments by UV spectroscopy	126
5.4.5 Characterization of atazanavir and posaconazole crystals by SHG microscopy	126
5.4.6 Characterization of atazanavir and posaconazole crystals by scanning electron microscopy (SEM).....	127
5.4.7 Characterization of atazanavir precipitates by powder X-ray diffraction (PXRD) .	127
5.5 Results.....	128
5.5.1 Crystalline and amorphous of atazanavir and posaconazole in pre-centrifuged FaHIF	128
5.5.2 Nucleation induction times	128
5.5.3 Characterization of atazanavir and posaconzole crystallization using SHG	132
5.5.4 Characterization of atazanavir and posaconzole crystals using SEM	136
5.5.5 Characterization of atazanavir precipitates by PXRD	141
5.6 Discussion.....	142
5.7 Conclusions.....	151
APPENDIX A. SUPPORTING INFORMATION	152
REFERENCES	156
VITA	175

LIST OF TABLES

Table 2-1. Equilibrium solubility of ezetimibe in three different media at 37°C. (n=6)	43
Table 2-2. Summary of LLPS concentrations measured in sodium phosphate buffer (10mM, pH 6.8) and FaSSIF at 37°C. (n=3)	44
Table 2-3. Nucleation and growth kinetics obtained from SHG microscopy images analysis measured in different dissolution media. (n=3)	60
Table 3-1. Equilibrium solubility of posaconazole in FaSSGF and FaSSIF at 37°C. (n=3)	76
Table 4-1. Detailed composition of the bile salts and lecithin for FaSSIF-V1, FaSSIF-V2 and composite-FaSSIF.....	100
Table 4-2. Crystalline solubility values of atazanavir and posaconazole in different media. (n=3, ± standard deviation).....	104
Table 4-3. Amorphous solubility values in atazanavir and posaconazole in different media. (n=3, ± standard deviation).....	105
Table 4-4. Estimation of $K_{m/w}$ values for atazanavir and posaconazole at the crystalline and amorphous solubilities in FaSSIF-V1, composite-FaSSIF and FaHIF media	115
Table 5-1. Detailed composition of the bile salts and lecithin for FaSSIF-V1, FaSSIF-V2 and composite-FaSSIF.....	124
Table 5-2. Crystalline and amorphous solubilities of atazanavir and posaconazole pre-centrifuged FaHIF at 37°C. (n=3)	128
Table 5-3. Summary of desupersaturation rates, obtained from the nucleation induction time profiles for atazanavir and posaconazole, in buffer-V1, FaSSIF-V1 and composite-FaSSIF....	131
Table 5-4. Summary of AR values of atazanavir needles in the different media. (n=15)	150
Table A.1. Normalized diffusive flux values ($\mu\text{g}/\text{min} \cdot \text{cm}^2$), derived from the slope of mass transport rates of atazanavir and posaconazole. Values were normalized by dividing the slopes by the surface area of the membrane.	153
Table A.2. Calculated values of $P_{app,uncorr}$ for atazanavir and posaconazole at (J_{ampm}/C_{ampm}) and (J_{eq}/C_{eq}) in all media.	154
Table A.3. Calculated values of $P_{app,corr}$ for atazanavir and posaconazole at (J_{ampm}/C_{ampm}) and (J_{eq}/C_{eq}) in all media.	155

LIST OF FIGURES

Figure 1-1. Variation of enthalpy/volume with temperature phase diagram. ⁵⁶	23
Figure 1-2. Free energy diagram for CNT. Adapted from Erdemir et al. ⁶⁷	28
Figure 1-3. Schematic comparing two supersaturated systems with LLPS. ⁷⁵ The upper system is stable, and supersaturation is maintained and hence membrane transport is maximized. The lower system underwent crystallization, thus depleting the supersaturated state and reducing membrane transport.	30
Figure 1-4. Schematic illustrating phase boundaries in solution with respect to concentration and temperature.	31
Figure 1-5. Spring and parachute model for the dissolution of ASDs. Adapted from Williams et al. ⁸³	32
Figure 1-6. Schematic illustration of crystallization routes during dissolution of ASDs: Crystallization from the dissolving matrix vs. solution-mediated crystallization.	34
Figure 2-1. Molecular structures of (A) Ezetimibe, (B) PAA, (C) PVP and (D) HPMC-AS. Chiral centers are marked on (A) ezetimibe by (*).	38
Figure 2-2. LLPS onset concentration for ezetimibe in sodium phosphate buffer at 37°C, in the presence of 2 µg/mL of HPMC-AS, as determined from the sudden increase in UV extinction at 350 nm, indicating a second phase has formed.....	44
Figure 2-3. Apparent concentration versus time plots for supersaturated solutions of ezetimibe in the absence (black) and presence of 10 µg/mL of PAA (blue), PVP (red) and HPMC-AS (green), in sodium phosphate buffer (10 mM, pH 6.8) at 37°C. (n=3, error bars omitted for clarity).	45
Figure 2-4. Summary of experimental induction times observed for supersaturated ezetimibe solutions in the absence and presence of polymers in sodium phosphate buffer (10 mM, pH 6.8) (upper Panel A), and in FeSSIF (lower panel B) at 37°C. (n=3).	46
Figure 2-5. Ezetimibe concentration-time profiles for ASDs formulated with PAA (blue circles in the expanded inset), ASDs with PVP (red circles) and HPMC-AS (green circles) upon dissolution in sodium phosphate buffer (10 mM, pH 6.8) at 37°C for 6 hours. The dashed horizontal purple and cyan lines indicate the measured equilibrium solubility and LLPS concentration of ezetimibe in buffer at 37°C. (n=3).....	48
Figure 2-6. Polarized light microscopy images of ezetimibe ASDs with (A) PAA at 10 minutes, (B) PVP at 60 minutes and (C) HPMC-AS at 60 minutes upon dissolution in sodium phosphate buffer (10 mM, pH 6.8) at 37°C. Scale bar is 50 µm.....	49
Figure 2-7. SHG microscopy images of ezetimibe ASDs; (A) PAA at 6, 15, 35, and 120 minutes, (B) PVP at 10, 20, 35 and 120 minutes, and (C) HPMC-AS at 10, 20, 35 and 120 minutes, upon dissolution in sodium phosphate buffer (10 mM, pH 6.8) at 37°C. Scale bar is 100 µm.....	50

Figure 2-8. Ezetimibe concentration-time profiles for ASDs formulated with PAA (blue circles in the expanded inset), ASDs with PVP (red circles), and ASDs with HPMC-AS (green circles), upon dissolution in FeSSIF at 37°C for 8 hours. The dashed horizontal purple and cyan lines indicate the measured equilibrium solubility and LLPS concentration of ezetimibe in FeSSIF at 37°C. (n=3).....	52
Figure 2-9. Polarized light microscopy images of ezetimibe ASDs with (A) PAA at 30 minutes, (B) PVP at 30 minutes and (C) HPMC-AS at 180 minutes upon dissolution FeSSIF at 37°C. Scale bar is 50 μm.	53
Figure 2-10. PXRD patterns of (A) dry ezetimibe monohydrate powder (purple pattern), and slurried ezetimibe ASDs prepared with (B) PAA, (C) PVP, and (D) HPMC-AS, after dissolution in FeSSIF at 37°C at 1 (blue), 2 (red), and 3 hours (green).....	54
Figure 2-11. SHG microscopy images of ezetimibe ASDs; (A) PAA at 15, 30 and 120 minutes, (B) PVP at 15, 30, and 120 minutes, and (C) HPMC-AS at 30, 120 and 240 minutes, upon dissolution in FeSSIF at 37°C. Scale bar is 100 μm.	55
Figure 2-12. Ezetimibe concentration-time profiles for ASDs formulated with (A) PAA, (B) PVP, and (C) HPMC-AS upon dissolution in Ensure Plus® at 37°C for 6 hours; Blue and red circles indicate ezetimibe dissolution in the aqueous (left axis) and the oily (right axis) phases of Ensure Plus®, respectively. The dashed horizontal blue and red lines indicate the measured equilibrium solubility of ezetimibe in the aqueous and the oily phases of Ensure Plus®, respectively. (n=3).	57
Figure 2-13. SHG microscopy images of ezetimibe ASDs; (A) PAA at 25, 45, 60 and 120 minutes, (B) PVP at 30, 60, 75 and 120 minutes, and (C) HPMC-AS at 75, 120, 150 and 180 minutes, upon dissolution in Ensure Plus® at 37°C. Scale bar is 100 μm.....	58
Figure 3-1. Chemical structures of (A) posaconazole and (B) HPMC-AS.....	70
Figure 3-2. Schematic of the two-stage dissolution experiments.	74
Figure 3-3. LLPS onset concentration of Posaconazole in FaSSIF at 37 °C as illustrated by the sudden increase in UV extinction at 350 nm, indicating the incidence of LLPS.	77
Figure 3-4. Fluorescence emission spectra of posaconazole at different concentrations in FaSSIF. The inset documents the noticeable increase in I ₃₆₈ of posaconazole for concentrations >20 μg/mL consistent with the formation of drug-rich aggregates.	78
Figure 3-5. Fluorescence emission spectra of posaconazole at different concentrations in buffer. A hypsochromic or blue shift (to shorter wavelengths) is observed upon reaching and exceeding the LLPS concentration, as illustrated by the dashed vertical lines.....	78
Figure 3-6. Posaconazole concentration-time profiles for ASDs formulated at (A) 10 %, (B) 25 %, (C) 50 %, and (D) tablet powder upon dissolution at 37 °C; blue circles indicate posaconazole dissolution in FaSSGF then FaSSIF, whilst red squares indicate posaconazole dissolution in FaSSIF only. An amount of ASD or tablet powder equivalent to 400 μg/mL of posaconazole was added to the acid stage; this decreases to 200 μg/mL in the FaSSIF stage. The dashed horizontal grey and green lines indicate the measured equilibrium solubility and LLPS concentration of posaconazole in FaSSIF at 37 °C respectively (n = 3).	81

Figure 3-7. Posaconazole nanodroplet mean size measurements for the 10%, 25%, and tablet powder, at high dose (blue columns) and low dose (green columns), upon dissolution in FaSSIF (n=3).....	82
Figure 3-8. PXRD patterns of slurried posaconazole ASDs prepared at (A) 10%, (B) 25%, (C) 50% drug loading, and (D) Noxfil® tablet powder after dissolution in FaSSIF for 180 minutes, in addition (E) posaconazole form 1 crystalline powder. The * and ** symbols denote the presence of sodium chloride and titanium oxide in the samples, respectively.	83
Figure 3-9. SHG images of posaconazole ASDs prepared at (A) 10%, (B) 25%, (C) 50% drug loading and (D) tablet powder upon suspension/dissolution in FaSSGF for 30 minutes (left column), dissolution in FaSSIF for 30 minutes (middle column), and dissolution in FaSSIF for 180 minutes (right column).	85
Figure 3-10. Brightfield and TPE-UVF images of posaconazole ASDs prepared at (A) 10%, (B) 25%, (C) 50% drug loading and (D) tablet powder upon suspension/dissolution in FaSSGF for 30 minutes (left column), dissolution in FaSSIF for 30 minutes (middle column), and dissolution in FaSSIF for 180 minutes (right column). The corresponding brightfield images for (A) 10% ASDs are shown in the first row. The blue regions indicate undissolved posaconazole, either arising from crystallized posaconazole or undissolved ASD.	86
Figure 3-11. Volume fraction (%) calculated for (A) SHG signal (crystallinity) and (B) TPE-UVF signal (undissolved posaconazole either in amorphous or crystalline form) for all ASDs and the tablet powder at different time points, upon dissolution in FaSSGF up to 60 minutes, then in FaSSIF onwards. The dashed vertical line denotes media transfer at that timepoint. Error bars are omitted for clarity.	87
Figure 3-12. Ratio of volume fraction crystallinity to volume fraction posaconazole (from Figure 3-11) during suspension/dissolution in FaSSGF after 30 minutes.....	90
Figure 3-13. Posaconazole concentration-time profiles for high dose ASDs (blue circles) and low dose ASDs (orange circles) formulated at 10 % drug loading upon dissolution at 37°C in FaSSGF then FaSSIF. The dashed horizontal grey and green lines indicate the measured equilibrium solubility and LLPS concentration of posaconazole in FaSSIF at 37 °C respectively (n = 3)	92
Figure 3-14. Schematic illustration of the mechanisms of dissolution and crystallization of the A) low drug loading ASDs and B) high drug loading ASDs, upon dissolution in FaSSGF followed by FaSSIF.....	93
Figure 4-1. Molecular structures of atazanavir (left), and posaconazole (right).	99
Figure 4-2. Fluorescence emission spectra of atazanavir (left side) and posaconazole (right side) at different concentrations in (A), (D) FaSSIF-V1, (B), (E) composite-FaSSIF, and (C) and (F) FaHIF. The arrows and vertical dashed lines illustrate a blue shift in the peak maximum for some samples. The inset illustrates the increase in intensity as a function of concentration where the change of slope corresponds to the formation of the second phase of amorphous nanodroplets.	106
Figure 4-3. SEM images of A) atazanavir and B) posaconazole amorphous nanodroplets precipitated from FaHIF. Posaconazole nanodroplets were stabilized by HPMC-AS to prevent crystallization.....	107

Figure 4-4. Atazanavir mass transport versus time at the amorphous solubility (upper x-axis) and at the crystalline solubility (lower x-axis), in different media. Error bars were omitted for clarity. (n=3).....	109
Figure 4-5. Posaconazole mass transport versus time at the amorphous solubility (upper x-axis) and at the crystalline solubility (lower x-axis), in different media. Error bars were omitted for clarity. (n=3). ..	109
Figure 4-6. Maximum supersaturation ratio for atazanavir in different media obtained using activity-based ratio (blue bars) versus concentration-based ratio (red bars). The n.s. indicates when the difference between FaSSIF-V1 and other datasets was nonsignificant (t-test, p value > 0.05). Error bars represent standard deviations where n=3.....	110
Figure 4-7. Maximum supersaturation ration for posaconazole in different media obtained using activity-based ratio (blue bars) versus concentration-based ratio (red bars). The n.s. indicates when the difference between FaSSIF-V1 and other datasets was non-significant (t-test, p value > 0.05), whereas the * and ** symbols indicate that the difference was statistically significant (t-test, p value = 0.002 and 5.3×10^{-7} , respectively). Error bars represent standard deviations where n=3.	111
Figure 4-8. Schematic illustration of posaconazole micellar partitioning at saturation (crystalline solubility/SR=1) and maximum supersaturation (amorphous solubility/SR _{max}) levels.....	117
Figure 5-1. Molecular structures of atazanavir (left), and posaconazole (right). ..	123
Figure 5-2. Schematic illustrating nucleation induction time measurements where the change in the slope of the solution apparent concentration (left y-axis) and increase in extinction (right y-axis) were used to assess the induction time.....	129
Figure 5-3. Summary of nucleation induction times observed for supersaturated solutions of atazanavir in different media at 37°C; in the absence of polymer (blue columns) and presence of 10 µg/mL HPMC-AS (light green columns). * 1 of 3 measurements of atazanavir in FaHIF did not demonstrate change in UV-absorbance for 480 min, i.e. no nucleation. (n=3, except for * n=2).	130
Figure 5-4. Summary of nucleation induction times observed for supersaturated solutions of posaconzole in different media at 37°C; in the absence of polymer (red columns), presence of 10 µg/mL HPMC-AS (light green columns) and 50 µg/ml HPMC-AS (dark green columns). (n=3).	131
Figure 5-5. SHG images for aliquots of atazanavir samples undergoing crystallization in A) buffer-V1 and B) FaSSIF-V1, at 90 min, C) composite-FaSSIF and D) FaHIF, at 120 min. Trace crystallinity in C) and D) are highlighted in yellow circles.....	132
Figure 5-6. SHG images for aliquots of posaconazole samples undergoing crystallization in A) buffer-V1, B) FaSSIF-V1, C) buffer-V2 and D) FaSSIF-V2, at 16 min.....	133
Figure 5-7. SHG images for aliquots of posaconazole samples undergoing crystallization in A) composite-FaSSIF at 12 min, B) composite-FaSSIF at 24 min, C) FaHIF at 24 min and D) FaHIF at 40 min. Trace crystallinity in C) and D) is highlighted in yellow circles.....	134

Figure 5-8. Estimated nucleation rate (SHG signal count/min) for atazanavir and posaconazole in different media	135
Figure 5-9. Estimated growth rate (SHG signal size/min) for atazanavir and posaconazole in different media. *Growth rate could not be quantitated.	136
Figure 5-10. SEM images of A) as received atazanavir crystals and B) atazanavir crystallized from FaSSIF-V1 (150 min).	137
Figure 5-11. SEM images of atazanavir during crystallization at different times in buffer-V1 at A) and B) 150 min and C) 300 min, and in FaHIF, D) and E) at 180 min and F) at 300 min.....	137
Figure 5-12. SEM images showing a higher magnification view of crystallized atazanavir needles formed in A) buffer-V1 and B) FaHIF at 300 min time-point.....	138
Figure 5-13. SEM images of atazanavir crystalline needles in composite-FaSSIF. A) General morphology of atazanavir needles showing branching and secondary growth on the surface. B) Atazanavir needles with bile salt/lecithin deposited species that showed contrast in brightness through the backscattering detector due to elemental atomic number differences.	138
Figure 5-14. SEM images of crystallized atazanavir in the presence of 10 ug/mL of HPMC-AS in different media; A) buffer-V1, B) FaSSIF-V1, C) composite-FaSSIF, and D) FaHIF.	139
Figure 5-15. SEM images of posaconazole crystals formed under different conditions; A) as-received posaconazole crystals, B) & C) crystallized posaconazole from buffer-V1, and D) crystallized posaconazole from FaSSIF-V1.....	140
Figure 5-16. SEM images of crystallized posaconazole in different media; A) and B) composite-FaSSIF, C) and D) FaHIF.	140
Figure 5-17. SEM images of crystallized posaconazole in the presence of 10 µg/mL of HPMC-AS in different media; A) buffer-V1, FaSSIF-V1, C) composite-FaSSIF, and D) FaHIF.	141
Figure 5-18. PXRD patterns of atazanavir starting material (blue), Acetonitrile-slurried (orange), Buffer-V1 precipitate (grey), FaSSIF-V1 precipitate (yellow) and FaHIF precipitate (green)..	142
Figure 5-19. A schematic illustrating different growth patterns for posaconazole crystal plates in the different media (adapted from Kubota's illustration). ²³⁰ The schematic demonstrates posaconazole crystals in A) Buffer-V1 where impurities were absent, B) FaSSIF-V1, C) composite-FaSSIF and D) FaHIF, where adsorption of impurities (bile salts/lecithin) at kink sites on the surface of a growing crystal resulted in curvature of the step advancement.	148
Figure 5-20. A schematic illustrating different growth patterns for atazanavir needle crystals in the different media; A) Buffer-V1 (lower AR with surface nucleation/branching), B) FaSSIF-V1 and composite-FaSSIF (higher AR with surface nucleation/branching) and C) FaHIF (higher AR without surface nucleation/branching).....	150
Figure A.1 Posaconazole concentration-time profiles for ASDs formulated at (A) 10 %, (B) 25 %, (C) 50 %, and (D) tablet powder upon dissolution at 37 °C; blue circles indicate posaconazole dissolution in FaSSGF then FaSSIF, whilst red squares indicate posaconazole dissolution in FaSSIF only. An amount of ASD or tablet powder equivalent to 80 µg/mL of posaconazole was added to the acid stage; this decreases to 40 µg/mL in the FaSSIF stage. The dashed horizontal	

grey and green lines indicate the measured equilibrium solubility and LLPS concentration (amorphous solubility) of posaconazole in FaSSIF at 37 °C respectively (n = 3)..... 152

Figure A.2. Posaconazole nanodroplet particle concentration measurements for the 10%, 25%, and tablet powder, at high dose (blue columns) and low dose (green columns), upon dissolution in FaSSIF (n=3)..... 153

ABSTRACT

Supersaturating formulations have become a popular approach for enhancing the oral bioavailability of poorly water-soluble drugs. These formulation strategies can increase the intraluminal concentration by generating and maintaining supersaturation, which provides an enhanced driving force for *in vivo* absorption across the gastrointestinal tract membrane. Due to their inherent metastability however, crystallization in these systems can occur, negatively impacting their bioperformance. Therefore, it is critical to characterize the phase behavior and crystallization tendency of supersaturated solutions under biorelevant conditions in order to assess their potential for maximized oral absorption. Biorelevant media are commonly employed to simulate the presence of bile salts and phospholipids found in the human intestinal fluids. These endogenous surfactants which can form aggregates, micelles, mixed micelles and vesicles, can directly influence the *in vivo* stability of supersaturated solutions. Currently, there is little knowledge of how simulated and aspirated intestinal media can impact the complex phase behavior of supersaturated solutions. More importantly, commonly-used simulated media rely on oversimplified recipes in terms of bile salt composition. As a result, comprehensive understanding of how well simulated media correlate with aspirated media with respect to supersaturation stability and phase transition outcomes, is still lacking. The work presented within this thesis aims to address the knowledge gap by assessing the phase behavior of supersaturated solutions using complementary analytical approaches. Depending on the type of medium used to evaluate supersaturation, variations in crystallization outcomes can be observed. Therefore, this research provides insights into how media composition impacts solubility, supersaturation thermodynamics, phase transitions and crystallization kinetics of supersaturated solutions. This understanding can aid future efforts to optimize simulated media, design supersaturating formulations and predict their *in vivo* performance.

CHAPTER 1. INTRODUCTION

1.1 Research significance, specific aims and hypotheses

Modern advances in drug discovery strategies that are based on combinatorial chemistry and high throughput screening, have resulted in significant challenges in the area of drug development. In particular, drug candidates advancing through pharmaceutical pipelines are trending towards higher molecular weights and lipophilicity, resulting in poor aqueous solubility.^{1,2} In the context of oral drug delivery, supersaturating formulations, such as amorphous solid dispersions (ASDs), are usually employed to overcome the poor solubility of these drug molecules.^{3–5} By increasing the drug concentration in solution, in excess of the crystalline solubility, supersaturation drives rapid and sustained absorption, provided that crystallization is avoided. For oral drug delivery, intestinal drug absorption is a key process for determining bioavailability and systemic drug exposure. During dissolution, the passive absorption of a drug across a membrane is governed by the diffusive flux, which increases as the supersaturation level increases, therefore, the rate of drug delivery can be maximized *in vivo* for supersaturated systems.^{6–8} The supersaturated state is however, metastable, which drives the system to revert to a more energetically favorable state through crystallization to achieve the equilibrium solubility (with concurrent desupersaturation).^{9–11}

¹¹ *In vivo*, this decrease in solution concentration counteracts the solubility advantage of supersaturated systems, which can negatively impact absorption and bioavailability. During formulation of ASDs, crystallization inhibitors, usually polymers, are typically employed to maintain the supersaturated state over a physiologically-relevant time for absorption.^{5,12} Polymers delay crystallization by inhibiting nucleation and/or crystal growth. Although the precise mechanisms are not fully understood, it has been shown that polymers can increase the glass transition temperature of the system,¹³ decrease the molecular mobility,¹⁴ and form interactions with the drug such as hydrogen bonding.¹⁵ Since the phase behavior of supersaturated solutions is inherently complex, any prior knowledge of crystallization kinetics occurring during dissolution of supersaturating formulations, is of great significance. Various considerations have to be taken in account when assessing the dissolution and phase behavior of ASDs, such as the intrinsic solubility of the drug, the drug/polymer interactions the drug loading, and the overall degree of supersaturation.^{5,10} In addition, the impact of the dissolution media on the process itself can be a

crucial factor.¹⁶ Accordingly, understanding the phase behavior of supersaturated systems under biorelevant conditions can be regarded as critical to obtain a reliable prediction of intraluminal supersaturation. The use of biorelevant dissolution media that are designed to mimic and reflect the composition and physicochemical characteristics of the proximal human gastrointestinal tract, has grown as a standard tool to achieve an improved predictability of the *in vivo* dissolution behavior for oral formulations.^{17–20} Simulated intestinal fluids, containing bile salts and phospholipids, such as the fasted/fed-state simulated intestinal fluid (FaSSIF/FeSSIF) are available commercially. Other less conventional media like Ensure Plus®, a nutrition shake, have been often used in a clinical setting to simulate the gastric postprandial conditions.^{20–25} Unlike bile salt-based media, Ensure Plus® is an oil-in-water emulsion that contains a combination of fats, proteins, carbohydrates, vitamins, and electrolytes.²⁶ Little *in vitro* work has been undertaken to investigate supersaturation and phase behavior in biorelevant media, and most research in this area does not extend beyond the direct analysis of the drug release and the resulting solution concentration profiles. That said, achieving a more thorough characterization of supersaturated systems and phase behavior necessitates the incorporation of innovative and complementary methodologies, in the pursuance of a more comprehensive understanding of crystallization kinetics in these systems. Accordingly, the first aim of this work was to **elucidate the impact of using different *in vitro* media on phase behavior and crystallization kinetics of supersaturated solutions through complementary analytical approaches.** The hypothesis for this aim is:

Different types of media (simple buffers versus bile salt-based media versus lipid/protein-based media) will have a variable influence on the phase behavior of supersaturated solution formed following dissolution of ASDs.

For weakly basic drugs, the increase in pH during intraluminal transit from the gastric compartment to the intestinal compartment in the fasted-state, can drastically decrease their aqueous solubility, resulting in supersaturation (ionized to unionized state). Although the generated supersaturation is favorable for intestinal absorption to occur, there is also a higher driving force for precipitation.^{27–29} This becomes particularly interesting, when supersaturating formulating formulations like ASDs, comprise a weakly basic drug, formulated with an enteric polymer such hydroxypropyl methylcellulose acetyl succinate (HPMC-AS). These ASDs will form suspensions under gastric conditions, due to polymer insolubility at acidic pH,^{30–34} which will considerably delay drug release to the small intestine, where absorption is typically favored.

Therefore, *in vitro* dissolution experiments, for ASDs containing weak bases and pH-sensitive polymers, should take into consideration the pH-shift occurring during the gastrointestinal transit. In this regard, the second aim of this research was to **demonstrate that weak base ASDs can undergo expedited precipitation, which is drug loading-dependent, upon pH shift from a stomach simulated environment to an intestinal one.** The hypothesis for that aim is:

Crystallization induced in the ASD matrix during suspension in the gastric stage provides a source of seeds that creates a crystal burden upon media transfer to the intestinal stage, which will eventually promote further crystallization, even when supersaturation is initially observed. The extent and duration of supersaturation in the intestinal stage will depend on the degree of matrix crystallization, which is, in turn dictated by the drug loading of the system.

The presence of solubilizing species including bile salts and phospholipids, in addition to other solution properties such as pH, can greatly alter supersaturation and phase behavior of lipophilic compounds. Bile salts are endogenous surfactants that exist in GI tract, which can interact with drug molecules modifying their solubilities and supersaturation behavior.^{35–37} For supersaturating formulations, the impact of media composition on factors such as the amorphous solubility (maximum degree of supersaturation) and supersaturation duration, is poorly understood. In particular, comparisons between the thermodynamic properties and membrane transport rates of supersaturated drug solutions in simulated versus human intestinal fluids have not been made. Recent characterization studies of human intestinal fluids (HIF) have identified six main bile salts that constitute approximately 98.4% of the biological surfactant content in the gastrointestinal tract.³⁸ These include sodium taurocholate (STC), sodium taurodeoxycholate (STDC), sodium taurochenodeoxycholate (STCDC), sodium glycocholate (SGC), sodium glycocodeoxycholate (SGDC), and sodium glycochenodeoxycholate (SGCDC). The molecular structure of bile salts is distinctive with a steroid ring system to which three (STC and SGC) or two hydroxyl groups (STDC, STCDC, SGDC and SGCDC) are attached.^{39–41} The positioning/orientation of the hydroxyl or presence of tauro/glyco groups on the bile salt structure affect the critical micelle concentration (CMC) range, resulting in different solubilization capacities among the various bile salts.⁴² In addition to bile salts, lecithin (composed of a mixture of phospholipids) is another main component of HIF. The presence of lecithin has been shown to lower the CMC of bile salts and leads to the formation of mixed micelles.^{43,44} Theoretically, differences in solubilization capacities between media may impact the level of supersaturation extent when assessed on a concentration-

based criterion, i.e. amorphous to crystalline solubility ratio, as it has been typically employed in the literature.^{45,46} However, it is essential to evaluate supersaturation based on measurement of the solute activity, and to determine how well the concentration-based value correlates with the thermodynamic-based parameter. Accordingly, the third aim of this work was to **determine the true activity-based supersaturation level in simulated and aspirated media**. The hypothesis for this aim is:

Membrane transport rates, and subsequently the true supersaturation level, are dictated by the 'free' drug concentration in solution, when a crystalline/amorphous suspension is given.

Supersaturated solutions are thermodynamically metastable and therefore a high tendency exists for phase transitions to reduce their free energy through crystallization. Maintaining the maximum supersaturation for a physiologically-relevant timeframe for absorption is of critical importance for adequate *in vivo* performance. Bile salts were shown to greatly impact drug crystallization kinetics, where the nucleation inhibition ability of different bile salts was found to vary depending on the structure of both the bile salt and the drug.^{36,37,46,47} On the other hand, lecithin was noted to expedite drug crystallization.⁴⁶ Since these biological surfactants are not interchangeable from a crystallization standpoint, it is of critical importance to consider their impact on phase behavior in supersaturated solutions. Current recipes of commercially available simulated media (FaSSIF and FeSSIF) employ only varying concentrations of STC and lecithin.^{17,19,20} As mentioned before, other bile salts exist in HIF, yet are omitted from Fa/FeSSIF composition, and therefore these *in vitro* testing media are likely oversimplified. Therefore, the fourth and final aim of this thesis was to **investigate and compare the complex phase behavior and crystallization kinetics of supersaturated solutions in simulated and aspirated human fluids**. The hypothesis behind this aim was:

Compositional differences between current simulated and aspirated intestinal fluids will result in variable outcomes for nucleation and crystal growth kinetics of supersaturated solutions.

In summary, this thesis work presents an in-depth study on understanding and evaluating the phase behavior and crystallizations kinetics of supersaturated solutions in biorelevant and aspirated media. The thesis has five sections. The first section discusses the pharmaceutical significance, hypotheses and aims of this work, and reviews the essential background relevant to this research.

In the second section, a study is presented showing the impact of different media on dissolution and phase behavior of ASDs and demonstrating the applicability of combining complementary methods to characterize crystallization kinetics. The third section investigates the influence of pH-shift on phase transitions of ASDs, containing a weakly basic compound dispersed in a pH-sensitive polymeric matrix, through a multi-compartmental biorelevant dissolution setting. The fourth section details a study on the impact of different media on the crystalline and amorphous solubilities, supersaturation ratios and membrane transport rates, where both supersaturation and solubilization mechanisms occur concomitantly. Lastly, the fifth section describes a comparative study on evaluating nucleation and crystal growth kinetics of supersaturated solutions in different simulated and aspirated intestinal fluids.

1.2 Background

1.2.1 Crystalline versus amorphous solids

Understanding the physical properties of solids is crucial for successfully formulating oral delivery systems. Molecules in their solid form can exist in multiple different states. A crystalline solid has a highly ordered and symmetrical structure in the crystal lattice, which accounts for its high chemical and physical stability. In the solid state, intermolecular interactions exist between molecules in the form of hydrogen bonds or other noncovalent bonds (such as van der Waals forces or π - π interactions).⁴⁸ For crystalline solids, the periodic arrangement of molecules leads to lowered free energy and stabilization, and dictates the main physical properties of the resultant crystal such as the melting point, heat capacity and solubility.^{48,49} In a crystal lattice, the smallest unique arrangement of molecules is referred to as the unit cell. For organic compounds, a molecule can pack itself into different arrangements in the crystal lattice resulting in crystalline solids with different physical properties. This is referred to as polymorphism.⁵⁰ The most stable polymorph is the one that forms the most favorable packing arrangement in the crystal lattice, and subsequently has the highest melting point. Other forms of crystalline solids can also exist such as hydrates/solvates (water/solvent molecules are incorporated into the crystal lattice) and salts (the molecule is ionizable and a counterion is present in the lattice).⁵¹

Since crystalline lipophilic drug compounds exist in a thermodynamically stable state, this results in poor aqueous-solubility that limits their rate of dissolution. Amorphous materials on the other

hand lack the three-dimensional long-range order, while retaining the chemical identity of the molecule.⁵² Although they share the same type of intermolecular hydrogen bonding and other non-covalent forces as found in the corresponding crystalline state, the periodicity and molecular packing that define an ordered lattice structure are absent in these forms. At best, amorphous forms can have only some short-range order in their molecular arrangement.⁵³ Consequently, amorphous forms have greater free energy and molecular mobility in comparison to crystals, and are metastable relative to crystal forms. Since an amorphous solid possess a highly disordered structure, there are fewer bonds between molecules to be broken and this can facilitate the dissolution of the system when introduced to a medium. As a result, amorphous solids often demonstrate higher solubility compared to crystals, which subsequently can lead to enhanced bioavailability.^{3,54,55}

1.2.2 Thermodynamics of the amorphous state

Hancock and Zografi explained the variation of enthalpy or specific volume with relation to temperature in the amorphous glassy state, as demonstrated in Figure 1-1.⁵⁶ In the crystalline state, a minimal increase in enthalpy and volume is observed upon increasing the temperature, until the melting temperature (T_m) is reached, where there is a first-order phase transition to the liquid state. When the process is reversed and the temperature is reduced below the melting temperature, molecular motions starts to slow down significantly. This temperature reduction has to be rapid enough to avert crystallization.⁵⁶⁻⁵⁸ Both enthalpy or specific volume will follow an equilibrium line until a solidification point is reached; above this solidification point, the liquid is known as a supercooled liquid. During the transition process, the rapid reduction of temperature is accompanied by an increase in viscosity, where the molecules will move very slowly, and thus cannot reorient before the temperature is lowered again.^{56,57,59} Further cooling to a certain temperature results in a change in the temperature dependence of the enthalpy and volume. This specific temperature is known as the glass transition temperature (T_g), where a change in the slope is usually observed. The glass transition is an experimental phenomenon in which an amorphous system undergoes a reversible change from a supercooled liquid (above T_g) to a glassy-state like (below T_g), a process also referred to as vitrification.^{57,59,60} The cooling rate affects T_g , but not significantly (an order of magnitude change in cooling rate modifies T_g by 3-5°C).^{59,60} Below T_g , the unstable glassy material exists in a non-equilibrium state where the values of enthalpy and

specific volume are higher than would have been expected for the supercooled liquid.^{56,57,59,60} Additionally, glassy amorphous solids differ from those of the corresponding supercooled liquid, in having a lower heat capacity and molecular mobility than the latter.

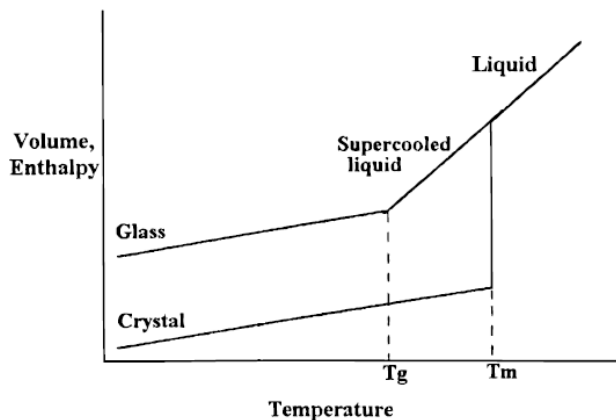


Figure 1-1. Variation of enthalpy/volume with temperature phase diagram.⁵⁶

1.2.3 Mixing energy and solubilization

As mentioned, the thermodynamics and kinetics of both the crystalline and amorphous states are inherently different, and phase transitions within these systems proceed from a higher energy state to a lower energy state. The free energy of mixing (ΔG_{mix}) can be given by:

$$\Delta G_{mix} = \Delta H_{mix} - T\Delta S_{mix} \quad (1-1)$$

Where ΔH_{mix} is the enthalpy of mixing, ΔS_{mix} is the entropy of mixing, and T is the temperature at which the mixing occurs. ΔH_{mix} depends on how strong the intermolecular interactions are, and can vary among the different polymorphs, or the amorphous form, for the same molecule. On the other hand, ΔS_{mix} promotes mixing, and the higher the degree of randomness and disorder in the system, the more favorable solubilization will be. Furthermore, temperature contributes to the entropy term, thus mixing becomes more feasible at higher temperatures. For solubilization to occur, the energy of the system has to overcome the intermolecular forces within the crystal lattice, through a heat and cool cycle. First, energy must be provided to heat the solid up to the melting point and break the bonds between molecules to form a liquid. The energy required for this process is the enthalpy of fusion (ΔH_f). This is followed by release of energy (cooling down), and then the liquid form of the compound (solute molecules) forms new interactions with the solvent molecules forming a homogenous solution. Together, these processes describe the solubilization process. In

an ideal solution, assuming all molecules are similar in size and polarity, the solubility is only dictated by the properties of the crystal and ΔH_f can be estimated from the melting data. ΔS_{mis} will be dependent on the mole fraction of the solute. The free energy change for forming a solution (ΔG_{soln}) can be best described as:⁶¹

$$\Delta G_{soln} = -RT \ln X_{solute} \quad (1-2)$$

Where R is the gas constant and X_{solute} is the crystalline solubility in mole fraction. Assuming ideality, this equation can be rearranged to be expressed in terms of mole fraction solubility, i.e. X_{solute} , whilst considering the difference in heat capacity (ΔC_p) between the solid and melt state.⁶² Accordingly, this yields equation (1-3):

$$\ln X_{solute} = \frac{-\Delta H_f}{R} \left(\frac{1}{T} - \frac{1}{T_m} \right) - \frac{\Delta C_p}{R} \left(1 - \frac{T_m}{T} + \ln \frac{T_m}{T} \right) \quad (1-3)$$

However, solute and solvent molecules differ in structure and interactions and thus real solutions deviate from ideality. In such a case, the activity coefficient (γ) describes the deviation of the system from ideality and where the product of γ and X yields the thermodynamic activity of a molecule (a). The solubility of real solutions can be then given by the following expression, where γ represents how far the system deviates from ideality:

$$\ln X_{solute} = \frac{-\Delta H_f}{R} \left(\frac{1}{T} - \frac{1}{T_m} \right) - \frac{\Delta C_p}{R} \left(1 - \frac{T_m}{T} + \ln \frac{T_m}{T} \right) - \ln \gamma \quad (1-4)$$

1.2.4 The amorphous solubility advantage

With the absence of a crystal lattice, the amorphous solubility for the same compound ($X_{amorphous}$) can be represented by a simpler equation and is dictated only by the activity coefficient of the molecule in water:

$$\ln X_{amorphous} = -\ln \gamma \quad (1-5)$$

To estimate the solubility advantage of the amorphous form, the free energy difference can be approximated using the Hoffman equation,⁶³ assuming that the heat capacity difference between the solid and liquid states, is constant, as described below in equation (1-6):

$$\Delta G_{c \rightarrow a} = \frac{\Delta H_m (T_m - T)}{T_m^2} \quad (1-6)$$

This can be rewritten with respect to the ratio of the solubility of the amorphous form (σ_a) and the crystalline form (σ_c), as shown in equations (1-7) and (1-8):³

$$\Delta G_{c \rightarrow a} = RT \ln \frac{\sigma_a}{\sigma_c} \quad (1-7)$$

$$\frac{\sigma_a}{\sigma_c} = e^{\frac{(\Delta H_m (T_m - T))}{RT}} \quad (1-8)$$

Given the higher tendency for water sorption in amorphous materials, an additional term $[-I(a_2)]$ is added as a correction factor for estimating the amorphous solubility of solids saturated with water.^{54,64} Additionally, a reduction in the amorphous solubility due to ionization can also be accounted for, as shown below:

$$\frac{\sigma_a}{\sigma_c} = e^{[-I(a_2)]} \times e^{\frac{(\Delta H_m (T_m - T))}{RT}} \times \left(\frac{1 - X_{crystal}^{ionized}}{1 - X_{amorphous}^{ionized}} \right) \quad (1-9)$$

1.2.5 Supersaturation

At equilibrium, the solution will have a certain amount of solute molecules completely dissolved, which is limited by the equilibrium solubility (C_{eq}), at a particular temperature. At this point, the system is described as ‘saturated’. If the concentration of solute molecules exceeds the equilibrium solubility, the system becomes ‘supersaturated’. Supersaturation (S) can be described as the ratio between the activity of a solute in the supersaturated solution and that of the solute in a saturated solution.⁶⁵ In the absence of solution additives, supersaturation can also be approximated by the ratio of solution concentration (C) and the equilibrium solubility (C_{eq}) as shown in equation (1-10):

$$S = \frac{a}{a_{eq}} \approx \frac{C}{C_{eq}} \quad (1-10)$$

For a saturated solution, the activity (a) of the dissolved solute is equal to that of the undissolved solute and is the product of the activity coefficient and supersaturation level (in this case $S=1$). In a supersaturated state ($S>1$), the activity increases, and subsequently the chemical potential (μ) of the solute increases. This can be illustrated by:⁶⁶

$$\mu = \mu_{eq} + \ln a \quad (1-11)$$

1.2.6 Crystallization

At higher μ , the tendency for phase transformation becomes more likely. In other words, as the supersaturation level increases, the driving force for crystallization increases, because the difference in chemical potential ($\Delta\mu$) between the solute molecules in the supersaturated state and in the equilibrium state, is larger, as noted by equation (1-12):

$$\Delta\mu = RT \ln S = RT \ln \frac{a}{a_{eq}} \quad (1-12)$$

In solutions, phase transformations can take place in different ways; the most common scenario is crystallization. Crystallization is the process by which the molecules nucleate to create a new crystalline phase and undergo subsequent crystal growth. Since the system is thermodynamically unstable, these new crystals will continue to grow until the supersaturated state is consumed and the system reverts to equilibrium. Crystallization is therefore composed of two stages; nucleation and crystal growth.

Nucleation

Nucleation describes the onset of the second phase and the formation of a stable nucleus. The classical nucleation theory (CNT) describes such process as the formation an ordered arrangement of molecules in a lattice structure (critical nucleus) that can resist the tendency to re-dissolve in solution.^{49,67} Nucleation can be divided into primary or secondary nucleation based on the absence or the presence of existing nuclei, respectively. Assuming the system is free of existing crystals, primary nucleation in solution can be homogeneous or heterogenous. Homogenous nucleation can only happen without the influence of foreign particles/surfaces in pure solutions, therefore it less common and usually observed in monodisperse systems of metals.⁶⁸ Heterogenous nucleation however, is a more common process and instigated by the presence of interfaces in the system.⁶⁹ According to CNT, the rate of nucleation (J) is dependent on the energy required to form a critical nucleus (ΔG_{crit}), one that will eventually grow into a crystal, as illustrated in equations (1-13) and (1-14):

$$J = J_o \exp\left(\frac{-\Delta G_{crit}}{K_B T}\right) \quad (1-13)$$

$$\Delta G_{crit} = \Delta G_v + \Delta G_s \approx \frac{16 \pi \gamma_s^3}{3 S^2} \quad (1-14)$$

Therefore, ΔG_{crit} is a balance between the free energy of interface (ΔG_s) which is unfavorable, and the volume free energy (ΔG_v) which is favorable.⁴⁹ K_B is the Boltzmann constant, T is the temperature and γ_s is the interfacial tension. ΔG_{crit} is the energy barrier that must be overcome for a stable nucleus of critical size (r_{crit}) to form. This balance is illustrated in the free energy diagram in Figure 1-2. r_{crit} is given by:

$$r_{crit} = \frac{-2\gamma_s}{\Delta G_v} \quad (1-15)$$

The expressions above in equations (1-13) and (1-14) were reworked by Volmer who reconsidered the mechanisms and kinetics of nucleation dependence on other factors as the molecular volume, monomer attachment frequency and the stationary rate of homogeneous or heterogeneous nucleation.^{70,71} As a result, J is now more commonly now described as:

$$J = A \exp\left(\frac{16\pi v_o^2 \gamma_s^3}{3(K_B T)^3 (\ln S)^2}\right) \quad (1-16)$$

Where A is the pre-exponential kinetic parameter and v_o is the molecular volume. A is influenced by several factors and can be expressed as:⁷⁰

$$A = f Z n \quad (1-17)$$

In Equation (1-17), f is the rate of monomer attachment to the critical nucleus, whether through volume diffusion of solute or interface transfer. Z is the Zeldovich factor which is the probability of formation or dissolution of the crystal nucleus. Finally, n is the number density of molecules in solution. Overall, the CNT considers many assumptions to drive equation (1-16), most notably is that the model assumes free and direct exchange of solution molecules with the growing nucleus. The CNT has been also criticized for other limitations such as the assumption of spherical particles and reliance on ‘critical radius’.^{67,71} Additionally, the CNT model assumes sequential addition of monomers and does not account well for the presence of additives in the system. These shortcomings of the CNT led to the development of another model, the two-step nucleation theory. The two-step nucleation theory was originally developed to describe nucleation in proteins. In the two-step nucleation mechanism, a sufficient-sized disordered cluster of solute molecules forms initially.^{67,72} This is usually referred to as the formation of a dense liquid-phase, which is metastable to both the solution and crystal phase. This is then followed by rearrangement of these molecules into an ordered structure forming the crystalline phase, which is the rate-limiting step

for nucleation.^{67,72} To date, there is still debate about the applicability of these nucleation theories and mechanisms. Some nucleation experimental data fit well within the CNT analytical simplicity (ex. dilute systems), whereas some other systems demonstrate an evidence of a transient dense liquid-phase before crystallization.⁷²

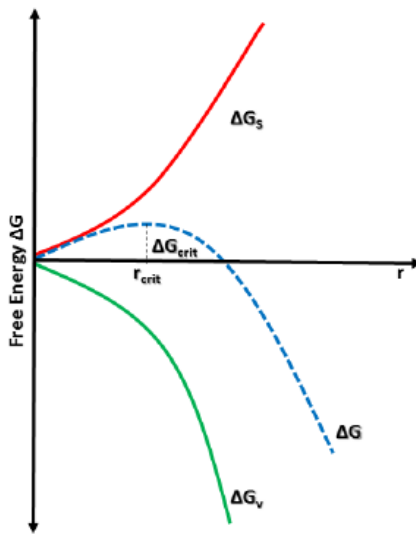


Figure 1-2. Free energy diagram for CNT. Adapted from Erdemir et al.⁶⁷

Crystal Growth

Once nucleation has commenced, the kinetics of crystal growth dominates the system.⁴⁹ In solution crystallization, crystal growth will proceed at the expense of supersaturation until equilibrium is reached. Crystal growth is usually simplified by the equation:

$$R_G = K_G(C - C^*)^g \quad (1-18)$$

Where R_G is the overall growth per unit area, K_G is the crystal growth coefficient and g is the order of the crystal growth process (typically between 1 and 2). $C-C$ represents the driving force for crystal growth where C is the solute concentration in the supersaturated solution and C^* is the equilibrium concentration. Crystal growth involves two main stages; diffusion and integration. First, the solute molecules arrive at the crystal face with some freedom to migrate forming an adsorbed layer. The attachment occurs at the certain favorable (or kink) sites, usually defects at the surface where more interactions are possible. The integration is complete as the molecules become part of the lattice. This goes layer-by-layer where the addition of new molecules to the

surface will continue to create new kink sites for further deposition. The presence of additives in the systems however could greatly alter the kinetics of crystal growth.

1.2.7 Liquid-liquid phase separation

For highly supersaturated solutions, another phase transformation that can occur is liquid-liquid phase separation (LLPS). LLPS is a phenomenon where drug-rich phase aggregates are formed in solution, which are colloidal and non-crystalline. LLPS occurs when the concentration of solute molecules exceeds the amorphous solubility and marks the upper limit of supersaturation.^{73,74} The mass flow across a membrane is a function of the thermodynamic activity of the ‘free’ drug in solution. Once LLPS is reached, the amount of ‘free’ drug is steady, and hence the thermodynamic activity is constant, and the diffusive flux becomes relatively constant for concentrations beyond that limit.⁷⁵ The formation of these amorphous drug-rich aggregates has been hypothesized to be beneficial for oral drug delivery, by continuously replenishing the absorbed drug.^{75,76} It should be noted that supersaturated solutions containing drug-rich LLPS aggregates will only exist if crystallization is prevented or retarded. Additives such as polymers, are often used to stabilize the resultant drug-rich colloids.⁷⁷⁻⁷⁹ Figure (1-3; adapted from reference 75) demonstrates two alternative scenarios of supersaturated systems with LLPS; one is stabilized and supersaturation is maintained, whereas the other crystallization has occurred. In the second outcome, the solution concentration drops reducing the driving force for membrane transport.⁷⁵

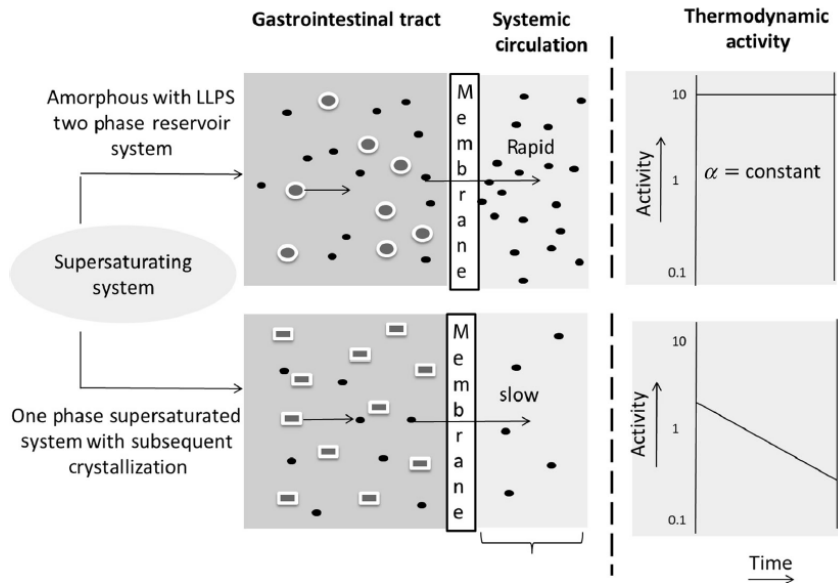


Figure 1-3. Schematic comparing two supersaturated systems with LLPS.⁷⁵ The upper system is stable, and supersaturation is maintained and hence membrane transport is maximized. The lower system underwent crystallization, thus depleting the supersaturated state and reducing membrane transport.

1.2.8 Phase-boundaries of supersaturated solutions

Figure 1-4 demonstrates a concentration/temperature diagram and summarizes the phase boundaries of supersaturated solutions, as discussed in previous sections. In region I, the concentration is below the equilibrium solubility (unsaturated), and the solution phase is stable. Above the equilibrium solubility (region II), the system is thermodynamically metastable as the supersaturation ratio is greater than 1, yet the solution is still one-phase. Crystallization (nucleation and crystal growth) can occur in this zone, depending on the level of supersaturation, and how relatively stable the system is (e.g. absence/presence of a crystallization inhibitor). Finally, in region III, the solution concentration is high enough to exceed the amorphous solubility (LLPS boundary), and any further concentration addition contributes to the drug-rich phase, rather than the ‘free’ drug in solution. In this region, supersaturation is maximized, and therefore spontaneous nucleation will occur.^{49,72}

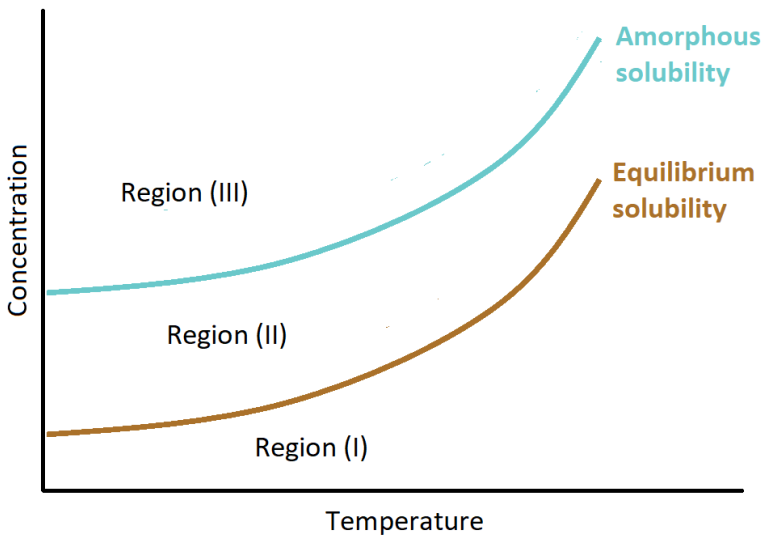


Figure 1-4. Schematic illustrating phase boundaries in solution with respect to concentration and temperature.

1.2.9 Dissolution of ASDs

Dissolution is a process by which drug molecules (solute) leave the crystal lattice, and form new bonds with the solvent molecules, and subsequently become a one-phase solution. Dissolution is the primary step preceding the absorption process in the GI tract, and the rate at which dissolution takes place (dC/dt) can be summarized by the Noyes-Whitney equation:

$$\frac{dC}{dt} = \frac{D \times A (C_s - C_b)}{h} \quad (1-19)$$

Where D is the diffusion coefficient, A is the surface area of the solid, C_s is the saturation solubility at the diffusive layer, C_b is the bulk solution concentration, and h is the thickness of the diffusion layer. Aside from parameters that are dependent on the intrinsic properties of the compound (D), or the physiological characteristics (h), the dissolution rate can potentially be enhanced by other formulation means. One way is to decrease the particle size, and therefore increase the available surface area (A) for dissolution. Another way is to increase the apparent solubility by using a supersaturating delivery system (e.g. an ASD), thereby generating a supersaturated solution. In contrast to equilibrium solubility, the term ‘apparent solubility’ is usually used to refer to the solution concentration of a solid that is not the most stable form i.e. when using the amorphous form.^{11,80,81} Evaluation of the dissolution performance of ASDs is one of the most important characterization steps in amorphous materials research. For these high energy systems, various

scenarios can take place during the dissolution process. Upon introduction of ASDs to dissolution media, a thermodynamically-unstable supersaturated state is generated. The dissolution profiles of ASDs have been traditionally described using the ‘spring and parachute’ approach.⁸² First, the ASDs undergo an accelerated dissolution rate resulting in a higher apparent solubility of the free drug in solution. This supersaturated state has to be maintained for enough time for absorption to take place, and therefore precipitation would have to be inhibited using ‘precipitation inhibitors’, which are usually polymers present in the formulations. Precipitation inhibitors such as polymers can prevent or delay the onset of crystallization in these solutions, thereby preserving their supersaturated state. The spring and parachute model is illustrated in Figure 1-5. As shown, a typical dissolution profile of a stable ASD - usually in the presence of a good precipitation inhibitor - will exhibit an accelerated dissolution rate (solid black line), followed by a relatively sustained supersaturation for a prolonged time (dashed green line), where the rate of phase separation is slow. If a rapid desupersaturation occurs due to nucleation and crystal growth (dashed red line), the solution concentration drops down to the equilibrium solubility of the crystalline form (dashed black line).

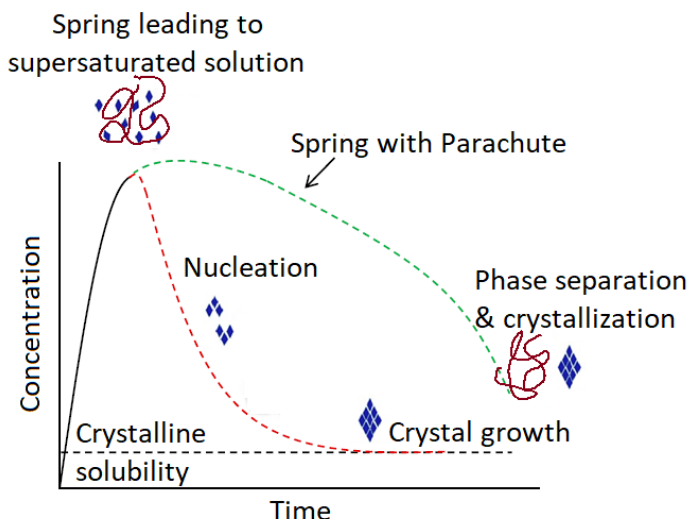


Figure 1-5. Spring and parachute model for the dissolution of ASDs.
Adapted from Williams et al.⁸³

1.2.10 Routes of crystallization during dissolution of ASDs

Crystallization during the dissolution of an ASD can occur once phase separation has occurred between the drug and the stabilizing precipitation inhibitor i.e. the polymer. Both the dissolving

amorphous material and the generated supersaturated solution are thermodynamically unstable, therefore crystallization can initiate from either phase. The kinetics of this phase transformation is governed by many factors including the drug solubility, the drug loading, the overall effectiveness of the polymer, temperature, the supersaturation level, and the composition of the dissolution medium. If the rate of crystallization is rapid once the ASD comes in contact with the dissolution medium, supersaturation will not be observed, and the solution concentration-time profile will be similar to that of the crystalline material. In this case, crystallization initiates at the surface or in the bulk of the solid amorphous material during dissolution. This route of crystallization usually implies a rapid phase separation between the drug and the stabilizing precipitation inhibitor i.e. the polymer. Alternatively, if no crystallization occurs in the dissolving matrix, crystallization may then commence from the supersaturated solution phase. This second route is referred to ‘solution-mediated crystallization’, and it dictates the longevity of the supersaturation during dissolution. Previous studies have demonstrated these different routes of crystallization for ASDs of different drugs including felodipine, indomethacin and celecoxib.^{10,81} In some instances, supersaturation can be observed only transiently, and both mechanisms can be observed together causing the short-lived supersaturation to be rapidly depleted. In either case, once crystal nuclei are formed, they act as seeds that grow rapidly during the dissolution process, and accordingly the amorphous solubility advantage will be lost. A summarized illustration of the competing processes of supersaturation and crystallization occurring during dissolution of ASDs, is depicted in Figure 1-6.

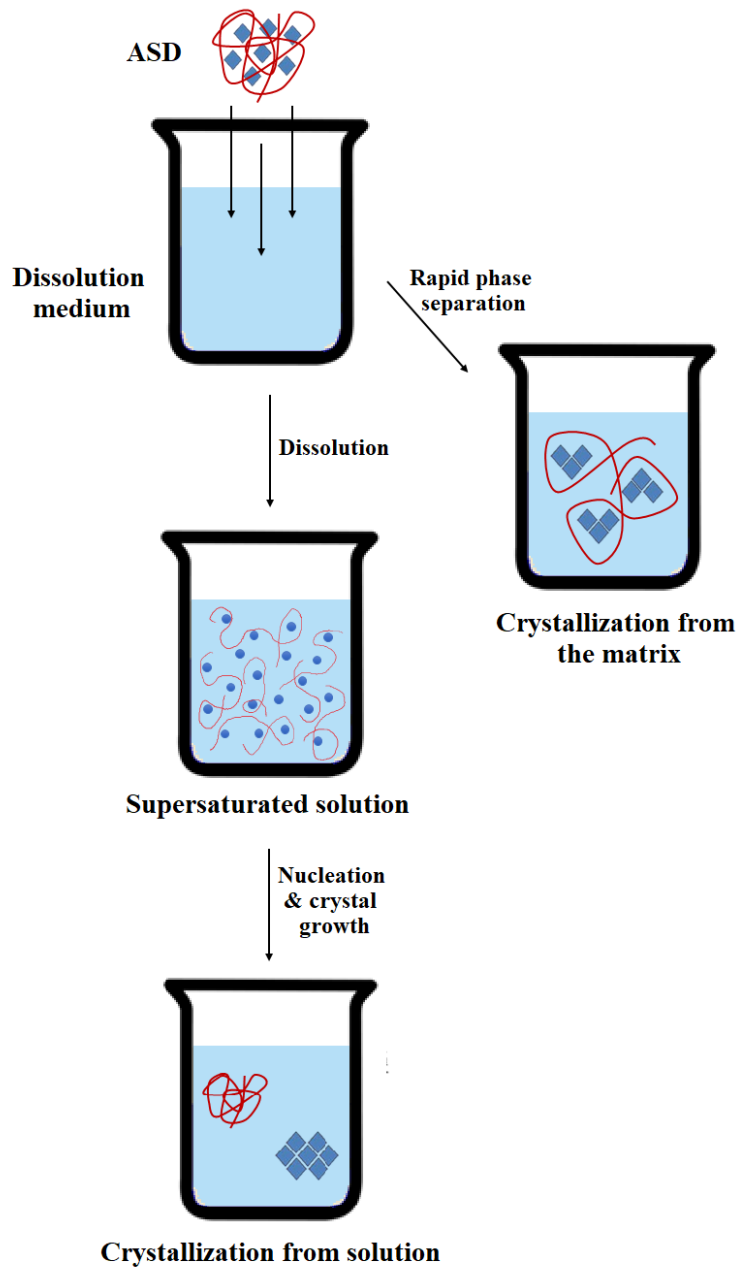


Figure 1-6. Schematic illustration of crystallization routes during dissolution of ASDs: Crystallization from the dissolving matrix vs. solution-mediated crystallization.

CHAPTER 2. VARIATION IN SUPERSATURATION AND PHASE BEHAVIOR OF EZETIMIBE AMORPHOUS SOLID DISPERSIONS UPON DISSOLUTION IN DIFFERENT BIORELEVANT MEDIA

This chapter is a reprint with minor modifications of a manuscript published in *Molecular Pharmaceutics* in November 2017 with the same title by: Ahmed Elkhabaz, Sreya Sarkar, Janny K. Dinh, Garth J. Simpson, and Lynne S. Taylor.

2.1 Abstract

The delivery of poorly water-soluble drugs using amorphous solid dispersions (ASDs) has been widely acknowledged as a promising strategy for enhancing oral bioavailability. Upon dissolution, ASDs have accelerated dissolution rates and yield supersaturated solutions leading to higher apparent solubilities. Understanding the complex phase behavior of ASDs during dissolution is crucial for developing an effective formulation. Since the absorption of a lipophilic, high permeability drug is determined primarily by the intraluminal dissolution process and the final concentration achieved, there is a need for evaluation in biorelevant dissolution media that simulate both fasting and fed gastrointestinal states. In this study, using ezetimibe as a model drug, three different ASDs were prepared using polyacrylic acid (PAA), polyvinyl pyrrolidone (PVP), and hydroxypropyl methylcellulose acetyl succinate (HPMC-AS). Dissolution of ASDs was carried out in sodium phosphate buffer, fed-state simulated intestinal fluid (FeSSIF), and Ensure Plus®, to evaluate the impact of different dissolution media on release profile, supersaturation and phase behavior. The supersaturation level and crystallization kinetics varied among the dispersions and were found to be highly dependent on the medium employed. The presence of solubilizing additives in biorelevant media greatly affected the generation and stabilization of supersaturated solutions. Second harmonic generation microscopy was found to enable the detection of crystals in all media, including the highly turbid Ensure Plus® system. In conclusion, it is important to evaluate the impact of complex biorelevant media on the dissolution performance of ASDs to better design supersaturating formulations for oral delivery.

2.2 Introduction

Contemporary drug discovery approaches over the last few decades have resulted in a pipeline of molecules trending towards higher molecular weight and greater lipophilicity, a situation which is unlikely to be remedied in the foreseeable future.^{84,85} As a consequence of the typically sub-optimal solubility of such compounds, various formulation strategies have been implemented to enhance the drug solubility and bioavailability, following oral dosing. Approaches such as amorphous solid dispersions (ASDs) have been shown to accelerate dissolution rates and generate supersaturated solutions upon introduction to aqueous media.^{3,4} A supersaturated solution has a solute concentration that exceeds that achieved by dissolving the thermodynamically stable crystalline form.^{5,56} Despite potential benefits for oral drug delivery, supersaturation is a metastable state, hence the system has the potential to undergo phase transformation to a lower energy state, through crystallization, resulting in a decrease in the dissolved drug concentration (desupersaturation).^{10,86} Several considerations should be taken into account when assessing the dissolution behavior of an amorphous solid dispersion (ASD) including the intrinsic solubility of the drug, the drug loading, and the overall degree of supersaturation that can be achieved following dissolution in a given volume. In addition, the impact of the media employed for dissolution testing can be a crucial factor.⁸⁷ Studies have shown that the solubility of a hydrophobic drug is not only dependent on its crystallinity, melting point and partition coefficient, but also on the medium into which it dissolves.^{17,18,88} Thus for conventional immediate release formulations, dissolution experiments performed in simple aqueous media have often demonstrated poor predictive capability of the *in vivo* performance after oral administration, particularly for poorly water-soluble molecules.⁸⁹ Accordingly, establishment of a good *in vitro-in vivo* correlation (IVIVC) requires an *in vitro* dissolution testing environment that can simulate the realistic composition and hydrodynamics of the gastrointestinal lumen. For highly lipophilic drugs, fed vs. fasted state effects were successfully predicted from *in vitro* dissolution data, showing good correlations with the *in vivo* performance upon oral administration.^{20,87}

The physicochemical properties of the gastrointestinal contents such as pH, buffer capacity, osmolality, surface tension, and the presence of solubilizing species, can greatly alter the extent and duration of supersaturation achieved following dissolution of an amorphous formulation. Thus, intraluminal components such as bile salts and phospholipids can affect the dissolution phase

behavior and the degree of supersaturation.⁵ Bile salts are endogenous surfactants that can interact with drug molecules modifying their crystallization kinetics and supersaturation behavior.^{35–37} It is also possible that synergistic effects may arise between bile salts and polymers present in the formulation, which can affect both the generation and the stabilization of supersaturated solutions.

In order to minimize time and costs associated with conducting pharmacokinetic and clinical studies, *in vitro* dissolution tests should be ideally designed to be capable of predicting the *in vivo* bioavailability of drug formulations. In this regard, the use of dissolution media that are designed to mimic and reflect the composition and physicochemical characteristics of the proximal human gastrointestinal tract are considered key to achieve these goals.²⁰ Consequently, the use of biorelevant media has grown as a standard tool to achieve an improved predictability of the *in vivo* dissolution behavior for immediate release formulations.^{19,20} In contrast, for supersaturating formulations, little *in vitro* work has been undertaken to investigate supersaturation and detailed phase behavior in biorelevant media; such studies would presumably lead to improved insight into the intraluminal supersaturated state.

The goal of this study was to characterize the phase transformations occurring during the dissolution of ezetimibe ASDs, upon introduction to different dissolution media. Ezetimibe is a biopharmaceutics classification (BCS) class II drug with suboptimal aqueous solubility, that has been indicated for lowering cholesterol levels in the blood.⁹⁰ Ezetimibe is a weak acid due to the presence of a phenol group, with a pKa of 9.72, and therefore it is primarily un-ionized across the physiological pH range.⁹¹ ASDs of ezetimibe: polymer (50:50 w/w) were prepared with polyacrylic acid (PAA), polyvinyl pyrrolidone (PVP), and hydroxypropyl methylcellulose acetyl succinate (HPMC-AS). Dissolution testing was performed in different media including sodium phosphate buffer (10 mM, pH 6.8), fed state simulated intestinal fluid (FeSSIF) and Ensure Plus®. Both FeSSIF and Ensure Plus® are well-established biorelevant media, and have been widely used to mimic intestinal and gastric fed state conditions respectively.^{19–25,87,92,93} Additionally, the utility of second order nonlinear optical imaging of chiral crystals (SONICC) for the detection of crystallization in turbid biorelevant media was explored. SONICC has been previously shown to be a powerful analytical tool for the identification and detection of chiral crystals.^{94–97} SONICC relies on second harmonic generation (SHG), a phenomenon that describes a nonlinear interaction between light and matter and can only arise in systems lacking inversion symmetry (non-

centrosymmetric), as in the case of chiral crystals. In contrast, in an isotropic system, such as a solution or amorphous solid, there is an equal probability for all molecular orientations resulting in nearly perfect cancellation, and therefore no coherent SHG signal generation. Ezetimibe contains three chiral centers (two are located on the β -lactam ring, while the last one (alcohol) is present in the side chain),⁹⁸ and is therefore expected to crystallize into an SHG-active space group, enabling this approach to differentiate between undissolved amorphous material/dissolution media components and crystals.

2.3 Materials

Ezetimibe monohydrate (Cambridge Structural Database ref code QATNEF), which crystallizes as the orthorhombic SHG-active space group ($P2_12_12_1$) (Figure 2-1A) was purchased from Attix Pharmaceuticals (Toronto, Ontario, Canada). Polyacrylic acid (PAA) and polyvinyl pyrrolidone (PVP) K29/32 were supplied by Sigma-Aldrich (St. Louis, MO), while hydroxypropyl methylcellulose acetyl succinate (HPMC-AS) MF grade was supplied by Shin-Etsu Chemical Co. (Tokyo, Japan). Methanol and acetonitrile were purchased from Fisher Scientific (Pittsburgh, PA). FaSSIF/FeSSIF/FaSSGF powder (Version 1) was acquired from Biorelevant (London, UK). Ensure Plus® vanilla nutrition shake (8 oz bottles) was obtained from Abbott Laboratories (Chicago, IL).

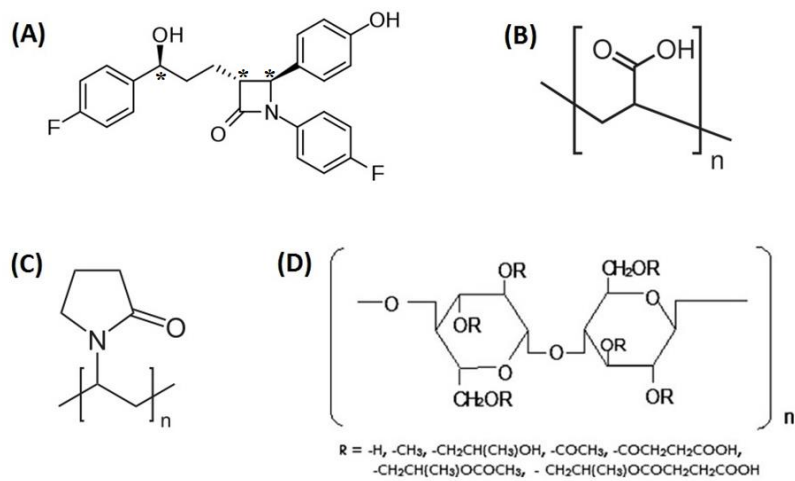


Figure 2-1. Molecular structures of (A) Ezetimibe, (B) PAA, (C) PVP and (D) HPMC-AS. Chiral centers are marked on (A) ezetimibe by (*).

2.4 Methods

2.4.1 Equilibrium solubility experiments of ezetimibe in different media

To determine the equilibrium crystalline solubility of ezetimibe in different media, an excess amount of the drug was added to sodium phosphate buffer (10 mM, pH 2.0), FeSSIF and Ensure Plus®. Due to the strain of the beta-lactam ring, ezetimibe is susceptible to hydrolysis where several degradation products can form under neutral-alkaline conditions. Previous stability studies of ezetimibe have reported that ezetimibe undergoes intramolecular rearrangement of the beta-lactam ring forming an amide and a tetrahydropyran ring in aqueous tertiary amine buffers (pH 7-12) at 39°C,⁹⁹ and in sodium phosphate buffer (pH 6.8) at room temperature.¹⁰⁰ Accordingly, the solubility measurements in buffer were carried out at low pH to avoid degradation; ezetimibe does not undergo ionization at pH 2. Samples were stirred at 300 rpm at 37°C for 48 hours. Both sodium phosphate buffer (10 mM, pH 2) and FeSSIF, solutions were then ultra-centrifuged at 35,000 rpm for 30 minutes at 37°C, using an Optima L-100 XP ultracentrifuge equipped with Swinging-Bucket Rotor SW 41 Ti (Beckman Coulter, Inc., Brea, CA). For the samples in Ensure Plus®, a similar approach to the one described by Diakidou et al. was used.¹⁰¹ Briefly, samples were centrifuged at 14,800 rpm (21,000 g) for 20 minutes at 8°C to facilitate phase separation, using a Sorvall Legend™ Micro 17 Centrifuge (Thermo Fisher Scientific, Waltham, MA). This resulted in phase separation into an upper oily phase, an intermediate aqueous phase, and a lower pellet phase. Both the aqueous and oily phases were isolated separately, diluted in acetonitrile, vortexed for 30 seconds, and further centrifuged at 14,800 rpm (21,000 g) for an additional 15 minutes to extract the solubilized ezetimibe concentration in both phases, and precipitate the remaining components from Ensure Plus®. For all sodium phosphate buffer (10 mM, pH 2.0), FeSSIF and Ensure Plus® samples, the supernatant was further diluted in methanol and the ezetimibe solution concentration was determined using an Agilent HP 1260 high performance liquid chromatography (HPLC) system (Agilent Technologies, Santa Clara, CA). The chromatographic separation was performed with an Agilent Eclipse Plus C18 column (4.6 mm × 250 mm, 5 µm). The mobile phase consisted of water and acetonitrile (40:60 by volume). Each analytical run duration was 12 minutes, where the injection volume was 20 µL and the mobile phase flow was held constant at 1.0 mL/min. Ezetimibe was detected by ultraviolet (UV) absorbance at a wavelength of 233 nm. A single peak was observed in the chromatogram for all solubility experiments indicating that degradation was

avoided over the equilibration period. Standards (0.05 - 10 µg/mL) were prepared in methanol, where the standard curve exhibited good linearity ($r^2 = 0.9998$) over this concentration range.

2.4.2 Liquid-liquid phase separation (LLPS) onset determination using ultraviolet (UV) spectroscopy

The formation of an ezetimibe drug-rich colloidal phase was evaluated using UV spectroscopy, to determine the concentration at which LLPS was observed in both sodium phosphate buffer (10 mM, pH 6.8) and FeSSIF as described before.^{74,102} Briefly, the UV extinction was monitored at 350 nm as a function of ezetimibe concentration to determine the concentration at which phase separation occurs, using a UV fiber optic dip probe coupled to SI Photonics UV/vis spectrometer (Tucson, AZ). Experiments were performed at 37°C using a Kontes jacketed beaker (Randor, PA) connected to a Julabo MA water bath (Seelbach, Baden-Wurttemberg, Germany), stirred at 300 rpm, and ezetimibe was added to the system using an Advance 1200 Syringe Pump (Gaithersburg, MD) at a rate of 2 µg/min in the presence of small amounts of PVP and HPMC-AS (1-2 µg/mL).

2.4.3 Nucleation induction time experiments using UV spectroscopy

Supersaturated solutions of ezetimibe in aqueous sodium phosphate buffer (10 mM, pH 6.8) and FeSSIF were generated at 21 and 123 µg/mL respectively, and the changes in UV spectra were monitored as a function of time, using the UV system described above, at 30-second intervals. Experiments were performed at 37°C using a jacketed beaker water bath, with solutions stirred at 300 rpm.

2.4.4 Preparation of ezetimibe bulk ASDs

Binary ASDs, 50:50 w/w drug: polymer, were prepared using the solvent evaporation method. 500 mg of ezetimibe and 500 mg of PAA, PVP or HPMC-AS were dissolved in methanol, and the solvent was removed by rotary evaporation at 45°C, followed by overnight drying in a vacuum oven. The resultant dispersions were cryo-milled using a 6750 Freezer/Mill (Metuchen, NJ) to obtain a fine powder. Polarized light microscopy and SHG microscopy were used to inspect prepared ASDs to confirm the absence of detectable crystallinity prior to dissolution experiments.

All ASDs were freshly prepared for the dissolution experiments and stored in closed vials with indicating Drierite desiccants at room temperature.

2.4.5 Dissolution studies of ezetimibe ASDs

An amount of 15 mg of 50:50 ezetimibe-polymer ASD was added to 15 mL of either sodium phosphate buffer (10 mM, pH 6.8), FeSSIF or Ensure Plus®. All dissolution experiments were performed at 37°C, and stirred at 300 rpm. For dissolution experiments in sodium phosphate buffer (10 mM, pH 6.8) and FeSSIF, samples were filtered through 0.45 µm glass fiber syringe filters (Tisch Scientific, North Bend, OH), followed by dilution of the supernatant in methanol, and ezetimibe solution concentrations were measured applying the same HPLC method used for solubility experiments, at different time points. No signs of degradation were observed in the chromatograms for ezetimibe ASDs dissolution in pH 6.8 buffer. For Ensure Plus® dissolution samples, phase separation and isolation of ezetimibe solution concentration could not be achieved using direct filtration approaches. Accordingly, all Ensure Plus® dissolution samples were centrifuged and analyzed with HPLC in a similar fashion to the solubility experiments. The time point was taken as the time at which the first cycle of centrifugation commenced.

2.4.6 Polarized light microscopy and powder X-ray diffraction (PXRD) for evaluation of ezetimibe suspended ASDs

An Eclipse E600 POL polarized light microscope equipped with DS-Fi1 camera (Nikon Corporation, Tokyo, Japan) was used to evaluate the presence or absence of birefringence in ezetimibe ASDs suspended/dissolved in both sodium phosphate buffer (10 mM, pH 6.8) and FeSSIF. Additionally, precipitates pelleted by centrifugation of solutions sampled from the dissolution experiments in FeSSIF, were further assessed for crystallinity by PXRD analysis. After removing the supernatant, the pellet was removed using a spatula and the water content was reduced by carefully applying a gentle airflow (Fisherbrand Air’It Aerosol, Houston, TX) for a few minutes. PXRD evaluation was then performed using a Rigaku Smartlab™ diffractometer (Rigaku Americas, The Woodlands, TX) equipped with a Cu-K α radiation source and a D/tex ultra-detector. Glass sample holders were used and powder patterns were obtained from 5-50° 2θ at a scan speed of 4°/min and a step size of 0.02°. The voltage and current used were 40kV and 44mA respectively. Polarized light microscopy and PXRD experiments were unsuccessful for

ezetimibe ASDs dispersed in Ensure Plus®, due to the extensive turbidity of the media, and inability of these methods to distinguish any crystalline material from other media components.

2.4.7 Detection of crystallization during dissolution of ezetimibe ASDs using SHG microscopy

The evolution of ezetimibe crystallinity during ASD dissolution in sodium phosphate buffer (10 mM, pH 6.8), FeSSIF and Ensure Plus® was investigated as a function of time using SHG microscopy. All three media were confirmed to show no significant SHG background signal prior to adding the prepared dispersions for dissolution. Dissolution experiments were performed as described above, and samples for SHG analysis were prepared by removing a small aliquot of the dissolution media at different time points. Each sample was pipetted into a round nylon 6/6 flat washer (inner diameter: 6.069 mm, outer diameter: 11.938 mm, thickness: 0.381 mm, Small Parts Inc., Logansport, IN) mounted on a glass slide. A coverslip was then added to form a small liquid cell of known thickness. SHG images were acquired using a commercial SHG microscope instrument manufactured by Formulatrix (Waltham, MA). This instrument utilizes a Fianium FemtoPower laser (1064 nm, 51 MHz repetition rate and a 166 fs pulse width) equipped with resonant mirror/galvanometer beam scanning (8 kHz fast axis) to generate images. All SHG microscopy images were acquired with 350 mW infrared (IR) power and an exposure time of 894 milliseconds. SHG microscopy images had fields of view of dimensions of 1925 µm × 1925 µm, and scans were obtained in different focal planes in the Z direction, with 100 µm increments. SHG imaging analysis was performed using ImageJ 1.05b software. The number of new particles formed per unit time can be obtained by using the built-in particle counting algorithm in ImageJ from the time dependent SHG images. Low background and high contrast in SONICC images makes quantitative evaluation of nucleation rate (number of particles formed per unit time per unit volume) and crystal growth rate (size of particles per unit time) possible. Nucleation rates can be monitored from a standard threshold-based particle counting algorithm from a single set of measurements with multiple fields of views.

2.5 Results

2.5.1 Equilibrium solubility experiments of ezetimibe in different media

The aqueous solubility of crystalline ezetimibe monohydrate at 37°C was found to be 0.97 µg/mL. The equilibrium solubility values in the different media, in the absence and presence of polymers, are summarized in Table 2-1. FeSSIF resulted in a nearly twenty-fold enhancement in solubility. The highest solubilities were observed in Ensure Plus®; approximately 48 and 162 µg/mL were dissolved in the aqueous and the oily phases respectively. Generally, the presence of polymers had minor effects on the measured solubility values in these media.

Table 2-1. Equilibrium solubility of ezetimibe in three different media at 37°C. (n=6).

Medium	Equilibrium solubility (µg/mL)			
	No polymer	+10 µg/mL of PAA	+10 µg/mL of PVP	+10 µg/mL of HPMC-AS
Sodium phosphate buffer (10mM, pH 2)	0.97 ± 0.09	0.93 ± 0.08	0.9 ± 0.1	NP*
FeSSIF	18.6 ± 0.6	18.3 ± 0.7	19.7 ± 0.9	26.3 ± 0.7
Ensure Plus® - aqueous phase	48 ± 3	45 ± 1	53 ± 3	51 ± 3
Ensure Plus® - oily phase	162 ± 9	166 ± 13	169 ± 6	179 ± 5

*NP, not performed.

2.5.2 LLPS onset determination using UV spectroscopy

The formation of a non-crystalline drug-rich phase in highly supersaturated solutions marks the commencement of liquid-liquid phase separation. To determine the concentration at which LLPS occurs in ezetimibe supersaturated solutions, UV extinction was monitored at a non-absorbing wavelength (350 nm), where an increase in turbidity is considered indicative of the formation of a second phase. Data were collected in the presence of a small amount of polymer (2 µg/mL), in order to inhibit crystallization, in both sodium phosphate buffer (10 mM, pH 6.8) and FeSSIF at 37°C with results presented in Table 2-2. In buffer, light scattering increased rapidly when the ezetimibe concentrations reached approximately 21 µg/mL (Figure 2-2). In FeSSIF, the value increased to approximately 120 µg/mL.

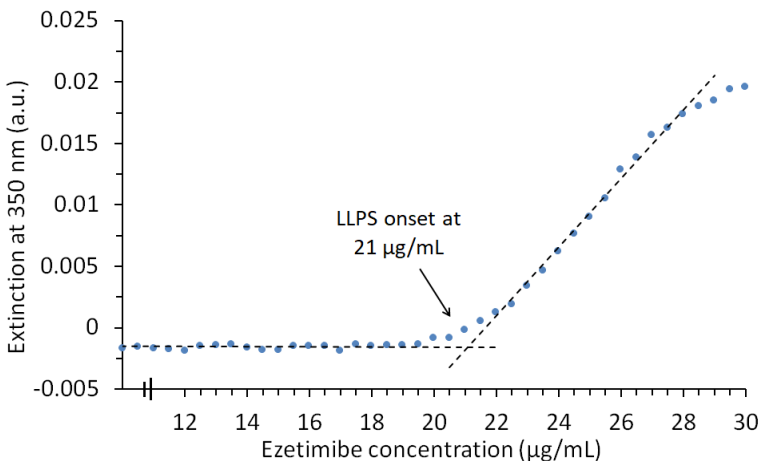


Figure 2-2. LLPS onset concentration for ezetimibe in sodium phosphate buffer at 37°C, in the presence of 2 μg/mL of HPMC-AS, as determined from the sudden increase in UV extinction at 350 nm, indicating a second phase has formed.

Table 2-2. Summary of LLPS concentrations measured in sodium phosphate buffer (10mM, pH 6.8) and FeSSIF at 37°C. (n=3).

Medium	LLPS concentration (μg/mL)	
	With PVP	With HPMC-AS
Sodium phosphate buffer (10 mM, pH 6.8)	20.5 ± 0.3	21.0 ± 0.5
FeSSIF	NP*	123 ± 4

*NP, not performed.

2.5.3 Nucleation induction time experiments using UV spectroscopy

To assess the effectiveness of PAA, PVP and HPMC-AS polymers in inhibiting crystallization of ezetimibe, nucleation induction time experiments were performed in the absence and the presence of pre-dissolved polymers in sodium phosphate buffer (10 mM, pH 6.8) and FeSSIF at 37°C. For buffer, experiments were performed at the measured LLPS concentration (21 μg/mL). Hence the system is at the maximum supersaturation and contains a drug-rich phase in equilibrium with the bulk solution. Nucleation induction times were measured by observing the drop in the UV absorbance at 233 nm as a function of time, indicating formation of a crystalline phase with concurrent desupersaturation, as well as monitoring changes in the scattering properties of the solution at 350 nm, where ezetimibe shows no UV absorbance. In the absence of polymers, ezetimibe crystallized rapidly, with immediate desupersaturation (approximately 1 minute), as demonstrated in Figure 2-3. The presence of PAA (10 or 100 μg/mL) did not delay the onset of

crystallization. In contrast, pre-dissolved PVP or HPMC-AS extended the duration of supersaturation, as shown in Figure 2-3, with PVP appearing to be the most effective crystallization inhibitor at this concentration. A summary of induction time measurements at 2, 10 and 100 µg/mL of pre-dissolved polymer is given in Figure 2-4A, where it is apparent that PVP was generally more effective than HPMC-AS in delaying the onset of crystallization, while PAA is ineffective at all concentrations. For FeSSIIF, ezetimibe was added at 123 µg/mL (measured LLPS concentration), and only the light scattering of the solution was monitored at 350 nm. As shown in Figure 2-4B, the presence of HPMC-AS delayed the onset of crystallization to a greater extent than either PAA or PVP, at all polymer concentrations, with the latter two polymers being generally ineffective even when tested at a higher concentration of 50 µg/mL. In contrast, HPMC-AS inhibited crystallization completely for up to 6 hours at this concentration, as shown in Figure 2-4B.

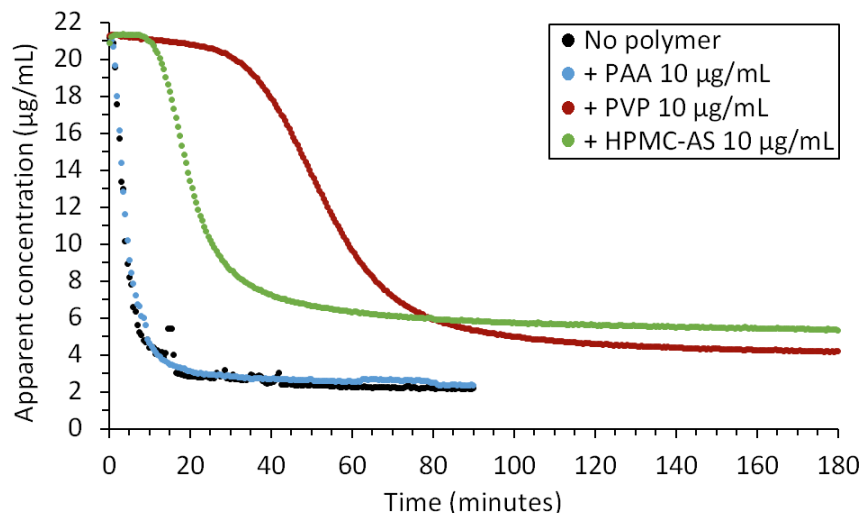


Figure 2-3. Apparent concentration versus time plots for supersaturated solutions of ezetimibe in the absence (black) and presence of 10 µg/mL of PAA (blue), PVP (red) and HPMC-AS (green), in sodium phosphate buffer (10 mM, pH 6.8) at 37°C. (n=3, error bars omitted for clarity).

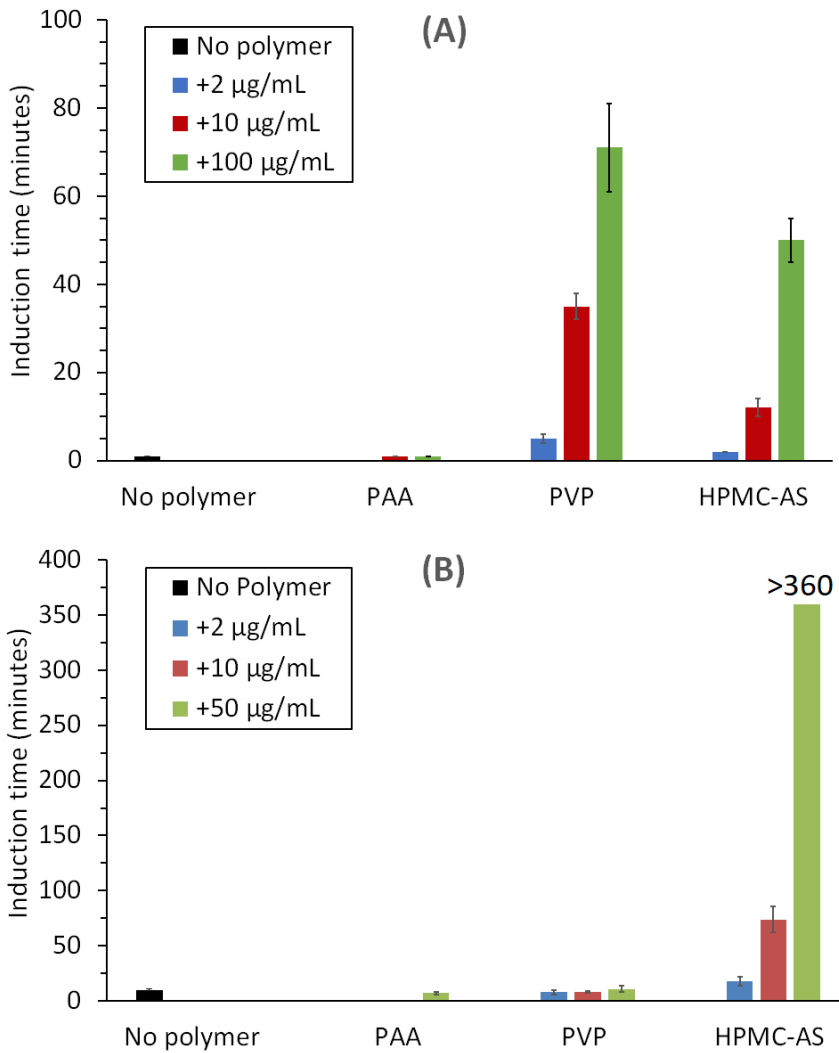


Figure 2-4. Summary of experimental induction times observed for supersaturated ezetimibe solutions in the absence and presence of polymers in sodium phosphate buffer (10 mM, pH 6.8) (upper Panel A), and in FeSSIF (lower panel B) at 37°C. (n=3).

2.5.4 Characterization of ezetimibe ASDs dissolution in different media

The dissolution profiles of ezetimibe ASDs in buffer are shown in Figure 2-5. As shown in the expanded view, ezetimibe ASDs prepared with PAA did not show any noticeable supersaturation, with the exception of the 2-minute time point, indicating that crystallization occurred rapidly when the ASDs came into contact with the medium. Neither PVP nor HPMC-AS ezetimibe ASDs dissolved to reach the amorphous solubility, although some degree of supersaturation was observed. For both systems, the solution concentration began to drop after approximately 30 minutes, indicating crystallization with concomitant desupersaturation. The highest concentrations

achieved were approximately 13 and 11 µg/mL, for PVP and HPMC-AS dispersions respectively. After the peak was observed, the solution concentration declined slowly over a period of several hours for both dispersions. Inspection of a sample of the dissolution medium with polarized light microscopy confirmed the presence of crystalline material in all investigated systems, as demonstrated in Figure 2-6. For the ASDs with PAA, the birefringent crystals were clearly visible after 10 minutes (Figure 2-6A). Figures 2-6B and 2-6C demonstrate the formation of small crystalline domains on the surface of the dissolving matrix (highlighted by arrows) at the 1-hour time point, for ASDs with PVP and HPMC-AS respectively. In addition, SHG microscopy images were acquired for samples withdrawn from the dissolution media at different time points, with results shown in Figure 2-7. The ASDs formulated with PAA showed SHG-active crystalline domains as early as 6 minutes, after which the SHG signal increased with time, both in terms of the size of crystalline regions and the total SHG count. For the ASDs prepared with PVP, the presence of crystals was minimal at 10 and 20 minutes. At 35 minutes, however, a few SHG active domains started to appear, with a notable increase in size and number at 120 minutes (Figure 2-7B). The appearance of significant crystallinity in the SHG images coincided with the decrease in ezetimibe concentration observed in Figure 2-5, after 30 minutes. ASDs prepared with HPMC-AS showed minimal (but not zero) crystallinity initially, with increased crystallinity emerging at 20 minutes and evolving at the 35-minute and 120-minute time points. After 35 minutes of dissolution, and based on the SHG signals, the PVP dispersion showed fewer crystals than the other dispersions. However, all three ASDs demonstrated a comparable degree of crystallinity after 120 minutes of dissolution.

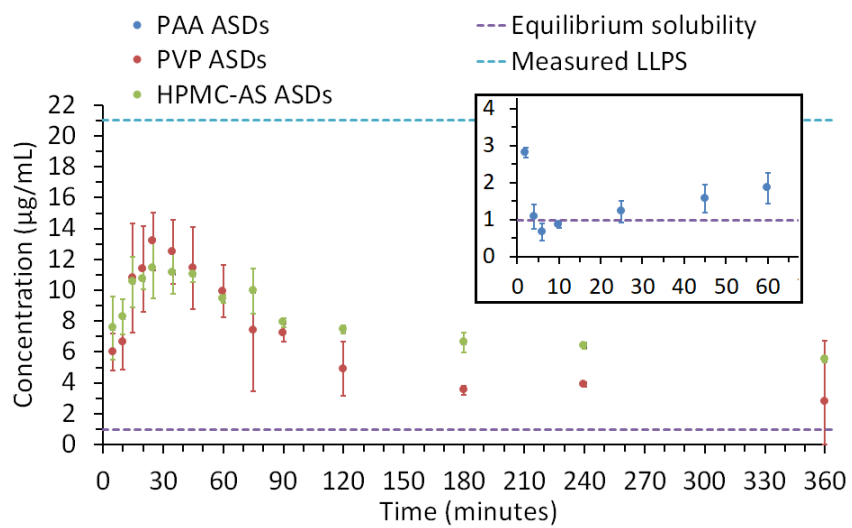


Figure 2-5. Ezetimibe concentration-time profiles for ASDs formulated with PAA (blue circles in the expanded inset), ASDs with PVP (red circles) and HPMC-AS (green circles) upon dissolution in sodium phosphate buffer (10 mM, pH 6.8) at 37°C for 6 hours. The dashed horizontal purple and cyan lines indicate the measured equilibrium solubility and LLPS concentration of ezetimibe in buffer at 37°C. (n=3).

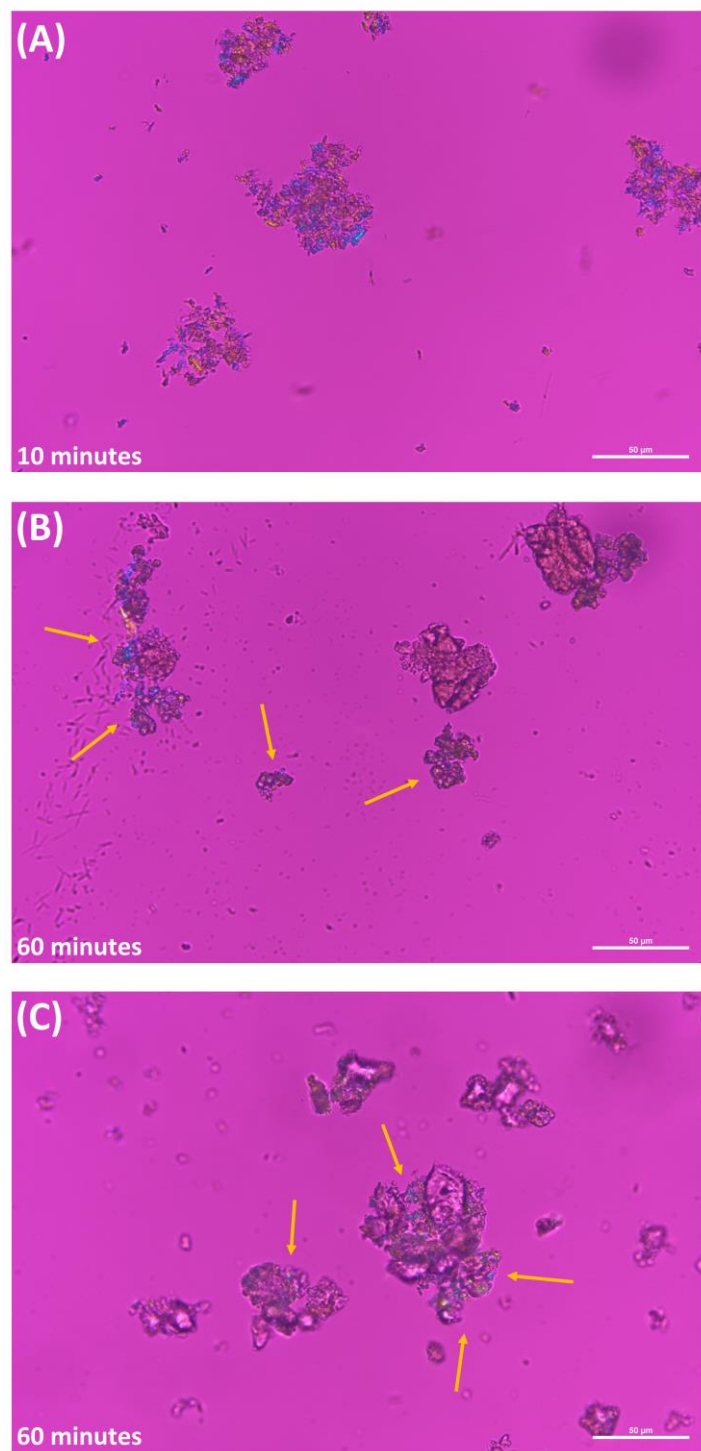


Figure 2-6. Polarized light microscopy images of ezetimibe ASDs with (A) PAA at 10 minutes, (B) PVP at 60 minutes and (C) HPMC-AS at 60 minutes upon dissolution in sodium phosphate buffer (10 mM, pH 6.8) at 37°C. Scale bar is 50 μ m.

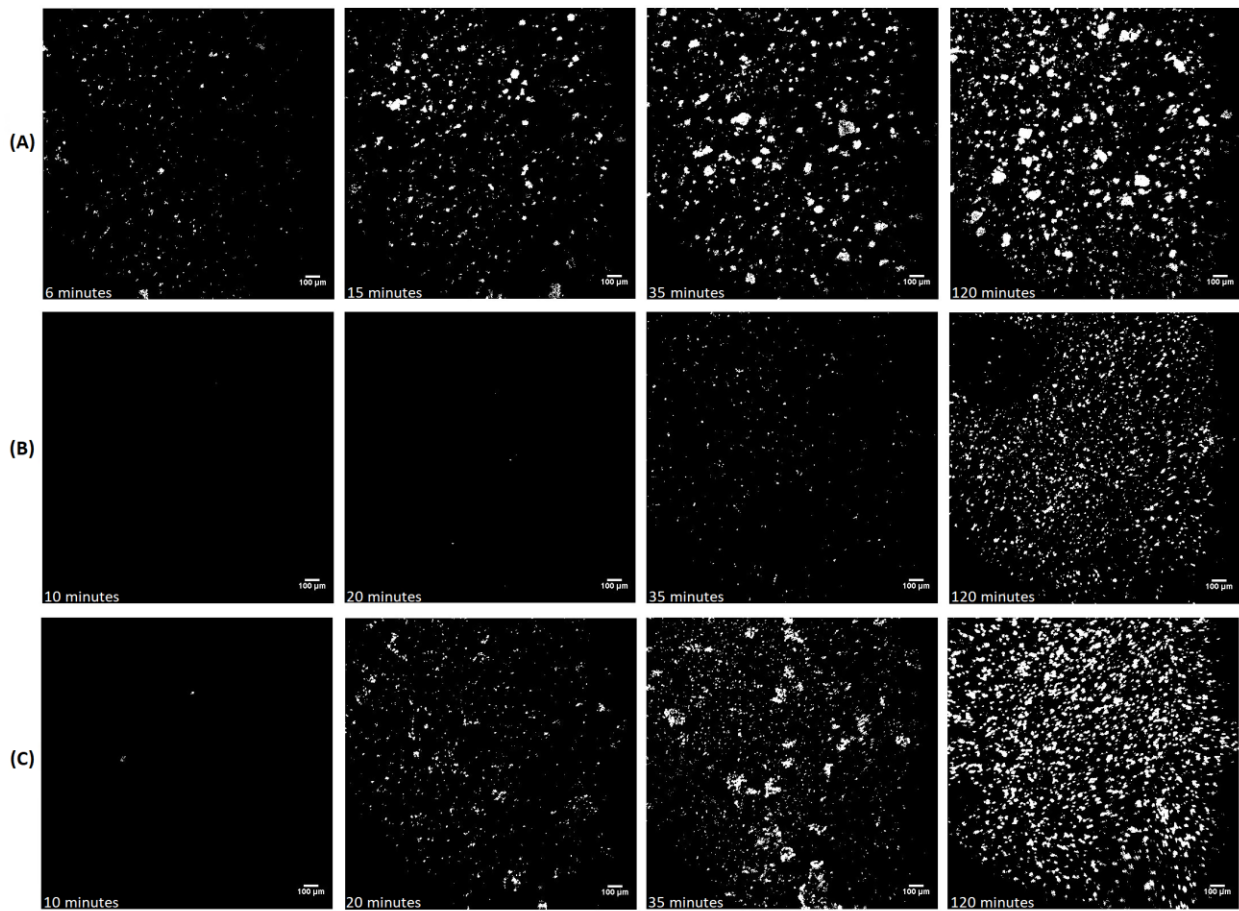


Figure 2-7. SHG microscopy images of ezetimibe ASDs; (A) PAA at 6, 15, 35, and 120 minutes, (B) PVP at 10, 20, 35 and 120 minutes, and (C) HPMC-AS at 10, 20, 35 and 120 minutes, upon dissolution in sodium phosphate buffer (10 mM, pH 6.8) at 37°C. Scale bar is 100 μ m.

Analogous dissolution experiments in FeSSIF were also performed. Interestingly, considerable differences were observed between the various ASDs with respect to the extent and longevity of supersaturation achieved, as demonstrated in Figure 2-8. Similar to the dissolution behavior in buffer, the PAA ASDs exhibited very low supersaturation, whereby the ezetimibe solution concentration remained constant (between 30 and 35 μ g/mL) from the 2-minute time-point onwards. Interestingly, ASDs formulated with PVP displayed an initial burst release, reaching a peak ezetimibe concentration of approximately 200 μ g/mL after 15 minutes, however the concentration dropped rapidly thereafter, presumably due to crystallization. ASDs prepared with HPMC-AS displayed a slightly slower release rate compared to PVP, but maintained supersaturation for a longer period, over 15-90 minutes. However, desupersaturation was still observed, and the solution concentration dropped to around 65 μ g/mL after 2 hours. Figure 2-9

shows polarized light microscopy images of ASDs prepared with PAA (Figure 2-9A) and PVP (Figure 2-9B) after exposure to FeSSIF for 30 minutes. Both ASDs exhibited rapid crystallization with crystals appearing both in the solution phase and on undissolved ASD particles. For HPMC-AS ASDs, ezetimibe needle-shaped crystals were clearly visible at the edges of the undissolved particles after 3 hours, as illustrated in Figure 2-9C. PXRD measurements were also used to determine if crystalline ezetimibe was present at different timepoints of dissolution (Figure 2-10). ASDs prepared with PAA (Figure 2-10B) and PVP (Figure 2-10C) displayed diffraction peaks characteristic of crystalline ezetimibe monohydrate, and analogous to the diffraction pattern of the reference API (Figure 2-10A). In contrast, for the HPMC-AS dispersion, minimal crystallinity was observed in the sample, with a small increase being observed after 3 hours. It should be noted that the two peaks at 32 and 46° 2-theta, were due to precipitation of sodium chloride from the FeSSIF medium. SHG images for these systems are shown in Figure 2-11. PAA dispersions were highly crystalline after 15 minutes, with no apparent evolution of the SHG signals in terms of size and count after that time point. PVP ASDs displayed very few crystalline regions at 15 minutes, however the extent of crystallinity rapidly increased at later time-points whereby the crystallites were much smaller than those observed for the PAA systems. In contrast, HPMC-AS ASDs showed much more stable dissolution behavior, with SHG images indicating very few crystallized regions in the first hour, which gradually increase at later time-points although the crystallinity is lower in comparison to the PAA and PVP dispersions. These results are also consistent with the PXRD data shown in Figure 2-10.

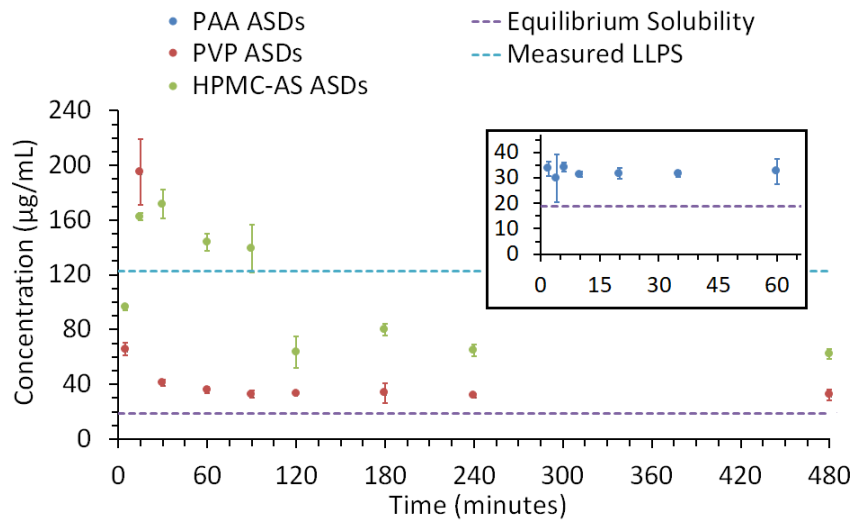


Figure 2-8. Ezetimibe concentration-time profiles for ASDs formulated with PAA (blue circles in the expanded inset), ASDs with PVP (red circles), and ASDs with HPMC-AS (green circles), upon dissolution in FeSSIF at 37°C for 8 hours. The dashed horizontal purple and cyan lines indicate the measured equilibrium solubility and LLPS concentration of ezetimibe in FeSSIF at 37°C. (n=3).

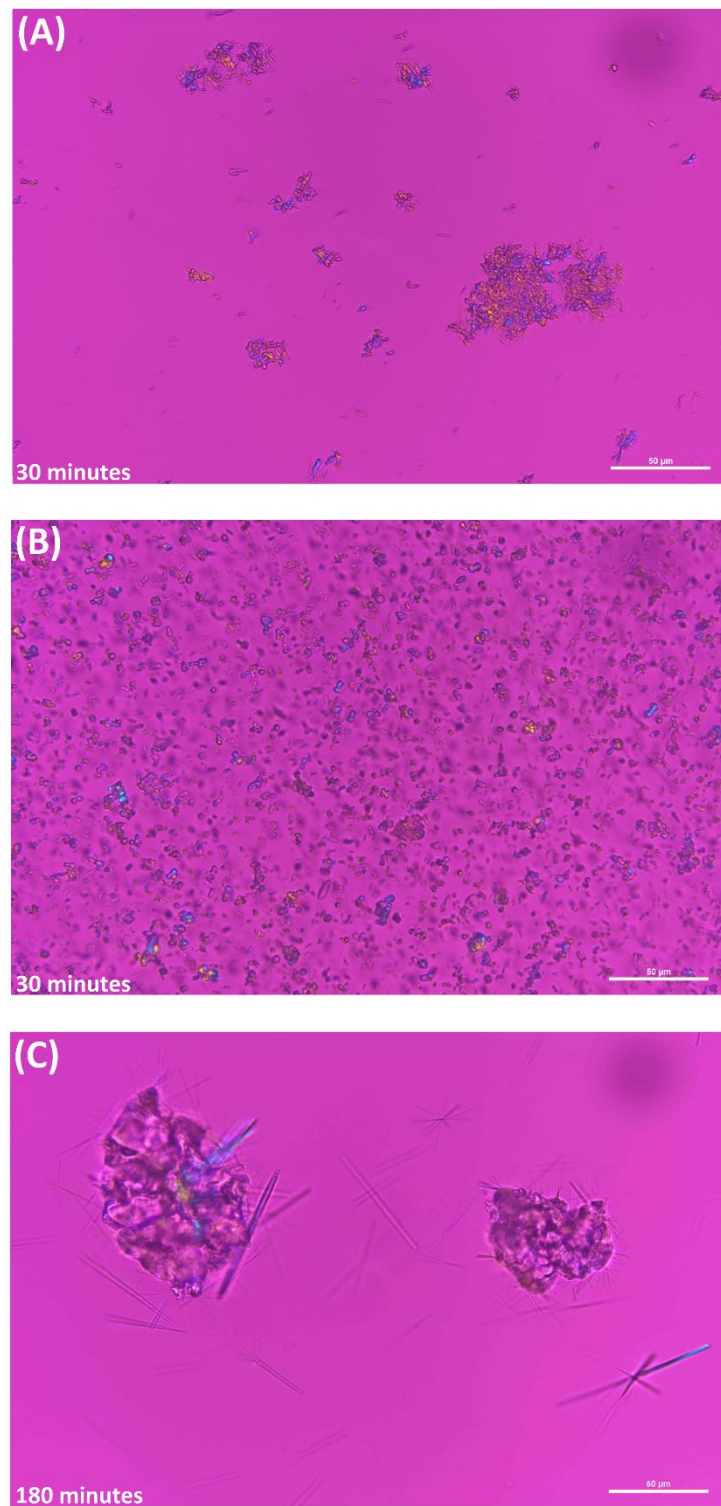


Figure 2-9. Polarized light microscopy images of ezetimibe ASDs with (A) PAA at 30 minutes, (B) PVP at 30 minutes and (C) HPMC-AS at 180 minutes upon dissolution FeSSIF at 37°C. Scale bar is 50 μm.

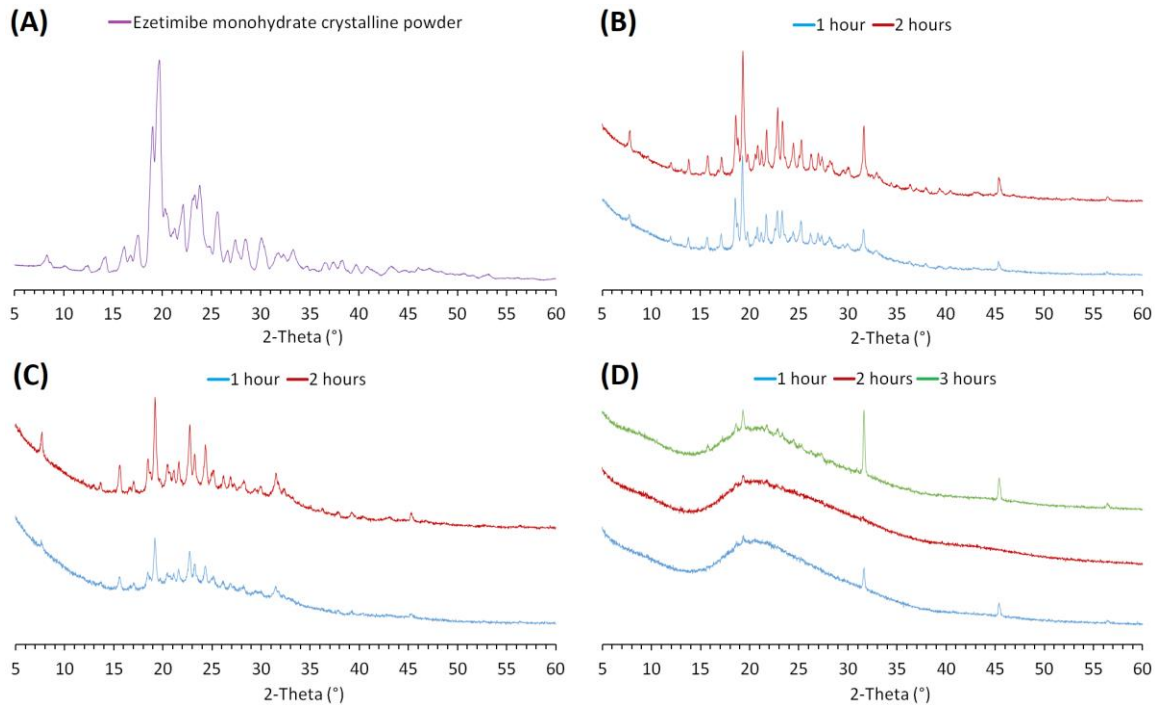


Figure 2-10. PXRD patterns of (A) dry ezetimibe monohydrate powder (purple pattern), and slurried ezetimibe ASDs prepared with (B) PAA, (C) PVP, and (D) HPMC-AS, after dissolution in FeSSIF at 37°C at 1 (blue), 2 (red), and 3 hours (green).

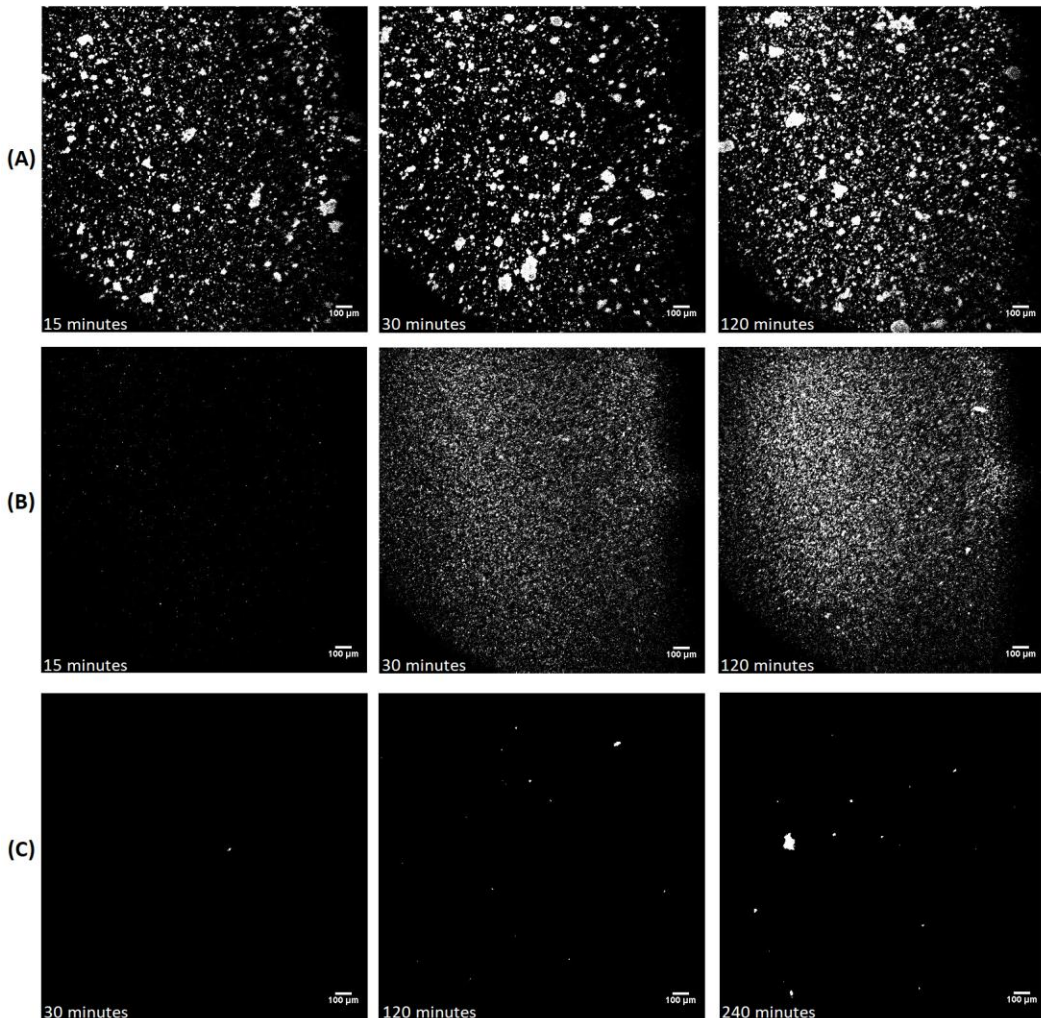


Figure 2-11. SHG microscopy images of ezetimibe ASDs; (A) PAA at 15, 30 and 120 minutes, (B) PVP at 15, 30, and 120 minutes, and (C) HPMC-AS at 30, 120 and 240 minutes, upon dissolution in FeSSIF at 37°C. Scale bar is 100 μ m.

The dissolution of ezetimibe ASDs in Ensure Plus® at 37°C was characterized using both HPLC to analyze concentration-time profiles and SHG microscopy to evaluate crystallinity. As mentioned before, Ensure Plus® separated into three different phases upon centrifugation (pellet, aqueous and oily), where the upper two were analyzed by HPLC to evaluate the dissolved ezetimibe concentration. Figure 2-12 demonstrates the different dissolution profiles of all ezetimibe ASDs, both in the aqueous phase (left axes – blue), and the oily phase (right axes – red), of Ensure Plus®. As shown in Figure 2-12A, dissolution of ezetimibe PAA ASDs in the aqueous phase showed a short-lived supersaturation, which started decreasing slowly after 30 minutes. Aqueous phase dissolution profiles for ASDs prepared with PVP and HPMC-AS are shown in

Figures 2-12B and 2-12C, where it is apparent that both systems underwent dissolution to produce more stable supersaturated solutions, compared to the PAA ASDs. Interestingly, the ASDs with PVP displayed a faster release rate, and overall higher concentrations, compared to HPMC-AS ASDs. With regard to the ezetimibe concentrations in the oily phase of Ensure Plus®, it is apparent that PAA and PVP dispersions resulted in plateau-like profiles, where the concentration evolution of ezetimibe was rapid, and remained almost unchanged over the entire experiment time, as demonstrated in Figures 2-12A and 2-12B. Alternatively, the dispersions with HPMC-AS (Figure 2-12C) exhibited a slow-release dissolution profile in terms of the oily phase. SHG images showed that ASDs formulated with PAA (Figure 2-13A) and PVP (Figure 2-13B) had small levels of crystalline material present after 10 and 20 minutes respectively. In contrast, the HPMC-AS ASD exhibited no SHG signal initially, with the first indications of crystallinity occurring at the 120-minute time-point (Figure 2-13C). Regardless of the polymer used, the evolution of the SHG signal during dissolution of all dispersions in Ensure Plus®, with respect to count and size with time, was much lower in comparison to observations in other media.

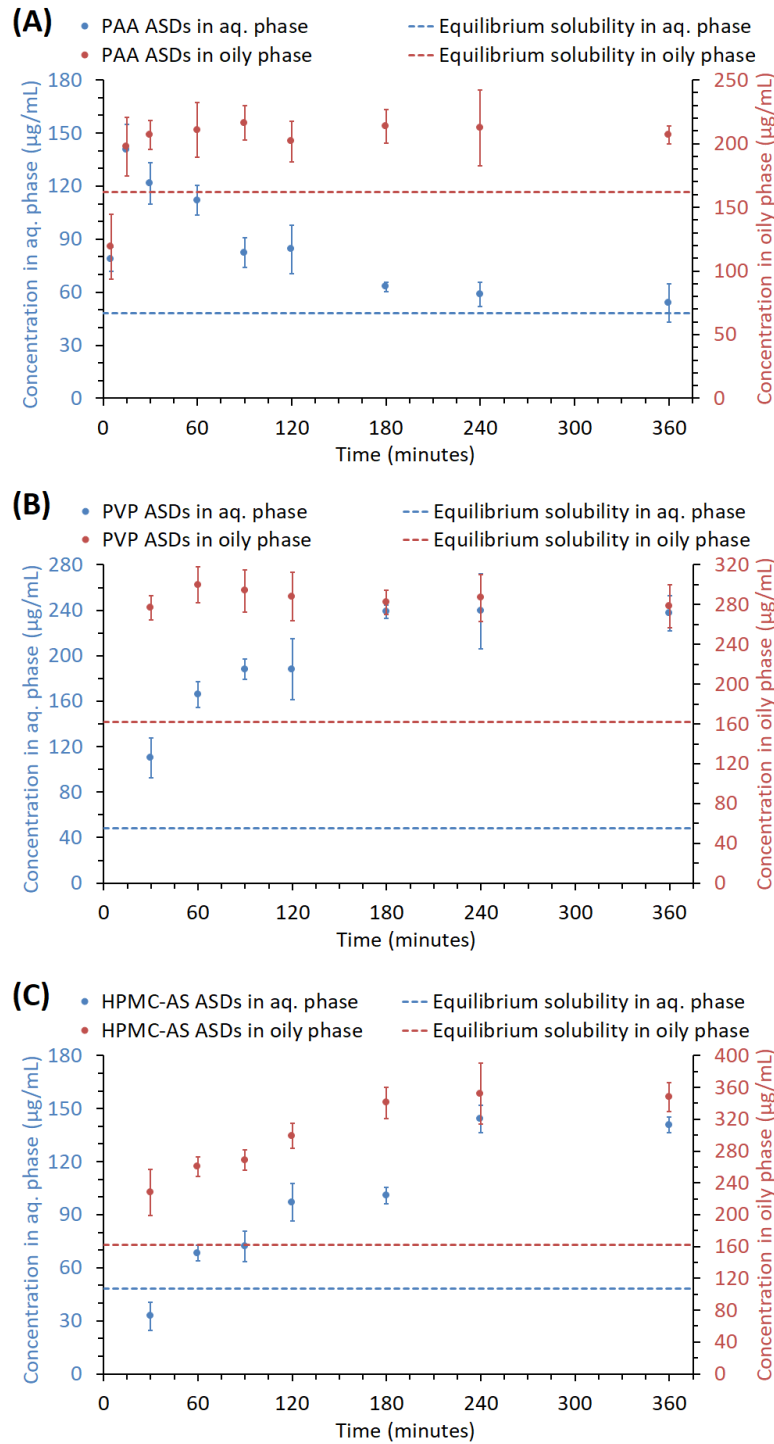


Figure 2-12. Ezetimibe concentration-time profiles for ASDs formulated with (A) PAA, (B) PVP, and (C) HPMC-AS upon dissolution in Ensure Plus® at 37°C for 6 hours; Blue and red circles indicate ezetimibe dissolution in the aqueous (left axis) and the oily (right axis) phases of Ensure Plus®, respectively. The dashed horizontal blue and red lines indicate the measured equilibrium solubility of ezetimibe in the aqueous and the oily phases of Ensure Plus®, respectively. (n=3).

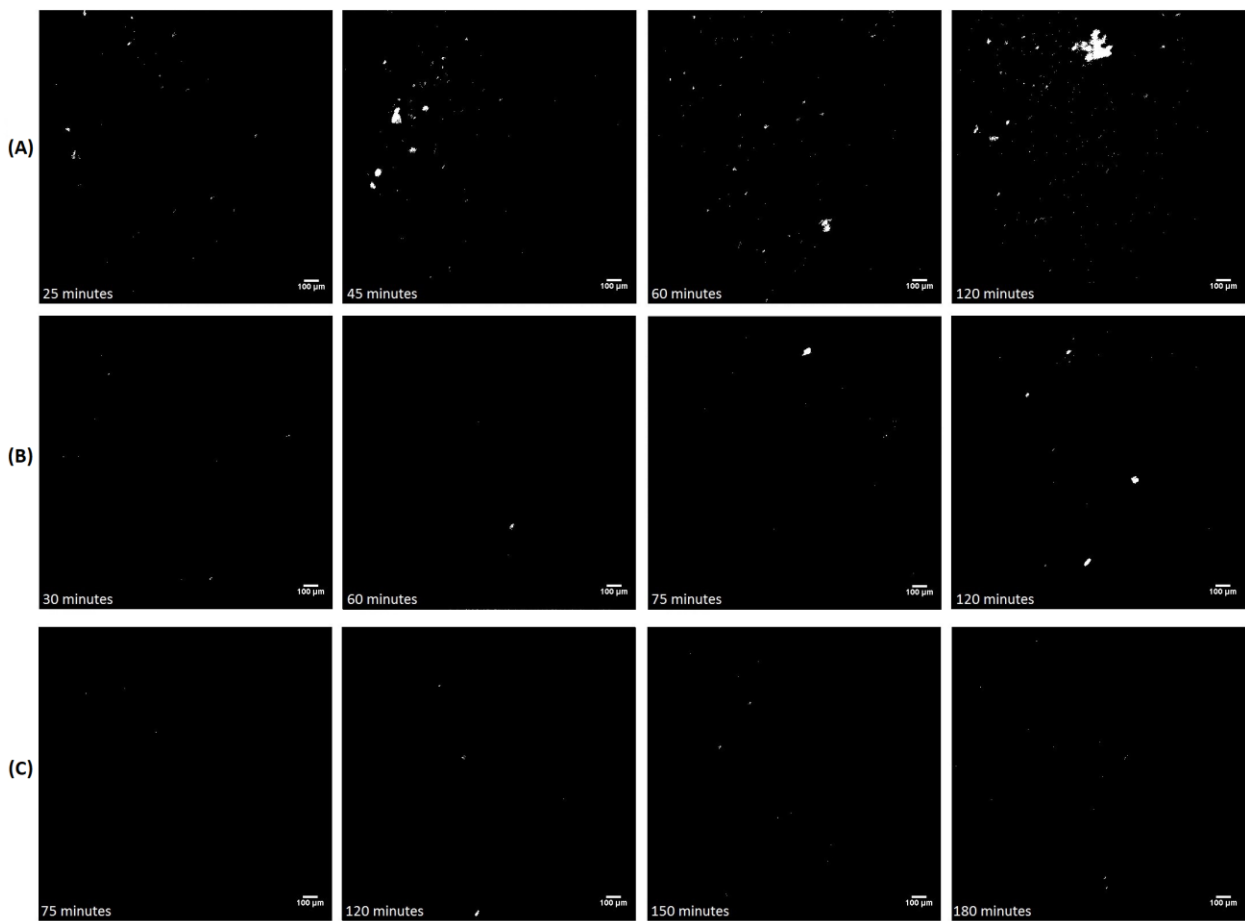


Figure 2-13. SHG microscopy images of ezetimibe ASDs; (A) PAA at 25, 45, 60 and 120 minutes, (B) PVP at 30, 60, 75 and 120 minutes, and (C) HPMC-AS at 75, 120, 150 and 180 minutes, upon dissolution in Ensure Plus® at 37°C. Scale bar is 100 μ m.

2.6 Discussion

It is generally accepted that supersaturation in the gastrointestinal tract is an important factor influencing the absorption of certain poorly water soluble compounds.^{89,103} However, the current understanding of possible phase transformations of supersaturated solutions in the complex media used as surrogates for gastrointestinal fluids is rather limited, and has not been adequately investigated to date. Crystallization is of particular interest, since this process will ultimately result in the loss of supersaturation and consequently a reduced driving force for membrane transport. One difficulty that can be associated with the use of biorelevant media is their turbidity. Biorelevant media can initially be turbid depending on their composition, and turbidity can also evolve depending on the phase behavior of the dissolving system.¹⁹ For example, Ensure Plus®,

which is often used in a clinical setting to simulate the impact of gastric postprandial conditions on absorption,^{20–25} is an opaque, viscous fluid. While it would be of interest to understand how such a medium impacts the phase behavior of an amorphous solid dispersion, it is challenging to utilize conventional spectroscopic and optical techniques to study crystallization kinetics. In addition, the dissolution behavior of amorphous solid dispersions can be quite complex, resulting in the formation of turbid solutions due to the formation of an amorphous, drug-rich phase.^{74,102,104} Solutions containing small scattering species, such as those generated during ASD dissolution, can affect UV concentration measurements,¹⁰⁵ and it is also difficult to differentiate phase separation to a non-crystalline versus to a crystalline phase using non-specific techniques such as light scattering. The presence of dissolving amorphous particles in supersaturated solutions, together with the formation of new species via LLPS or crystallization, thereby necessitates the use of complementary analytical methods for adequate characterization of the system. Thus, a full mechanistic understanding of the phase behavior of supersaturated solutions cannot rely solely on concentration-time profiles, and analytical methods that enable crystallization to be detected in complex turbid media, such as SHG microscopy, are needed as a complement.

Quantitative analysis of the SHG images allows disentanglement of nucleation and growth kinetics in driving crystal formation in the different media. For the crystal growth kinetics, the change in average crystal size was recorded as a function of time. The majority of the images contained too many overlapping crystals for reliable determination of the average crystal size by particle counting. Instead, Fourier analysis of the images allowed estimation of the mean particle sizes from the first minimum in the radial power spectrum.¹⁰⁶ The results of the crystallization kinetics are summarized in Table 2-3. Both the nucleation and growth rates are averaged values representing the progression of crystallinity throughout the experiments. Integration of the total SHG intensity was used to assess the fractional crystallinity at the longest time-points in the experiments, which are also included in Table 2-3. Final crystallinity represents the percentage values of the crystalline material per unit volume of each field of view in the SHG images, i.e. the amount of crystallinity in a given volume of medium, and not the percentage of crystallinity in the ASDs.

Table 2-3. Nucleation and growth kinetics obtained from SHG microscopy images analysis measured in different dissolution media. (n=3).

Medium	Polymer in ASDs	Nucleation rate (Number of particles/minute/ μm^3)	Growth rate ($\mu\text{m}/\text{minute}$)	Final crystallinity %
Sodium phosphate buffer (10 mM, pH 6.8)	PAA	15 ± 2	0.3 ± 0.2	30 ± 5
	PVP	80 ± 40	0.4 ± 0.1	13 ± 2
	HPMC-AS	110 ± 40	1.0 ± 0.3	32 ± 2
FeSSIF	PAA	>>30*	0.2 ± 0.1	4 ± 0.6
	PVP	600 ± 200	0.020 ± 0.001	8 ± 4
	HPMC-AS	0.04 ± 0.03	0.05 ± 0.02	0.04 ± 0.02
Ensure Plus®	PAA	0.07 ± 0.03	0.7 ± 0.2	0.08 ± 0.03
	PVP	0.03 ± 0.02	0.2 ± 0.1	0.03 ± 0.01
	HPMC-AS	0.02 ± 0.01	0.2 ± 0.1	0.02 ± 0.01

*Indefinite due to particle overlapping and large variations in particle size.

In this study, all dissolution experiments were performed under non-sink conditions, with respect to the crystalline and amorphous solubilities of ezetimibe in both pH 6.8 sodium phosphate buffer and FeSSIF. Interestingly, we note a huge diversity of supersaturation profiles and crystallization kinetics, which depend not only on the polymer used to form the ASD, but also on the medium. For the PAA dispersions, no supersaturation was observed in either buffer or FeSSIF whereby the solution concentration was more or less equivalent to the equilibrium solubility measured for that particular medium (Figures 2-5 and 2-9). Thus, it is apparent that crystallization occurred once the solid amorphous material was added to the dissolution media, as confirmed by the SHG imaging results. Based on the polarized light microscopy images (Figure 2-6A and 2-9A), it can be inferred that crystallization from the solid matrix was the dominant mechanism, as the PAA dispersions showed extensive birefringent domains after a few minutes of immersion in either media. Alonzo et al. observed similar behavior with amorphous felodipine following addition to buffer, where crystallization from the solid matrix was extremely rapid, and consequently no supersaturation or any drug release behavior beyond the crystalline solubility was observed.¹⁰ Both SHG imaging and PXRD data (for FeSSIF only) confirmed the rapid phase separation of this system, and the emergence of ezetimibe crystals, leading to no noticeable supersaturation for this system.

PVP and HPMC-AS dispersions showed interesting behavior in that the relative effectiveness of the polymer and supersaturation profiles seemed to be highly dependent on the medium employed. Based on the induction time experiments (Figures 2-3 and 2-4), PVP provided the greatest inhibition of crystallization for ezetimibe in buffer, while HPMC-AS was more efficient in preventing crystallization (particularly nucleation) in FeSSIF. In buffer, neither ASD reached the amorphous solubility, and the supersaturation was short-lived for both systems, with only small differences in the concentration time profiles being observed, as demonstrated in Figure 2-5. Desupersaturation was observed after about 30 minutes, in good agreement with the SHG imaging where a significant increase in the number of crystalline domains was observed at the 20-minute time-point for HPMC-AS, and at the 35-minute for PVP. Despite the slight delay in the onset of crystallization, the average nucleation rate throughout the dissolution experiment was higher for PVP and HPMC-AS dispersions relative to the PAA dispersions, whereby these samples demonstrated continuous crystal number progression until the 120-time point (Table 2-3). At 25°C (results not shown), dissolution experiments of both systems in buffer achieved a relatively longer-lived supersaturation, maintaining a plateau concentration that was equivalent to the measured LLPS concentration at 25°C for a few hours (PVP was more effective than HPMC-AS). At 37°C, crystallization kinetics were much faster, and it is likely that solution-mediated crystallization commenced earlier leading to rapid depletion of supersaturation, and therefore the maximum “amorphous” solubility advantage was not achieved in either case.

It has been shown previously that the dissolution of a supersaturating formulation can result in either a crystalline or an amorphous precipitate.^{74,102,104} In the first case, crystallinity can evolve either in the dissolving matrix, or as a result of nucleation from the supersaturated solution generated upon dissolution, whereby the supersaturation is reduced upon crystal growth. However, if the amorphous solubility is exceeded and crystallization is inhibited, a drug-rich phase forms whereby the solution remains supersaturated with respect to the crystalline solubility. Liquid-liquid phase separation to a non-crystalline phase is a metastable phase transition, whereby crystal nucleation can initiate from either the drug-rich or the solution phase. Given the difference in supersaturation profiles, it is important to determine if solution turbidity arises because of LLPS or crystallization. The presence of polymers in the system can greatly impact the LLPS process by interfering with the nucleation process. Additionally, sodium taurocholate, the only bile salt present in FeSSIF, as well as FaSSIF have been shown to increase the concentration at certain

compounds undergo phase separation to amorphous drug,¹⁰⁷ consistent with the observations herein that FeSSIF increases the LLPS concentration for ezetimibe. It should be noted that in such systems with solubilizing additives, the thermodynamic activity-boundaries remain the same, although the amorphous solubility increases.¹⁰⁷ Results from the dissolution studies in FeSSIF provide an interesting example of the complex interplay between dissolution medium, polymer, supersaturation and crystallization kinetics. The PVP dispersions dissolved very rapidly in FeSSIF (Figure 2-8), and the system briefly exceeded the amorphous solubility, leading to a turbid solution. The supersaturation, however, was only transient, and the SHG imaging confirmed that there were a considerable number of crystals present in the system at 30 minutes, as shown in Figure 2-11B. This time-point coincides nicely with the reduced solution concentration observed in the dissolution profile. Moreover, the good agreement seen between the polarized light and SHG microscopy images for the PVP samples (Figures 2-9B and 2-11B), with respect to the small crystal sizes and large number, is interesting. These images suggest that PVP acts as a poor nucleation inhibitor for ezetimibe in FeSSIF. Hence, at the high supersaturation generated by rapid release of ezetimibe from PVP ASDs in FeSSIF, the nucleation rate is high (Table 2-3), leading to many small crystals appearing for these dispersions. These observations are in contrast with the dissolution results in buffer, where crystallization was slower based on the SHG results shown in Figure 2-7B. This could be due either to the slower release of ezetimibe from the ASD in buffer, or a lower effectiveness of PVP as a crystallization inhibitor in FeSSIF. Conversely, the HPMC-AS dispersions vastly outperformed the PVP ASDs in FeSSIF. Again, the amorphous solubility was exceeded upon dissolution leading to a turbid solution (Figure 2-8), but the elevated supersaturation was maintained for 90-120 minutes. Additionally, SHG imaging demonstrated a reduced extent of crystallization for this system (Figure 2-11C), which is clearly illustrated by the low nucleation and crystal growth rates for this system, as shown Table 2-3. The high concentrations achieved following dissolution of the HPMC-AS dispersions are interesting considering that the MF grade used in this study, has been reported to be sparingly soluble at pH 5.2 in aqueous solutions, only dissolving to form a colloidal solution at pH 6-7.5.^{108,109} It thus appears that this polymer has a greater solubility in FeSSIF (pH 5) than it would be expected based on a consideration of solution pH alone; information on HPMC-AS solubility in FeSSIF is not currently available. In support of this conjecture, Bevernage et al. prepared solid dispersions with HPMC-AS and tested supersaturation in several media including FeSSIF; HPMC-AS was superior

for 4 out of 5 different APIs.¹¹⁰ Despite desupersaturation after 2 hours, dissolution of the HPMC-AS ASDs still led to improved concentration-time profiles compared to the other dispersions. Therefore, HPMC-AS appeared to be an effective crystallization inhibitor in the presence of the drug-rich colloidal phase of ezetimibe, and the components of FeSSIF did not reduce that inhibitory effect, as in the case of PVP. Once crystallization occurred, the solution concentration decreased towards the solubility of crystalline ezetimibe in FeSSIF, however residual supersaturation was observed, and the equilibrium solubility was not attained over the timeframe of the experiment. This was probably because HPMC-AS is an effective crystal growth inhibitor at low supersaturation, as shown previously,^{37,111,112} or that the crystals formed in the presence of HPMC-AS have some disorder.

Dissolution experiments performed in Ensure Plus® provide an interesting approach to mimic the fed-state gastric state, and better understand how ASDs can perform in a complex biorelevant lipid-rich medium. An extensive history of research on lipid-based formulations can be found in the literature, however, understanding of the role of lipid solubilization in the context of biorelevant media is still limited. Ensure Plus® is a high-energy oil-in-water emulsion, that contains a combination of fats, proteins, carbohydrates, vitamins and electrolytes.²⁶ The high lipid content and the possible binding of drug to peptides or proteins present in this medium, account for its high solubilizing power.^{13,14} In addition, Ensure Plus® contains casein which can lead to micelle formation, raising the solubility of highly lipophilic compounds.¹¹³ Consequently, it was important to characterize the dissolved ezetimibe concentration and partitioning between the aqueous and oily phases during dissolution, to better evaluate the overall supersaturation in this medium. Due to the enhanced solubility of ezetimibe in this medium, the maximum theoretical supersaturation level was lower than for the other media, and therefore the driving force for crystallization was not as high. This explains why the SHG images for Ensure Plus® dissolution demonstrated fewer SHG-active regions in comparison to other media. It should be noted that differences in the absorption coefficient and laser penetration depth between the buffer/FeSSIF and Ensure Plus® might also contribute to these observations. Further, it should be noted that the extent of supersaturation may change during digestion of the lipid components of Ensure Plus®, as observed for other lipid delivery systems.^{114–116}

In the case of PAA (Figure 2-12A), moderate supersaturation was maintained for a longer time period than for the other media, and a gradual decline in ezetimibe concentration was seen after 30 minutes, decreasing until it was nearly equivalent to the equilibrium solubility of ezetimibe in the aqueous phase. In the oily phase, the concentration profile is maintained above the equilibrium solubility for the duration of the experiment (6 hours). Both PVP and HPMC-AS ASDs (Figures 2-12B and 2-12C) achieved supersaturation in the aqueous phase of Ensure Plus®, where the SHG imaging demonstrated less crystallinity compared to the PAA system (Figure 2-13). It is noteworthy that the PVP ASDs showed a higher concentration than the HPMC-AS ASDs, in the aqueous phase. Paradoxically, the situation is reversed in the oily phase, where the supersaturation level of the HPMC-AS dispersions was noticeably higher than for the PVP system. This finding is interesting as it raises questions about the role of polymers in maintaining supersaturation from a hydrophilicity/hydrophobicity perspective. Stabilization of supersaturation usually relies on the presence of a polymer as a crystallization inhibitor, and generally the effectiveness of a given polymer in inhibiting crystallization is thought to be highly dependent on its solvation conformation, hydrophilicity/hydrophobicity balance, and the overall interaction with the drug molecule under investigation.¹¹¹ However, the current research still lacks sufficient information on possible interactions between polymers and drug molecules, in the different phases of a complex biorelevant medium such as Ensure Plus®. HPMC-AS ASDs were the most stable formulation during dissolution in Ensure Plus®, where only tiny crystals could be observed after 2 hours, with little progression in size and number by 3 hours (Figure 2-13C). Additionally, HPMC-AS ASDs displayed a unique slow-release behavior in the oily phase, which seemed to reach the maximum supersaturation after 3 hours of dissolution. For HPMC tablets, previous studies have shown that fat-rich media such as Ensure Plus® can retard water permeation by forming a rate-controlling gel on the surface of the matrices during dissolution, thereby slowing the drug release rate.^{23,117} Moreover, the sum of the maximum concentrations attained in the aqueous and oily phases (at the end of the experiment), was roughly 500 µg/mL, which is equivalent to the total mass of ezetimibe added. The same was true for the PVP system. This was not the case for the PAA ASDs, in agreement with the SHG data, which suggests precipitation as crystalline material. Ensure Plus® is a complex medium containing lipid vesicles and micelles, which can enhance the solubilization capacity and alter the kinetics of drug crystallization.^{118–120} The impact of such components on the generation and stabilization of ASD-derived supersaturated

solutions provides ample fodder for further exploration and characterization. In this context, SHG microscopy provides a valuable tool in selective identification of crystalline domains, which is challenging in a densely opaque media such as Ensure Plus®. This capability is advantageous for performing otherwise challenging measurements of supersaturated systems in complex biorelevant media, allowing better mechanistic understanding of phase transformations in such systems.

2.7 Conclusions

With limited knowledge of the impact of gastrointestinal environments on supersaturating delivery systems, the application of biorelevant media is crucial to improving the relevance of *in vitro* testing of enabled formulations. Ezetimibe ASDs formulated with different polymers demonstrated different release profiles, supersaturation levels and solution crystallization kinetics depending on the dissolution testing medium. It is apparent that the presence of solubilizing additives in the dissolution medium can significantly alter crystal nucleation and growth kinetics and impact the crystallization inhibitory properties of the polymer used in the ASD formulation. SHG microscopy was instrumental in enabling detection of crystallization in highly turbid media. This approach provided highly complementary information to the dissolution profiles, with the appearance of crystalline material coinciding with the onset of desupersaturation. From analysis of the SHG micrographs, it is clear that differences in the nucleation kinetics rather than growth rates dominate the overall trends in crystallinity. The multifaceted approach employed herein enables variations in ASD dissolution behavior as well as phase transformation kinetics to be explored in a variety of media of relevance to oral delivery, which in turn will facilitate the formulation of ASDs that maximize supersaturation and are robust to crystallization.

CHAPTER 3. CHARACTERIZATION OF PHASE TRANSFORMATIONS FOR AMORPHOUS SOLID DISPERSIONS OF A WEAKLY BASIC DRUG UPON DISSOLUTION IN BIORELEVANT MEDIA

This chapter is a reprint with minor modifications of a manuscript published in *Pharmaceutical Research* in December 2019 with the same title by: Ahmed Elkhabaz, Sreya Sarkar, Garth J. Simpson, and Lynne S. Taylor.

3.1 Abstract

For weakly basic drugs dosed under fasted conditions, the increase in pH upon transit from the stomach to the small intestine can lead to a drastic decrease in aqueous solubility, resulting in generation of a supersaturated solution as the molecules become more extensively un-ionized. Although the generated supersaturation is favorable for promoting intestinal absorption, there is also a higher driving force for crystallization. The goal of this study was to investigate the dissolution performance of amorphous solid dispersions (ASDs) of a weakly basic compound, posaconazole, dispersed a pH-sensitive polymer matrix consisting of hydroxypropyl methylcellulose acetate succinate (HPMC-AS), using fasted-state simulated media. ASDs with three different drug loadings, 10, 25 and 50 wt. %, and the commercially available tablets were exposed to acidic media (pH 1.6), followed by transfer to and dissolution in intestinal media (pH 6.5). Parallel dissolution experiments in only simulated intestinal media were also performed to better understand the impact of the gastric stage. Different analytical methods, including second harmonic generation and two-photon excitation ultraviolet fluorescence microscopy, were used to characterize the phase behavior of these systems at different stages of dissolution. Results revealed that all ASDs exhibited some degree of drug release and were also vulnerable to matrix crystallization during suspension in acidic media. Upon transfer to intestinal media conditions, supersaturation was observed, albeit short-lived, due to the release of the crystals formed in the acid immersion stage, which acted as seeds for crystal growth. Lower drug loading ASDs also exhibited transient formation of amorphous nanodroplets prior to crystallization. This work emphasizes the significance of assessing the impact of pH change on dissolution and provides a fundamental basis of understanding the phase behavior kinetics of ASDs of weakly basic drugs when formulated with pH sensitive polymers.

3.2 Introduction

In oral drug delivery, dissolution of the drug from the dosage form and subsequent intestinal absorption is crucial for adequate bioavailability and therapeutic performance. Apart from the permeability of an active pharmaceutical ingredient (API), the intraluminal drug concentration i.e. solubility is a key determinant of drug absorption rate and extent^{121,122}. However, the majority of newly discovered molecules in pharmaceutical development are poorly water-soluble, limiting their absorption^{1,123}. To address this, formulation strategies that generate supersaturated solutions have been employed⁵. Supersaturation can be attained through different drug delivery systems including salt forms⁸², prodrugs¹²⁴, cocrystals^{125,126}, or amorphous solid dispersions (ASDs)^{127,128}. A drug in a supersaturated solution has a higher chemical potential relative to its equilibrium crystalline state⁴⁹. Through enhancing the flux of drug molecules across the intestinal wall and extending the window of passive transport, supersaturation can significantly improve the intestinal absorption for poorly water-soluble drugs^{6,7,129,130}. However, the supersaturated solution generated is metastable. Therefore, there is a high driving force for drug crystallization, whereby crystallization results in a depletion of the supersaturation and a loss of the solubility advantage^{27,29,131}. During ASD dissolution, the tendency of the system to undergo crystallization can be influenced by many different factors, including the degree of supersaturation. Crystallization inhibitors, usually polymers, are typically employed with the goal of maintaining the supersaturated state over a sufficient period for absorption to take place^{5,12}. Polymers delay crystallization by impacting nucleation and/or crystal growth. The mechanisms by which polymers prevent crystallizations are not fully understood. Within the ASD matrix it has been shown that polymers can increase the glass transition temperature of the system¹³, decrease the molecular mobility¹⁴, and form interactions with the drug such as hydrogen bonding¹⁵. Inhibition of crystallization in the matrix is of relevance during storage and prior to complete dissolution *in vivo*. The latter is of particular importance for ASDs formulated with enteric polymers such as hydroxypropyl methylcellulose acetyl succinate (HPMC-AS) and Eudragit L100, which form suspensions under fasted gastric conditions, due to polymer insolubility at acidic pH³⁰⁻³⁴. This allows delay of drug release until the small intestine where absorption is typically favored. Despite the increasing use of enteric polymers in ASD formulations, there is insufficient understanding of their *in vivo* performance with respect to the intraluminal supersaturation and phase behavior, in

particular, the influence of suspension in an acidic medium prior to encountering intestinal pH conditions where drug release occurs.

Understanding how the gastrointestinal physiology influences the solubility of an API after oral administration is crucial in pharmaceutical drug development, since crystallization kinetics may vary significantly depending on physiological attributes such as pancreatic secretions, local pH, gastrointestinal transfer and residence times. For weakly basic drugs, the increase in pH during intraluminal transit from the gastric compartment to the intestinal compartment in the fasted-state can drastically decrease the aqueous solubility (conversion from ionized to nonionized state), resulting in supersaturation. Therefore, *in vitro* dissolution experiments for weak bases should take into consideration the pH-shift occurring during the gastrointestinal transit. Over the years, biorelevant media have been increasingly applied in dissolution testing of drug formulations. Accordingly, a more reliable prediction of the intraluminal supersaturation and phase behavior can be attained when carrying out dissolution assays using biorelevant conditions, that mimic the pH-change from stomach to intestine and the presence of solubilizing species and bile salts.

Posaconazole, an extended-spectrum triazole antifungal, is currently regarded as one of the most potent antifungals for treatment or prophylaxis against many yeast and mold endemic infections including *Aspergillus*, *Blastomyces*, *Candida*, *Cryptococcus*, *Fusarium* and *Zygomycetes* species^{132–138}. However, posaconazole has very low aqueous solubility and is considered a biopharmaceutics classification (BCS) class II drug (Log P: 4.6)¹³⁹. Another important feature is that posaconazole is a polyprotic weak base (acid dissociation constants [pKa] 3.6 for the piperazine group, and 4.6 for the triazole group). Studies have shown that posaconazole suffers from variable and unpredictable absorption, which is affected by several factors including meal intake, dosing regimen and gastric dysfunction in some patient groups. This leads to suboptimal bioavailability which ranges from 8 to 47%^{140–143}. Some of the factors that impact bioavailability of posaconazole suspensions have been explored. Posaconazole shows a large positive food effect; the oral absorption of posaconazole suspensions varied with administration in the fasted state, or with a non-fat or high-fat meal, resulting in 2.7-fold and 3.9-fold improvements in the area under the curve respectively for the fed states¹⁴⁴. Coadministration with a proton pump inhibitor decreased absorption, while taking with an acidic drink increased the extent of absorption, illustrating the importance of gastric pH¹⁴⁵. Hens et al., further evaluated the impact of pH by studying aspirated

gastric and duodenal fluids of human volunteers after administration of acidified (pH 1.6) and neutral (pH 7.1) suspensions of posaconazole¹⁴⁶. Results revealed extensive precipitation in both cases, however some intestinal supersaturation (45 minutes) was observed for the acidified suspension. Noxafil® is the marketed delayed-release tablet comprising posaconazole molecularly mixed with hydroxypropylmethyl cellulose acetate succinate (HPMC-AS) where the ASD is prepared by hot melt extrusion¹⁴⁷. In the view of the fact that HPMC-AS is a pH sensitive polymer, Noxafil® tablets provide a formulation approach to avoid extensive drug release in the stomach and thus avoid some of the variability described above. When Noxafil® tablets were administrated, gastric aspirates under fasted and fed state indeed showed only a small extent of release in the stomach²⁵. On the other hand, fasted state jejunal aspirates demonstrated supersaturation for approximately 90 minutes, while posaconazole precipitation seemed to be predominant for the fed state aspirates.

In the present study, we evaluate the drug release, supersaturation and crystallization kinetics of posaconazole ASDs, as well as Noxafil® tablets, using *in vitro* fasted-state biorelevant media representing gastric and small intestinal conditions. To accomplish this, we adapt a two-stage dissolution setup that was previously introduced to test the role of pH shift on drug dissolution behavior^{148,149}. This simple setup avoids the necessity of a flow pump, eliminates pH inconsistencies, and provides volume flexibility in the dissolution media used. Accordingly, the impact of an abrupt shift from an acidic gastric environment represented by fasted-state simulated gastric fluid (FaSSGF [pH 1.6]), to a fasted state intestinal environment represented by fasted-state simulated intestinal fluid (version 2) (FaSSIF [pH 6.5]), on the phase behavior was studied using several novel analytical methods to evaluate both solid state and solution state phase transitions.

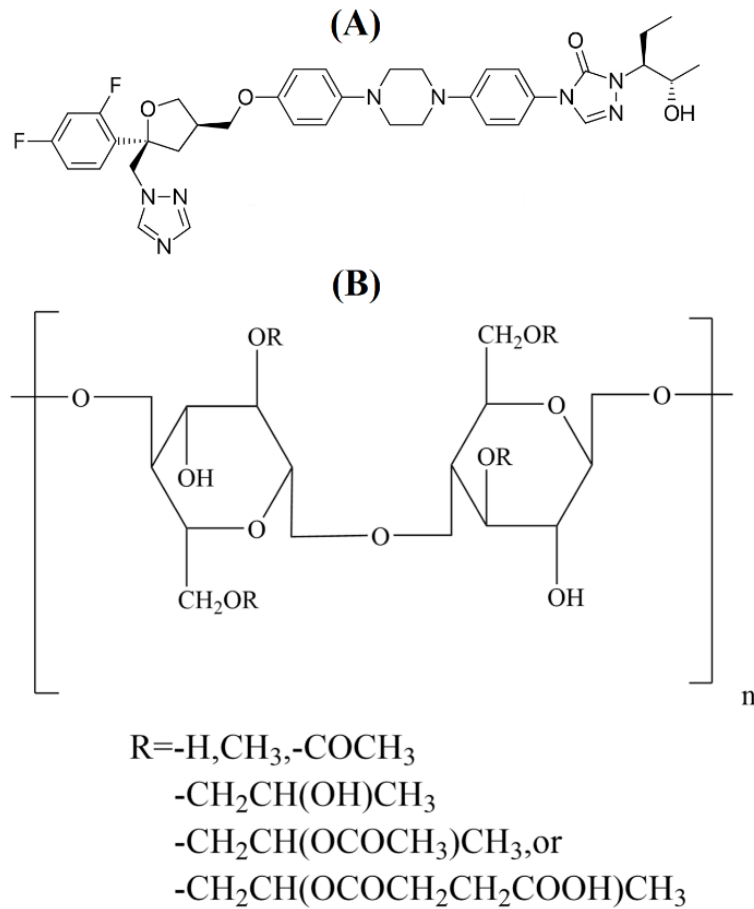


Figure 3-1. Chemical structures of (A) posaconazole and (B) HPMC-AS.

3.3 Materials

Posaconazole (Form I) was purchased from Chemshuttle (Hayward, CA). Noxfil® delayed-release tablets manufactured by Merck & Co. (Kenilworth, NJ) were purchased from the Purdue Pharmacy (West Lafayette, IN). Hydroxypropyl methylcellulose acetyl succinate (HPMC-AS) MF grade was supplied by Shin-Etsu Chemical Co. (Tokyo, Japan). Acetonitrile, hydrochloric acid (HCl), maleic acid, methanol and sodium chloride were purchased from Fisher Scientific (Pittsburgh, PA). Sodium hydroxide (NaOH) was obtained from Avantor Performance Materials, LLC (Radnor, PA). FaSSIF/FeSSIF/FaSSGF and FaSSIF version 2 powders were bought from Biorelevant (London, UK). Structures of posaconazole and HPMC-AS are shown in Figure 3-1.

3.4 Methods

3.4.1 Equilibrium solubility measurements

The equilibrium solubility of posaconazole in FaSSGF and FaSSIF was determined by adding an excess amount of crystalline drug to both media at 37°C and stirring the samples at 300 rpm for 48 hours. Solutions were then ultracentrifuged at 35,000 rpm for 30 min at 37°C using an Optima L-100 XP ultracentrifuge equipped with Swinging-Bucket Rotor SW 41 Ti (Beckman Coulter, Inc., Brea, CA). The supernatant was further diluted in methanol and the posaconazole solution concentration was determined using an Agilent HP 1260 high performance liquid chromatography (HPLC) system (Agilent Technologies, Santa Clara, CA). The chromatographic separation was performed with an Agilent Eclipse Plus C18 column (4.6 mm × 250 mm, 5 µm). The mobile phase consisted of water and acetonitrile (40:60 by volume). Each analytical run duration was 12 min, where the injection volume was 20 µL and the mobile phase flow was held constant at 1.0 mL/min. Posaconazole was detected by ultraviolet (UV) absorbance at a wavelength of 262 nm. Standards (0.05–30 µg/mL) were prepared in methanol, where the standard curve exhibited good linearity ($R^2 = 0.9993$) over this concentration range.

3.4.2 UV/Vis extinction measurements

UV extinction measurements were used to determine the onset of liquid-liquid phase separation (LLPS) in supersaturated posaconazole solutions in FaSSIF. 50 mL of FaSSIF was stirred at 300 rpm and maintained at 37°C using a Kontes jacketed beaker (Randor, PA) connected to a Julabo MA water bath (Seelbach, Baden-Wurttemberg, Germany). A predissolved posaconazole solution in methanol was added to FaSSIF using an Advance 1200 Syringe Pump (Gaithersburg, MD) at a rate of 4 µg/min, in the presence of 20 µg/mL of HPMC-AS to avoid crystallization. The UV extinction was monitored at 350 nm as a function of posaconazole concentration to determine the concentration at which phase separation occurs using a UV fiber optic dip probe coupled to SI Photonics UV/Vis spectrometer (Tucson, AZ).

3.4.3 Fluorescence spectroscopy measurements

Fluorescence spectroscopy was used to confirm the appearance of the non-crystalline drug-rich phase formed upon LLPS by analyzing the changes in the emission spectra of posaconazole. The

LLPS concentration coincides with the amorphous solubility of the compound. Posaconazole is an auto-fluorescent compound and the emission spectrum was found to vary depending on the hydrophobicity of the local environment which in turn depends if the drug is molecularly dissolved or present in drug aggregates. This has been previously observed for other hydrophobic compounds^{150,151}. Fluorescence spectra were collected for posaconazole solutions with concentrations ranging from 0 to 26 µg/mL in FaSSIF, in the presence of 20 µg/mL of HPMC-AS. Solutions were prepared via the solvent shift method by adding a small aliquot of a methanolic solution of posaconazole into the FaSSIF solution, which was maintained at 37°C using a jacketed vessel. Samples were analyzed using a Shimadzu RF- 5301pc Spectrofluorometer (Kyoto, Japan). The excitation wavelength was 240 nm, and the emission spectrum was collected at 0.2 nm intervals from 220 to 450 nm. The excitation slit width was 5 nm, while the emission slit width was 10 nm.

3.4.4 Preparation of posaconazole ASDs

ASDs of posaconazole and HPMC-AS at 3 different drug loadings (10, 25 and 50 wt. %) were prepared using solvent evaporation. Posaconazole and HPMC-AS were weighed in three different ratios; 10:90, 25:75 and 50:50 w/w drug/polymer and fully dissolved in methanol. The solvent was then removed by rotary evaporation at 45°C. The resultant ASDs were further dried for 24 h under vacuum to remove residual solvents. Afterwards, cryo-milling was performed using a 6750 Freezer/Mill (Metuchen, NJ) to obtain a fine powder. Polarized light microscopy and powder x-ray diffraction were used to evaluate prepared ASDs to confirm the absence of detectable crystallinity prior to dissolution experiments. All ASDs were freshly prepared for the dissolution experiments and stored in closed vials with indicating Drierite desiccants at room temperature.

3.4.5 Dissolution studies

The dissolution testing for posaconazole ASDs consisted of two stages using two dissolution media: gastric (FaSSGF) and intestinal (FaSSIF-V2). Two different drug-to-medium ratios were used in the dissolution studies. First, 160, 64, and 32 mg of the 10%, 25%, and 50% ASDs respectively, was weighed, yielding 16 mg of posaconazole in each case. For Noxafil®, the tablets were crushed, and 100 mg of the resultant powder was weighted. Each tablet contains 100 mg of posaconazole

with a total tablet weight of \approx 625 mg, and hence this amount of powder also corresponds to 16 mg of posaconazole. Tablet powder was used in all dissolution tests to avoid confounding effects of tablet disintegration. Additional dissolution experiments were performed, where lower doses of ASD were used. 32, 12.8, 6.4 and 20 mg of the 10%, 25%, 50% ASDs and tablet powder was weighed, respectively, yielding an equivalent 3.2 mg of posaconazole. All ASDs and tablet powder, at both 16 and 3.2 mg dose levels, were initially dispersed in 40 mL of FaSSGF (medium 1) for 60 minutes, during which samples were removed after 15, 30, 45, and 60 minutes. The second stage involved adding 40 mL of modified pH-FaSSIF concentrate (medium 2) to achieve a final volume of 80 mL of FaSSIF (medium 3), where samples were also taken at the following time points: 5, 15, 30, 60, 90, 120, 150, 180, 240 and 300 minutes. The modified pH-FaSSIF concentrate was prepared such that the bile salt/lecithin concentration (in the FaSSIF powder) is double relative to standard FaSSIF, and the pH was adjusted to pH 7.5. By adding 40 mL of medium 2 to 40 mL of medium 1, the final concentration of bile salt/lecithin was equivalent to FaSSIF-V2¹⁹, and the pH was further adjusted to 6.5 with additional NaOH, where the pH was continuously monitored throughout the experiments using a Mettler Toledo FiveEasy™ FE20 benchtop pH-meter (Schwerzenbach, Switzerland). The two-stage dissolution setup is summarized in Figure 3-2. During both stages of dissolution, the media were stirred at 300 rpm, and the temperature was maintained at 37°C. Time-point samples were micro-centrifuged at 14,800 rpm using a Sorvall Legend Micro 17 Centrifuge (Thermo Fisher Scientific, Waltham, MA) for 15 minutes, and the supernatants were analyzed by HPLC using the same methodology as for the solubility experiments. Control experiments where all ASDs and tablet powder were dispersed immediately in the FaSSIF medium, without pre-exposure to FaSSGF, were also performed at the same conditions of the two-stage dissolution experiments.

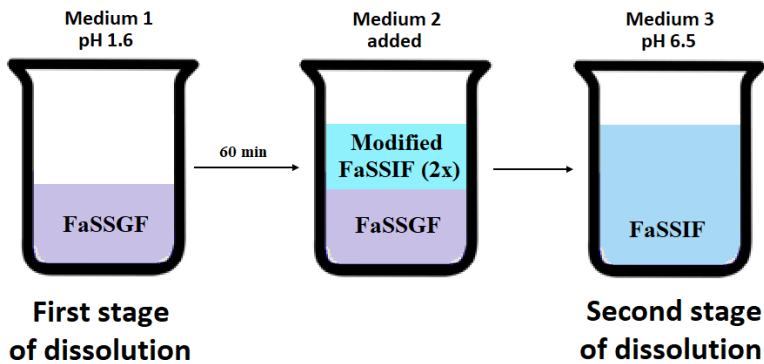


Figure 3-2. Schematic of the two-stage dissolution experiments.

3.4.6 Nanoparticle tracking analysis (NTA) and powder x-ray diffraction (PXRD)

NTA was used to characterize the formation of posaconazole nanodroplets in supersaturated solutions generated once the dissolution media are shifted to the second stage i.e. FaSSIF. One mL samples were withdrawn after 5 or 30 minutes of dissolution in FaSSIF and micro-centrifuged at 14,800 rpm for 15 minutes. These centrifugation conditions allow large undissolved particles of the ASDs and the tablet powder as well most of the posaconazole amorphous precipitate to pellet. The supernatant was analyzed using a NanoSight LM10 from Malvern Instruments (Westborough, MA) with nanoparticle tracking analysis software (NTA 3.1) to characterize the size of nanodroplets that did not pellet. The instrument was equipped with a 75-mW green laser (532 nm) and a temperature-controlled flow-through cell stage. Samples were analyzed at 37°C for 30 s in triplicate. The camera settings were kept constant throughout all experiments (screen gain = 2.0, camera level = 8). The detection threshold used in all analysis was 5, while the camera gain was held at 10.

PXRD analysis was used to assess the crystallinity of the posaconazole precipitate during the dissolution of ASDs and tablets. After 180 minutes of dissolution in FaSSIF, 5 mg of posaconazole dissolved in 0.5 mL of methanol was added to increase the amount of the drug and allow crystals to grow to a detectable range for PXRD. Dissolution samples were then ultra-centrifuged at 35,000 rpm for 20 minutes. After the supernatant was removed, the pellet was recovered and further dried under vacuum at room temperature for 2 h. PXRD measurements were then performed using Rigaku Smartlab diffractometer (Rigaku Americas, The Woodlands, TX) equipped with a Cu-K α

radiation source and a D/tex ultradetector. Glass sample holders were used, and powder patterns were obtained from 5 to 50° 2θ at a scan speed of 2°/min and a step size of 0.02°. The voltage and current used were 40 kV and 44 mA, respectively.

3.4.7 Second harmonic generation (SHG) and two-photon excitation ultraviolet fluorescence (TPE-UVF) microscopy

SHG microscopy was used to detect the onset of crystallinity during dissolution of posaconazole ASDs and tablet powder. The crystallization of SHG-active compounds can be detected by relying on second order nonlinear optical imaging of chiral compounds (SONICC), a technique that differentiates chiral crystals from an amorphous or solution state^{94–96}. Posaconazole possesses four chiral centers (two R and two S)^{152,153}. TPE-UVF microscopy was also used as a compliment to SHG for sensitive detection of posaconazole presence irrespective of its physical state. The two-stage dissolution experiments were performed as described before, where the higher dose was selected to provide adequate SHG and TPE-UVF signals for image analysis. Accordingly, 80, 32, 16 and 50 mg of the 10%, 25%, 50% ASDs and the tablet powder respectively, were weighed and dispersed in 20 mL of FaSSGF. After 60 minutes, 20 mL of modified pH-FaSSIF concentrate was added to generate normal strength FaSSIF. Samples for SHG and TPE-UVF analysis were prepared by removing a small aliquot of the dissolution media at different time points. Time points taken for each sample were typically at 30 and 60 minutes of dissolution in FaSSGF, and at 30, 60, 120 and 180 minutes of dissolution in FaSSIF. Each sample was pipetted into a round nylon-6/6 flat washer (inner diameter, 6.069 mm; outer diameter, 11.938 mm; thickness, 0.381 mm; Small Parts Inc., Logansport, IN) mounted on a glass slide. SHG and TPE-UVF images were acquired using a commercial second order nonlinear imaging of chiral crystals (SONICC) instrument manufactured by Formulatrix (Waltham, MA). SONICC uses the Fianium FemtoPower laser operating at 1064 nm with 51 MHz repetition rate and a 166 fs pulse width. Beam scanning with resonant mirror/galvanometer with 8 kHz fast axis beam scanning generates images. For TPE-UVF experiments, the fundamental beam was doubled to 532 nm through focusing onto and through a lithium triborate crystal (LBO, 5×5×2 mm). The 532 nm incident light was then directed through the beam scanning unit and then focused onto the sample with a dichroic mirror centered at 532 nm with a 10x objective (Nikon, 0.3 NA). The SHG signal at 532 nm was collected in epi-transmission by a 10x near-UV objective (Thorlabs, 0.25 NA). Brightfield and TPE-UVF images

were also collected in the epi-transmission. SHG microscopy images were acquired at 350 mW infrared (IR) power and an exposure time of 894 ms, while TPE-UVF images were acquired at 50 mW power and 447 ms as an exposure time. SHG and TPE-UVF images had fields of view of dimensions of 1925 $\mu\text{m} \times 1925 \mu\text{m}$, whereas the brightfield images had dimensions of 2300 $\mu\text{m} \times 1700 \mu\text{m}$. All scans were obtained in different focal planes in the Z direction, at 100 μm steps. Imaging analysis was performed using ImageJ 1.05b software ¹⁵⁴. The number of new particles formed per unit time was obtained by employing the built-in particle counting algorithm in ImageJ, using the time dependent SHG and TPE-UVF images.

3.5 Results

3.5.1 Equilibrium solubility measurements

The equilibrium solubility of posaconazole at 37°C was measured in FaSSGF and FaSSIF with results shown in Table I. The solubility was much higher in FaSSGF versus FaSSIF, due to the nearly complete ionization of the drug in the acidic medium, in good agreement with previous reports ¹⁵⁵.

Table 3-1. Equilibrium solubility of posaconazole in FaSSGF and FaSSIF at 37°C. (n=3).

Medium	Equilibrium solubility ($\mu\text{g/mL}$)
FaSSGF	115.1 \pm 9.4
FaSSIF	1.69 \pm 0.06

3.5.2 UV/Vis extinction measurements

The concentration at which LLPS occurs in posaconazole supersaturated solutions was determined by monitoring the UV extinction at a non-absorbing wavelength (350 nm). These measurements were performed in the presence of HPMC-AS polymer (20 $\mu\text{g/mL}$) to prevent crystallization. At low concentrations of posaconazole, there was minimal light scattering and the solution remained clear. However, at approximately 20 $\mu\text{g/mL}$ of posaconazole, light scattering and total extinction at 350 nm increased, indicating the formation of a new drug-rich phase, as demonstrated in Figure 3-3.

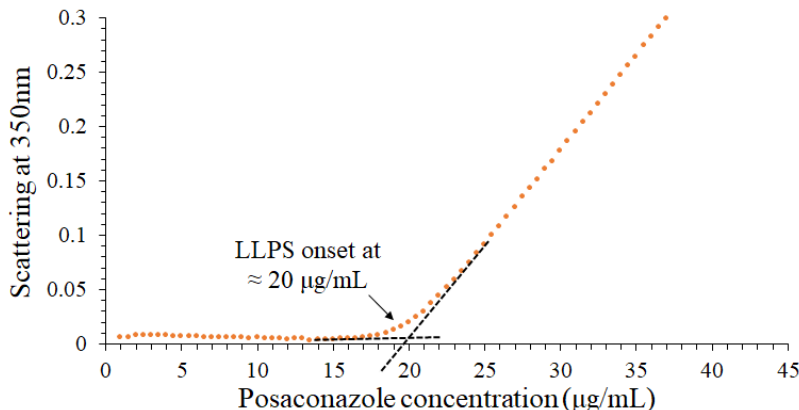


Figure 3-3. LLPS onset concentration of Posaconazole in FaSSIF at 37 °C as illustrated by the sudden increase in UV extinction at 350 nm, indicating the incidence of LLPS.

3.5.3 Fluorescence spectroscopy measurements

Fluorescence spectroscopy was used to confirm the concentration at which the amorphous drug-rich phase was formed by LLPS. The emission spectrum was evaluated as a function of increasing posaconazole concentration in FaSSIF. It has been shown previously that the emission spectrum of a compound varies in response to the hydrophobicity of the environment^{150,151}. As the solvent polarity decreases, the quantum yield increases and the emission maximum shifts to shorter wavelengths (blue shift)¹⁵⁶. When a disordered posaconazole-rich phase was formed at concentrations above of 20 µg/mL, a sudden increase in the peak intensity at 368 nm (I_{368}) of posaconazole was observed, as demonstrated in Figure 3-4. This is due to the formation of posaconazole-rich amorphous phase with different fluorescence characteristics. Subsequently, as the concentration of posaconazole increased, I_{368} increased, indicating that the local posaconazole environment was changing. LLPS determination of posaconazole in sodium phosphate buffer (pH 6.5) using fluorescence spectroscopy was performed as a reference, and the LLPS onset concentration was found to be 8 µg/mL. As shown in Figure 3-5, a gradually increasing blue shift in the emission peak maximum (from 385 nm) is observed with increasing posaconazole concentration above 8 µg/mL, as well as an intensity increase. This is similar to the emission spectra plots previously reported for felodipine¹⁵⁰ and indomethacin¹⁵¹. Interestingly, the peak seen in buffer for concentrations above the LLPS concentration occurs at the same wavelength as the peak that evolves in intensity in FaSSIF, helping confirm that the presence of this peak represents the formation of drug-rich aggregates.

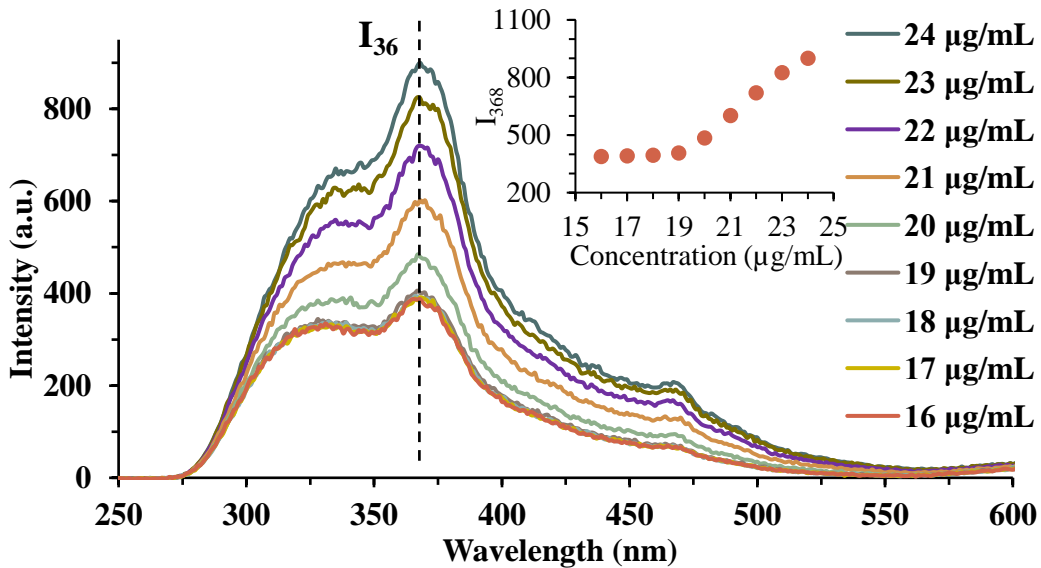


Figure 3-4. Fluorescence emission spectra of posaconazole at different concentrations in FaSSIF. The inset documents the noticeable increase in I_{368} of posaconazole for concentrations $>20 \mu\text{g/mL}$ consistent with the formation of drug-rich aggregates.

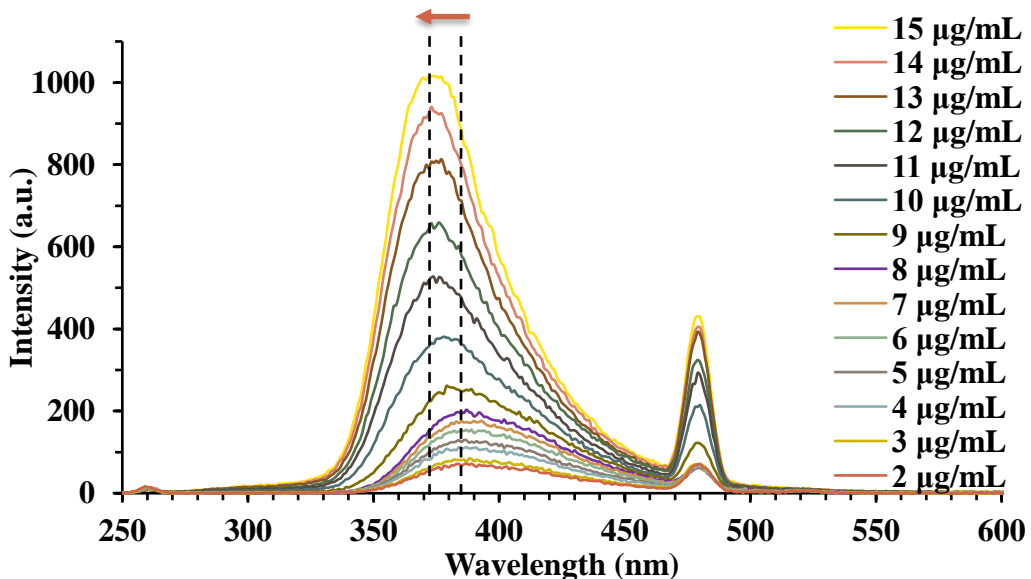


Figure 3-5. Fluorescence emission spectra of posaconazole at different concentrations in buffer. A hypochromic or blue shift (to shorter wavelengths) is observed upon reaching and exceeding the LLPS concentration, as illustrated by the dashed vertical lines.

3.5.4 Dissolution studies of posaconazole ASDs and tablets

Figure 3-6 shows the dissolution profiles of posaconazole ASDs at 10%, 25% and 50% drug loading, and the commercial tablet powder, when the higher dose (16 mg) was added. Upon dissolution directly in FaSSIF (i.e. a one stage dissolution test mimicking fasted state intestinal conditions; red squares/top x-axes), 10% ASDs led to posaconazole supersaturation, maintaining a concentration level around the amorphous solubility for the duration of the experiment, as shown in Figure 3-6A. The supersaturation generated by the dissolution of the 25% ASDs lasted for approximately 90 minutes (Figure 3-6B), where the posaconazole concentration subsequently dropped and then maintained a steady concentration of around 6 µg/mL from 2 hours onwards. The 50% ASDs however, did not reach the amorphous solubility, with moderate supersaturation observed after 15 minutes as shown in Figure 3-6C. The concentration of posaconazole dropped rapidly thereafter to approximately 5 µg/mL, suggesting these ASDs were the fastest to crystallize. Finally, posaconazole tablet powder displayed an initial supersaturation, reaching a peak drug concentration of approximately 21 µg/mL after 15 minutes, as illustrated in Figure 3-6D. Desupersaturation was then observed, however residual posaconazole solution concentration was relatively higher (approximately 11 µg/mL) compared to the 25% and 50% ASDs following crystallization.

Next, analogous two-stage dissolution experiments were performed by exposing the ASDs and tablets powder to FaSSGF for 1 hour, prior to transfer to and dissolution in FaSSIF (blue circles/bottom x-axes). In the FaSSGF stage, the amount of posaconazole release from the ASDs was influenced by the drug loading. Given that 400 µg of posaconazole was added per mL in the FaSSGF stage of dissolution at the higher dose level (16 mg), the amount of drug release from the 10% ASDs was around 7.5% after 60 minutes. For higher drug loading ASDs, posaconazole release increased to approximately 10% and 11.5% from the 25% and 50% ASDs respectively. Therefore, the released posaconazole concentration was lower than the crystalline solubility in the medium, and the resultant solution was subsaturated in all instances. In the FaSSIF stage of dissolution, the media volume was diluted twofold, and the maximum amount of posaconazole available for dissolution was 200 µg per mL, which is 10 times the amorphous solubility. For the 10% ASDs, supersaturation of posaconazole was observed instantly in FaSSIF, where the maximum concentration observed was approximately 25 µg/mL in agreement with the amorphous

solubility of posaconazole in that medium, as demonstrated in Figure 3-6A. After 210 minutes in FaSSIF however, desupersaturation of posaconazole was observed and the concentration decreased to approximately 6 µg/mL. As shown in Figure 3-6B, ASDs formulated at 25% posaconazole loading displayed an initial supersaturation in FaSSIF, lasting about 120 minutes. After this time, desupersaturation was observed. In contrast, the 50% ASDs showed immediate desupersaturation upon shifting the dissolution media to FaSSIF (Figure 3-6C). Noxafil® tablet powder exhibited low release in FaSSGF, with only 8.5% of the drug released after 60 minutes. In FaSSIF, the dissolution profile for the tablet powder displayed supersaturation corresponding to the amorphous solubility that lasted for 30 minutes before the posaconazole concentration dropped, as illustrated in Figure 3-6D. The residual supersaturation at 240 min was higher compared to that observed for the other ASDs evaluated. Finally, the dissolution profiles of posaconazole ASDs and tablet powder at the lower dose of posaconazole (3.2 mg) are provided in Figure A1 of Appendix A. Generally, all systems exhibited similar profiles to the higher dose ASDs upon dissolution in FaSSIF only. In the two-stage dissolution experiments, less amount of drug was released in FaSSGF as expected, since less amount of posaconazole was added per mL of FaSSGF. Upon media transfer to FaSSIF, the 10% and 25% ASDs exhibited relatively faster desupersaturation when compared to their higher dose counterparts. Alternatively, the dissolution profiles for the 50% ASDs and tablet powder did not change notably at the lower posaconazole dose.

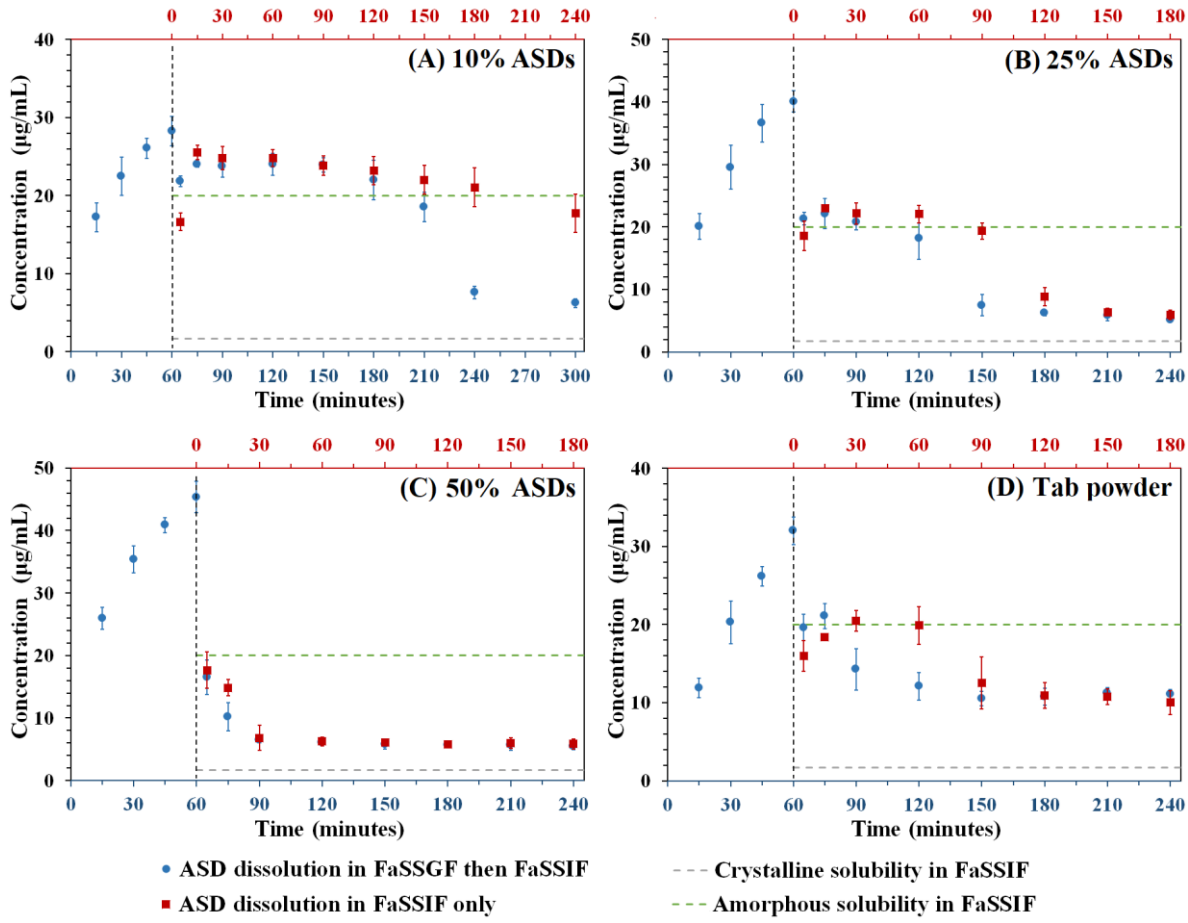


Figure 3-6. Posaconazole concentration-time profiles for ASDs formulated at (A) 10 %, (B) 25 %, (C) 50 %, and (D) tablet powder upon dissolution at 37 °C; blue circles indicate posaconazole dissolution in FaSSGF then FaSSIF, whilst red squares indicate posaconazole dissolution in FaSSIF only. An amount of ASD or tablet powder equivalent to 400 μg/mL of posaconazole was added to the acid stage; this decreases to 200 μg/mL in the FaSSIF stage. The dashed horizontal grey and green lines indicate the measured equilibrium solubility and LLPS concentration of posaconazole in FaSSIF at 37 °C respectively ($n = 3$).

3.5.5 Characterization of posaconazole ASDs and tablet powder dissolution

NTA was used to characterize the supersaturated solution generated when the dissolution medium was changed from FaSSGF to FaSSIF. Any posaconazole amorphous nanodroplets formed in the supersaturated solutions generated by media change can be tracked by NTA, which utilizes the Brownian motion and light scattering of colloidal species to assess their size and concentration. The mean size measurements are summarized in Figure 3-7. Generally, the 10% and 25% drug loading generated nanodroplets were similar in size, around 300 nm, whereas the nanodroplets produced from the tablet powder dissolution were smaller (Figure 3-7). Additionally, NTA

experiments provided particle concentration assessments, as illustrated in Figure A2 of Appendix A. The most notable observations were the lower particle concentration when a lower dose of ASDs was added, as well as the decrease in the nanodroplet concentration of the 10% ASDs after 30 minutes relative to the 5-minute time-point.

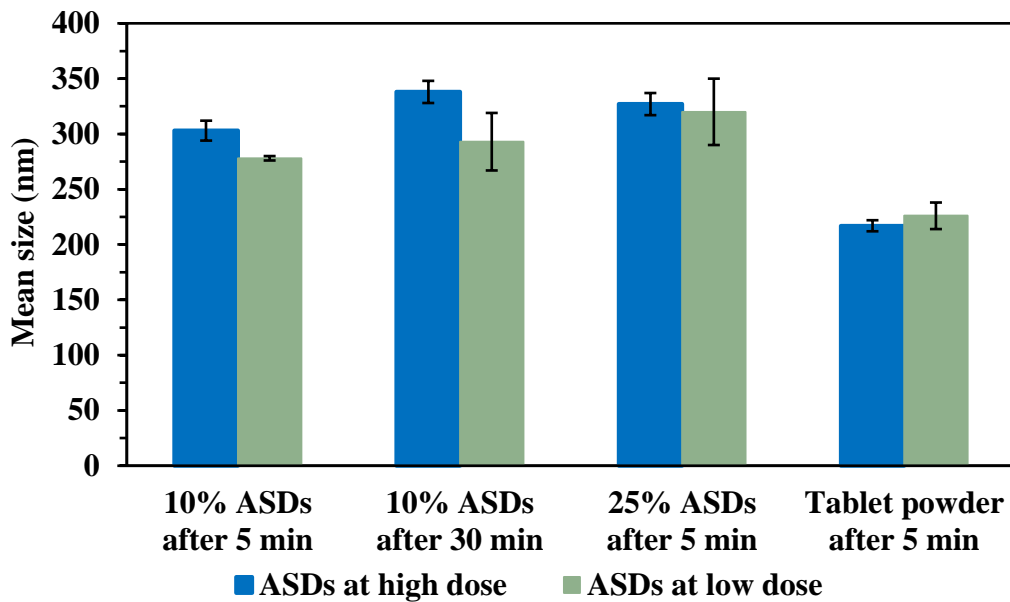


Figure 3-7. Posaconazole nanodroplet mean size measurements for the 10%, 25%, and tablet powder, at high dose (blue columns) and low dose (green columns), upon dissolution in FaSSIF ($n=3$).

PXRD measurements were also used to examine the precipitated posaconazole after 180 minutes of dissolution in FaSSIF, as demonstrated in Figure 8. Precipitates of posaconazole ASDs prepared with HPMC-AS at 10% (Figure 3-8A) 25% (Figure 3-8B) and 50% (Figure 3-8C) displayed diffraction peaks characteristic of the form 1 posaconazole polymorph (peaks 7.5, 10, 18, 20, 22 and 26° 2-theta), which can be found in the diffraction pattern of the reference API (Figure 3-8E). The 50% ASDs demonstrated higher intensity diffraction peaks compared to the 10% and 25% ASDs, indicating a higher extent of crystallization. The diffraction pattern from the precipitate of the tablet powder (Figure 3-8D) showed also some characteristics peaks of posaconazole form 1, however with less clarity and peak broadening, which could suggest that the crystals precipitated from this formulation are smaller and/or more defective possibly due to the presence of other tablet excipients. The peaks at 32 and 46° 2-theta are characteristic of sodium chloride ¹⁵⁷, which was

precipitated from the FaSSIF medium during drying, while the peaks at 25, 38 and 48° 2-theta in Figure 3-8D are due to titanium oxide ¹⁵⁸, which is present in the tablet formulation.

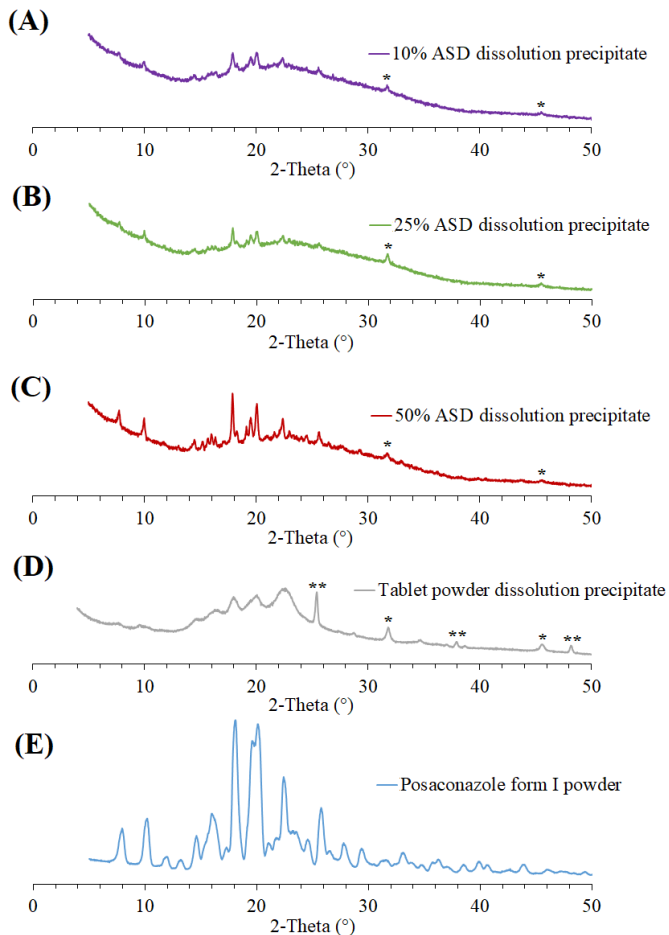


Figure 3-8. PXRD patterns of slurried posaconazole ASDs prepared at (A) 10%, (B) 25%, (C) 50% drug loading, and (D) Noxfil® tablet powder after dissolution in FaSSIF for 180 minutes, in addition (E) posaconazole form I crystalline powder. The * and ** symbols denote the presence of sodium chloride and titanium oxide in the samples, respectively.

SHG images acquired during dissolution of these systems, at different time-points are shown in Figure 3-9. SHG selectively measures the crystalline material. All three dispersions, plus the tablet powder, displayed the presence of crystallinity early on during the FaSSGF stage. As shown in Figures 3-9A, 3-9B and 3-9D, the 10%, 25% ASDs and tablet powder showed a few crystals after 30 minutes of immersion in acidic media. In FaSSIF, SHG-active domains were also present at 30 minutes and 180 minutes with an increase in number at the later timepoint. The 50% ASDs were highly crystalline in terms of size and number of crystals compared to the other dispersions, throughout all timepoints of the dissolution experiments (Figure 3-9C). It should be noted that no

crystals were observed in the ASDs prior to dissolution studies, strongly suggesting that crystallization was initiated by suspension in gastric conditions. SHG experiments were also attempted at the lower ASD dose level (data not shown). Although limited crystallinity was observed, reliable qualitative and quantitative observations could not be established due to weak signal intensity.

Figure 3-10 shows TPE-UVF images which can be used to monitor the suspension/dissolution of ASDs and tablet powder in FaSSGF and FaSSIF. TPE-UVF signal is generated from posaconazole in the ASD, and unlike the SHG signal, does not require the drug to be in the crystalline state. During suspension in FaSSGF, TPE-UVF images revealed large ASD particles containing posaconazole (posaconazole is not fully released in the gastric medium due to the polymer insolubility). Upon media transfer to FaSSIF, the TPE-UVF- active signals notably decreased for the 10%, 25% ASDs and tablet powder, consistent with drug release as the polymer dissolved in the higher pH environment. This was not the case for the 50% ASDs however, which is consistent with extensive crystallinity in the ASD matrix. It should be noted that the fields of views from both SHG and TPE-UVF were not exactly congruent, thus overlaid images cannot be trivially generated. The corresponding brightfield images for the 10% ASDs are also displayed (Figure 3-10) providing further information about the ASD particles during dissolution.

Integration of the SHG signal intensity was utilized to calculate the fractional volume crystallinity using the SHG signal, while the overall fractional volume of posaconazole species (crystalline and amorphous) was assessed by using the TPEF signal intensity. These results are summarized in Figure 3-11. In Figure 3-11A, the volume fraction SHG %, i.e. crystallinity, appeared to increase with time for all systems until it reached a maximum at 240 minutes of dissolution. Additionally, the 50% ASDs had the highest average volume crystallinity compared to the other systems, where the final crystallinity at end of the experiment was roughly 250 times that of 25% ASDs. Figure 3-11B demonstrates the volume fraction of undissolved posaconazole species as detected from the TPE-UVF signal intensity. Except for the 50% ASDs, all systems demonstrated higher volume fraction values of detectable posaconazole species in the FaSSGF dissolution stage, in comparison to the FaSSIF dissolution stage, since the majority of the drug was not released in the gastric medium.

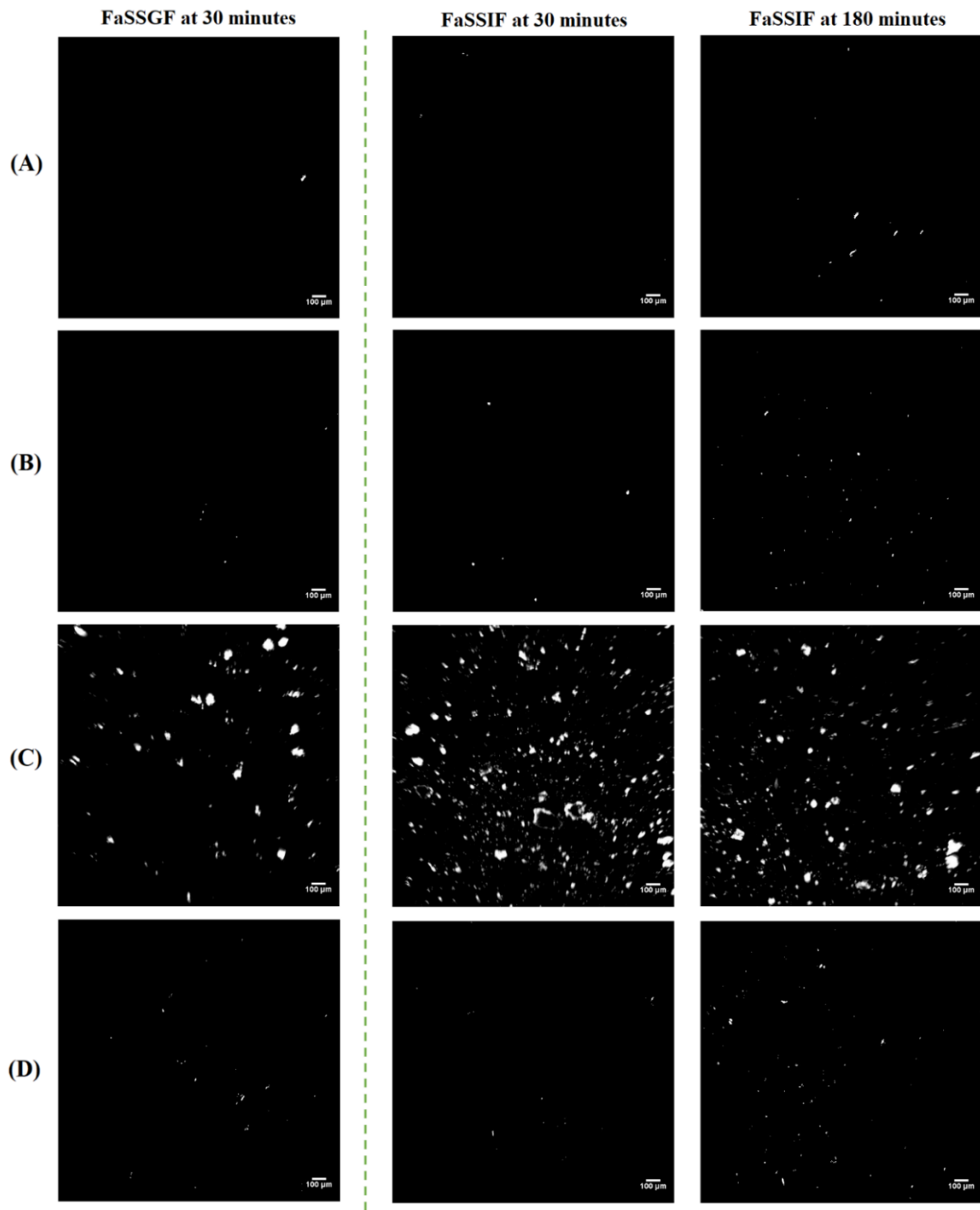


Figure 3-9. SHG images of posaconazole ASDs prepared at (A) 10%, (B) 25%, (C) 50% drug loading and (D) tablet powder upon suspension/dissolution in FaSSGF for 30 minutes (left column), dissolution in FaSSIF for 30 minutes (middle column), and dissolution in FaSSIF for 180 minutes (right column).

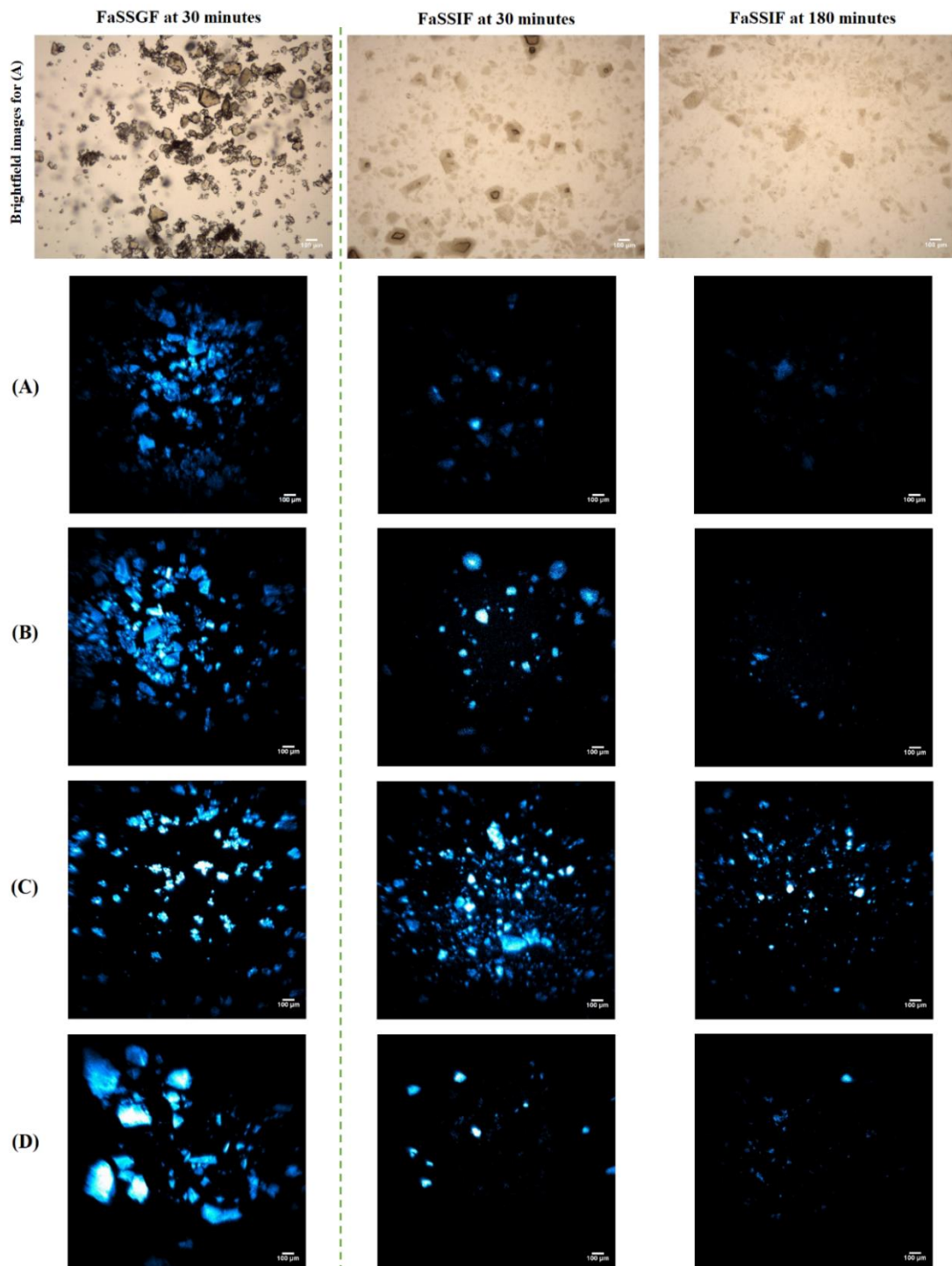


Figure 3-10. Brightfield and TPE-UVF images of posaconazole ASDs prepared at (A) 10%, (B) 25%, (C) 50% drug loading and (D) tablet powder upon suspension/dissolution in FaSSGF for 30 minutes (left column), dissolution in FaSSIF for 30 minutes (middle column), and dissolution in FaSSIF for 180 minutes (right column). The corresponding brightfield images for (A) 10% ASDs are shown in the first row. The blue regions indicate undissolved posaconazole, either arising from crystallized posaconazole or undissolved ASD.

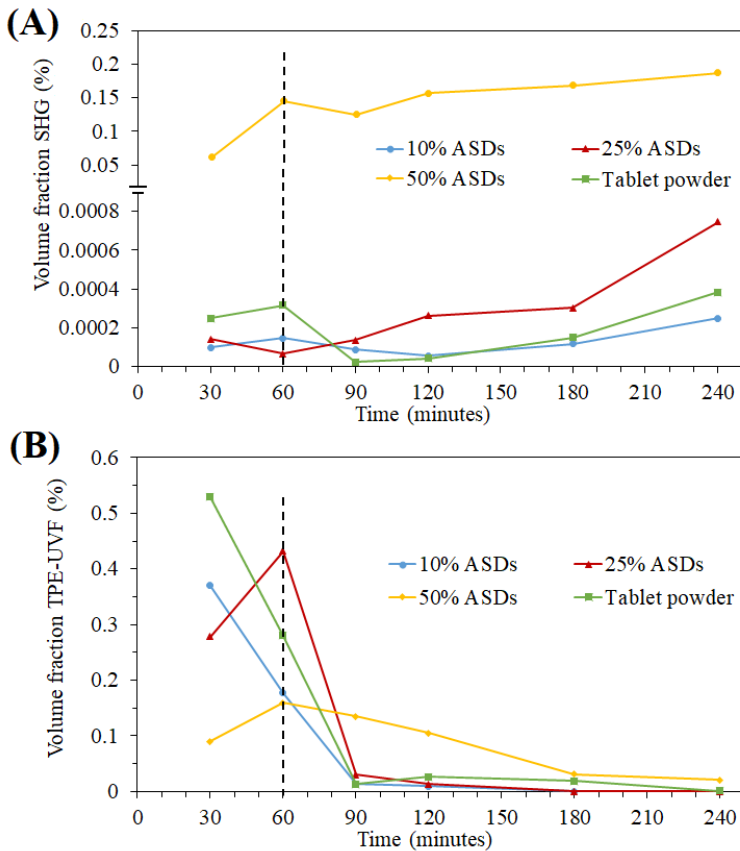


Figure 3-11. Volume fraction (%) calculated for (A) SHG signal (crystallinity) and (B) TPE-UVF signal (undissolved posaconazole either in amorphous or crystalline form) for all ASDs and the tablet powder at different time points, upon dissolution in FaSSGF up to 60 minutes, then in FaSSIF onwards. The dashed vertical line denotes media transfer at that timepoint. Error bars are omitted for clarity.

3.6 Discussion

ASDs are supersaturating drug delivery systems formulated with the aim of increasing *in vivo* drug concentrations beyond those achievable with the crystalline drug, thereby improving the bioavailability of compounds where intestinal absorption is solubility-limited. However, different phase transformations can occur during ASD dissolution and alter the dissolution outcomes^{5,102,159}. The first scenario considers solution phase transformations that occur after the drug has dissolved. The most well-known transition is crystallization from the supersaturated solution formed upon dissolution^{10,159}. A less described transformation is the formation of amorphous nanodroplets via LLPS that can remain kinetically stable for a sufficient window of time to positively impact absorption and bioavailability⁷⁵. LLPS occurs when the concentration of the drug surpasses the

amorphous solubility, where the excess drug precipitates as amorphous nanodroplets. Accordingly, the final solution consists of amorphous nanodroplets in equilibrium with a solution saturated at the amorphous solubility and supersaturated with respect to the crystalline solubility. With time, nanodroplets may agglomerate to form larger amorphous precipitates. Crystallization and desupersaturation can also occur subsequent to LLPS, since supersaturation, and hence the driving force for crystallization, is maximized. Crystallization can also occur in the matrix, prior to ASD dissolution¹⁰. Matrix crystallization provides a source of seeds. The polymer in the ASD ideally not only improves the dissolution rate, but also acts as a matrix crystallization inhibitor and, by inhibiting solution crystallization, enables supersaturation to be maintained^{5,12}.

The posaconazole ASD formulation studied herein contains two components with pH-dependent solubility, potentially leading to a complex landscape of phase behaviors. The drug has some solubility at gastric pH, while the polymer has extremely low solubility¹⁰⁸. It is generally thought that formulations prepared with weakly acidic polymers such as HPMC-AS will not undergo any drug dissolution in the stomach due to polymer insolubility under these conditions. However, some posaconazole release was observed from these dispersions when suspended at low pH. This observation is consistent with a recent study by Li and Taylor¹⁶⁰. It was demonstrated that for ASDs formulated with a non-ionizing drug and different poorly soluble polymers, the extent of drug release was related to the amorphous solubility, the drug loading and strength of drug-polymer interactions. The extent of release suppression was dependent on the specific polymer employed and more extensive release was observed for higher drug loading ASDs¹⁶⁰. The same trend is observed herein, whereby the high drug loading posaconazole ASDs led to more release in the gastric compartment (where the polymer is insoluble), as shown in Figure 3-6. However, release was incomplete from all dispersions, and thus dispersion of posaconazole in HPMC-AS substantially reduces drug release into the gastric medium.

Fasted-state gastric transient times for oral formulations are reported to be inconstant and subject to individual variation^{161,162}. Interestingly, posaconazole remaining in the undissolved ASD bulk appears to be susceptible to fairly rapid crystallization when suspended in acidic media, particularly for the high drug loading formulation. This is clearly demonstrated in Figure 3-9, where SHG images indicate that some crystals were present following suspension of the ASDs in the gastric medium, after only 30 minutes. In these experiments, the dose of posaconazole

evaluated was 400 µg of drug per mL of FaSSGF, which is equivalent to one Noxafil® tablet (100 mg) when given with 250 mL of fluid. Due to the insoluble nature of the polymer, <15% of drug is released for any system in the gastric environment, and the concentration never reached the crystalline solubility (Figure 3-6). TPE-UVF images (Figure 3-10) confirm that posaconazole was still present in the matrix, in agreement with the dissolution studies. Solution-phase crystallization cannot occur, since the thermodynamic driving force needed for posaconazole to nucleate from the solution phase was absent due to the subsaturated concentration. Therefore, and perhaps somewhat counterintuitively, we see the formation of crystals in the ASD matrix when suspended in a solution subsaturated with respect to crystalline solubility, i.e. in conditions where dissolution of crystals is thermodynamically favored. This is an important observation since it indicates that crystals formed in the HPMC-AS matrix were apparently “protected” from dissolution in the surrounding media, and thus are available for transfer to the intestinal compartment. The extent of crystal formation was found to be much greater in the 50% ASD, although varying levels of crystallinity evolved in all formulations. This finding is interesting as it raises questions about the functionality of polymers with pH dependent solubility, not only in terms of controlling drug release, but also in mitigating drug crystallization in the matrix. Notably, no crystallinity was detected in any ASD prior to immersion in gastric media indicating that HPMC-AS is effective at preventing crystallization during ASD fabrication, but not upon suspension in acid. In Figure 3-12, the ratio of the average volume fraction crystallinity (based on SHG analysis) and the average volume fraction of undissolved posaconazole (based on TPE-UVF analysis) is shown for all dispersions during suspension/dissolution in FaSSGF after 30 minutes. This ratio provides an estimate of the percentage of matrix crystallization that occurred in the gastric media and highlights the much higher extent of crystallization in the 50% ASDs. In contrast, the other formulations only show limited crystallinity.

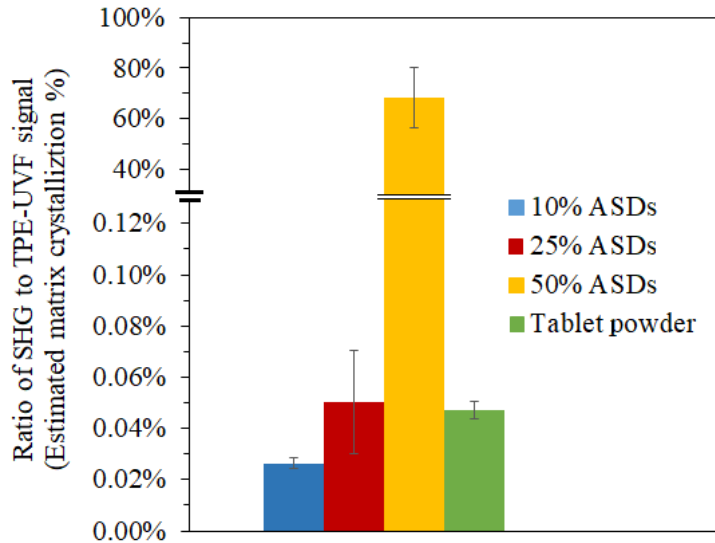


Figure 3-12. Ratio of volume fraction crystallinity to volume fraction posaconazole (from Figure 3-11) during suspension/dissolution in FaSSGF after 30 minutes.

In this study, the ASD composition impacted several processes; the extent of drug release, the degree of matrix crystallization and the formation of amorphous nanodroplets upon media transfer. The release of the drug into the gastric medium from the ASD at concentrations higher than the drug solubility at intestinal pH is important as it leads to the potential for supersaturation upon media transfer. Supersaturation occurs because when the pH increases, the ionization state of posaconazole changes from ionized to neutral and the solubility decreases. The theoretical extent of supersaturation upon media transfer is greatest for the 50% drug loading ASDs and smallest for the 10% posaconazole ASDs based on the different gastric posaconazole release extents (Figure 3-6). In FaSSIF, an additional source of supersaturation is posaconazole release from the remaining undissolved, uncristallized ASD, as the polymer is now soluble. Despite the higher dissolved concentration in gastric conditions, a reduced extent of supersaturation was observed for the 50% ASD upon media transfer, compared to other systems. This can be attributed to the presence of extensive matrix crystallization during the gastric stage (Figure 3-9C and Figure 3-12). Crystals present in the undissolved matrix at the time of media transfer were released when HPMC-AS dissolved in the higher pH environment. These posaconazole crystals are expected to grow rapidly consuming the high initial ambient supersaturation present in the intestinal medium, created by transfer of the dissolved posaconazole from the low to higher pH environment. Given that the rate

of desupersaturation depends on the surface area available for crystal growth, the extent of the initial supersaturation, as well the occurrence of any additional primary or secondary nucleation events, it is unsurprising that the 50% ASD shows such rapid desupersaturation, and the amorphous solubility is not achieved. Interestingly, even in the absence of a gastric stage, the 50% ASD showed relatively poor supersaturation in FaSSIF (Figure 3-6C), highlighting the overall susceptibility of this high drug-loading formulation to competitive crystallization during the release process. In contrast, the lower drug loading systems had a much lower crystal burden and consequently a largely amorphous content at the time of media transfer (Figure 3-12), and thus, a greater potential for supersaturation. For these systems, when the dissolution medium was shifted to FaSSIF, supersaturation was generated via two mechanisms 1) by a change in the ionization state of drug released in the gastric medium, and 2) the rapid release of posaconazole from matrix due to polymer dissolution. Given the low amount of drug released in the gastric medium, mechanism 2 seemingly predominated. The 10% and 25% dispersions underwent LLPS with the formation of nanodroplets (~300 nm, Figure 3-7) and generated supersaturated solutions of posaconazole, that lasted for 150 and 60 min, respectively (Figure 3-6). Interestingly, the duration of supersaturation decreased notably for both drug loadings, at the low dose level (Figure 3-S1). Figure 3-13 compares the dissolution profiles of the 10% ASDs at the two dose levels (extracted from Figure 3-6A and Figure 3-S1A). Given that the amorphous solubility was reached in both instances, the same maximum supersaturation was achieved for both dose levels. While supersaturation extent is known to impact crystallization kinetics, this factor clearly cannot explain the variations in the observed concentration-time profiles. Given that we know from SHG images that a small amount of crystals is present at the beginning of the FaSSIF stage for all ASDs, the explanation for the more prolonged duration of supersaturation in the case of the higher dose can be most likely be explained by a reservoir effect. In other words, as drug is removed from solution by crystal growth, additional drug dissolves to replenish the lost drug. The source of the drug reservoir is either undissolved ASD, or drug present in the amorphous nanodroplets, formed when the concentration exceeds the amorphous solubility. Obviously, in the case of the lower dose, less overall drug is available, and hence any amorphous drug reservoir will be depleted at a sooner time point, leading to the earlier onset of desupersaturation observed in Figure 3-13. At this juncture, it is important to point out that the onset of desupersaturation for this complex system does not represent the onset of crystallization, as is commonly assumed. Rather, it represents the time point

when the rate of crystal growth exceeds the rate of dissolution of any undissolved amorphous material, and/or the time when all undissolved amorphous material is depleted. Finally, Figure 3-14 provides a schematic summarizing the different states of the drug present in the two media, as well as the impact of drug loading on the dissolution and phase behavior.

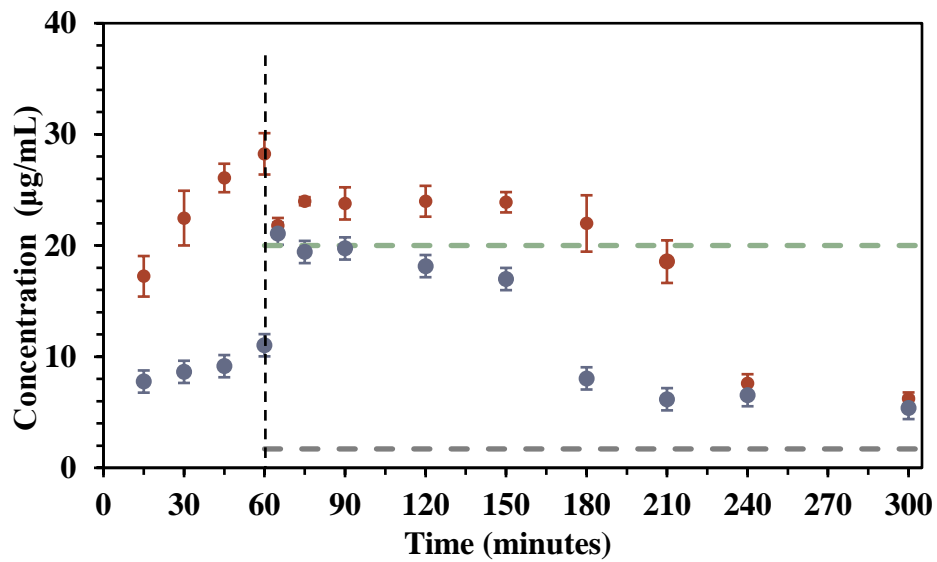


Figure 3-13. Posaconazole concentration-time profiles for high dose ASDs (blue circles) and low dose ASDs (orange circles) formulated at 10 % drug loading upon dissolution at 37°C in FaSSGF then FaSSIF. The dashed horizontal grey and green lines indicate the measured equilibrium solubility and LLPS concentration of posaconazole in FaSSIF at 37 °C respectively ($n = 3$).

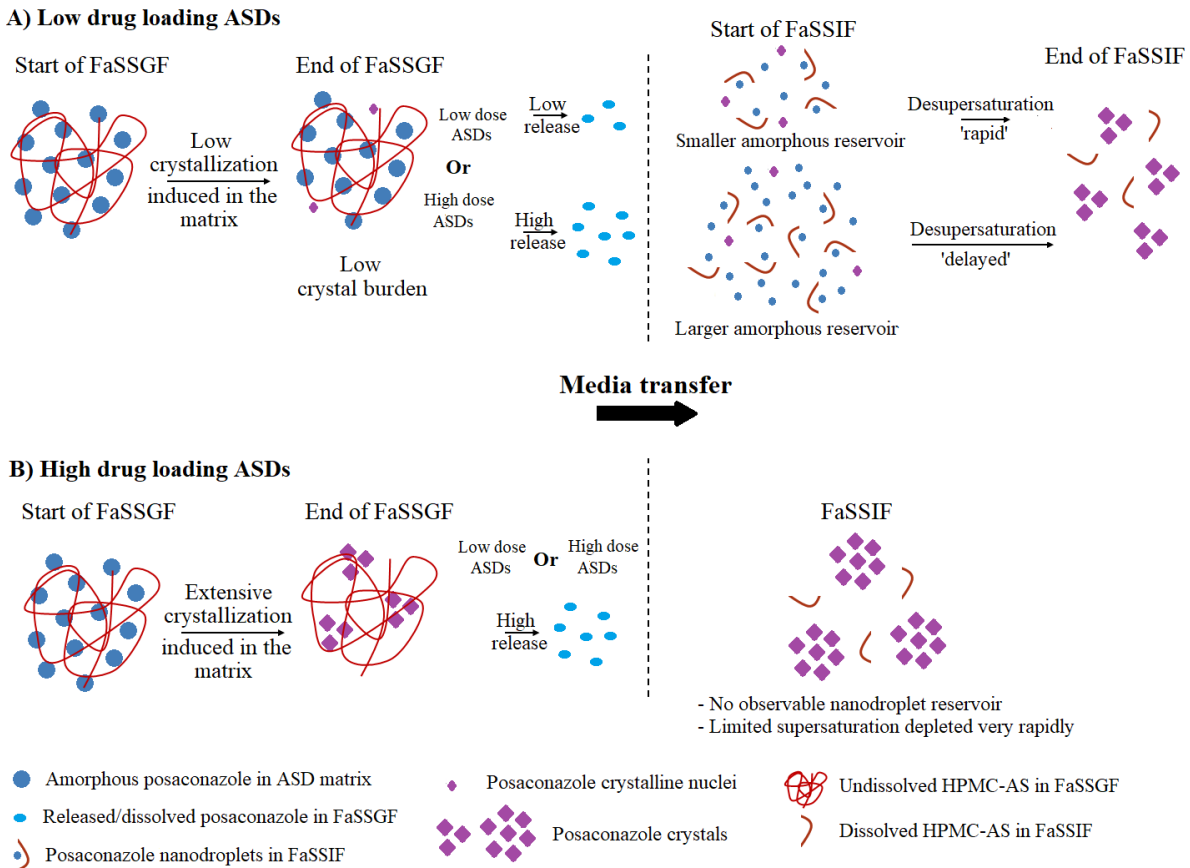


Figure 3-14. Schematic illustration of the mechanisms of dissolution and crystallization of the A) low drug loading ASDs and B) high drug loading ASDs, upon dissolution in FaSSGF followed by FaSSIF.

The importance of evaluating the impact of the gastric stage (which leads to the formation of crystals in the matrix) on the release profile is highlighted by considering the FaSSIF-only dissolution profiles, whereby longer durations of supersaturation are observed in all instances, but most notably for the lower drug loading ASDs, presumably due to the initial absence of seeds. This suggests that HPMC-AS in itself is potentially an effective solution-crystallization inhibitor for posaconazole, when matrix crystallization is absent, and provided that the dissolution experiments are carried out in a medium where the polymer is soluble. The complex crystallization patterns observed herein suggest that the ability of ASD polymers to act as crystallization inhibitors should be assessed in different environments, varying both the ionization state of the drug and polymer via pH change, and evaluating drug crystallization from both the matrix and supersaturated solutions.

3.7 Conclusions

Characterization of posaconazole ASDs in a multi-compartmental biorelevant dissolution setting was essential to understanding the impact of pH-shift on drug release, supersaturation and precipitation kinetics. The extent of posaconazole supersaturation generated upon conversion to the unionized state in the intestinal medium was impacted by the amount of posaconazole released in the gastric medium and the extent of matrix crystallization in the undissolved ASD particles. SHG microscopy images revealed the presence of crystals during the gastric stage of dissolution for all systems. These seed crystals were transferred to the intestinal compartment and promoted further crystallization. Supersaturation profiles in the intestinal medium were found to depend on the drug loading in the ASD, as well as the amount of ASD that was dosed. These *in vitro* dissolution results provide insights for better formulation prediction of poorly soluble weakly basic drugs, in the context of utilizing delayed-release ASDs, as well as understanding potential origins of intraluminal absorption variability for such systems.

CHAPTER 4. INTERPLAY OF SUPERSATURATION AND SOLUBILIZATION: LACK OR CORRELATION BETWEEN CONCENTRATION-BASED SUPERSATURATION MEASUREMENTS AND MEMBRANDE TRANSPORT RATES IN SIMULATED AND ASPIRATED HUMAN FLUIDS

This chapter is a reprint with minor modifications of a manuscript published in *Molecular Pharmaceutics* in October 2019 with the same title by: Ahmed Elkhabaz, Dana E. Moseson, Joachim Brouwers, Patrick Augustijns, and Lynne S. Taylor.

4.1 Abstract

Supersaturating formulations are increasingly being used to improve the absorption of orally administered poorly water-soluble drugs. To better predict outcomes *in vivo*, we must be able to accurately determine the degree of supersaturation in complex media designed to provide a surrogate for the gastrointestinal environment. Herein, we demonstrate that relying on measurements based on consideration of the total dissolved concentration leads to underestimation of supersaturation and consequently membrane transport rates. Crystalline and amorphous solubilities of two compounds, atazanavir and posaconazole, were evaluated in six different media. Concurrently, diffusive flux measurements were performed in a side-by-side diffusion cell to determine the activity-based supersaturation by evaluating membrane transport rates at the crystalline and amorphous solubilities. Solubility values were found to vary in each medium due to different solubilization capacities. Concentration-based supersaturation ratios were also found to vary for the different media. Activity-based measurements however, were largely independent of the medium, leading to relatively constant values for the estimated supersaturation. These findings have important consequences for modeling and prediction of supersaturation impact on the absorption rate, as well as for better defining the thermodynamic driving force for crystallization in complex media.

4.2 Introduction

Modern drug discovery strategies have led to an increase in therapeutic candidates with complex molecular structures and challenging physicochemical properties.^{83,84} One major issue with these prospective drugs is their poor aqueous solubility which potentially hinders oral delivery. As a

result, there has been a great deal of interest in formulations that generate supersaturated solutions of these practically insoluble compounds.^{5,163} Supersaturation is attained when the thermodynamic activity (and the related entity, the chemical potential) of a solute in the solution phase is higher than that of the solute at equilibrium with the most stable crystalline form.⁴⁹ Supersaturation is typically reported as the supersaturation ratio (SR_{conc}) using concentration measurements:

$$SR_{conc} = \frac{C}{C_{eq}} \quad (4-1)$$

where C is the concentration of the drug in the medium of interest and C_{eq} is the drug crystalline solubility in exactly the same medium (i.e., identical pH, buffer components, ionic strength, micellar species, etc.). From a clinical perspective, the presence of a drug at a higher concentration than its equilibrium solubility i.e. in a supersaturated state, provides an enhanced driving force for absorption, which in turn can positively impact bioavailability.^{75,164–168} Hence, diffusive flux across a membrane increases linearly with supersaturation, up to a certain supersaturation limit.^{74,75} Beyond this limit, liquid-liquid phase separation (LLPS) occurs, with the formation of colloidal drug-rich aggregates.^{73,74} The occurrence of LLPS marks the upper limit of supersaturation which can be achieved, whereby the concentration at which LLPS occurs is closely related to the amorphous solubility of a compound. Since no further increase in the free drug concentration in the solution phase can be achieved above the amorphous solubility, the diffusive flux becomes relatively constant for concentrations beyond that limit.⁷⁵ Nevertheless, the formation of these colloidal species has been hypothesized to be beneficial for oral drug delivery, by serving as a reservoir and continuously replenishing the absorbed drug.^{75,76} Diffusion through the unstirred water layer is often considered the rate-limiting step for intestinal uptake of highly permeable lipophilic compounds.^{169–171} Therefore, particle drifting into the unstirred water layer has also been suggested as a mechanism by which absorption is enhanced.^{172,173} It should be noted that supersaturated solutions as well as phase separated systems containing colloidal drug-rich aggregates will only exist if crystallization is prevented or retarded.

When assessing supersaturating formulations during preclinical development, it is important to consider a variety of factors including the physicochemical properties of the drug and the relative stability of the supersaturated state in the dissolution medium. Understanding supersaturation thermodynamics for relevant *in vivo* conditions can be advantageous from a formulation design standpoint. Thus, performing supersaturation assessment in biorelevant conditions is pivotal for

reasonable prediction of eventual intraluminal performance. Biorelevant media have gained increasing attention in pharmaceutical development, where their utilization is intended to better mimic the composition of the gastrointestinal fluids, as compared to simple aqueous buffer solutions. The presence of solubilizing species including bile salts and phospholipids, in addition to other solution properties such as pH, can greatly alter supersaturation and phase behavior of lipophilic compounds. In particular, for supersaturating formulations, the impact of dissolution media on factors such as the amorphous solubility (maximum degree of supersaturation) and supersaturation duration, is poorly understood. Further, comparisons between the thermodynamic properties and membrane transport rates of supersaturated drug solutions in simulated versus human intestinal fluids have not been made, yet are essential to enhance the predictability of *in vitro* assessments. Recent characterization studies of human intestinal fluids (HIF) have identified six main bile salts that constitute approximately 98.4% of the biological surfactant content in the gastrointestinal tract.³⁸ These include sodium taurocholate (STC), sodium taurodeoxycholate (STDC), sodium taurochenodeoxycholate (STCDC), sodium glycocholate (SGC), sodium glycocodeoxycholate (SGDC), and sodium glycochenodeoxycholate (SGCDC). The molecular structure of bile salts is distinctive with a steroid ring system to which three (STC and SGC) or two hydroxyl groups (STDC, STCDC, SGDC and SGCD) are attached.^{39–41} The critical micelle concentration (CMC) of bile salts is usually not well-defined, since they exhibit a complex pattern of self-association, including dimerization as well as the formation of micellar aggregates and higher oligomers/multimers.^{174–176} Variations in the substitution/orientation of the hydroxyl or presence of tauro/glyco groups on the bile salt structure alter the CMC range, resulting in different solubilization capacities among the various bile salts.⁴² In addition to bile salts, lecithin (composed of a mixture of phospholipids) is another main component of HIF. The presence of lecithin lowers the CMC of bile salts and leads to the formation of mixed micelles.^{43,44}

Current commercial biorelevant media such as fasted/fed-state simulated intestinal fluid (Fa/FeSSIF) contain a single bile salt, STC. The first version of FaSSIF (FaSSIF-V1) utilizes a sodium phosphate buffer and contains STC and lecithin in concentrations of 3 mM and 0.75 mM, respectively.²⁰ The refined version of FaSSIF (FaSSIF-V2), introduced in 2008,¹⁹ replaces the sodium phosphate buffer with a maleic acid-based buffer, and decreases the lecithin content to 0.2 mM. Both versions of FaSSIF have a pH of 6.5. However, both commercial media are oversimplified in their composition relative to HIF since they contain only a single bile salt (STC).

Studies from our group have shown that bile salts are not interchangeable in terms of their impact on the solution thermodynamic properties,¹⁷⁷ or on the stability of supersaturated solutions to crystallization.^{36,37} Moreover, little is known about the behavior of supersaturated drug solutions in aspirated HIF, and how well this behavior can be mimicked by simulated biorelevant media. The difference in the composition of the commercially-available biorelevant media versus HIF could affect their relative solubilization capacity, both for crystalline drug, as well as for supersaturated solutions. Theoretically, differences in solubilization capacity between media may impact the perceived supersaturation extent when evaluated based on the total dissolved concentration (equation 4-1).^{45,46} This could be particularly important when evaluating aspirated fluids following oral dosing to assess the extent to which supersaturation has occurred, as well as using simulated media to predict *in vivo* supersaturation. Thus, it is imperative to evaluate supersaturation based on measurement of the solute activity, which can be viewed as the ‘effective’ drug concentration, and to determine how well the concentration-based value correlates with this more rigorous parameter.

In this work, the hypothesis to be tested is that the maximum supersaturation that can be achieved is dictated by the effective drug concentration (i.e., the solute activity) at the amorphous solubility of the compound. Further, the effective drug concentration in the presence of an amorphous precipitate is expected to be largely independent of the type of biorelevant medium employed. We further hypothesize that using the total dissolved concentrations to determine the supersaturation ratio, as per equation 4-1, will lead to incorrect conclusions about the thermodynamic driving force for membrane transport and solute crystallization. To test this hypothesis, we assess the impact of different media on the crystalline and amorphous solubilities, supersaturation ratios and membrane transport rates, for two poorly-soluble drugs. Here, the assumption is that the membrane transport rate is dictated by the solute activity gradient.¹⁷⁸ The two model compounds used are atazanavir ($\log P: 4.5$, $pK_a: 4.52$)¹⁷⁹ and posaconazole ($\log P: 4.6$, $pK_a: 3.6$ and 4.6).^{146,180} These compounds are both weak bases, and therefore likely to undergo supersaturation upon transfer from the gastric environment to the small intestine. The media used included two simple buffers namely sodium phosphate and maleic acid buffer, and two commercial biorelevant media, FaSSIF-V1 and FaSSIF-V2. Additionally, fasted-state aspirated human intestinal fluid (FaHIF) was used to systematically evaluate differences between both simulated media and aspirated biologic fluid. Finally, a modified version of FaSSIF comprised of the six most prevalent bile salts, plus lecithin,

(Composite-FaSSIF) was prepared to more closely mimic the composition of FaHIF, from a simulated medium perspective. By measuring the crystalline solubility, the amorphous solubility and diffusive flux across a membrane, the varying impact of all six media on the thermodynamic properties of supersaturated solutions for two compounds was investigated.

4.3 Materials

Atazanavir (free base) and posaconazole (Form I), shown in Figure 4-1, were purchased from ChemShuttle (Hayward, CA). Hydroxypropyl methylcellulose acetyl succinate (HPMC-AS) MF grade was supplied by Shin-Etsu Chemical Co. (Tokyo, Japan). Acetonitrile, dichloromethane (DCM), dimethyl sulfoxide (DMSO), hydrochloric acid (HCl), maleic acid, methanol, sodium chloride, and sodium phosphate monobasic monohydrate were bought from Fisher Scientific (Pittsburgh, PA). Sodium hydroxide (NaOH) was purchased from Avantor Performance Materials, LLC (Radnor, PA). A regenerated cellulose membrane with a molecular weight cutoff (MWCO) of 6-8 kDa was acquired from Spectrum Laboratories, Inc. (Rancho Dominguez, CA). FaSSIF/FeSSIF/FaSSGF and FaSSIF-V2 powders were purchased from Biorelevant (London, UK). L- α -Phosphatidylcholine (lecithin, $\geq 99\%$), sodium taurocholate hydrate, (STC [$\geq 97\%$]), sodium glycocholate, (SGC [$\geq 95\%$]), sodium taurodeoxycholate, (STDC [$\geq 95\%$]), sodium glycocodeoxycholate, (SGDC [$\geq 97\%$]), sodium taurochenodeoxycholate, (STCDC [$\geq 97\%$]), and sodium glycochenodeoxycholate, (SGCDC [$\geq 97\%$]) were obtained from Sigma-Aldrich (St. Louis, MO). Fasted-stated human intestinal fluid (FaHIF) was collected from healthy human volunteers as detailed below.

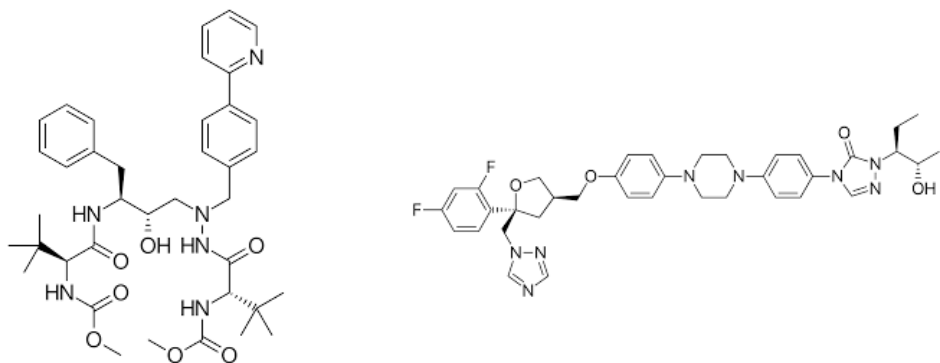


Figure 4-1. Molecular structures of atazanavir (left), and posaconazole (right).

4.4 Methods

4.4.1 Media selection and preparation

Six different media were used in this study. Two blank (without bile salts/lecithin) aqueous buffers were prepared as described previously.^{19,20} These two buffers are referred to as FaSSIF-V1 blank phosphate buffer (buffer-V1) and FaSSIF-V2 blank maleic acid buffer (buffer-V2), respectively. FaSSIF/FeSSIF/FaSSGF powder was added to buffer-V1 to create FaSSIF-V1,²⁰ whilst FaSSIF-V2 powder was added to buffer-V2 to make FaSSIF-V2.¹⁹ Composite-FaSSIF was prepared using buffer-V1. The composition of composite-FaSSIF was based on a recent characterization of FaHIF by Riethorst et al.,³⁸ where the total bile salts concentration was 3 mM, which is equivalent to the STC concentration in FaSSIF-V1 and FaSSIF-V2. In addition, 0.2 mM of lecithin was added to this medium. Preparation of composite-FaSSIF was performed as described before.⁴⁶ Briefly, all six bile salts were weighed, added to buffer-V1, stirred and then allowed to settle for 30 min. Meanwhile, 0.2 mM of lecithin was dissolved in dichloromethane (DCM) and titrated into the aqueous bile salt mixture. The composite-FaSSIF mixture was then stirred at 500 rpm, maintained at 50°C for 30 min to evaporate the organic phase from the aqueous mixture. The initial volume of added DCM was always kept to less than 1% of the total solution volume. All of the aforementioned media were adjusted to pH 6.5. The composition of the various media is summarized in Table 4-1.

Table 4-1. Detailed composition of the bile salts and lecithin for FaSSIF-V1, FaSSIF-V2 and composite-FaSSIF.

	FaSSIF-V1	FaSSIF-V2	Composite-FaSSIF
STC	3 mM	3 mM	0.36 mM
STDC			0.36 mM
STCDC			0.18 mM
SGC			0.84 mM
SGDC			0.45 mM
SGCDC			0.81 mM
Lecithin	0.75 mM	0.2 mM	0.2 mM

4.4.2 Sampling and handling of FaHIF

Human intestinal fluids were collected at the University Hospitals Leuven as part of a previously published study.³⁸ The sampling procedure was approved by the Ethics Committee Research

UZ/KU Leuven (reference numbers ML7918 and S53791); healthy Caucasian volunteers were enrolled in the study after giving written informed consent. Briefly, intestinal fluids were collected from the duodenum (near the ligament of Treitz) from 20 healthy volunteers every ten minutes for a period of 90 min in both fasted and fed state. After an overnight fast of at least 12 h (no food and only water), volunteers were given 250 mL of water before initiating the sampling of fasted state intestinal fluids. Following fasted state sampling, 400 mL of Ensure® Plus (Abbott Nutrition, Zwolle, the Netherlands) was ingested to simulate a standard meal. Fed state sampling was initiated after drinking 250 mL water, 20 min after the intake of the liquid meal. For each volunteer, the collected fractions were pooled to obtain a fasted and fed state individual volunteer pool. For the present study, a mixed pool of FaHIF was created by gently mixing samples from 16 individual volunteer pools. Afterwards, these samples were kept frozen at -80°C until use. The pH of the FaHIF pool used in this study was measured using a Mettler Toledo FiveEasy™ FE20 benchtop pH-meter (Schwerzenbach, Switzerland), and was found to be 7.3.

4.4.3 Crystalline solubility measurements

The equilibrium solubilities of atazanavir and posaconazole were determined in all six media. An excess amount of crystalline solid was first equilibrated in each medium (1 mL) for 48 hours at 37°C. Afterwards, the solubilized drug was separated by ultracentrifugation at 50,000 rpm (135,700 g) for 30 minutes, while maintained at 37°C, using an Optima MAX-XP ultracentrifuge equipped with a Swinging-Bucket Rotor TLA-110 (Beckman Coulter, Inc., Brea, CA). For atazanavir, the supernatant concentration was determined by high performance liquid chromatography (HPLC) with a Hewlett Packard 1100 series system, using an Agilent Eclipse Plus C18 column (4.6 mm × 250 mm, 5 µm) (Agilent Technologies, Santa Clara, CA). The mobile phase consisted of 60% water acidified to pH 2.5 with o-phosphoric acid, and 40% acetonitrile. An injection volume of 20 µL was used. The flow rate was set to 0.8 mL/min where each analytical run was adjusted to 15 min. Atazanavir was detected by ultraviolet (UV) absorbance at a wavelength of 247 nm. Standards (0.1-10 µg/mL) were prepared in methanol, where the standard curve exhibited good linearity ($R^2 = 0.999$) over this concentration range. For posaconazole, an Agilent 1260 Infinity II HPLC system coupled with an Agilent Eclipse Plus C18 column (4.6 mm × 250 mm, 5 µm) was used to analyze the concentration in the supernatant. The mobile phase was 60% acetonitrile and 40 % deionized water. The analytical run duration was 6 min, where the

injection volume was 20 μ L and the mobile phase flow was held constant at 2.0 mL/min. Posaconazole was detected by fluorescence emission where the excitation wavelength was at 240 nm and the emission wavelength was at 385 nm. Using posaconazole standards prepared in methanol, two calibration curves (0.01-0.1 μ g/mL, $R^2 = 0.997$ and 0.1-20 μ g/mL, $R^2 = 1$) were used to calculate the crystalline solubility in different media.

4.4.4 Amorphous solubility measurements

To measure the amorphous solubility, aliquots from an atazanavir DMSO stock solution (50 mg/mL) and a posaconazole methanol stock solution (10 mg/mL) were added to 1 mL of each medium, while stirred at 300 rpm and maintained at 37°C, to generate supersaturated solutions of both compounds where the total concentration exceeds the ‘expected’ amorphous solubilities, based on previous findings.^{46,181} To prevent crystallization, pre-dissolved HPMC-AS was added at a concentration of 10 μ g/mL for atazanavir samples, and 100 μ g/mL for posaconazole samples. Samples were then ultra-centrifuged using the same conditions used for the crystalline solubility measurements to pellet the drug-rich phase. The supernatant was separated from the precipitated drug-rich phase, diluted in methanol, and analyzed using the HPLC methodologies described above.

4.4.5 Confirmation of amorphous solubility and formation of LLPS nanodroplets by fluorescence spectroscopy and scanning electron microscopy (SEM)

To confirm the formation of colloidal aggregates which occurs when the amorphous solubility is exceeded, fluorescence spectroscopy was used to monitor the corresponding changes in the emission spectra of atazanavir and posaconazole. Both compounds are auto-fluorescent, and the emission spectrum varies depending on the hydrophobicity of the local environment, for example, whether the drug is molecularly dissolved or present in colloidal aggregates, as demonstrated previously.^{150,151,182} Fluorescence spectra were collected for both drugs at different concentrations, below and above the amorphous solubility, in the presence of HPMC-AS to prevent crystallization. Solutions were prepared via the solvent shift method as described before and maintained at 37°C while stirring at 300 rpm. Samples were analyzed using a Shimadzu RF- 5301pc Spectrofluorometer (Kyoto, Japan). The excitation wavelength used was 250 nm for atazanavir and 240 nm for posaconazole. The emission spectrum was collected at 0.2 nm intervals from 220

to 450 nm. The excitation and emission slits width were kept at 5 or 10 mm depending on the medium and the intensity of the resulting emission spectra. Additionally, to further characterize the colloidal species formed in human fluids at concentrations above the amorphous solubility, SEM was utilized. This technique has been previously used to demonstrate the formation of the amorphous nanodroplets of cyanophenyl furanone dye in water⁷³ and ritonavir in pH 6.8 phosphate buffer.⁷⁹ Briefly, highly supersaturated solutions of atazanavir and posaconazole above the measured amorphous solubility were prepared in FaHIF. 100 µg/mL of HPMC-AS were added to the posaconazole sample to avoid crystallization. Samples were then centrifuged at 14,800 rpm for 10 min, using a Sorvall Legend Micro 17 Centrifuge (Thermo Fisher Scientific, Waltham, MA). The supernatants were then discarded, and a small amount of the amorphous pellet was fixed on an SEM stub and sputter-coated with platinum for 60 s. Imaging was performed with a FEI Teneo VS™ scanning electron microscope (FEI Company, Hillsboro, Oregon) in OptiPlan mode with T1 and T2 detectors to capture backscatter and secondary electron images. Operating conditions were 5 kV accelerating voltage, 0.20 nA current, and ~2 mm working distance.

4.4.6 Diffusion cell experiments

A side-by-side diffusion cell (PermeGear Inc., Hellertown, PA) of 1.5 mL volume (each compartment) and 9 mm orifice diameter was used to determine the flux, J , at both the amorphous solubility (J_{amp}) and the crystalline solubility (J_{eq}) for each drug and medium. The donor and receiver compartments were separated by a regenerated cellulose membrane with a MWCO of 6-8KDa. Each compartment had 1 mL of media, was stirred using a magnetic stirrer (2×7 mm) at ~600 rpm to minimize the thickness of the unstirred water layer,¹⁷¹ and maintained at 37°C. Using an atazanavir DMSO stock solution (50 mg/mL) and a posaconazole methanol stock solution (10 mg/mL), a concentration of each drug corresponding to the amorphous solubility for each medium, was added to the donor compartment to determine J_{amp} . To prevent crystallization, pre-dissolved HPMC-AS was added to both the donor and receiver compartments at concentrations of 10 µg/mL and 100 µg/mL for atazanavir and posaconazole experiments, respectively. Control experiments were performed with atazanavir in the absence of HPMC-AS in buffer-V1, demonstrating that the polymer had no effect on the mass flow rate. For determining J_{eq} , a suspension of crystalline drug, equilibrated for 48 h in each medium was added to the donor compartment. A 15 µL aliquot was

withdrawn from the receiver compartment at different timepoints, diluted in methanol, and analyzed by HPLC using the methods described above.

4.5 Results

4.5.1 Crystalline solubility measurements

The measured crystalline solubility values of atazanavir and posaconazole at 37°C in the six media are summarized in Table 4-2. Atazanavir crystalline solubilities were slightly higher in FaSSIF-V1, FaSSIF-V2, Composite-FaSSIF and FaHIF relative to in the two blank buffers. For posaconazole, the differences in the crystalline solubilities between both buffers and the other biorelevant media were more pronounced (7-14 fold) relative to atazanavir. This suggests that posaconazole was more effectively solubilized by the presence of mixed micelles in the media. Additionally, for posaconazole, the amount of lecithin influences the solubility, which was highest in FaSSIF-V1. Posaconazole solubilities in FaSSIF-V1, FaSSIF-V2 and FaHIF were in good agreement with values reported previously.^{86,155,183}

Table 4-2. Crystalline solubility values of atazanavir and posaconazole in different media. (n=3, \pm standard deviation).

Medium	Equilibrium solubility ($\mu\text{g/mL}$)	
	Atazanavir	Posaconazole
Buffer-V1	1.4 \pm 0.2	0.23 \pm 0.03
Buffer-V2	1.5 \pm 0.3	0.22 \pm 0.02
FaSSIF-V1	2.7 \pm 0.1	3.2 \pm 0.3
FaSSIF-V2	2.6 \pm 0.4	1.6 \pm 0.1
Composite-FaSSIF	3.1 \pm 0.6	1.7 \pm 0.2
FaHIF	7.1 \pm 0.6	2.6 \pm 0.5

4.5.2 Amorphous solubility measurements

Table 4-3 summarizes the measured amorphous solubilities of atazanavir and posaconazole in the six media at 37°C as determined by the ultracentrifugation method. As expected, the amorphous solubility was not notably different between buffer-V1 and buffer-V2 for either drug. In the presence of solubilizing species, atazanavir amorphous solubility increased by a factor of \approx 1.25. FaSSIF-V1, FaSSIF-V2, composite-FaSSIF and FaHIF yielded similar amorphous solubility values for atazanavir, suggesting the different configurations of bile salts/lecithin in these media

had minimal effect on the solubilization of atazanavir in a supersaturated solution. This was not the case for posaconazole. Following the same trend as for the crystalline solubility, posaconazole amorphous solubility was highest in the medium with the greatest lecithin content (FaSSIF-V1). In FaSSIF-V2, the amorphous solubility value obtained was equivalent to our previous finding.¹⁸³ Finally, the amorphous solubility appeared to be lower in composite-FaSSIF and FaHIF, compared to FaSSIF-V1 and FaSSIF-V2. Such differences between FaSSIF-V1/V2 and composite-FaSSIF have been observed previously for ritonavir, tacrolimus and cilnidipine.⁴⁶

Table 4-3. Amorphous solubility values in atazanavir and posaconazole in different media. (n=3, \pm standard deviation).

Medium	Amorphous solubility ($\mu\text{g/mL}$)	
	Atazanavir	Posaconazole
Buffer-V1	79 \pm 4	8.11 \pm 0.02
Buffer-V2	82 \pm 1	8.17 \pm 0.03
FaSSIF-V1	102 \pm 3	43.3 \pm 2.3
FaSSIF-V2	101 \pm 10	20.8 \pm 1.6
Composite-FaSSIF	100 \pm 3	15.5 \pm 0.7
FaHIF	99 \pm 2	13.2 \pm 0.4

Figure 4-2 shows the fluorescence emission spectra as a function of atazanavir/posaconazole concentration in the different media. When the amorphous drug-rich phase was formed at concentrations above the amorphous solubility, an increase in the peak intensity was observed. The concentration where the increase in intensity occurred showed good correspondence to the amorphous solubility values measured by the ultra-centrifugation method (Table 4-3). Additionally, some samples exhibited a shift in the peak maximum to shorter wavelengths (blue shift). This is attributed to the decrease in local polarity experienced by the drug molecules when colloidal species form. As a result, the quantum yield increases and the emission maximum shifts to shorter wavelengths (hypsochromic shift).

The size and morphology of the atazanavir and posaconazole colloidal species formed in FaHIF is illustrated by the SEM images shown in Figure 4-3. Amorphous aggregates for both drugs were mostly spherical and clearly different from crystalline material, such as atazanavir crystals which are needle-shaped.^{184,185}

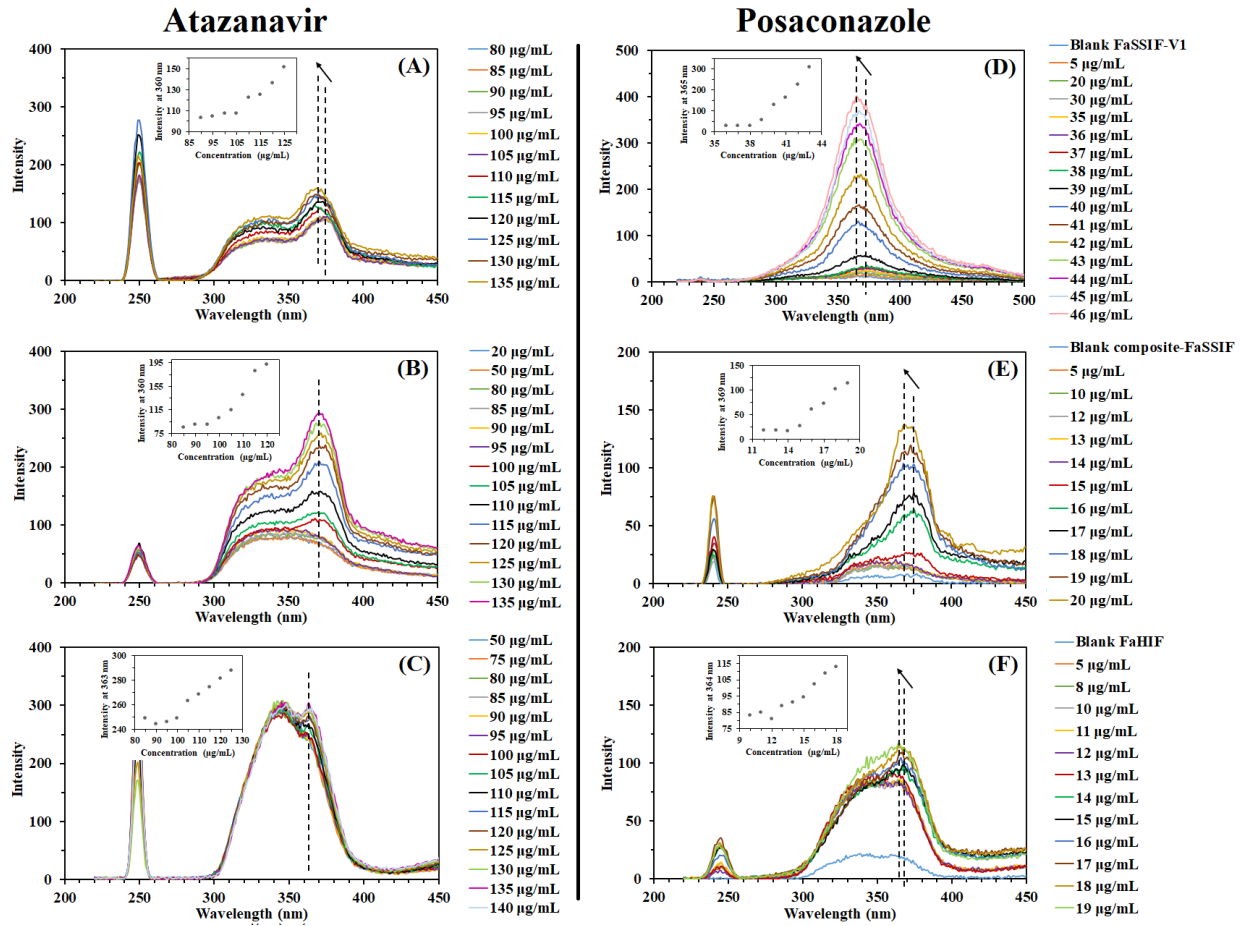


Figure 4-2. Fluorescence emission spectra of atazanavir (left side) and posaconazole (right side) at different concentrations in (A), (D) FaSSIF-V1, (B), (E) composite-FaSSIF, and (C) and (F) FaHIF. The arrows and vertical dashed lines illustrate a blue shift in the peak maximum for some samples. The inset illustrates the increase in intensity as a function of concentration where the change of slope corresponds to the formation of the second phase of amorphous nanodroplets.

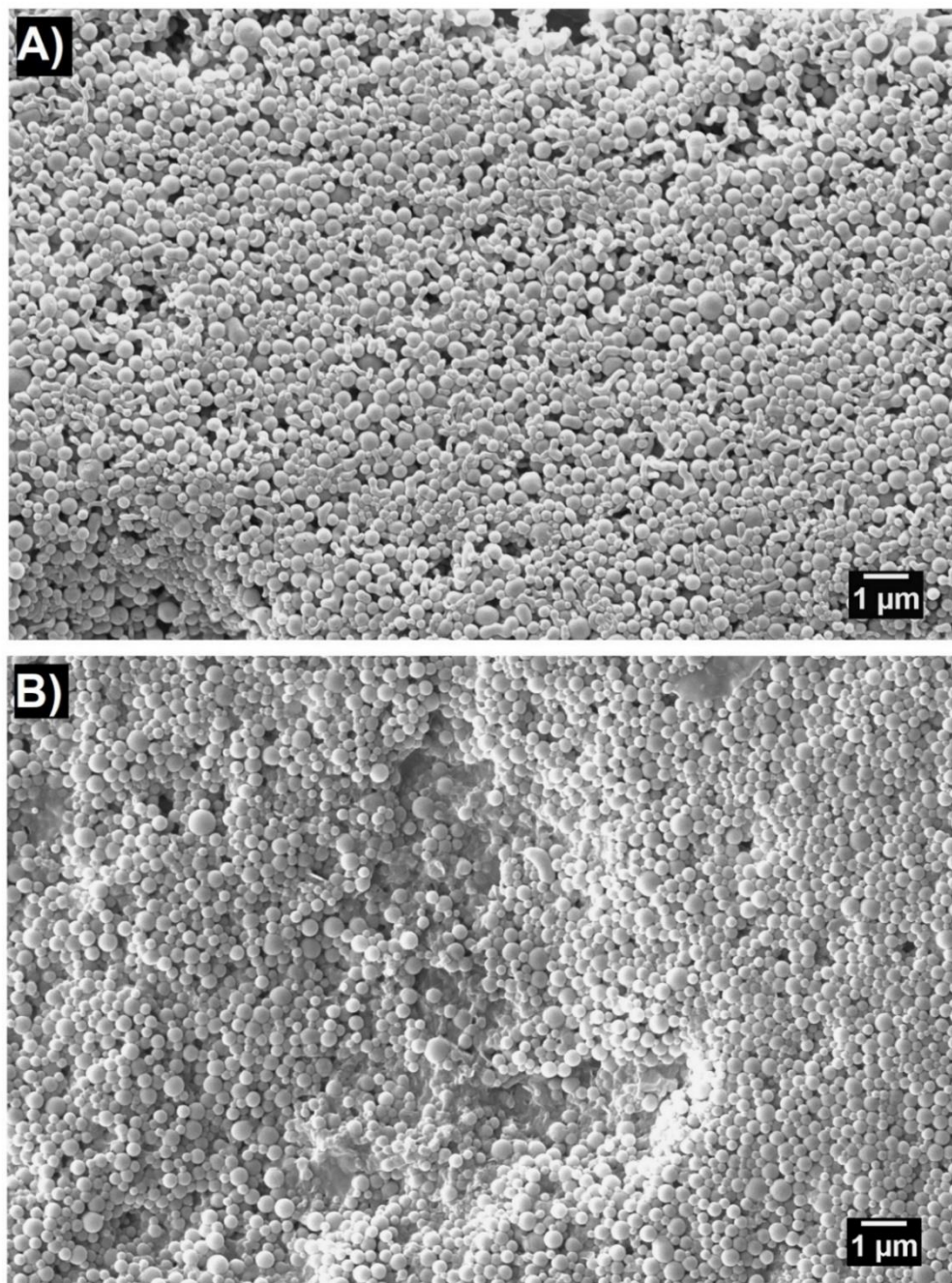


Figure 4-3. SEM images of A) atazanavir and B) posaconazole amorphous nanodroplets precipitated from FaHIF. Posaconazole nanodroplets were stabilized by HPMC-AS to prevent crystallization.

4.5.3 Supersaturation determination by diffusive flux measurements

The supersaturation ratio (SR) was determined using the ratio of the thermodynamic activity of the solute in the solution, a , to the activity of the solute at its crystalline state, a_{eq} , as shown in equation

4-2. The activity can be described in terms of γ , the activity coefficient of the drug in the solution and C , the drug concentration, where the subscript, eq , refers to the property at equilibrium.

$$SR = \frac{a}{a_{eq}} = \frac{\gamma C}{\gamma_{eq} C_{eq}} \quad (4-2)$$

Solute activity at the crystalline and amorphous solubilities can be assessed using diffusion cell experiments to determine the diffusive flux, J , across a semipermeable membrane, as shown in equation 4-3:

$$J = \frac{D a}{h \gamma_m} \quad (4-3)$$

where D is the diffusion coefficient of the solute, h is the thickness of the membrane and γ_m is the activity coefficient of the solute in the membrane, which are all assumed to be constants for a particular drug and medium. Consequently, the maximum attainable supersaturation, SR_{max} , in a given medium can be derived from the ratio of the diffusive flux of the solute at the amorphous solubility, J_{amp} , to the diffusive flux at the crystalline solubility, J_{eq} , as demonstrated in equation 4-4:

$$SR_{max} = \frac{J_{amp}}{J_{eq}} \quad (4-4)$$

In deriving Equation 4-4, we assume that the thermodynamic activity of the solute is the same as the thermodynamic activity of the second phase present in the system; this is either crystalline or amorphous drug. To achieve a well-defined activity, we therefore measure the flux of systems containing a suspension of either crystalline or amorphous drug. The impact of different media on mass transport and maximum supersaturation level was studied using diffusion cell experiments performed at both the amorphous and crystalline solubilities at 37°C. The mass transport time-profiles and J (derived from the slope of the concentration versus time profiles) values for atazanavir and posaconazole in buffer-V1, composite-FaSSIF and FaHIF are shown in Figures 4-4 and 4-5, respectively. For both compounds, J_{amp} and J_{eq} were relatively close between the different media. All normalized flux values for atazanavir and posaconazole are shown in Table A1 (Appendix A). Additionally, the apparent permeability values were calculated accordingly and are shown in Tables A2 and A3.

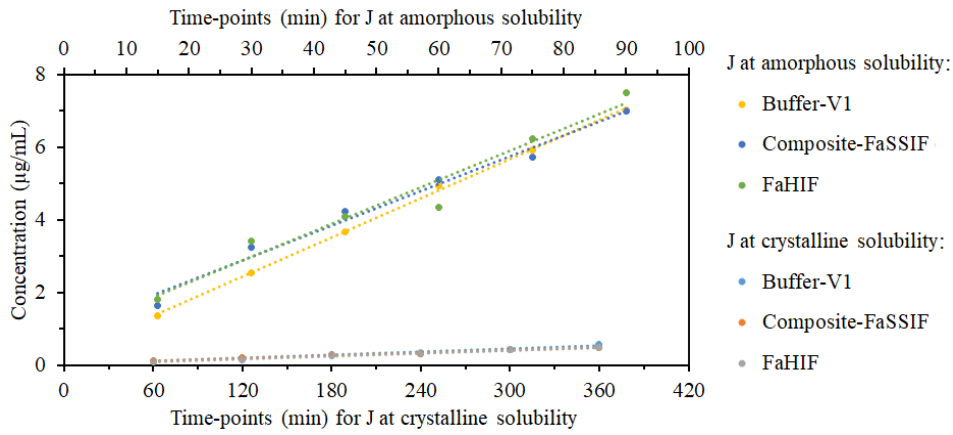


Figure 4-4. Atazanavir mass transport versus time at the amorphous solubility (upper x-axis) and at the crystalline solubility (lower x-axis), in different media. Error bars were omitted for clarity. (n=3).

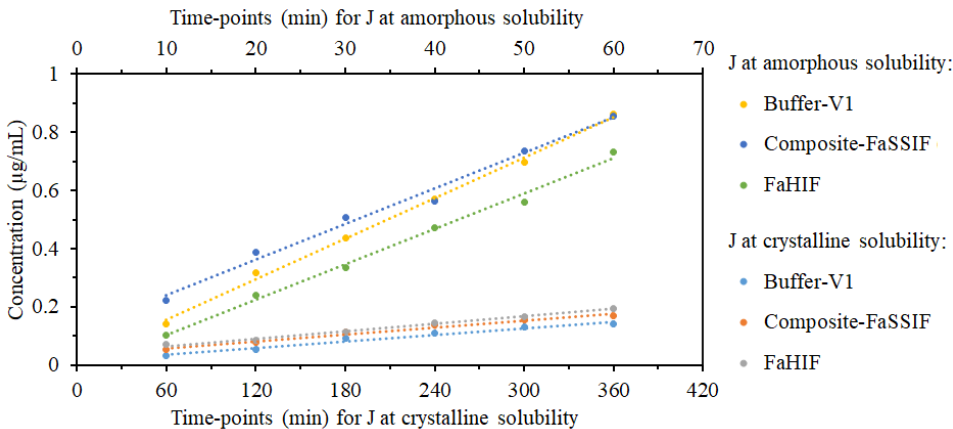


Figure 4-5. Posaconazole mass transport versus time at the amorphous solubility (upper x-axis) and at the crystalline solubility (lower x-axis), in different media. Error bars were omitted for clarity. (n=3).

Figures 4-6 and 4-7 show the SR_{max} determined in different media for atazanavir and posaconazole, respectively, based on equations 4-1 (concentration-based) and 4-4 (activity-based). For both compounds, large differences between the concentration- and activity-based SR_{max} are apparent for some media. The concentration-based SR_{max} is the ratio of the amorphous and crystalline solubilities for the various media, (i.e. the ratio of the values presented in Tables 4-2 and 4-3), while the activity-based values are calculated from the ratio of the flux measured for a crystalline and amorphous suspension in the different media (i.e. the ratio of the values presented in Figures 4-4 and 4-5). While SR_{max} was relatively consistent between the two approaches for the aqueous

buffers, the concentration-based SR_{max} values decreased in all other biorelevant media and was lowest in aspirated FaHIF. Thus, if the concentration-based SR_{max} is considered, the maximum achievable supersaturation appears to decrease in FaHIF. In contrast, the activity-based SR_{max} ratios were approximately the same across the various media types. For atazanavir, the activity-based SR_{max} averaged ~54 between the different media, where no values were significantly different from the value measured for FaSSIF-V1 (based on two-tailed t-test, $p > 0.05$). Therefore, all media achieved an equivalent maximum supersaturation for atazanavir. Indulkar et al. previously reported an average activity-based supersaturation of 65.⁴⁶ The activity-based SR_{max} was found to be ~36 for posaconazole. Although the values were generally similar for different media, a slight decrease was noticed for the activity-based SR_{max} for posaconazole in both composite-FaSSIF and FaHIF (based on two tailed t-test, $p < 0.05$).

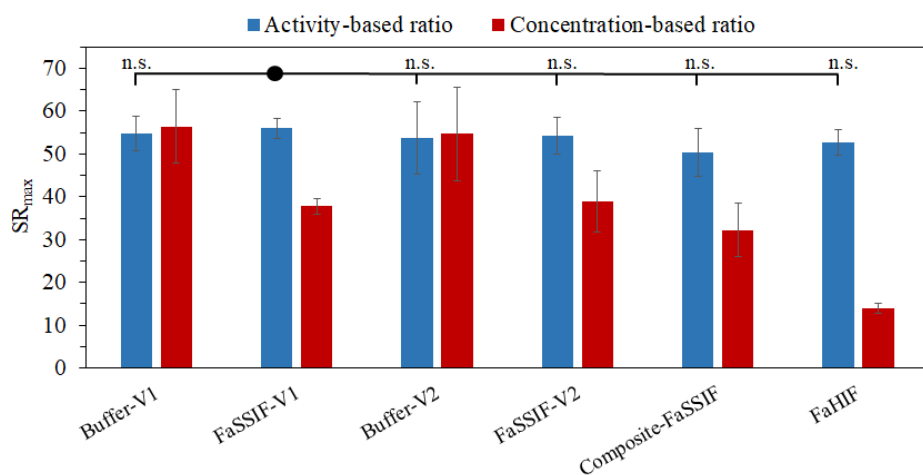


Figure 4-6. Maximum supersaturation ratio for atazanavir in different media obtained using activity-based ratio (blue bars) versus concentration-based ratio (red bars). The n.s. indicates when the difference between FaSSIF-V1 and other datasets was nonsignificant (t-test, p value > 0.05). Error bars represent standard deviations where $n=3$.

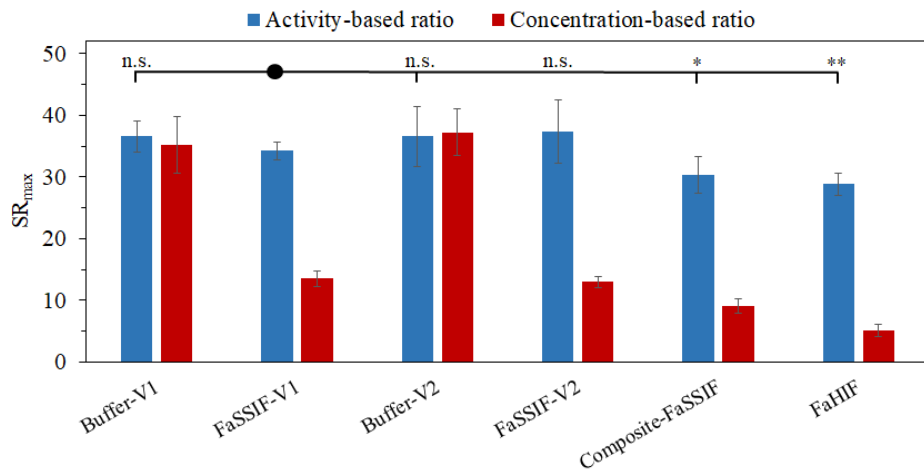


Figure 4-7. Maximum supersaturation ratio for posaconazole in different media obtained using activity-based ratio (blue bars) versus concentration-based ratio (red bars). The n.s. indicates when the difference between FaSSIF-V1 and other datasets was non-significant (t-test, p value > 0.05), whereas the * and ** symbols indicate that the difference was statistically significant (t-test, p value = 0.002 and 5.3×10^{-7} , respectively). Error bars represent standard deviations where n=3.

4.6 Discussion

Supersaturation is considered an important factor impacting the extent of absorption of drugs with solubility-limited absorption.^{5,186} following oral administration. Supersaturation can be generated via a variety of routes, including pH increase following gastrointestinal transit, which is of relevance for weakly-basic drugs, and by release of drugs formulated as amorphous solid dispersions. Understanding the extent and duration of supersaturation of a particular drug is critical to predict its absorption rate *in vivo*. This statement is based on the well-known relationship, derived from Fick's first law, shown in equation 4-5:

$$J = P C \quad (4-5)$$

where J is the flux across a biological membrane, P is the membrane permeability and C is drug concentration. This relationship implies that an increase in drug concentration beyond the crystalline solubility will lead to an increase in the transport rate across a membrane, and, in the absence of confounding factors such as efflux and first pass metabolism, will increase the absorption rate. Several studies have shown a linear relationship between the membrane flux and supersaturation in simple media,^{75,129,164} which is truncated when the amorphous solubility is reached. Thus, as the concentration of the drug is increased (supersaturation is increased), the

thermodynamic activity of the drug increases until it reaches its maximum at the amorphous solubility and phase separation to an amorphous phase occurs.⁷⁵ This leads to the formation of a drug-rich colloidal phase in metastable equilibrium with a supersaturated solution. In the present study, the formation of such colloidal species in FaHIF, upon exceeding the amorphous solubility, is clearly demonstrated for the first time (Figure 4-3). Given that these colloidal species are thought to be advantageous for passive diffusion *in vivo* by maintaining the supersaturation at the maximum value through their reservoir effect,¹⁸⁷ this is a significant finding.

In contrast to the relationships established in simple media, the results shown in Figures 4-6 and 4-7 clearly suggest that using concentration ratios to determine supersaturation for the lipophilic, un-ionized compounds studied, is inaccurate in complex media given the absence of a linear relationship between solute concentration and membrane flux. These observations are of profound importance since concentration profiles are so routinely used to make predictions about *in vivo* formulation performance. Therefore, it is important to understand where the limitations arise with respect to the use of concentration-based measurements in complex media.

To explain the observed differences between total dissolved concentration- and activity-based measurements (Figures 4-6 and 4-7), it is important to first differentiate solubilization from supersaturation, and then to consider the interplay between the two for different media. Both phenomena result in an increase in the ‘apparent’ concentration of the drug in solution, yet have different thermodynamic consequences in terms of membrane mass transport rate. Supersaturation results in an increase in the ‘free’ drug concentration in solution relative to a saturated/equilibrium state. Consequently, solute thermodynamic activity (i.e. the effective concentration) is higher (equation 4-2), thus the membrane transport is increased (equation 4-3). Solubilization occurs through the presence of solubilizing agents that are either present naturally such as the biological surfactants (bile salts) or introduced as formulation excipients such as synthetically derived surfactants or complexing agents.¹⁸⁸ In intestinal fluids (simulated and real), micelles and other colloidal species, formed by bile salts and lecithin, provide a microphase with which drug molecules can associate by binding with surfactant or by incorporation into the micellar core. These additional solution species lead to a dynamic equilibrium between two populations of drug molecules, those associated with the micelles, and free drug molecules in solution. Thus, increases in equilibrium solubility are observed (as seen in Table 4-2), whereby the solute activity remains

constant since it is dictated by the crystalline form of the drug in equilibrium with the solution phase. Thus, solubilization does not increase the ‘free’ drug concentration (i.e. solute thermodynamic activity) in solution, although the total concentration measured is increased. As described in the literature, membrane transport rates do not correlate with total dissolved concentration in the presence of solubilizing species.^{45,189–192} This is because for small molecules, only the ‘free’ unionized drug will undergo membrane partitioning and transport.¹⁹³ We see the same outcome in the current study, where the flux values at the crystalline solubility do not show any correlations with increases in the equilibrium solubility due to solubilization (Figures 4-4 and 4-5).

The complexity of the situation increases considerably when both supersaturation and solubilization occur. To assess the supersaturation ratio in the presence of solubilizing components, equation 4-1 is typically employed.^{5,146,194–196} Here, the crystalline solubility is measured in the medium of interest for the supersaturation determination to take into account the solubilization effect. For example, crystalline solubility has been determined in partially digested lipid media,^{114,194,197,198} or intestinal fluids collected at different time points following oral dosing.^{25,103,146,199,200} The assumption implicit in this approach is that the fraction of the drug that is solubilized at the crystalline solubility is the same as the fraction of the drug that is solubilized in the supersaturated solution. Thus, the solubilization effect is cancelled by taking the ratio of the two values. This can be seen mathematically from equation 4-2. If the ratio γ/γ_{eq} (equation 4-2) is 1, a situation that would arise where the extent of solubilization is the same over the concentration range of interest and there are no other non-idealities, then equation 4-1 reasonably describes the true supersaturation. However, if the solubilization capacity varies as a function of concentration and supersaturation, then $\gamma/\gamma_{eq} \neq 1$, and equation 4-1 will not accurately describe the supersaturation of the system.¹⁸² This appears to be the situation in the biorelevant media tested herein and warrants consideration of the solubilization capacity of the various media at different supersaturations.

Interestingly, our *in vitro* studies appear to be in good agreement with observations made following oral dosing of posaconazole and subsequent investigations of supersaturation evolution. Posaconazole is a highly permeable compound with solubility-limited absorption.²⁰¹ Hens et al. conducted a study to investigate posaconazole supersaturation *in vivo* in the small intestine upon administration of an acidified/neutral posaconazole suspension,¹⁴⁶ or a posaconazole solid dispersion.²⁵ Here, samples were collected from the intestine and the supersaturation was

determined by measuring the posaconazole solution concentration, and the crystalline solubility in the individual fluid samples, i.e. a concentration-based supersaturation measurement as per equation 4-1. In the first study with suspensions, the mean maximum supersaturation ratio observed was ≈ 4 , whereas the results of the second study with amorphous solid dispersions showed a mean maximum supersaturation of ≈ 7 upon fasted-state administration. Remarkably, these values are in close agreement with our FaHIF concentration-based supersaturation assessment at the amorphous solubility limit, which is ≈ 5 (Figure 4-6). Notably, our study shows that the solution in FaHIF at the amorphous solubility displays a 30-fold increase in mass transport rate relative to a crystalline suspension, indicating that the amorphous solubility advantage is not lost in FaHIF, despite the apparent reduction in the concentration-based supersaturation ratio. This once again illustrates the necessity of using activity-based assessments to avoid underestimation of supersaturation and suggests that the solutions generated *in vivo* in the previous studies were likely much more highly supersaturated than they appeared based on the concentration-based measurement approach employed.

A simple model for describing solubilization capacity of a given surfactant for a particular drug is to apply the concept of a micellar partition coefficient ($K_{m/w}$), which is given by equation 4-6:¹⁸⁸

$$K_{m/w} = \frac{C_m}{C_w} \quad (4-6)$$

Where C_m is the surfactant-associated drug concentration, and C_w is the free drug concentration. While this model is likely oversimplified for a complex system of bile acids and lecithin, it serves to illustrate how the extent of solubilization may vary as a function of concentration and supersaturation. In biorelevant media, solubilizing components interact with the solute of interest, whereby the interactions vary depending on the level of supersaturation. Specifically, mixed bile salt-lecithin micelles exist in the test fluids and these can solubilize drugs.^{43,44} We can estimate the micelle partition coefficient at the amorphous and crystalline solubilities using equation 4-6. Here, the denominator is taken as the solubility in buffer, where only free drug is present. Assuming that the solubilizing components do not mix with either the crystalline or amorphous phase, then the free drug concentration is the same in the complex media as for buffer (since it is determined by the thermodynamic properties of the second phase present, i.e. either crystalline or water-saturated amorphous drug). The excess concentration of drug relative to buffer is therefore associated with the solubilizing species, enabling determination of $K_{m/w}$. $K_{m/w}$ values for both compounds in

FaSSIF-V1, composite-FaSSIF and FaHIF, are shown in Table 4-4. Evaluating the $K_{m/w}$ values for the crystalline solubilities, we note that posaconazole has a higher value than atazanavir indicating that this compound is more effectively solubilized by the micelles. Of particular interest, we note that $K_{m/w}$ is much lower at the amorphous solubility than at the crystalline solubility for both compounds. This observation is in agreement with the result reported by Indulkar et al. for atazanavir and sodium dodecyl sulfate systems,¹⁸² where $K_{m/w}$ was observed to be highly concentration dependent. Of further note, is the observation that $K_{m/w}$ varies as a function of medium, reflecting a difference in their solubilization capacity. Of final note, $K_{m/w}$ is dependent on the drug, i.e. posaconazole had higher solubilization capacities than atazanavir, which explains why the discrepancies in supersaturation ratios were more prominent for posaconazole (Figure 4-7) compared to atazanavir (Figure 4-6).

Table 4-4. Estimation of $K_{m/w}$ values for atazanavir and posaconazole at the crystalline and amorphous solubilities in FaSSIF-V1, composite-FaSSIF and FaHIF media.

Medium	$K_{m/w}$ at crystalline solubility		$K_{m/w}$ at amorphous solubility	
	Atazanavir	Posaconazole	Atazanavir	Posaconazole
FaSSIF-V1	1.9	13.9	1.3	5.3
Composite-FaSSIF	2.2	7.4	1.3	1.9
FaHIF	5.1	11.3	1.3	1.6

In examining the data shown in Table 4-2 and 4-3, it is clear that the crystalline solubility showed a proportionally greater increase in the presence of bile salts and lecithin in comparison to the amorphous solubility, for both compounds. For instance, the crystalline solubility for posaconazole in FaSSIF-V1 is ≈ 14 times that in buffer-V1, while the amorphous solubility in FaSSIF-V1 is ≈ 5 times that in buffer-V1. Moreover, posaconazole exhibited a notably lower amorphous solubility in composite-FaSSIF and FaHIF compared to commercial FaSSIF media. This can be attributed in large part to the change in $K_{m/w}$ between these media (Table 4-4) given that these solutions show similar membrane flux values. In other words, the free drug concentration, and thus the supersaturation, remains similar between the different media, as evidenced by the similar membrane transport rates (Figure 4-7). Thus, the concentration-based supersaturation ratio drastically underpredicts the posaconazole membrane flux for micelle-containing media.

Figure 4-8 displays a schematic illustration of posaconazole micellar solubilization in FaSSIF-V1, composite-FaSSIF and FaHIF, in solutions saturated with respect to the crystalline or amorphous

forms. This schematic illustrates the concept that the free drug concentration remains constant for these conditions. On the other hand, the amount of drug associated with the micelle varies depending on the composition of the solubilizing species, which can be attributed to micelles with different properties. We can anticipate that for a given medium, the constituent micelles have a finite capacity to solubilize the drug molecules. Therefore, the decrease in $K_{m/w}$ at the amorphous solubility relative to the crystalline solubility, reflects the reduced ability of the micelles to accommodate the increased number of molecules in solution. This clearly varies between the different media; there is a notable increase in posaconazole amorphous solubility when more lecithin was present in the medium i.e. FaSSIF-V1. This indicates that this system can solubilize a relatively higher proportion of posaconazole molecules in the micelles, leading to a higher $K_{m/w}$ value relative to the other media. Lecithin is a mixture of poorly-soluble phospholipids that can interact with bile salts forming mixed micelles.^{44,202} These mixed micelles with greater lecithin content clearly improve posaconazole solubilization in supersaturated solutions. The same was not true for atazanavir. Atazanavir amorphous solubility values were largely unaffected in different media. While atazanavir and posaconazole have similar Log P values, their chemical structures are quite different. Hammad and Muller explored the differences in solubility of various drugs in bile salt phosphatidylcholine-based mixed micelles.²⁰³ Their results showed that the extent of solubilization was governed by several factors including the size of the mixed micelles, as well as the drug molecular size, chain branching, polarizability and structural conformations.²⁰³ Therefore, the difference in the extent of solubilization for posaconazole and atazanavir likely arises from structural differences between these two compounds. For the different media, we note that $K_{m/w}$ undergoes the largest decrease between the crystalline and amorphous solubilities for FaHIF. This means that using the concentration-based supersaturation ratio can be expected to lead to the largest discrepancies in the prediction of the membrane mass transport rates when attempting to evaluate supersaturation in this medium.

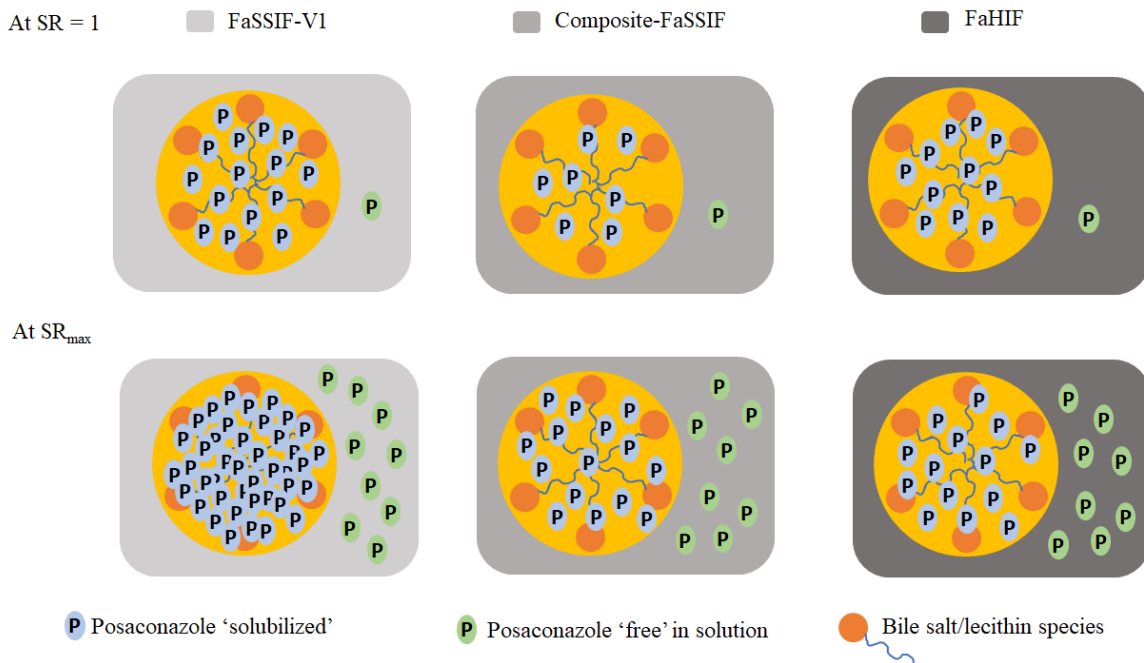


Figure 4-8. Schematic illustration of posaconazole micellar partitioning at saturation (crystalline solubility/SR=1) and maximum supersaturation (amorphous solubility/SR_{max}) levels.

Based on our observations, it is clearly important to carefully reconsider the appropriateness of concentration-based ratios for evaluation of the supersaturation level. It is undoubtedly more accurate to use the thermodynamic activity-based ratio in complex media with bile salts, albeit more complex from an experimental perspective.²⁰⁴ In the absence of micelles, e.g. in a simple aqueous buffer, there is no solubilization effect and therefore the drug concentration in solution reasonably represents the free drug concentration, leading to a good agreement between the activity-based ratio and the concentration-based ratio in the buffer systems, as seen for both compounds (Figures 4-4 and 4-5). In this instance, the activity coefficient ratio (γ/γ_{eq}) of the drug in solution is close to 1 (equation 4-2), due to the very dilute nature of the system whereby solution non-idealities are minimized. The differences in the degree of discrepancy for concentration vs. activity-based measurements for the two compounds as a function of media type correlates with the difference in the solubilization capacity for each drug. The activity-based SR_{max} values on the other hand were fairly consistent for atazanavir and posaconazole in all media. This was expected since the supersaturation level is largely independent of the medium used as the thermodynamic activity-based boundaries remain unchanged. It should be noted that for posaconazole, there was

statistically significant decrease in activity-based SR_{max} in composite-FaSSIF and FaHIF. The slight reduction in flux at the amorphous solubility for FaHIF and composite-FaSSIF (Figure 4-7) for posaconazole could be due to mixing of specific bile salts with the amorphous posaconazole phase, which can reduce the free drug concentration in equilibrium with the drug-rich phase.¹⁷⁷ This was observed previously for telaprevir in the presence of STCDC and SGCD dihydroxy bile salts, where the thermodynamic SR_{max} decreased to about three-fourths of the value in the absence of these bile salts.¹⁷⁷ Both composite-FaSSIF and FaHIF contain STCDC and SGCD, and the slight decrease in J_{amp} values in these media could arise via a similar mechanism as reported for telaprevir. Our observations have important implications regarding the interplay between solubilization and supersaturation as a function of concentration. The most important of these is that equation 4-1 cannot be used to estimate supersaturation in complex biorelevant media or aspirated human fluids, in particular for compounds showing solubilization. Using equation 1, supersaturation would be underestimated, as seen in Figures 4-6 and 4-7, and the amorphous solubility advantage would seem to decrease *in vivo*.

Composite-FaSSIF, containing six bile salts, more closely mimics the human bile composition relative to commercial FaSSIF recipes, which contains only STC. Simulating the FaHIF composition may be especially important in the context of intraluminal dissolution, supersaturation and absorption kinetics of supersaturating formulations. Nevertheless, a high degree of inter- and intra-subject variability is reported in the literature for FaHIF in terms of both composition and the absolute concentrations of the constituent components.³⁸ Additionally, other components are usually present in FaHIF at low concentration which are not present in composite-FaSSIF. These include cholesterol^{38,205,206} as well as lipid degradation products,^{38,207} such as fatty acids and monoacylglycerides. Although composite-FaSSIF comes closer to simulating FaHIF in terms of solubilization and supersaturation behavior relative to the commercially available media, more work needs to be done in order to optimize simulated fluids for *in vitro* testing of supersaturating formulations.

4.7 Conclusion

To improve the biopredictability of supersaturating formulations, it is important to understand the impact of different media composition on solubility and solution thermodynamics. Herein, we

demonstrated that crystalline and amorphous solubility values were greatly influenced by the solubilization capacity of each medium for two unionized, lipophilic weakly basic compounds. This resulted in different micellar partitioning between the solubilized and solution phases among the different media and reduced apparent supersaturation ratios based on concentration measurements. However, since the effective drug is approximately the same in all media, as shown by the flux measurements, the activity-based supersaturation was relatively independent of the media. These results provide the framework for further studies into the impact of different media on the phase behavior of supersaturated solutions.

CHAPTER 5. IMPACT OF SIMULATED AND ASPIRATED MEDIA ON CRYSTALLIZATION KINETICS OF ATAZANAVIR AND POSACONAZOLE SUPERSATURATED SOLUTIONS

5.1 Abstract

To enhance the bioavailability of poorly soluble therapeutics, enabling formulations that generate supersaturation are currently of great interest. Supersaturated solutions have been studied using many approaches; however, there is limited knowledge on how the gastrointestinal environment can influence the complex phase behavior of these systems. Conventionally, simulated media have been used to mimic physiologically-relevant parameters and compositions, although their predictability remains questionable since they are simplified models of the gastrointestinal fluids. The purpose of this study was to evaluate and compare how different simulated media, as well as aspirated intestinal fluid impact the phase behavior of supersaturated solutions of two poorly soluble compounds, atazanavir and posaconazole. The onset of nucleation and progression of crystallization kinetics were found to be highly medium-dependent. In the aspirated fluid, crystallization kinetics for both compounds were significantly reduced compared to commercial simulated media. The use of simple buffers or current simulated fluids as representatives for intestinal fluids appears to require further verification when attempting to predict crystallization kinetics of supersaturated solutions, based on the observed lack of correlation between commercial media and human fluids. The findings highlight the importance of considering the composition of *in vitro* testing media for assessing crystallization kinetics, particularly in the context of supersaturating formulations.

5.2 Introduction

Supersaturating formulations are a promising approach for oral drug delivery to address the low aqueous solubility of many new drug candidates.⁵ These formulation strategies increase the intraluminal concentration by generating and maintaining supersaturation at the absorptive site, resulting in enhanced bioavailability and therapeutic effect. Due to their increased solute chemical potential, supersaturated solutions can lead to enhanced membrane transport across the gastrointestinal tract (GI), provided that the solute has good permeability.^{8,164,165,178} To exploit

supersaturation as a viable strategy for improving the bioavailability of low aqueous-solubility compounds, there are two main factors to be considered: generation and maintenance of the supersaturated state. Supersaturation can be achieved through enabling formulation strategies such as amorphous solid dispersions (ASDs),¹²⁸ lipid-based formulations,¹¹⁵ nanocrystals,²⁰⁸ cosolvents²⁰⁹ and prodrugs,¹²⁴ or when an ionizable weakly basic drug transitions from the stomach to the small intestine.^{131,146} The supersaturated state is however unstable, which drives the system to revert to a more energetically favorable state through crystallization to achieve the equilibrium solubility.^{9,210} *In vivo*, this inherent tendency for crystallization must be either prevented, or significantly delayed for a physiologically-relevant timeframe for adequate absorption to occur. Hence, the kinetics of phase transitions that can impact intestinal drug concentrations, i.e. crystallization, are of great significance.

Solution crystallization can be described as a two-stage process: nucleation and crystal growth. Nucleation occurs when the activation energy barrier required to form a critical nucleus is overcome.⁴⁹ A new phase is formed which will then grow into a larger crystal, consuming the solution concentration and decreasing the extent of supersaturation until a saturated state is reached. For supersaturating formulations, particularly ASDs, additives such as polymers and surfactants are traditionally used to promote dissolution and inhibit crystallization. Many studies have focused on the role of polymers in mitigating crystallization, by delaying the onset of nucleation,^{12,111,211} or reducing crystal growth through adsorption of the polymer on the crystal surface.^{112,212} In contrast, surfactants have been found to both delay and promote crystallization, depending on the specific surfactant and drug..^{112,213,214}

Apart from formulation excipients, it is of critical importance to consider the impact of dissolution media components when assessing the stability of the drug to crystallization from a supersaturated solution. Biorelevant media, which mimic the *in vivo* physiological parameters and composition, are increasingly being used for dissolution testing. Many biorelevant media contain bile salts and phospholipids, endogenous surfactants found in the gastrointestinal (GI) tract, which can have an impact on drug crystallization kinetics. The nucleation inhibition ability of different bile salts has been found to vary depending on the structure of both the bile salt and the drug.^{36,37,46,47} In some instances, bile salts served as effective crystallization inhibitors in monomeric form, whereas micellar bile salts had diminished inhibitory effects.³⁷ Consequently, these biological surfactants

are not interchangeable, at least individually, when considering their impact on crystallization. Furthermore, increasing amounts of lecithin were noted to induce drug crystallization.⁴⁶ In principle, the use of biorelevant media for improved prediction of *in vivo* performance via well-designed *in vitro* formulation testing is essential. However, current recipes of commercially available simulated media employ only varying concentrations of sodium taurocholate (STC) and lecithin.^{17,19,20} In addition to STC, which in one study was found to constitute only 12% of the total bile salt concentration,³⁸ other abundant biologically relevant bile salts found in human intestinal fluid (HIF) include sodium taurodeoxycholate (STDC), sodium taurochenodeoxycholate (STCDC), sodium glycocholate (SGC), sodium glycdeoxycholate (SGDC), and sodium glycochenodeoxycholate (SGCDC).^{38,215} Further, bile salts exist along with lecithin, in HIF, as micelles and mixed micelles. Such diversity in HIF composition raises questions about whether existing simulated media are reliable substitutes for the complexity of GI fluids, in terms of their ability to provide information about crystallization kinetics. Previously, it was demonstrated that differences in media composition can impact crystalline and amorphous solubilities, micellar partition coefficient, and consequently solution thermodynamics and membrane transport, through the interplay between solubilization and supersaturation.²¹⁶ Supersaturating formulations exhibit complex phase behavior and the impact of simulated biorelevant and aspirated fluids on nucleation and crystal growth kinetics has not been widely investigated. The goal of the current study was to study crystallization kinetics from supersaturated solutions of two biopharmaceutical classification system (BCS) class II compounds, atazanavir and posaconazole, in aspirated HIF and simulated multicomponent media. The anti- or pro-nucleation effects of the various media were assessed via nucleation induction time experiments. Additionally, the onset of nucleation, as well as the kinetics and progression of crystallization were evaluated using second harmonic generation (SHG) microscopy. The morphology of the resultant crystalline species was studied using scanning electron microscopy (SEM).

5.3 Materials

Atazanavir (free base) and posaconazole (Form I), shown in Figure 5-1, were purchased from ChemShuttle (Hayward, CA). Hydroxypropyl methylcellulose acetyl succinate (HPMC-AS) MF grade was supplied by Shin-Etsu Chemical Co. (Tokyo, Japan). Acetonitrile, dichloromethane (DCM), dimethyl sulfoxide (DMSO), hydrochloric acid (HCl), maleic acid, methanol, sodium

chloride, and sodium phosphate monobasic monohydrate were obtained from Fisher Scientific (Pittsburgh, PA). Sodium hydroxide (NaOH) was purchased from Avantor Performance Materials, LLC (Radnor, PA). FaSSIF/FeSSIF/FaSSGF and FaSSIF (version 2) powders were bought from Biorelevant (London, UK). L- α -Phosphatidylcholine (lecithin, $\geq 99\%$), sodium taurocholate hydrate, (STC [$\geq 97\%$]), sodium glycocholate, (SGC [$\geq 95\%$]), sodium taurodeoxycholate, (STDC [$\geq 95\%$]), sodium glycodeoxycholate, (SGDC [$\geq 97\%$]), sodium taurochenodeoxycholate, (STCDC [$\geq 97\%$]), and sodium glychochenodeoxycholate, (SGCDC [$\geq 97\%$]) were purchased from Sigma-Aldrich (St. Louis, MO). Fasted-stated human intestinal fluid (FaHIF) was sampled from a pool of healthy human volunteers (as detailed below).

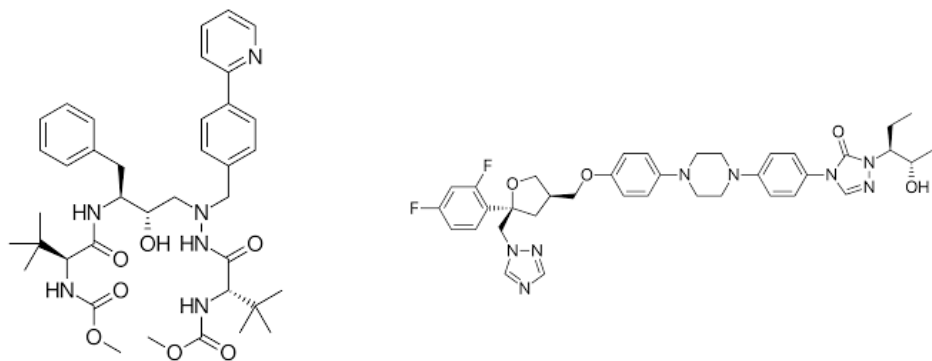


Figure 5-1. Molecular structures of atazanavir (left), and posaconazole (right).

5.4 Methods

5.4.1 Preparation of test media

FaSSIF/FeSSIF/FaSSGF powder was added to sodium phosphate buffer (pH 6.5) to prepare FaSSIF-V1, as described previously.^{17,20} FaSSIF-V2 powder was added to maleic acid buffer (pH 6.5) to create FaSSIF-V2.¹⁹ The two commercial FaSSIFs were used along with their corresponding blank buffers, which are referred to as FaSSIF-V1 blank buffer (buffer-V1) and FaSSIF-V2 blank buffer (buffer-V2), respectively. Another medium (composite-FaSSIF) containing six different bile salts was prepared using the sodium phosphate buffer, as detailed in Table 5-1. Preparation of composite-FaSSIF was performed by weighing all bile salts and adding them to the buffer solution. Meanwhile, 0.2 mM of lecithin was dissolved in dichloromethane (DCM) and added to the aqueous bile salt mixture. The composite-FaSSIF mixture was maintained

at 50°C, whilst stirring at 500 rpm for 30 min. This allowed the organic phase to evaporate from the aqueous mixture. The initial volume of added DCM was always kept to less than 1% of the total solution volume. All of the aforementioned media were adjusted to pH 6.5.

Table 5-1. Detailed composition of the bile salts and lecithin for FaSSIF-V1, FaSSIF-V2 and composite-FaSSIF.

	<i>FaSSIF-V1</i>	<i>FaSSIF-V2</i>	<i>Composite-FaSSIF</i>
<i>STC</i>	3 mM	3 mM	0.36 mM
<i>STDC</i>			0.36 mM
<i>STCDC</i>			0.18 mM
<i>SGC</i>			0.84 mM
<i>SGDC</i>			0.45 mM
<i>SGCDC</i>			0.81 mM
<i>Lecithin</i>	0.75 mM	0.2 mM	0.2 mM

5.4.2 Sampling and handling of FaHIF samples

Human intestinal fluids were collected at the University Hospitals Leuven as part of a previously published study.³⁸ The sampling procedure was approved by the Ethics Committee Research UZ/KU Leuven (reference numbers ML7918 and S53791); healthy Caucasian volunteers were enrolled in the study after giving written informed consent. Briefly, intestinal fluids were collected from the duodenum (near the ligament of Treitz) from 20 healthy volunteers every ten minutes for a period of 90 min in both fasted and fed state. After an overnight fast of at least 12 h (no food and only water), volunteers were given 250 mL of water before initiating the sampling of fasted state intestinal fluids. Following fasted state sampling, 400 mL of Ensure® Plus (Abbott Nutrition, Zwolle, the Netherlands) was ingested to simulate a standard meal. Fed state sampling was initiated after drinking 250 mL water, 20 min after the intake of the liquid meal. For each volunteer, the collected fractions were pooled to obtain a fasted and fed state individual volunteer pool. For the present study, a mixed pool of fasted state human intestinal fluid (FaHIF) was created by gently mixing samples from 16 individual volunteer pools. Afterwards, these samples were kept frozen at -80°C until use. The pH of the FaHIF pool used in this study was measured using a Mettler Toledo FiveEasy™ FE20 benchtop pH-meter (Schwerzenbach, Switzerland), and was found to be 7.3.

5.4.3 Crystalline and amorphous solubilities of atazanavir and posaconazole in FaHIF

The equilibrium and amorphous solubilities of atazanavir and posaconazole in all six media have been reported previously. For FaHIF samples, the medium was first centrifuged at low speed (3,000 rpm) for 2 min to remove visible particles from the sample. This significantly improves the clarity/transmittance of the FaHIF media and allows analytical techniques such as ultraviolet (UV) spectroscopy to be performed. Additionally, this removes the SHG signal found in native FaHIF, thus eliminating false positives when crystallization assessments are carried out in this medium. Accordingly, the equilibrium and amorphous solubilities of atazanavir were re-measured in FaHIF, after low speed-centrifugation, as described before. Briefly, the equilibrium solubilities were determined by adding an excess amount of crystalline atazanavir/posaconazole in FaHIF (1 mL), followed by equilibration for 48 h at 37°C. Afterwards, the sample was ultra-centrifugated at 50,000 rpm (135,700 g) for 30 minutes, while maintained at 37°C, using an Optima MAX-XP ultracentrifuge equipped with a Swinging-Bucket Rotor TLA-110 (Beckman Coulter, Inc., Brea, CA). For atazanavir, the supernatant concentration was determined by high performance liquid chromatography (HPLC) with a Hewlett Packard 1100 series system, using an Agilent Eclipse Plus C18 column (4.6 mm × 250 mm, 5 µm) (Agilent Technologies, Santa Clara, CA). The mobile phase consisted of 60% pH 2.5 water acidified with o-phosphoric acid, and 40% acetonitrile, by volume. An injection volume of 20 µL was used. The flow rate was set to 0.8 mL/min where each analytical run was adjusted to 15 min. Atazanavir was detected by ultraviolet (UV) absorbance at a wavelength of 247 nm. Standards (0.1-10 µg/mL) were prepared in methanol, where the standard curve exhibited good linearity ($R^2 = 0.999$) over this concentration range. For posaconazole, an Agilent 1260 Infinity II HPLC system coupled with an Agilent Eclipse Plus C18 column (4.6 mm × 250 mm, 5 µm) was used to analyze the sample concentration in the supernatant. The mobile phase was 60% acetonitrile and 40 % deionized water, by volume. Each analytical run duration was 6 min, where the injection volume was 20 µL and the mobile phase flow was held constant at 2.0 mL/min. Posaconazole was detected by fluorescence emission where the excitation wavelength was at 240 nm and the emission wavelength was at 385 nm. A calibration curve (0.1-20 µg/mL, $R^2 = 1.000$) was used to calculate the posaconazole solubility in FaHIF.

The amorphous solubility was determined by generating highly supersaturated solutions of atazanavir and posaconazole in FaHIF using a solvent-shift method. This was performed in the

presence of HPMC-AS (10 µg/mL for atazanavir and 100 µg/mL for posaconazole) while being stirred at 300 rpm and maintained at 37°C. Samples were then ultra-centrifuged using the same conditions used in the crystalline solubility determination measurements. The supernatant was diluted in methanol, and analyzed using the same HPLC methodologies as described before.

5.4.4 Nucleation induction time experiments by UV spectroscopy

The experimental nucleation induction time (T_{ind}) is defined as the sum of the time required for critical nucleus formation (T_{crit}), and the time for the crystals to grow for a detectable size (T_{grow}), as demonstrated by equation 5-1:⁴⁹

$$T_{ind} = T_{crit} + T_{grow} \quad (5-1)$$

To measure T_{ind} , supersaturated solutions of both atazanavir and posaconazole were created using a solvent-shift method in all six media at the amorphous solubility concentration reported before (REF first HIF paper). This was performed using an atazanavir DMSO stock solution (50 mg/mL) and a posaconazole methanol stock solution (10 mg/mL). Then, the changes in UV-absorbance spectra (280 nm for atazanavir and 260 nm for posaconazole) were monitored as a function of time, using a UV fiber optic dip probe coupled to SI Photonics UV/vis spectrometer (Tucson, AZ). For samples in buffer-V2 and FaSSIF-V2, scattering at a non-absorbing wavelength (400 nm) was observed instead due to the interference of maleic acid with UV-absorbance. A 0.5 and 1 cm path length dip probe were used for atazanavir and posaconazole measurements, respectively, except when experiments were done in FaHIF, where a 0.2 cm path length dip probe was used. Experiments were performed using a 4 mL sample volume, inside an 8 mL borosilicate glass vials (Fisher Scientific, Hampton NH), stirred at 300 rpm and maintained at 37°C using a jacketed beaker connected to a Julabo MA water bath (Seelbach, Baden-Wurttemberg, Germany).

5.4.5 Characterization of atazanavir and posaconazole crystals by SHG microscopy

The onset and progression of atazanavir and posaconazole crystallinity in supersaturated solutions were investigated using SHG microscopy. All media were confirmed to show non-significant SHG background signal (prior to adding the two compounds. Supersaturated solutions were prepared as described before, and small aliquots were withdrawn at different time points and pipetted onto a glass slide mounted on a multi-slide holder tray. SHG images were acquired using a commercial

second order nonlinear imaging of chiral crystals (SONICC) instrument manufactured by Formulatrix (Waltham, MA). SONICC utilizes a Fianium FemtoPower laser operating at 1064 nm with 51 MHz repetition rate and a 166 fs pulse width, equipped with resonant mirror/galvanometer beam scanning at 8 kHz fast axis to generate images. The SHG signal at 532 nm was collected in trans-illuminated mode by a 10x near-UV objective (Thorlabs, 0.25 NA). SHG microscopy images were acquired at 350 mW infrared (IR) power and an exposure time of 894 ms. SHG images had fields of view of dimensions of $1925 \mu\text{m} \times 1925 \mu\text{m}$. All scans were obtained in different focal planes in the Z direction, at $100 \mu\text{m}$ steps. Imaging analysis, particle counting and size measurements were performed using ImageJ 1.05b software.¹⁵⁴ The number and size of new particles formed per unit time were obtained by employing the built-in particle counting algorithm in ImageJ, using the time-dependent SHG images.

5.4.6 Characterization of atazanavir and posaconazole crystals by scanning electron microscopy (SEM)

Highly supersaturated solutions of atazanavir and posaconazole were prepared as described before, where samples were allowed to surpass their measured T_{ind} , while stirred at 300 rpm and maintained at 37°C. To prepare samples for SEM analysis, aliquots were then centrifuged at 14,800 rpm for 10 min, using a Sorvall Legend Micro 17 Centrifuge (Thermo Fisher Scientific, Waltham, MA). The supernatants were then discarded, and a small amount of the precipitate was fixed on a SEM stub and sputter-coated with platinum for 60 s. Imaging was performed with an FEI Nova nanoSEM field emission scanning electron microscope (FEI, Hillsboro, OR), operated at 10 kV accelerating voltage, ~6 mm working distance, and a spot size of 5. Secondary electron images were captured with the Everhart Thornley detector (ETD) and back-scatter electron images were collected using a vCD detector.

5.4.7 Characterization of atazanavir precipitates by powder X-ray diffraction (PXRD)

Atazanavir precipitates pelleted by centrifugation of solutions allowed to surpass their T_{ind} in the different media, were further inspected for crystallinity and polymorphic form using PXRD analysis. After the supernatant was discarded, the pellet was removed using a spatula and the water content was reduced by carefully applying a gentle airflow (Fisherbrand Air’It Aerosol, Houston, TX) for a few minutes. In addition, the as-received atazanavir active pharmaceutical ingredient

(API) was slurried with acetonitrile for 15 min (atazanavir is relatively insoluble in acetonitrile), to induce polymorphism in the starting material. The sample was then dried in a similar fashion to the media precipitates. PXRD evaluation was then performed using a Rigaku Smartlab diffractometer (Rigaku Americas, The Woodlands, TX) equipped with a Cu-K α radiation source and a D/tex ultradetector. Glass sample holders were used and powder patterns were obtained from 5 to 50° 2 θ at a scan speed of 4°/ min and a step size of 0.02°. The voltage and current used were 40 kV and 44 mA, respectively.

5.5 Results

5.5.1 Crystalline and amorphous of atazanavir and posaconazole in pre-centrifuged FaHIF

Table 5-2 shows the crystalline and amorphous solubilities of atazanavir and posaconazole at 37°C as measured in pre-centrifuged (3,000 rpm; 2 min) FaHIF. In comparison to our previous findings in non-centrifuged FaHIF,²¹⁶ atazanavir and posaconazole solubilities, crystalline or amorphous were similar where the differences between all values were statistically nonsignificant (based on two-tailed t-test, p > 0.05). This suggests that these centrifugation conditions did not impact the solubilizing species or alter the nature of the medium.

Table 5-2. Crystalline and amorphous solubilities of atazanavir and posaconazole pre-centrifuged FaHIF at 37°C. (n=3).

Drug	Crystalline solubility ($\mu\text{g/mL}$)	Amorphous solubility ($\mu\text{g/mL}$)
Atazanavir	6.6 ± 0.3	100 ± 5
Posaconazole	2.4 ± 0.4	13.0 ± 0.3

5.5.2 Nucleation induction times

The onset of nucleation of atazanavir and posaconazole was determined at 37°C at the maximum supersaturation level, equivalent to the amorphous solubility of the drug, in each medium. As illustrated in Figure 5-2, the crystallization induction time is taken as the time when the UV-absorbance data show a change in slope, simultaneous with an increase in extinction due to light scattering (for buffer-V2 and FaSSIF-V2, only the sudden increase in extinction was used to detect the induction time in these media). Additionally, the negative slope of the absorbance versus time profile (L_2) in Figure 5-2 was used to assess the desupersaturation rate once nucleation has

commenced. Desupersaturation rate ($\mu\text{g}/\text{mL}\cdot\text{min}$) was measured where L_2 showed good linearity for 5-10 time-points and could not be measured for all samples.

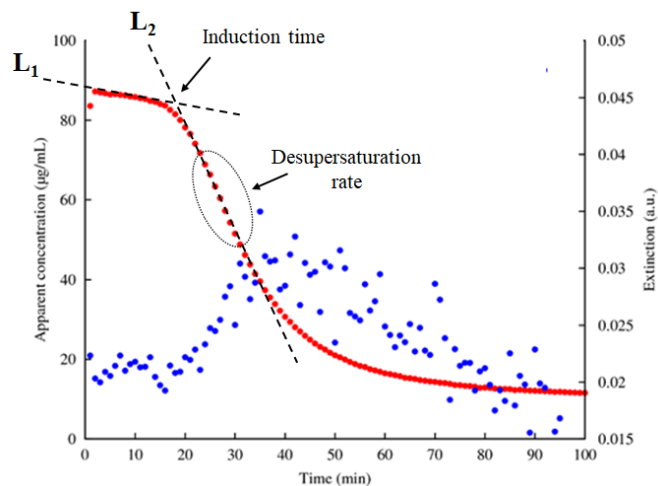


Figure 5-2. Schematic illustrating nucleation induction time measurements where the change in the slope of the solution apparent concentration (left y-axis) and increase in extinction (right y-axis) were used to assess the induction time.

Figure 5-3 summarizes the observed nucleation-induction times for atazanavir in different media. Generally, atazanavir is a relatively slow nucleator from supersaturated aqueous solutions, in agreement with previous findings.⁴⁶ In the absence of any additives or polymers, atazanavir started to crystallize after 102 min in buffer-V1 and 93 min in buffer-V2. Interestingly, the time until crystallization was shortest in the FaSSIF-V1 medium, and was just below 1 h. In FaSSIF-V2, the induction time was slightly prolonged (72 min), compared to FaSSIF-V1. Furthermore, atazanavir maintained supersaturation in FaHIF for approximately 140 min, and a similar, slightly shorter, nucleation induction time was observed in composite-FaSSIF (~130 min). When HPMC-AS was added at 10 $\mu\text{g}/\text{mL}$ concentration, crystallization onset times were substantially extended in all media. In blank buffers and composite-FaSSIF, the nucleation times were above 8 h. FaHIF again led to a longer induction time for atazanavir relative to the commercial simulated media.

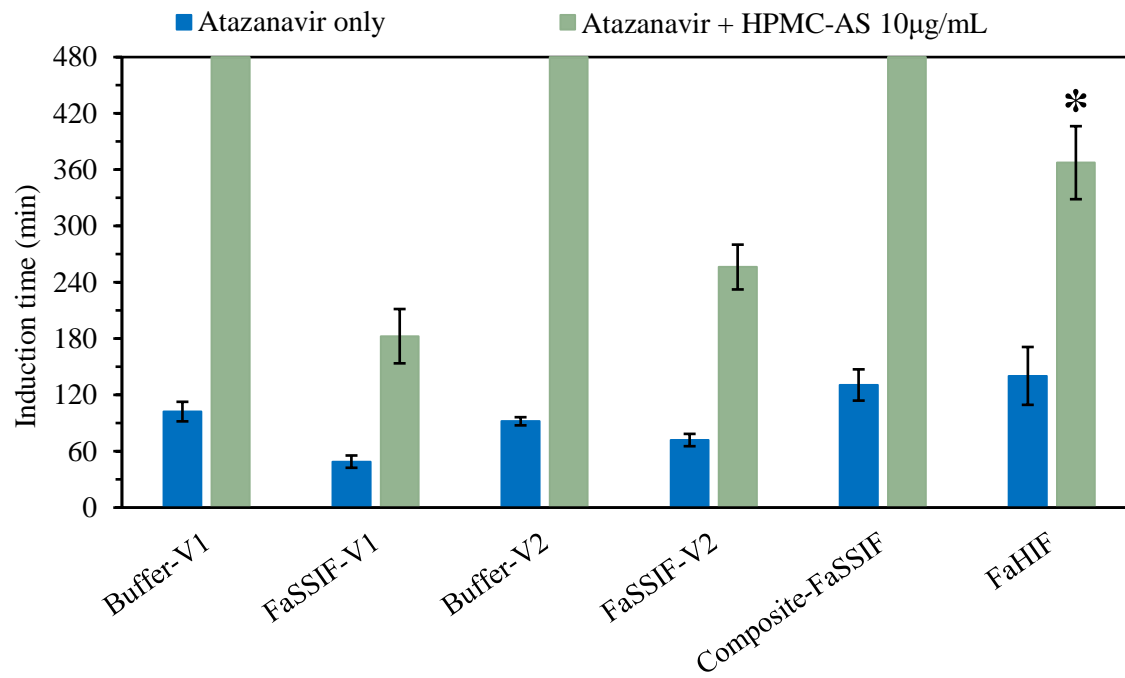


Figure 5-3. Summary of nucleation induction times observed for supersaturated solutions of atazanavir in different media at 37°C; in the absence of polymer (blue columns) and presence of 10 µg/mL HPMC-AS (light green columns). * 1 of 3 measurements of atazanavir in FaHIF did not demonstrate change in UV-absorbance for 480 min, i.e. no nucleation. (n=3, except for * n=2).

Posaconazole crystallizers faster relative to atazanavir, and induction times for various media are summarized in Figure 5-4. Although nucleation was rapid, slightly longer induction times were still observed for the blank buffers relative to the corresponding FaSSIF systems (approximately 2-fold increase). Compared to FaSSIF-V1, FaHIF and composite-FaSSIF demonstrated a 5-fold and 3-fold increases in nucleation onset times, respectively. In the presence of a low concentration of HPMC-AS (10 µg/mL), only minor increases in nucleation times were observed in the different media. For 50 µg/mL of HPMC-AS, nucleation-induction times were substantially extended, particularly for the simple buffer solutions. FaHIF had a longer induction time compared to other simulated media (about 2-fold). FaSSIFs and composite-FaSSIF had very close induction times, between 35 and 42 minutes.

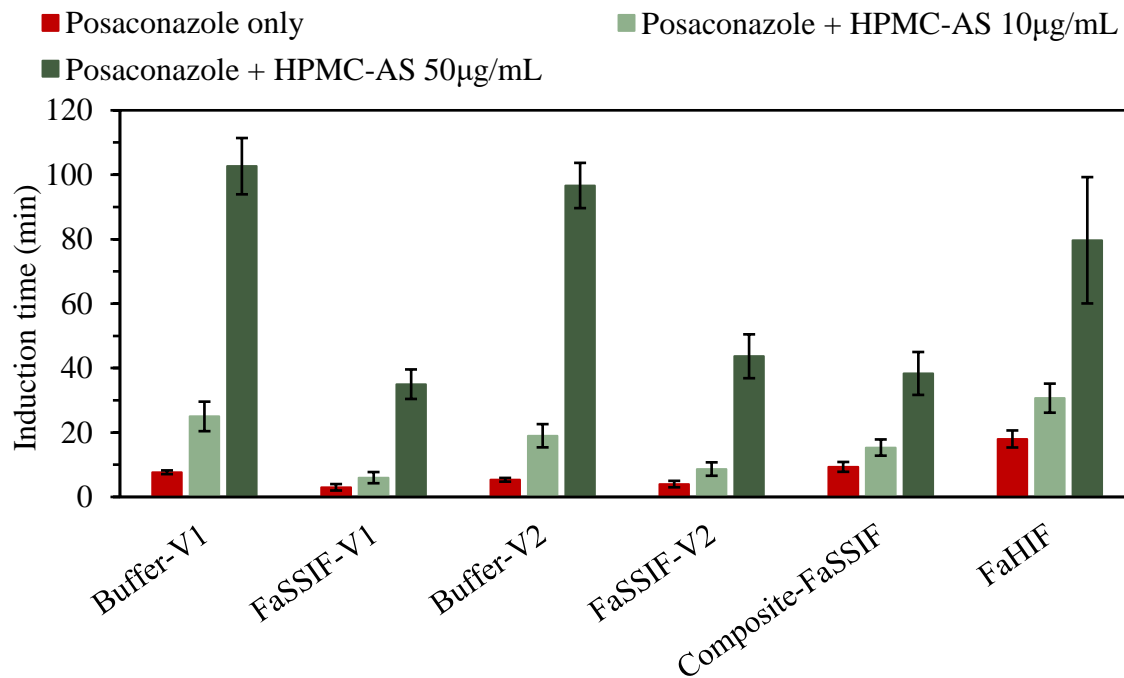


Figure 5-4. Summary of nucleation induction times observed for supersaturated solutions of posaconazole in different media at 37°C; in the absence of polymer (red columns), presence of 10 µg/mL HPMC-AS (light green columns) and 50 µg/ml HPMC-AS (dark green columns). (n=3).

Finally, the desupersaturation rates of atazanavir and posaconazole after the onset of nucleation in buffer-V1, FaSSIF-V1 and composite-FaSSIF are summarized in Table 5-3. For atazanavir, desupersaturation rates were fastest in FaSSIF-V1, and slowest in composite-FaSSIF. Alternatively, desupersaturation rates were notably slower in buffer-V1 than in media with solubilizing species in the case of posaconazole. When HPMC-AS was added to posaconazole solutions, desupersaturation rates were reduced with increasing concentration of the polymer.

Table 5-3. Summary of desupersaturation rates, obtained from the nucleation induction time profiles for atazanavir and posaconazole, in buffer-V1, FaSSIF-V1 and composite-FaSSIF.

Medium	Desupersaturation rate (µg/min)			
	Atazanavir		Posaconazole	
	No polymer	No polymer	HPMC-AS 10 µg/mL	HPMC-AS 50 µg/mL
Buffer-V1	1.0 ± 0.4	0.6 ± 0.1	0.3 ± 0.1	0.10 ± 0.03
FaSSIF-V1	4.2 ± 1.1	1.9 ± 0.2	2.0 ± 0.6	0.9 ± 0.2
Composite-FaSSIF	0.3 ± 0.1	1.7 ± 0.4	1.6 ± 0.5	1.3 ± 0.4

5.5.3 Characterization of atazanavir and posaconazole crystallization using SHG

SHG images were acquired for supersaturated solutions of atazanavir and posaconazole undergoing crystallization at different time-points. Both drugs exhibit SHG-active signal due to the presence of chiral centers (4 in each molecule). Time-points were determined according to the onset of nucleation of the drug in each medium. Atazanavir SHG images indicated the presence of a similar amount of crystals in buffer-V1 (Figure 5-5A) and FaSSIF-V1 (Figure 5-5B). Atazanavir crystallinity amounts were very similar in buffer-V2 and FaSSIF-V2. On the other hand, only limited SHG signals were detected in composite-FaSSIF and FaHIF, as shown in Figures 5-5C and 5-5D, respectively, indicating only trace crystallinity in these media.

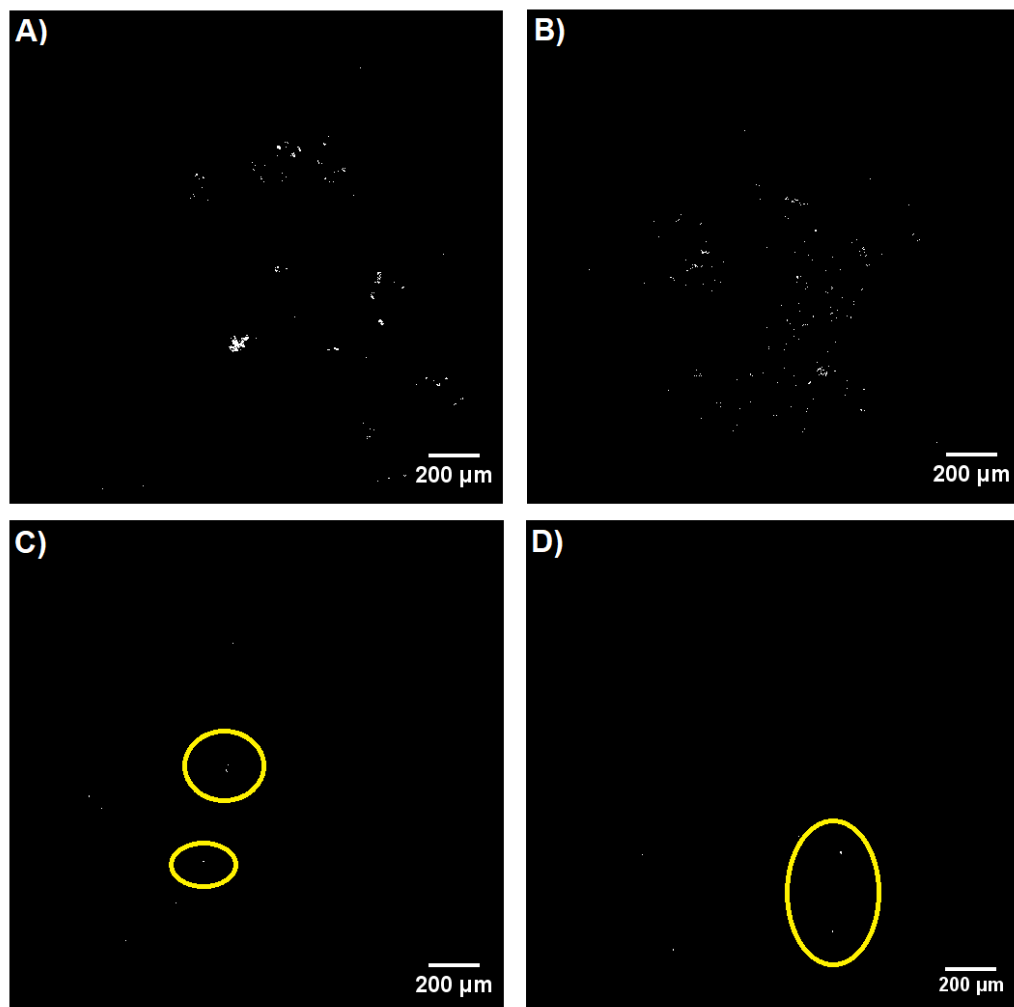


Figure 5-5. SHG images for aliquots of atazanavir samples undergoing crystallization in A) buffer-V1 and B) FaSSIF-V1, at 90 min, C) composite-FaSSIF and D) FaHIF, at 120 min. Trace crystallinity in C) and D) are highlighted in yellow circles.

SHG signal count and intensity for posaconazole were relatively higher. Figure 5-6 shows SHG images for posaconazole crystallization in buffer-V1, FaSSIF-V1, buffer-V2 and FaSSIF-V2 after 16 min. While posaconazole exhibited higher signal count in the FaSSIF media, the size of the crystallizing domains appeared bigger in the blank buffers. The progression of posaconazole crystallization in composite-FaSSIF and FaHIF is shown in Figure 5-7. For composite-FaSSIF, posaconazole crystalline SHG counts increased notably after 24 min (Figure 5-7B), similar to the SHG image of FaSSIF-V1 in Figure 5-6B. Conversely, posaconazole SHG count and intensity remained minimal up to 40 minutes in FaHIF (Figures 5-6C and 5-6D).

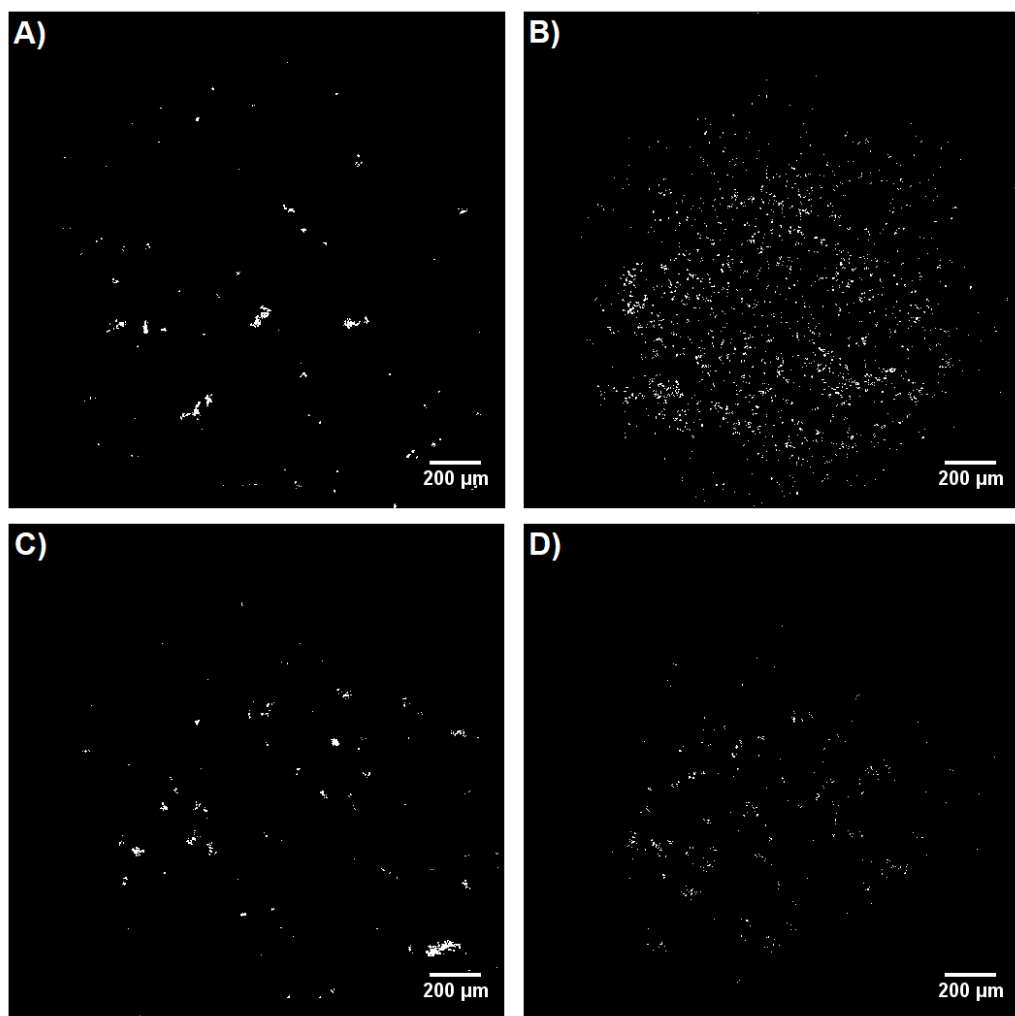


Figure 5-6. SHG images for aliquots of posaconazole samples undergoing crystallization in A) buffer-V1, B) FaSSIF-V1, C) buffer-V2 and D) FaSSIF-V2, at 16 min.

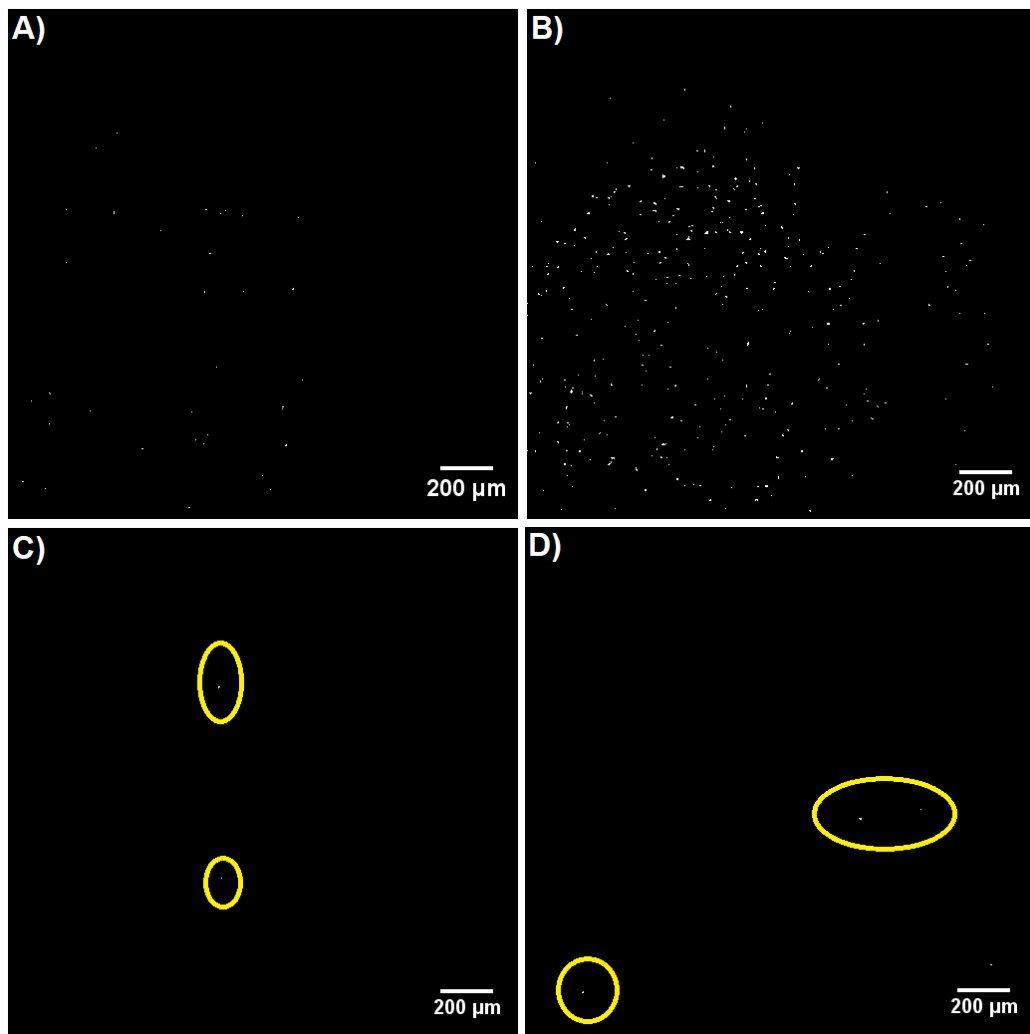


Figure 5-7. SHG images for aliquots of posaconazole samples undergoing crystallization in A) composite-FaSSIF at 12 min, B) composite-FaSSIF at 24 min, C) FaHIF at 24 min and D) FaHIF at 40 min. Trace crystallinity in C) and D) is highlighted in yellow circles.

Crystallization kinetics, consisting of nucleation rate (change in number of SHG signal count/min) and crystal growth rate (change in size/min) were assessed through further evaluation of the SHG images at different time-points. Results of nucleation rate kinetics for atazanavir and posaconazole in all media are summarized in Figure 5-8. For atazanavir, nucleation rates were mostly similar in buffer-V1, FaSSIF-V1, buffer-V2 and FaSSIF-V2. Compared to the highest value in FaSSIF-V1, the nucleation rate decreased approximately 4-fold and 16-fold in FaHIF and composite-FaSSIF, respectively. For posaconazole, the nucleation rate was more variable between the different media and was notably higher in FaSSIF-V1 at ~49 counts/min. In contrast, FaHIF exhibited the lowest

nucleation rate at ~0.06 counts/min, suggesting slow crystallization kinetics in this medium. When 10 µg/mL of HPMC-AS was added, nucleation rates for posaconazole dropped. For higher concentrations of polymer, SHG signals were too low for reliable qualitative and quantitative assessment. Additionally, SHG experiments were not performed for atazanavir in the presence of polymer due to the extensive nucleation times.

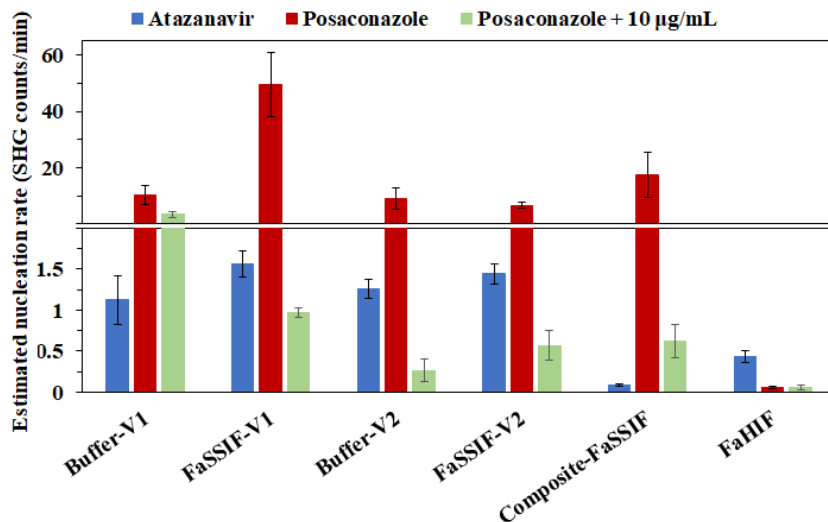


Figure 5-8. Estimated nucleation rate (SHG signal count/min) for atazanavir and posaconazole in different media.

Size analysis was also performed and changes per unit time (estimated crystal growth rates) are summarized in Figure 5-9. Crystal growth rates appeared highest in buffers for both drugs. FaSSIF-V1 had the slowest growth progression for atazanavir, whereas FaHIF was the slowest for posaconazole. In the presence of HPMC-AS with posaconazole, growth rates were suppressed for all media, and growth rates could not be measured in some media (FaSSIF-V1, buffer-V2 and FaHIF).

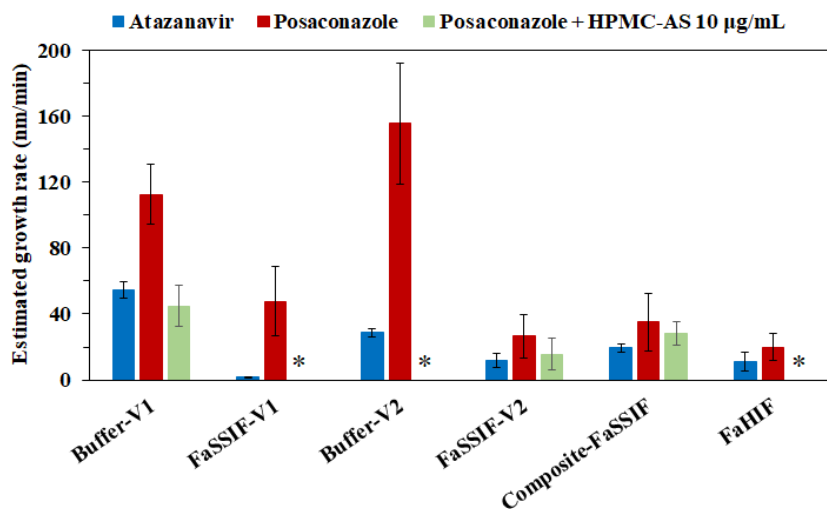


Figure 5-9. Estimated growth rate (SHG signal size/min) for atazanavir and posaconazole in different media. *Growth rate could not be quantitated.

5.5.4 Characterization of atazanavir and posaconazole crystals using SEM

SEM imaging was used to characterize precipitates of atazanavir and posaconazole formed after crystallization from the various media. The as supplied atazanavir crystals, shown in Figure 5-10A, are layers of crystalline sheets with rough ends, while atazanavir crystallized from all aqueous media showed characteristic needle-shaped crystals. FaSSIF-V1-crystallized atazanavir, which exhibited the fastest nucleation onset, is shown an example of the needle morphology Figure 5-10B. In Figure 5-11, atazanavir crystals from buffer-V1 (Figures 5-11A-C) and FaHIF (Figures 5-11D-F) are shown for different crystallization times. After 150 min in buffer-V1, precipitated atazanavir samples showed small needles/rods nucleating on the surface of what appeared to be amorphous atazanavir. At the 300 min time-point, well-defined atazanavir needles of variable size were observed. A similar pattern was observed in FaHIF where small bundles of needles were observable initially after 180 min. Subsequently, more well-developed atazanavir needles were clearly observed at 300 min. Higher magnification images of the atazanavir needles are shown in Figure 5-12. Atazanavir needles grown in buffer-V1 were wider and demonstrated secondary growth and imperfections on the surface. On the other hand, atazanavir needles from FaHIF were generally narrower with smoother ends and surfaces (Figure 5-12B). Atazanavir crystallized in composite-FaSSIF showed secondary crystal growth/branching on the surface as was the case in buffer-V1, although they exhibited a narrower width as compared to buffer (Figure 5-13A). The

SEM image in Figure 5-13B was collected via a backscattering detector, where the observable contrast in brightness seen in the deposited species on the needles infers elemental atomic number differences. This strongly suggests that these small regions are bile salts/lecithin; tauro-conjugated bile salts and lecithin have sulfur and phosphorus in their molecular structure, respectively. Similar observations were noted in Figure 5-11F which showed FaHIF media components. Finally, Figure 5-14 shows atazanavir needles formed in the different media in the presence of 10 µg/mL of HPMC-AS.

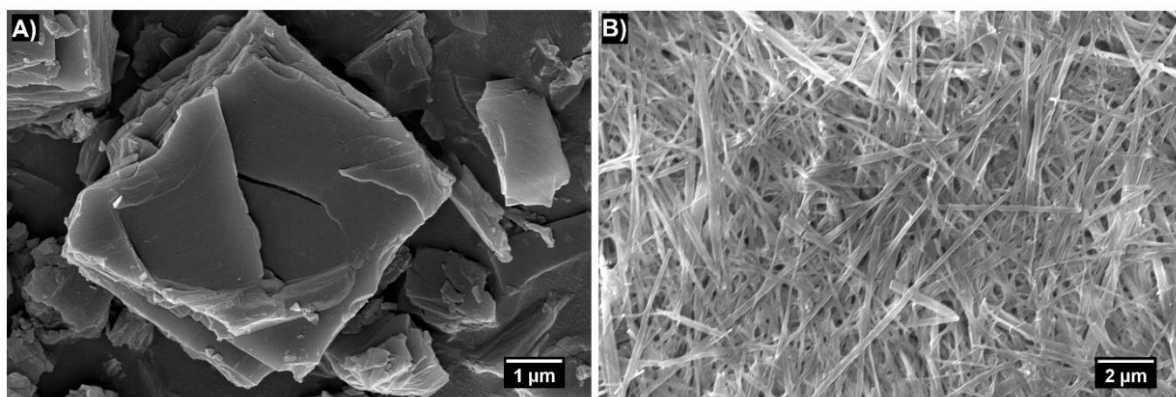


Figure 5-10. SEM images of A) as received atazanavir crystals and B) atazanavir crystallized from FaSSIF-V1 (150 min).

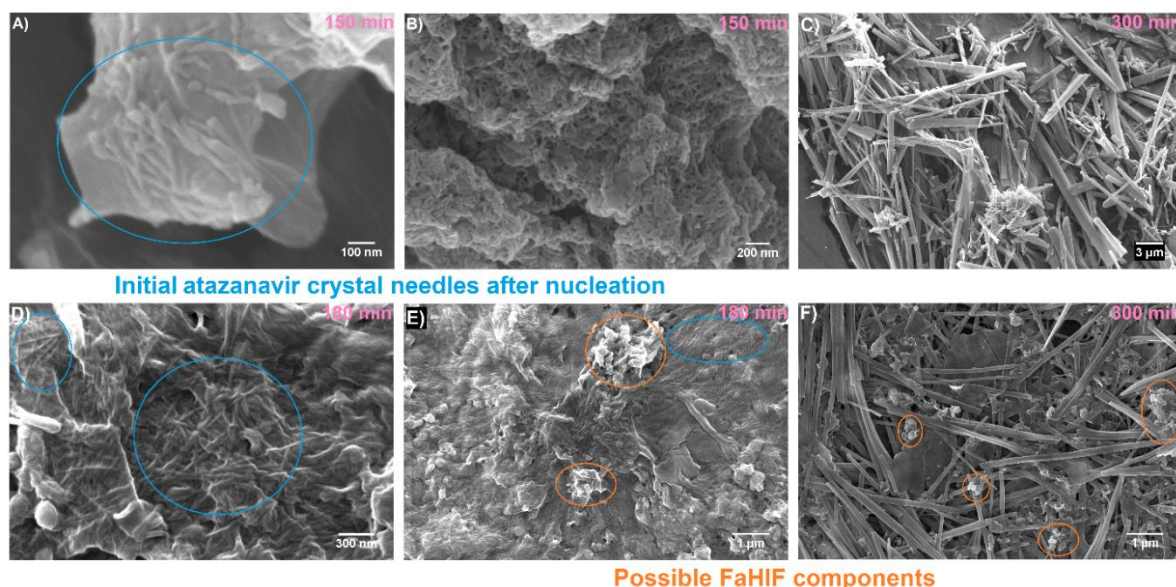


Figure 5-11. SEM images of atazanavir during crystallization at different times in buffer-V1 at A) and B) 150 min and C) 300 min, and in FaHIF, D) and E) at 180 min and F) at 300 min.

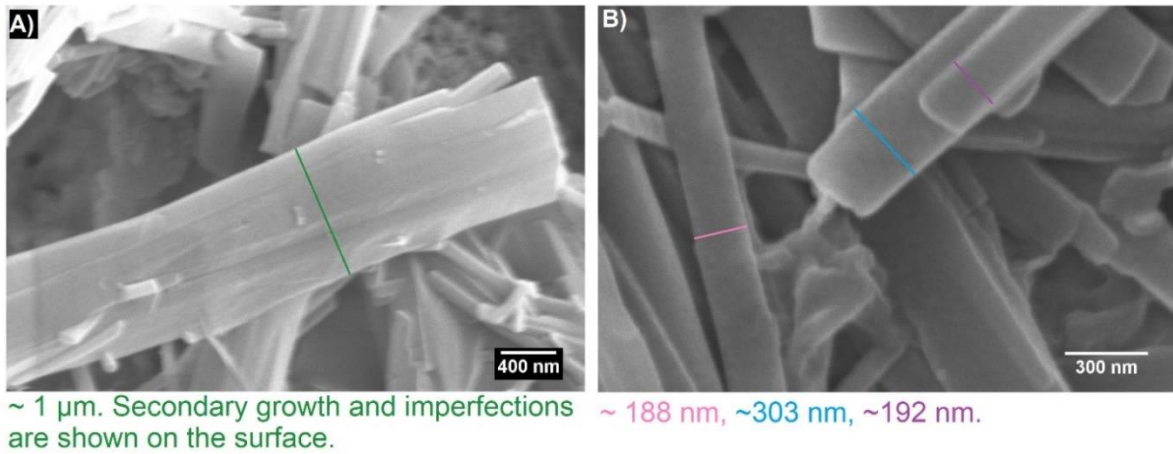


Figure 5-12. SEM images showing a higher magnification view of crystallized atazanavir needles formed in A) buffer-V1 and B) FaHIF at 300 min time-point.

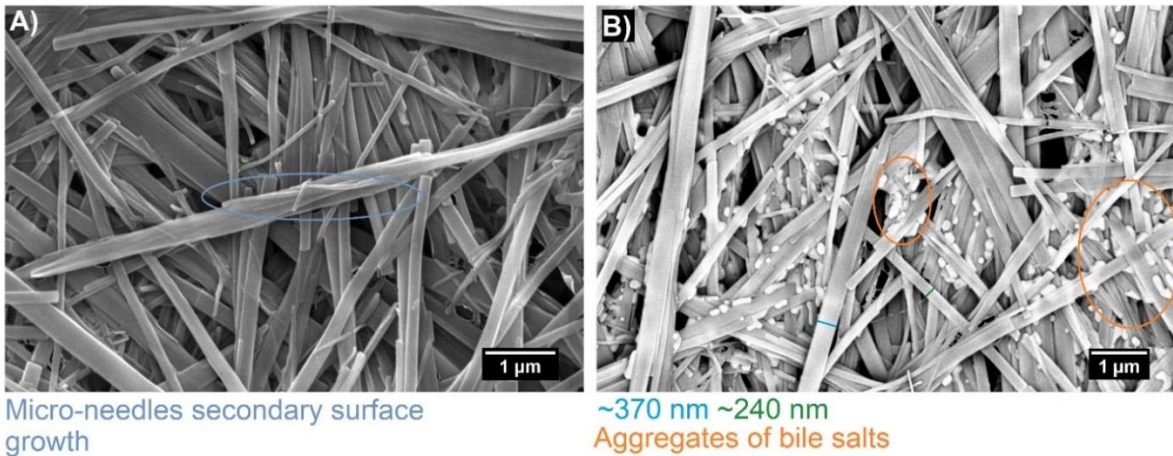


Figure 5-13. SEM images of atazanavir crystalline needles in composite-FaSSIF. A) General morphology of atazanavir needles showing branching and secondary growth on the surface. B) Atazanavir needles with bile salt/lecithin deposited species that showed contrast in brightness through the backscattering detector due to elemental atomic number differences.

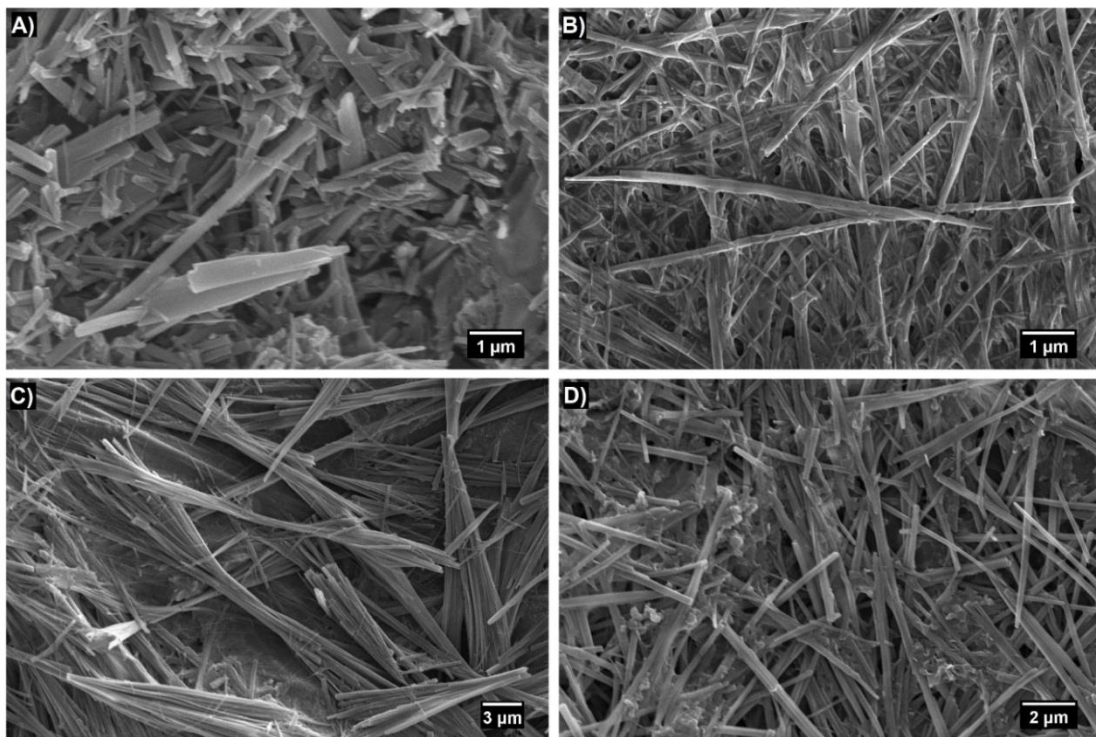


Figure 5-14. SEM images of crystallized atazanavir in the presence of 10 $\mu\text{g}/\text{mL}$ of HPMC-AS in different media; A) buffer-V1, B) FaSSIF-V1, C) composite-FaSSIF, and D) FaHIF.

For posaconazole, the as-received API crystals are shown in Figure 5-15A and appeared as rectangular bricks/sheets of approximately 1 μm in thickness. Posaconazole crystallized from buffer-V1 showed plate-like crystals of different sizes (Figures 5-15B and 5-15C). Although the crystalline sheets were deposited in layers, they were mostly discrete from each other. The crystals from all the media were much thinner (more than 20-fold, e.g. Figure 5-15C) than the as-received API crystals. Posaconazole crystallized in FaSSIF-V1 as plates with distinctive striations/imperfections on the surface and irregular ends (Figure 5-15D). Composite-FaSSIF crystals were somewhat similar to those obtained from FaSSIF-V1 in terms of morphology, as shown in Figures 16A and 16B. Posaconazole crystals formed in FaHIF were also thin plates (Figure 5-16C) and were more irregular at the ends, developing what appeared to be ‘finger-like’ structures (Figure 5-16D). Figure 5-17 shows images for posaconazole crystals in different media in the presence of 10 $\mu\text{g}/\text{mL}$ of HPMC-AS

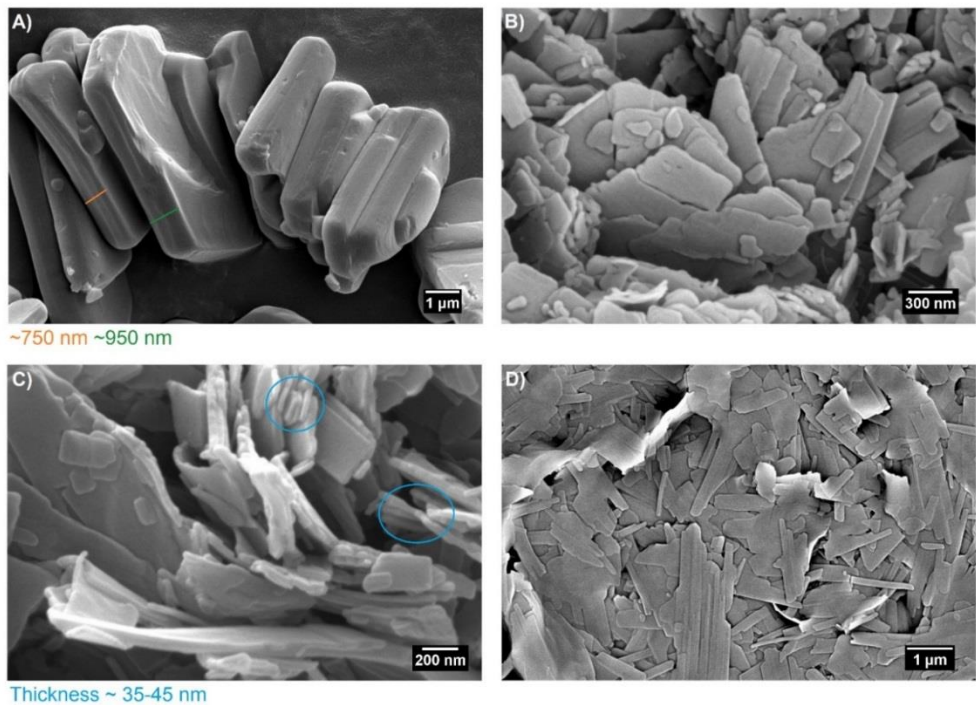


Figure 5-15. SEM images of posaconazole crystals formed under different conditions; A) as-received posaconazole crystals, B) & C) crystallized posaconazole from buffer-V1, and D) crystallized posaconazole from FaSSIF-V1.

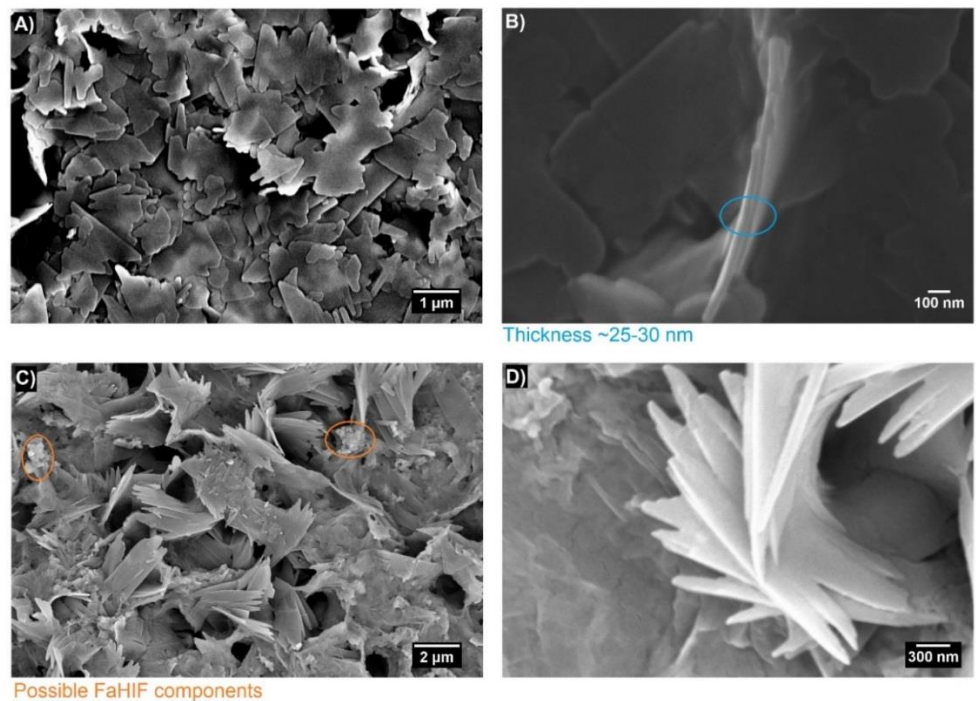


Figure 5-16. SEM images of crystallized posaconazole in different media; A) and B) composite-FaSSIF, C) and D) FaHIF.

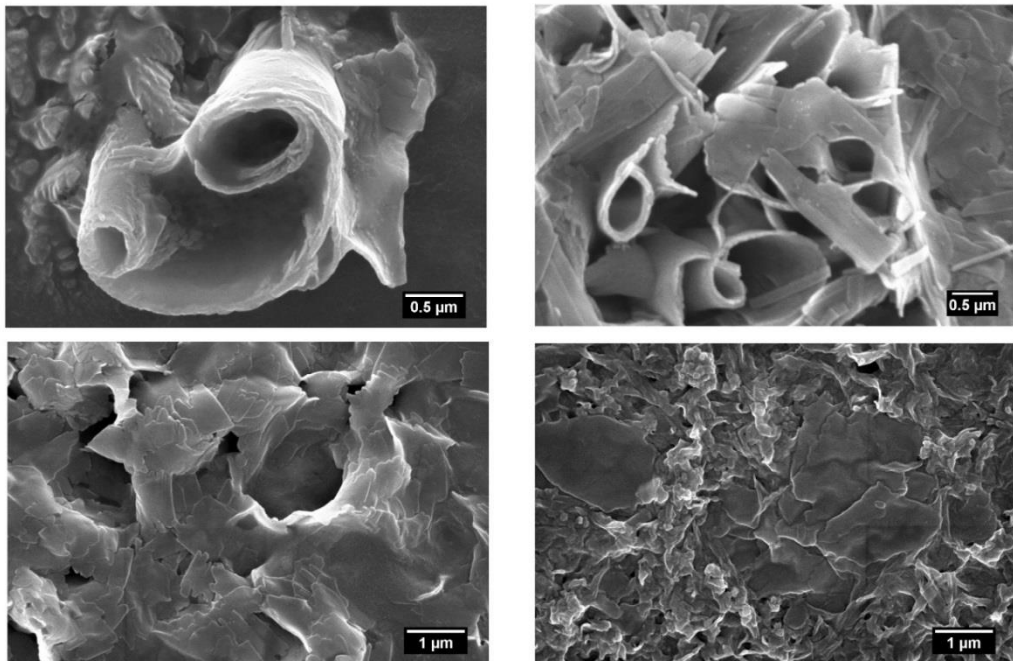


Figure 5-17. SEM images of crystallized posaconazole in the presence of 10 $\mu\text{g}/\text{mL}$ of HPMC-AS in different media; A) buffer-V1, FaSSIF-V1, C) composite-FaSSIF, and D) FaHIF.

5.5.5 Characterization of atazanavir precipitates by PXRD

PXRD measurements were used to examine the crystal form of atazanavir precipitated from different media, with results summarized in Figure 5-18. Following slurring in acetonitrile, a different powder pattern was obtained, suggesting that the as-received API material was a metastable polymorph that converted to a more stable form. Atazanavir precipitates from the different media displayed diffraction peaks similar to those observed for the slurried atazanavir, with peaks observed at 6.7, 10.6, 11.9, 12.8, 14.2 and 19° 2-theta. The characteristic peaks for the as-received material, were found at 4.4, 9.8 and twin-peak 14.8/15.1° 2-theta and were absent in the slurried and precipitates diffraction patterns.

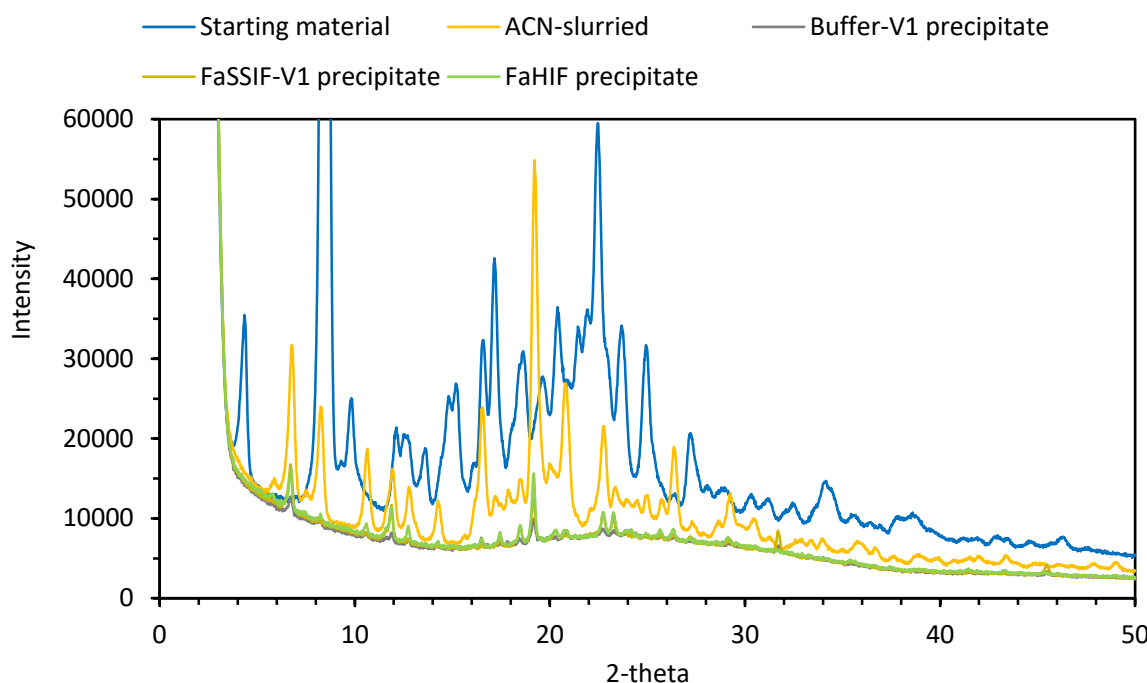


Figure 5-18. PXRD patterns of atazanavir starting material (blue), Acetonitrile-slurried (orange), Buffer-V1 precipitate (grey), FaSSIF-V1 precipitate (yellow) and FaHIF precipitate (green).

5.6 Discussion

Simulated media: Compositional variations and *in vivo* implications. As the use of supersaturating formulations is becoming more widespread, it is of particular interest to understand the impact of different media, and their composition, on crystallization kinetics of supersaturated solutions. From a solubility enhancing perspective, crystallization is regarded as an undesirable event, as it will deplete the supersaturation until ultimately, an equilibrium state is reached. Regardless of how supersaturation is induced, prolonged drug supersaturation has been linked to improved drug absorption *in vivo* for a variety of compounds including abiraterone,²¹⁷ celecoxib,²¹⁸ danazol,²¹⁹ halofantrine,²²⁰ paclitaxel,²²¹ and posaconazole.²⁵ For fenofibrate, Crum et al. demonstrated that even ‘transient’ supersaturation could be sufficient to drive absorptive drug flux for periods of up to an hour.¹⁹⁴ Supersaturation maintenance in HIF versus simulated media was found to show good correlation in etravirine and loviride, but not for itraconazole.²²² If simulated media erroneously underestimates or overestimates the kinetics of crystallization, this could have consequences for establishing accurate *in vitro-in vivo* correlations, as well as formulation design decisions. In this context, one of the main goals of this investigation was to use

FaHIF as an *ex vivo* control medium, as a comparator to current *in vitro* testing media, like FaSSIF, in terms of supersaturation duration and phase-transition outcomes. Differences between aspirated and simulated fluids would warrant further optimization of the simulated media to better mimic the observed crystallization behavior in human fluids.

Nucleation: Theoretical considerations. The medium composition was found to impact the nucleation behavior of two compounds, atazanavir and posaconazole, as determined via induction time measurements. Nucleation commences with the formation of small molecular clusters periodically arranged in a new crystalline phase. In solution, the factors affecting nucleation rate (J) can be described by the classical nucleation theory, as shown in equation 5-2:^{70,71,223}

$$J = A \exp\left(\frac{16\pi v_o^2 \gamma^3}{3(K_B T)^3 (\ln S)^2}\right) \quad (5-2)$$

Where A is the pre-exponential kinetic parameter, v_o is the molecular volume, γ is the interfacial tension between the crystal nucleus and the solution, K_B is the Boltzmann constant, T is the temperature and S is the supersaturation level. Since these experiments were performed at the maximum supersaturation level (amorphous solubility), all systems had the same crystallization driving force in terms of considering S . For a given molecule, other exponential factors are all constants except γ , which theoretically decreases in media with solubilizing species compared to the blank buffer media, due to the reduction in surface tension.²²⁴ However, our observations do not show rationalizable trends in nucleation rate and γ . For instance, the nucleation rate was lower in FaHIF than in buffer; a decrease in γ is expected to increase the nucleation rate. The pre-exponential term, A , is influenced by several factors and can be expressed according to equation 5-3:⁷⁰

$$A = f Z n \quad (5-3)$$

Here, f is the rate of monomer attachment to the critical nucleus, either through volume diffusion of solute or interface transfer. Z is the Zeldovich factor which is the probability of formation or dissolution of the crystal nucleus. Finally, n is the number density of molecules in solution. It is possible that adsorption of species onto the nucleus might impact the rate of monomer attachment.

Effect of different media on nucleation times and kinetics. As shown in Figures 5-4 and 5-5, a variable onset of nucleation was observed between the different media. The first observation from

the nucleation time results is the variation between FaSSIF-V1/V2 and their corresponding blank buffers. For both compounds, the onset of nucleation was always faster in the simulated media, suggesting that the current FaSSIF composition is likely to accelerate nucleation, relative to a simple buffer. In contrast, nucleation in FaHIF is reduced. This observation is of great significance as it demonstrates that crystallization kinetics could potentially be overestimated when *in vitro* testing is performed in FaSSIFs, and underestimated if performed in simple buffers. Thus, neither of these media are truly representative of the physiological environment in the GI tract as mentioned.

The presence of more lecithin evidently promoted more rapid crystallization as reported before,⁴⁶ which can be illustrated when comparing induction times of FaSSIF-V1 (0.75 mM of lecithin) and FaSSIF-V2 (0.2 mM of lecithin) (Figures 5-4 and 5-5). Lecithin is a mixture of phospholipids that can form micelles or mixed micelles with other bile salts. An increase in the lecithin-sodium cholate ratio, will result in an increase in the size of the mixed micelles.²²⁵ Although this can greatly enhance both crystalline and amorphous solubilities via additional solubilization (such as the case in posaconazole),²¹⁶ lecithin had been also shown to impact crystallization kinetics in an unfavorable manner with respect to supersaturation longevity. Two mechanisms had been suggested to be responsible for this effect; either lecithin renders STC/other bile salts less unavailable by forming mixed micelles, thereby reducing the capacity of the bile salts to inhibit crystallization and/or lecithin provide additional adsorption interfaces, promoting nucleation. It should be noted that in FaHIF, that the majority of phospholipids present in human fluids are in form of lyssolecithin rather than lecithin,^{131,205} a factor that can potentially impact crystallization behavior.

Furthermore, the presence of STC versus STC plus additional bile salts, at equivalent total concentration, was shown to influence crystallization. At equal concentrations of lecithin (0.2 mM), composite-FaSSIF demonstrated longer induction times than FaSSIF-V2, which was more clearly seen for atazanavir. Herein, composite-FaSSIF showed a strong correlation with FaHIF in terms of the nucleation kinetics for atazanavir (Figures 5-8), and crystallization was considerably delayed in comparison to commercial FaSSIF media (Figure 5-4). On the other hand, posaconazole still crystallized faster in composite-FaSSIF than FaHIF (Figure 5-4), and the estimated SHG nucleation rate was approximately 300 times higher in composite-FaSSIF (Figure 5-8). In fact,

nucleation rate of posaconazole in composite-FaSSIF was more comparable to FaSSIF-V1 and FaSSIF-V2 (Figure 5-8), as well as desupersaturation rates to FaSSIF-V1 (Table 5-2). Studies have shown that crystallization inhibitory effects for the different bile salts are not equivalent.^{36,37} Li et al. showed that the different capacities of bile salts to prolong nucleation times was dependent on structural differences among the bile salts and their hydrophobicity.³⁶ Although, composite-FaSSIF was prepared with the purpose of closely mimicking FaHIF, some minor components were omitted. These are glyco- and tauro-ursodeoxycholate bile salts (~1.6 % of the total bile concentration; not soluble at pH 6.5),^{38,215} as well as other non-bile salt components as cholesterol,^{38,205,206} fatty acids and monoacylglycerides.^{38,207} Such differences and their impact on crystallization are definitely an interesting area to further investigate in future studies.

Combined effect of polymer and media on nucleation. Polymers are usually used as crystallization inhibitors in supersaturating formulations to improve the bioavailability of APIs through stabilizing the drug in ASDs and maintaining the supersaturated state to longer times.²²⁶ The addition of HPMC-AS delayed the onset of nucleation for atazanavir and posaconazole (Figures 5-3 and 5-4), and similarly decreased desupersaturation (Table 5-2) and nucleation rates (Figure 5-8) for the later. For posaconazole, these effects were also polymer concentration-dependent. Interestingly, polymer effectiveness was not equivalent for all the testing media, whereby buffers showed the highest-fold increase in induction times in the presence of polymer. This suggests that polymer-solute interactions are maximized in the absence of solubilizing species in the medium. In one situation, the affinity of the polymer to the solute is stronger relative to that of the solvent (buffer system).²²⁷ In another, the affinity of the polymer to the solute is no longer as high, since the solvent now contains other species (bile salts/lecithin) that can potentially interact with the polymer, and/or block the polymer from interacting with the solute. Aside from blank buffers, HPMC-AS effectiveness (50 ug/mL concentration) for posaconazole was much greater in FaSSIF-V1/V2, where induction times were prolonged by ~10-fold, compared to ~4-fold for FaHIF and composite-FaSSIF. For atazanavir, HPMC-AS effectiveness was rather mixed and less consistent, where the fold-increase in induction times for FaSSIF-V1/V2 was slightly higher than FaHIF, albeit lower than composite-FaSSIF. These findings are in good agreement with previous results for the stability of supersaturated solutions in FaHIF and FaSSIF-V1 in the presence of HPMC-AS, reported by Bevillage et al.¹¹⁰ HPMC-AS-mediated area-under-curve (AUC) gain factor for supersaturation profiles was higher for FaSSIF-V1 than FaHIF for etravirine,

loviride and danazol, whereas it was mostly similar for ritonavir and fenofibrate. Perhaps the most significant finding from these media-HPMC-AS experiments is that extending the duration of supersaturation in FaHIF by using a polymer, is possible. For the two model compounds used herein, the onset of nucleation was delayed in FaHIF by using HPMC-AS (Figures 5-4 and 5-5), illustrating that excipients like HPMC-AS could positively impact intraluminal supersaturation *in vivo*. In support of this conjecture, we can compare our *in vitro* results with previous studies of posaconazole in human volunteers. When Noxfil® tablets (marketed posaconazole/HPMC-AS amorphous solid dispersions) were administrated orally in fasted-state, the average duration of supersaturation was 93 min.¹⁴⁶ This *in vivo* result is relatively close to our *in vitro* estimation of the onset of nucleation of posaconazole in FaHIF in the presence of 50 ug/mL of HPMC-AS (drug-to-polymer; ~1-to-3.8), which was ~80 min. To our knowledge, *in vivo* assessments of atazanavir supersaturation are currently unavailable in the literature for comparison with our results.

Crystal growth: Theoretical considerations. Crystal growth is well-known to be affected by the presence of additives.^{228–230} Kubota and Mullin described the crystal growth inhibition of a system in the presence of an impurity, assuming non-equilibrium, using the following relationship:²³¹

$$\frac{V}{V_o} = 1 - \alpha \theta_{eq} \quad (5-5)$$

Where V and V_o are the step velocities in the presence and absence of impurity, respectively. θ_{eq} is the fractional coverage of the surface by the impurity. α is the effectiveness factor of the impurity. In crystal growth kinetics, the step advancement can be hindered by an impurity species adsorbed at kink sites on the surface of a growing crystal.²³⁰ Here, step advancement is pinned at the adsorption sites forming what is referred to as a ‘curved’ step, where the step squeezes out between the adsorption sites. The modified step advancement of a curved step can be then described by equation 5-6:^{230,231}

$$\frac{V_\rho}{V_o} = 1 - \frac{\rho_c}{\rho} \quad (5-6)$$

Where V_ρ is the modified step velocity of the curved step at curvature ρ, and ρ_c is the critical radius of a two-dimensional nucleus (ρ is infinite, otherwise if ρ < ρ_c the step cannot move). The sites available for adsorption are limited and will vary according to the growing crystal surface i.e. the solute, and the nature of the impurity.²³¹ ρ can be linked to the spacing between adsorption sites (L), whereby:

$$2\rho = L \quad (5-7)$$

The effectiveness of the impurity, α , can be attributed to stereochemical effects, i.e. the size, shape, and/or orientation of the impurity molecules relative to the growing crystal surface. Additionally, α can be thermodynamically described by the equation 5-8:²³¹

$$\alpha = \frac{\eta a}{K_B T S L} \quad (5-8)$$

Where η is the edge free energy, a is the area occupied by one crystallizing molecule, K_B is the Boltzmann constant, T is the temperature, S is the supersaturation level, and L is the separation of sites available for impurities.

Effect of different media on crystalline morphology and growth kinetics. From Figures 5-15 and 5-16, it is evident that the morphology of posaconazole crystals grown from different media varies. In buffer-V1, posaconazole crystals show crystalline plates without any observable surface modifications or curved step advancements (Figures 5-15B and 5-15C), since there are no impurities in the system. Alternatively, crystal growth was suppressed (4 to 8-fold depending on the sample) in media containing bile salts acting as impurities (Figure 5-9). A schematic of how additives impact posaconazole crystal habit is proposed in Figure 5-19. Posaconazole crystalline sheets exhibited clear step lines along its surface in FaSSIF-V1, forming what appears to be curved steps with different ρ at the ends of the growing crystal sheet (Figures 5-15D and 5-19B). This can be seen also for composite-FaSSIF (Figures 5-16A and 5-19C) and FaHIF (Figures 5-16D and 5-19D). Interestingly, the curved steps in this sample at the ends of the crystals were relatively distinct from each other, which could suggest a higher ρ or L , or that the pinning mechanisms were stronger. By measuring L from different fields of views, the average values (at $n = 5$) for posaconazole crystals in FaSSIF-V1, composite-FaSSIF and FaHIF were 41, 79, 93 nm, respectively. According to equation 5-6, the closer the distance between adsorbed impurities (L), the slower the crystal growth rate will be. This finding could suggest that the presence of more lecithin in FaSSIF-V1 decreases L and suppresses growth rate even further, although more experiments could be needed to confirm this hypothesis. The presence of polymer suppresses the growth rate even further, as illustrated by the SHG growth rate estimations in Figure 5-9. In the solution state, polymer adsorption on the surface of a solid is generally accepted to be dependent on the affinity/interaction level between the polymer and solid, relative to the polymer and the

medium.²³² This adsorption is irreversible, whereby the polymer can form electrostatic, hydrogen bonding and/or chemical interactions. When both polymer and bile salts/lecithin are present in the system, the situation is more complex since two different types of impurities now exist. In Figure 5-17, posaconazole crystalline plates in buffer-V1 (Figure 5-17A), and to a lesser extent FaSSIF-V1 (Figure 5-17B), exhibit curvature of the crystalline plates. This could be due to unequal adsorption of the polymer on the large faces of the crystal. Unlike crystallized posaconazole without polymer in buffer-V1, posaconazole crystallized in the presence of HPMC-AS displayed evidence of curved step advancement and pinning on the surface (Figure 5-17A). The plate curvature mechanism was not observed in composite-FaSSIF and FaHIF (Figures 5-17C and 5-17D). This could be due to less interaction of posaconazole with HPMC-AS in these media, as suggested by the nucleation results. Schram et al. showed that HPMC-AS reduced growth rates of felodipine though extensive surface poisoning.¹¹² HPMC-AS effectiveness however was reduced when another surfactant (sodium dodecyl sulfate) was added to the system, presumably due to the decrease in interfacial energy, which in turn decreases α in equation 5-8.

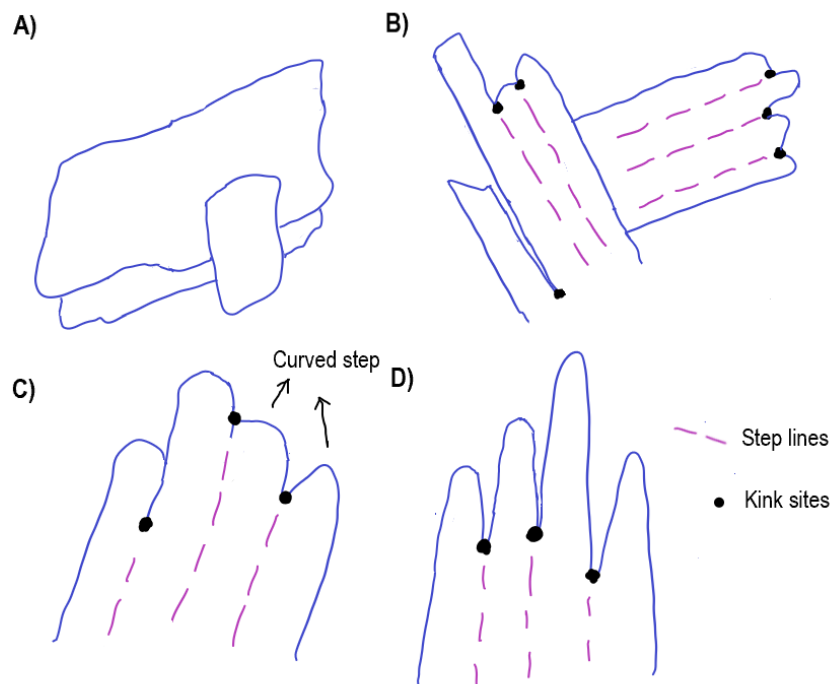


Figure 5-19. A schematic illustrating different growth patterns for posaconazole crystal plates in the different media (adapted from Kubota's illustration).²³⁰ The schematic demonstrates posaconazole crystals in A) Buffer-V1 where impurities were absent, B) FaSSIF-V1, C) composite-FaSSIF and D) FaHIF, where adsorption of impurities (bile salts/lecithin) at kink sites on the surface of a growing crystal resulted in curvature of the step advancement.

It is generally more difficult to describe growth kinetics for needle-shaped crystals, although the Kubota and Mullin model could still apply, and has been used to describe the growth kinetics for paclitaxel crystals with needle morphology.²³³ Assuming a cuboidal shape, the formation of a needle crystal for atazanavir requires that the crystal growth at the ends of the needles is much faster than that at the crystal faces forming the sides of the needle. Consequently, differences in aspect ratio could arise for crystals growing in different conditions. Aspect ratio (AR) is defined as the quotient of the length to width of a crystal. Measurements of length/width of different atazanavir needles were performed and AR values are summarized in Table 5-4. Atazanavir needles in buffer-V1 were highly irregular in size but generally with smaller aspect ratio (larger width and shorter length). For these needles, no particular impurities are present in the media, and growth rate was apparently not suppressed at certain facets relative to others, i.e. atazanavir crystals grow unrestrictively on all ends, albeit preserving their general acicular morphology. Hence, we see more ‘rod-like’ needles with broader width and lower AR. Additionally, atazanavir needles in buffer-V1 exhibited secondary nucleation (Figure 5-12A), where small needles and surface branching can be found on atazanavir needles. Atazanavir needles in simulated and aspirated media had higher AR. In such case, we hypothesize that bile salts suppress crystal growth on the faces of the needle except at the ends, leading to greater anisotropy and a higher AR. At the needle ends, bile salts are not likely to be adsorbed due to the extremely small ρ_c and therefore no restriction on crystal growth would be imposed. In addition, atazanavir needles showed, to some extent, limited secondary nucleation on their surfaces in the presence of bile salts, except in FaHIF. Needles in FaHIF had seemingly smooth surfaces and the presence of secondary nucleation/branching was not observed (Figure 5-12B). Our data do not provide enough explanation of why such effect was unique to needles in FaHIF. A schematic illustrating three different growth morphologies for atazanavir needles in the different media is shown in Figure 5-20. In the presence of HPMC-AS, no major changes were observed on atazanavir needles with respect to AR values in the different media (Figure 5-14), suggesting that the AR differences can be fully attributed to the presence of bile salts/lecithin. However, less secondary nucleation was observed on the samples. Of particular note, needles crystallized from composite-FaSSIF uniquely exhibited dendritic growth patterns, where needle bundles were seemingly originating from one end. This morphology was also observed before for paclitaxel needles in the presence of HPMC-

AS.²³³ It is likely that in this sample, a certain synergy between media components and HPMC-AS existed, as it was also inferred by the induction time results.

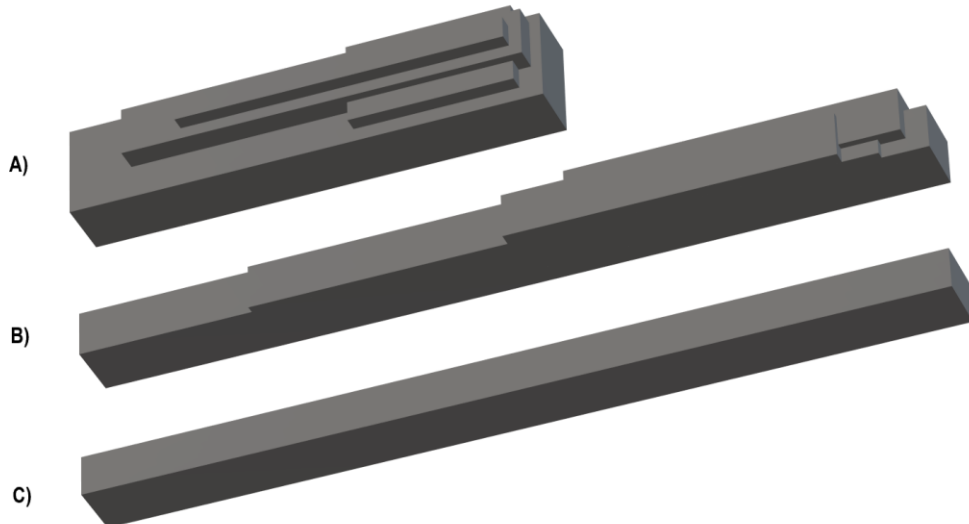


Figure 5-20. A schematic illustrating different growth patterns for atazanavir needle crystals in the different media; A) Buffer-V1 (lower AR with surface nucleation/branching), B) FaSSIF-V1 and composite-FaSSIF (higher AR with surface nucleation/branching) and C) FaHIF (higher AR without surface nucleation/branching).

Table 5-4. Summary of AR values of atazanavir needles in the different media. (n=15).

Medium	Buffer-V1	FaSSIF-V1	Composite-FaSSIF	FaHIF
AR	12.4 ± 7.4	54.2 ± 13.2	82.6 ± 32.3	40.6 ± 14.3

In vivo implications of crystal growth kinetics. In general, the impact of media components on the kinetics of crystal growth and secondary nucleation, has not been widely investigated before. For supersaturating formulations, maintaining supersaturation for a biologically relevant time frame in the GI tract is essential for improved absorption. Since, the onset of crystallization is thermodynamically favored, and hence likely to occur, the effect of media on mitigating the kinetics of desupersaturation is of great significance. If desupersaturation is considerably slowed, resulting in a concentration-time profile with a larger area-under-curve, the supersaturation advantage of a formulation is better retained. In addition, different media compositions can result in varying degrees of ‘residual’ supersaturation once crystallization has commenced. Finally, the size and morphology of the resultant crystals will impact their redissolution properties. Accordingly, the ability of media components, in the absence and presence of polymers, in

retarding supersaturation consumption by impacting crystal growth kinetics necessitates further investigation.

5.7 Conclusions

In order to take advantage of supersaturating formulations, there is a need to understand and predict how the GI fluid composition could affect the phase behavior of supersaturated solutions. In this study, we demonstrated the different impact of simulated and aspirated media on crystallization kinetics of atazanavir and posaconazole supersaturated solutions. Widely-used commercial media, particularly FaSSIF-V1, appeared to overestimate how quickly nucleation commenced for supersaturated solutions of both compounds, relative to the corresponding systems in FaHIF. Supersaturated solutions in FaHIF demonstrated longer induction times and relatively slower crystallization kinetics. Addition of a polymer was found to lead to positive, albeit variable, effects in the different media. From a biopharmaceutical perspective, these findings have significant implications on predicting *in vivo* crystallization outcomes from *in vitro* experiments in simulated media. Therefore, when it comes to supersaturation assessment, it is likely advisable to include the most biorelevant composition and concentration of endogenous surfactants in the *in vitro* testing medium. Finally, evaluation of crystallization kinetics of, structurally- and physicochemically-diverse small molecules, in simulated and aspirated fluids is of general importance in the context of supersaturating formulations.

APPENDIX A. SUPPORTING INFORMATION

Supporting Information for Chapter 3

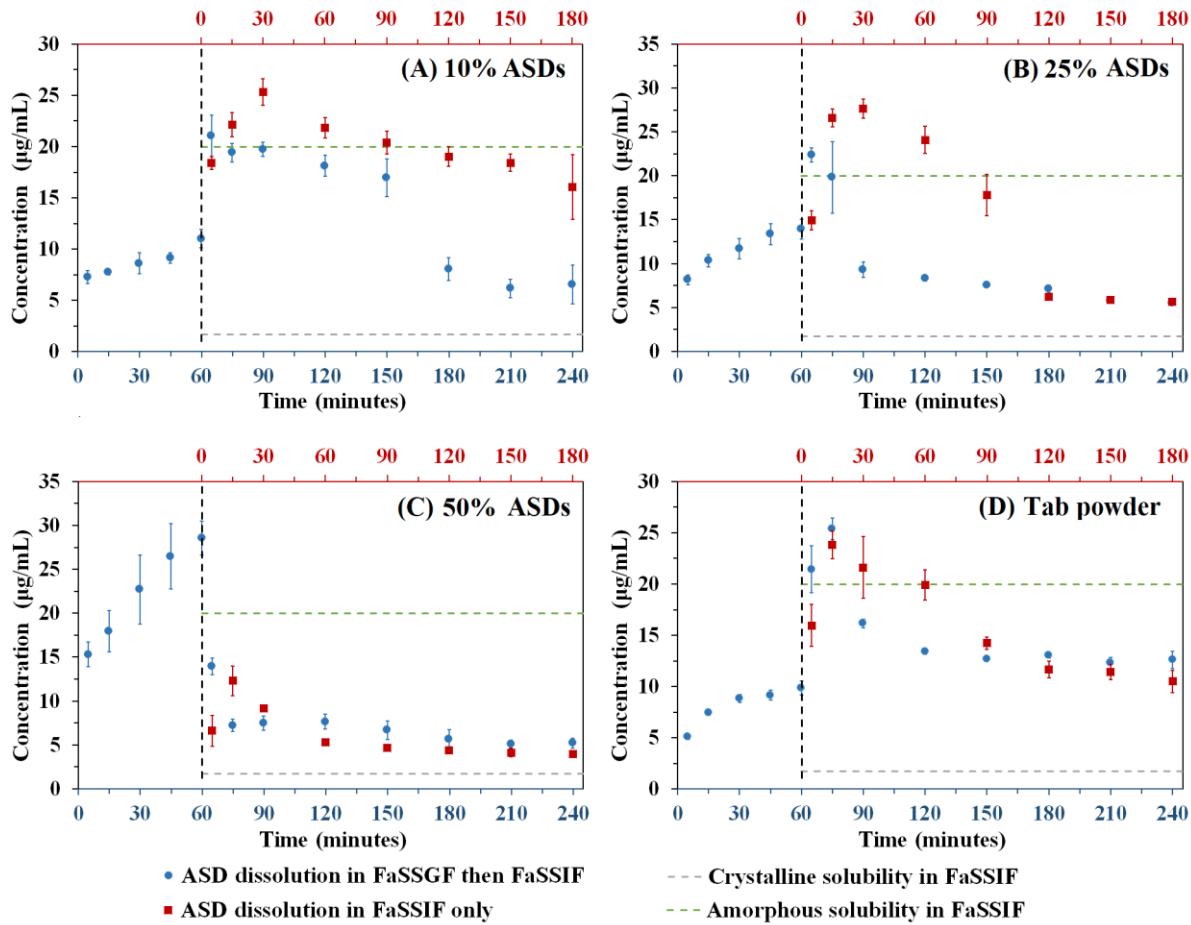


Figure A.1 Posaconazole concentration-time profiles for ASDs formulated at (A) 10 %, (B) 25 %, (C) 50 %, and (D) tablet powder upon dissolution at 37 °C; blue circles indicate posaconazole dissolution in FaSSGF then FaSSIF, whilst red squares indicate posaconazole dissolution in FaSSIF only. An amount of ASD or tablet powder equivalent to 80 µg/mL of posaconazole was added to the acid stage; this decreases to 40 µg/mL in the FaSSIF stage. The dashed horizontal grey and green lines indicate the measured equilibrium solubility and LLPS concentration (amorphous solubility) of posaconazole in FaSSIF at 37 °C respectively (n = 3).

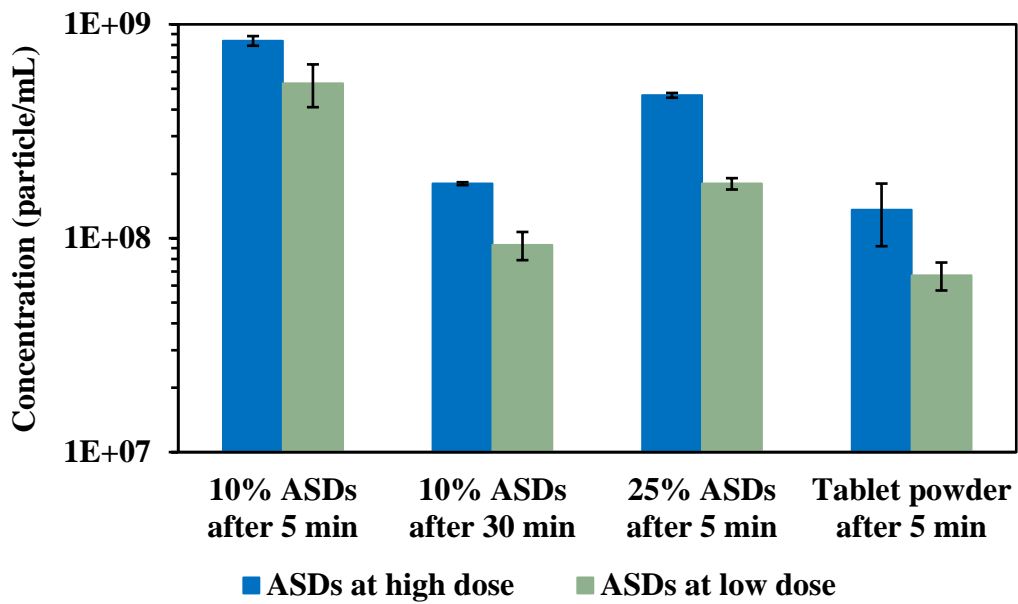


Figure A.2. Posaconazole nanodroplet particle concentration measurements for the 10%, 25%, and tablet powder, at high dose (blue columns) and low dose (green columns), upon dissolution in FaSSIF ($n=3$).

Supporting Information for Chapter 4

Table A.1. Normalized diffusive flux values ($\mu\text{g}/\text{min} \cdot \text{cm}^2$), derived from the slope of mass transport rates of atazanavir and posaconazole. Values were normalized by dividing the slopes by the surface area of the membrane.

Medium	Atazanavir		Posaconazole	
	J_{amp} ($\mu\text{g}/\text{min} \cdot \text{cm}^2$)	J_{eq} ($\mu\text{g}/\text{min} \cdot \text{cm}^2$)	J_{amp} ($\mu\text{g}/\text{min} \cdot \text{cm}^2$)	J_{eq} ($\mu\text{g}/\text{min} \cdot \text{cm}^2$)
Buffer-V1	$1.19 \times 10^{-1} \pm 6.19 \times 10^{-3}$	$2.17 \times 10^{-3} \pm 1.15 \times 10^{-4}$	$2.19 \times 10^{-2} \pm 7.20 \times 10^{-4}$	$5.98 \times 10^{-4} \pm 6.81 \times 10^{-5}$
Buffer-V2	$1.14 \times 10^{-1} \pm 8.72 \times 10^{-3}$	$2.12 \times 10^{-3} \pm 2.91 \times 10^{-4}$	$2.12 \times 10^{-2} \pm 2.65 \times 10^{-3}$	$5.79 \times 10^{-4} \pm 3.70 \times 10^{-5}$
FaSSIF-V1	$1.39 \times 10^{-1} \pm 1.95 \times 10^{-3}$	$2.48 \times 10^{-3} \pm 9.77 \times 10^{-5}$	$2.39 \times 10^{-2} \pm 6.59 \times 10^{-4}$	$6.97 \times 10^{-4} \pm 4.28 \times 10^{-5}$
FaSSIF-V2	$1.32 \times 10^{-1} \pm 7.38 \times 10^{-3}$	$2.44 \times 10^{-3} \pm 1.34 \times 10^{-4}$	$2.28 \times 10^{-2} \pm 4.49 \times 10^{-3}$	$6.10 \times 10^{-4} \pm 1.45 \times 10^{-5}$
Composite-FaSSIF	$1.05 \times 10^{-1} \pm 6.19 \times 10^{-3}$	$2.08 \times 10^{-3} \pm 1.27 \times 10^{-4}$	$1.92 \times 10^{-2} \pm 1.47 \times 10^{-3}$	$6.32 \times 10^{-4} \pm 2.71 \times 10^{-5}$
FaHIF	$1.11 \times 10^{-1} \pm 9.55 \times 10^{-3}$	$2.11 \times 10^{-3} \pm 4.42 \times 10^{-5}$	$1.91 \times 10^{-2} \pm 7.78 \times 10^{-4}$	$6.61 \times 10^{-4} \pm 6.54 \times 10^{-5}$

To calculate the apparent permeability, without accounting for solubilization, ($Papp_{uncorr}$), equation (4-5) was utilized where the normalized flux was divided by the concentration in the donor cell.

Table A.2. Calculated values of $Papp_{uncorr}$ for atazanavir and posaconazole at (J_{amph}/C_{amph}) and (J_{eq}/C_{eq}) in all media.

Medium	Atazanavir		Posaconazole	
	$Papp_{uncorr}$ (cm/min) at J_{amph} and C_{amph}	$Papp_{uncorr}$ (cm/min) at J_{eq} and C_{eq}	$Papp_{uncorr}$ (cm/min) at J_{amph} and C_{amph}	$Papp_{uncorr}$ (cm/min) at J_{eq} and C_{eq}
Buffer-V1	$1.51 \times 10^{-3} \pm 1.09 \times 10^{-4}$	$1.55 \times 10^{-3} \pm 2.36 \times 10^{-4}$	$2.70 \times 10^{-3} \pm 1.11 \times 10^{-4}$	$2.60 \times 10^{-3} \pm 4.50 \times 10^{-4}$
Buffer-V2	$1.39 \times 10^{-3} \pm 1.08 \times 10^{-4}$	$1.41 \times 10^{-3} \pm 3.43 \times 10^{-4}$	$2.59 \times 10^{-3} \pm 3.38 \times 10^{-4}$	$2.63 \times 10^{-3} \pm 2.92 \times 10^{-4}$
FaSSIF-V1	$1.36 \times 10^{-3} \pm 4.44 \times 10^{-5}$	$9.19 \times 10^{-4} \pm 1.41 \times 10^{-4}$	$5.52 \times 10^{-4} \pm 3.30 \times 10^{-5}$	$2.18 \times 10^{-4} \pm 2.44 \times 10^{-5}$
FaSSIF-V2	$1.31 \times 10^{-3} \pm 1.49 \times 10^{-4}$	$9.38 \times 10^{-4} \pm 6.29 \times 10^{-5}$	$1.10 \times 10^{-3} \pm 2.32 \times 10^{-4}$	$3.81 \times 10^{-4} \pm 2.55 \times 10^{-5}$
Composite-FaSSIF	$1.05 \times 10^{-3} \pm 6.59 \times 10^{-5}$	$6.71 \times 10^{-4} \pm 1.36 \times 10^{-4}$	$1.24 \times 10^{-3} \pm 1.10 \times 10^{-4}$	$3.72 \times 10^{-4} \pm 4.66 \times 10^{-5}$
FaHIF	$1.12 \times 10^{-3} \pm 9.91 \times 10^{-5}$	$3.01 \times 10^{-4} \pm 2.66 \times 10^{-5}$	$1.45 \times 10^{-3} \pm 7.35 \times 10^{-5}$	$2.54 \times 10^{-4} \pm 5.50 \times 10^{-5}$

To account for solubilization, a model adapted from Katneni et al., is used (reference 190), where the corrected apparent permeability ($Papp_{corr}$) is deduced from multiplying $Papp_{uncorr}$ by the solubilization factor, as shown in equation A1:

$$Papp_{corr} = Papp_{uncorr} \times \frac{D_{total}}{D_{free}} \quad (\text{A1})$$

Where D_{total} is the total dissolved concentration (amorphous or crystalline solubility) in the medium and D_{free} is the amorphous or crystalline solubility in the corresponding buffer (i.e. without solubilization). For composite-FaSSIF and FaHIF, the corresponding buffer is buffer-V1. For buffer-V1 and buffer-V2, the $\frac{D_{total}}{D_{free}}$ ratio is 1, and thus $Papp_{corr}$ is the same as $Papp_{uncorr}$.

Table A.3. Calculated values of $Papp_{corr}$ for atazanavir and posaconazole at (J_{amph}/C_{amph}) and (J_{eq}/C_{eq}) in all media.

Medium	Atazanavir		Posaconazole	
	$Papp_{corr}$ (cm/min) at J_{amph} and C_{amph}	$Papp_{corr}$ (cm/min) at J_{eq} and C_{eq}	$Papp_{corr}$ (cm/min) at J_{amph} and C_{amph}	$Papp_{corr}$ (cm/min) at J_{eq} and C_{eq}
Buffer-V1	$1.51 \times 10^{-3} \pm 1.09 \times 10^{-4}$	$1.55 \times 10^{-3} \pm 2.36 \times 10^{-4}$	$2.70 \times 10^{-3} \pm 1.11 \times 10^{-4}$	$2.60 \times 10^{-3} \pm 4.50 \times 10^{-4}$
Buffer-V2	$1.39 \times 10^{-3} \pm 1.08 \times 10^{-4}$	$1.41 \times 10^{-3} \pm 3.43 \times 10^{-4}$	$2.59 \times 10^{-3} \pm 3.38 \times 10^{-4}$	$2.63 \times 10^{-3} \pm 2.92 \times 10^{-4}$
FaSSIF-V1	$1.76 \times 10^{-3} \pm 1.18 \times 10^{-4}$	$1.77 \times 10^{-3} \pm 4.55 \times 10^{-4}$	$2.95 \times 10^{-3} \pm 3.47 \times 10^{-4}$	$3.03 \times 10^{-3} \pm 5.94 \times 10^{-4}$
FaSSIF-V2	$1.61 \times 10^{-3} \pm 2.43 \times 10^{-4}$	$1.63 \times 10^{-3} \pm 3.49 \times 10^{-4}$	$2.79 \times 10^{-3} \pm 6.36 \times 10^{-4}$	$2.77 \times 10^{-3} \pm 3.58 \times 10^{-4}$
Composite-FaSSIF	$1.33 \times 10^{-3} \pm 1.18 \times 10^{-4}$	$1.49 \times 10^{-3} \pm 4.68 \times 10^{-4}$	$2.37 \times 10^{-3} \pm 2.43 \times 10^{-4}$	$2.75 \times 10^{-3} \pm 5.93 \times 10^{-4}$
FaHIF	$1.41 \times 10^{-3} \pm 1.46 \times 10^{-4}$	$1.51 \times 10^{-3} \pm 2.84 \times 10^{-4}$	$2.36 \times 10^{-3} \pm 1.51 \times 10^{-4}$	$2.87 \times 10^{-3} \pm 9.12 \times 10^{-4}$

As shown in Table A3, the values of $Papp_{corr}$ for each compound are considerably similar (whether at the J_{amph} or J_{eq}), as it would be expected.

REFERENCES

- (1) Lipinski, C. A. Drug-like Properties and the Causes of Poor Solubility and Poor Permeability. *J. Pharmacol. Toxicol. Methods* **2000**, *44* (1), 235–249.
- (2) Gribbon, P.; Andreas, S. High-Throughput Drug Discovery: What Can We Expect from HTS? *Drug Discov. Today* **2005**, *10* (1), 17–22.
- (3) Hancock, B. C.; Parks, M. What Is the True Solubility Advantage for Amorphous Pharmaceuticals? *Pharm. Res.* **2000**, *17* (4), 397–404.
- (4) Murdande, S. B.; Pikal, M. J.; Shanker, R. M.; Bogner, R. H. Solubility Advantage of Amorphous Pharmaceuticals, Part 3: Is Maximum Solubility Advantage Experimentally Attainable and Sustainable? *J. Pharm. Sci.* **2011**, *100* (10), 4349–4356.
- (5) Brouwers, J.; Brewster, M. E.; Augustijns, P. Supersaturating Drug Delivery Systems: The Answer to Solubility-Limited Oral Bioavailability? *J. Pharm. Sci.* **2009**, *98* (8), 2549–2572.
- (6) Pellett, M. A.; Castellano, S.; Hadgraft, J.; Davis, A. F. The Penetration of Supersaturated Solutions of Piroxicam across Silicone Membranes and Human Skin in Vitro. *J. Control. Release* **1997**, *46* (3), 205–214.
- (7) Hou, H.; Siegel, R. A. Enhanced Permeation of Diazepam through Artificial Membranes from Supersaturated Solutions. *J. Pharm. Sci.* **2006**, *95* (4), 896–905.
- (8) Miller, J. M.; Beig, A.; Carr, R. A.; Spence, J. K.; Dahan, A. A Win-Win Solution in Oral Delivery of Lipophilic Drugs: Supersaturation via Amorphous Solid Dispersions Increases Apparent Solubility without Sacrifice of Intestinal Membrane Permeability. *Mol. Pharm.* **2012**, *9* (7), 2009–2016.
- (9) Veesler, S.; Lafferrère, L.; Garcia, E.; Hoff, C. Phase Transitions in Supersaturated Drug Solution. *Org. Process Res. Dev.* **2003**, *7* (6), 983–989.
- (10) Alonso, D. E.; Zhang, G. G. Z.; Zhou, D.; Gao, Y.; Taylor, L. S. Understanding the Behavior of Amorphous Pharmaceutical Systems during Dissolution. *Pharm. Res.* **2010**, *27* (4), 608–618.
- (11) Jackson, M. J.; Kestur, U. S.; Hussain, M. A.; Taylor, L. S. Dissolution of Danazol Amorphous Solid Dispersions: Supersaturation and Phase Behavior as a Function of Drug Loading and Polymer Type. *Mol. Pharm.* **2016**, *13* (1), 223–231.
- (12) Warren, D. B.; Benameur, H.; Porter, C. J. H.; Colin, W.; Warren, D. B.; Benameur, H.; Porter, C. J. H.; Pouton, C. W. Using Polymeric Precipitation Inhibitors to Improve the Absorption of Poorly Water-Soluble Drugs: A Mechanistic Basis for Utility. *J. Drug Target.* **2010**, *18* (10), 704–731.

- (13) Hancock, B. C.; Zografi, G. The Relationship Between the Glass Transition Temperature and the Water Content of Amorphous Pharmaceutical Solids. *Pharm. Res.* **1994**, *11* (4), 471–477.
- (14) Aso, Y.; Yoshioka, S. Molecular Mobility of Nifedipine – PVP and Phenobarbital – PVP Solid Dispersions as Measured by C-NMR Spin-Lattice Relaxation Time. *J. Pharm. Sci.* **2006**, *95* (2), 318–325.
- (15) Yuan, X.; Xiang, T.; Anderson, B. D.; Munson, E. J. Hydrogen Bonding Interactions in Amorphous Indomethacin and Its Amorphous Solid Dispersions with Poly(Vinylpyrrolidone) and Poly(Vinylpyrrolidone-Co-Vinyl Acetate) Studied Using C-13 Solid-State NMR. *Mol. Pharm.* **2015**, *12* (12), 4518–4528.
- (16) Dressman, J. B.; Reppas, C. In Vitro-in Vivo Correlations for Lipophilic, Poorly Water-Soluble Drugs. *Eur. J. Pharm. Sci.* **2000**, *11*, S73–S80.
- (17) Galia, E.; Nicolaides, E.; Hörter, D.; Löbenberg, R.; Reppas, C.; Dressman, J. B. Evaluation of Various Dissolution Media for Predicting In Vivo Performance of Class I and II Drugs. *Pharm. Res.* **1998**, *15* (5), 698–705.
- (18) Nicolaides, E.; Symillides, M.; Dressman, J. B.; Reppas, C. Biorelevant Dissolution Testing to Predict the Plasma Profile of Lipophilic Drugs after Oral Administration. *Pharm. Res.* **2001**, *18* (3), 380–388.
- (19) Jantratid, E.; Janssen, N.; Reppas, C.; Dressman, J. B. Dissolution Media Simulating Conditions in the Proximal Human Gastrointestinal Tract: An Update. *Pharm. Res.* **2008**, *25* (7), 1663–1676.
- (20) Klein, S. The Use of Biorelevant Dissolution Media to Forecast the In Vivo Performance of a Drug. *AAPS J.* **2010**, *12* (3), 397–406.
- (21) Slade, J. M.; Carlson, J. J.; Forbes, S. C.; Stein, N. J.; Moll, M. R.; Wiseman, R. W.; Meyer, R. A. The Postprandial Increase in Blood Triglycerides Has No Direct Effect on the Brain BOLD Response. *Hum. Brain Mapp.* **2009**, *30* (3), 749–756.
- (22) Sachdeva, P.; Kantor, S.; Knight, L. C.; Maurer, A. H.; Fisher, R. S.; Parkman, H. P. Use of a High Caloric Liquid Meal as an Alternative to a Solid Meal for Gastric Emptying Scintigraphy. *Dig. Dis. Sci.* **2013**, *58* (7), 2001–2006.
- (23) Franek, F.; Holm, P.; Larsen, F.; Steffansen, B. Interaction between Fed Gastric Media (Ensure Plus) and Different Hypromellose Based Caffeine Controlled Release Tablets: Comparison and Mechanistic Study of Caffeine Release in Fed and Fasted Media versus Water Using the USP Dissolution Apparatus 3. *Int. J. Pharm.* **2014**, *461* (1–2), 419–426.
- (24) Klein, S.; Butler, J.; Hempenstall, J. M.; Reppas, C.; Dressman, J. B. Media to Simulate the Postprandial Stomach I. Matching the Physicochemical Characteristics of Standard Breakfasts. *J. Pharm. Pharmacol.* **2004**, *56* (5), 605–610.

- (25) Hens, B.; Corsetti, M.; Brouwers, J.; Augustijns, P. Gastrointestinal and Systemic Monitoring of Posaconazole in Humans After Fasted and Fed State Administration of a Solid Dispersion. *J. Pharm. Sci.* **2016**, *105* (9), 2904–2912.
- (26) Abbott Nutrition. Ensure Plus® Detailed Ingredients.
- (27) Williams, H. D.; Sassene, P.; Kleberg, K.; Calderone, M.; Igonin, A.; Jule, E.; Vertommen, J.; Blundell, R.; Benameur, H.; Müllertz, A.; Pouton, C. W.; Porter, C. J. H. Toward the Establishment of Standardized in Vitro Tests for Lipid-Based Formulations, Part 3: Understanding Supersaturation versus Precipitation Potential during the in Vitro Digestion of Type I, II, IIIA, IIIB and IV Lipid-Based Formulations. *Pharm. Res.* **2013**, *30* (12), 3059–3076.
- (28) Sassene, P. J.; Knopp, M. M.; Hesselkilde, J. Z.; Koradia, V.; Larsen, A.; Rades, T.; Müllertz, A. Precipitation of a Poorly Soluble Model Drug during in Vitro Lipolysis: Characterization and Dissolution of the Precipitate. *J. Pharm. Sci.* **2010**, *99* (12), 4982–4991.
- (29) Shono, Y.; Jantratid, E.; Dressman, J. B. Precipitation in the Small Intestine May Play a More Important Role in the in Vivo Performance of Poorly Soluble Weak Bases in the Fasted State: Case Example Nelfinavir. *Eur. J. Pharm. Biopharm.* **2011**, *79* (2), 349–356.
- (30) Iqbal, Z.; Babar, A.; Ashraf, M. Controlled-Release Naproxen Using Micronized Ethyl Cellulose by Wet-Granulation and Solid-Dispersion Method. *Drug Dev. Ind. Pharm.* **2002**, *28* (2), 129–134.
- (31) Huang, J.; Wigent, R. J.; Schwartz, J. B. Nifedipine Molecular Dispersion in Microparticles of Ammonio Methacrylate Copolymer and Ethylcellulose Binary Blends for Controlled Drug Delivery : Effect of Matrix Composition. *Drug Dev. Ind. Pharm.* **2006**, *32* (10), 1185–1197.
- (32) Desai, J.; Alexander, K.; Riga, A. Characterization of Polymeric Dispersions of Dimenhydrinate in Ethyl Cellulose for Controlled Release. *Int. J. Pharm.* **2006**, *308*, 115–123.
- (33) Maulvi, F. A.; Lakdawala, D. H.; Shaikh, A. A.; Desai, A. R.; Choksi, H. H.; Vaidya, R. J.; Ranch, K. M.; Koli, A. R.; Vyas, B. A.; Shah, D. O. In Vitro and in Vivo Evaluation of Novel Implantation Technology in Hydrogel Contact Lenses for Controlled Drug Delivery. *J. Control. Release* **2016**, *226*, 47–56.
- (34) Sun, D. D.; Lee, P. I. Probing the Mechanisms of Drug Release from Amorphous Solid Dispersions in Medium-Soluble and Medium-Insoluble Carriers. *J. Control. Release* **2015**, *211*, 85–93.
- (35) Chen, J.; Mosquera-Giraldo, L. I.; Ormes, J. D.; Higgins, J. D.; Taylor, L. S. Bile Salts as Crystallization Inhibitors of Supersaturated Solutions of Poorly Water-Soluble Compounds. *Cryst. Growth Des.* **2015**, *15* (6), 2593–2597.

- (36) Li, N.; Mosquera-Giraldo, L. I.; Borca, C. H.; Ormes, J. D.; Lowinger, M.; Higgins, J. D.; Slipchenko, L. V.; Taylor, L. S. A Comparison of the Crystallization Inhibition Properties of Bile Salts. *Cryst. Growth Des.* **2016**, *16* (12), 7286–7300.
- (37) Lu, J.; Ormes, J. D.; Lowinger, M.; Mann, A. K. P.; Xu, W.; Litster, J. D.; Taylor, L. S. Maintaining Supersaturation of Active Pharmaceutical Ingredient Solutions with Biologically Relevant Bile Salts. *Cryst. Growth Des.* **2017**, *17* (5), 2782–2791.
- (38) Riethorst, D.; Mols, R.; Duchateau, G.; Tack, J.; Brouwers, J.; Augustijns, P. Characterization of Human Duodenal Fluids in Fasted and Fed State Conditions. *J. Pharm. Sci.* **2016**, *105* (2), 673–681.
- (39) Carey, M. C.; Small, D. M. Micelle Formation by Bile Salts: Physical-Chemical and Thermodynamic Considerations. *JAMA Intern. Med.* **1972**, *130* (4), 506–527.
- (40) Roda, a; Hofmann, A.; Mysels, K. The Influence of Bile-Salt Structure on Self Association in Aqueous Solutions. *J. Biol. Chem.* **1983**, *258* (10), 6362–6370.
- (41) Hofmann, A. F.; Mysels, K. J. Bile Salts as Biological Surfactants. *Colloids and Surfaces* **1987**, *30* (1), 145–173.
- (42) Rodas, A.; Hofmann, A. F.; Mysels, K. J. The Influence of Bile Salt Structure on Self-Association in Aqueous Solutions. *J. Biol. Chem.* **1983**, *258* (10), 6362–6370.
- (43) Mazer, N. A.; Benedek, G. B.; Carey, M. C. Quasielastic Light-Scattering Studies of Aqueous Biliary Lipid Systems. Mixed Micelle Formationin Bile Salt-Lecithin Solutions. *Biochemistry* **1980**, *19* (4), 601–615.
- (44) Claffey, W. J.; Holzbach, R. T. Dimorphism in Bile Salt/Lecithin Mixed Micelles. *Biochemistry* **1981**, *20*, 415–418.
- (45) Raina, S. A.; Zhang, G. G. Z.; Alonso, D. E.; Wu, J.; Zhu, D.; Catron, N. D.; Gao, Y.; Taylor, L. S. Impact of Solubilizing Additives on Supersaturation and Membrane Transport of Drugs. *Pharm. Res.* **2015**, *32* (10), 3350–3364.
- (46) Indulkar, A. S.; Gao, Y.; Raina, S. A.; Zhang, G. G. Z.; Taylor, L. S. Crystallization from Supersaturated Solutions: Role of Lecithin and Composite Simulated Intestinal Fluid. *Pharm. Res.* **2018**, *35* (158).
- (47) Chen, J.; Ormes, J. D.; Higgins, J. D.; Taylor, L. S. Impact of Surfactants on the Crystallization of Aqueous Suspensions of Celecoxib Amorphous Solid Dispersion Spray Dried Particles. *Mol. Pharm.* **2015**, *12* (2), 533–541.
- (48) Mersmann, A. *Crystallization Technology Handbook: 1st Edition*; Taylor & Francis, 2001.
- (49) Mullin, J. W. *Crystallization: 4th Edition*; 2001.
- (50) Brittain, H. G. *Polymorphism in Pharmaceutical Solids: 2nd Edition*; 2009; Vol. 192.

- (51) Byrn, S. R.; Pfeiffer, R. R.; Stowell, J. G. *Solid-State Chemistry of Drugs: 2nd Edition*; 1999.
- (52) Yu, L. Amorphous Pharmaceutical Solids: Preparation, Characterization and Stabilization. *Adv. Drug Deliv. Rev.* **2001**, *48* (1), 27–42.
- (53) Corrigan, O. I. Mechanisms of Dissolution of Fast Release Solid Dispersions. *Drug Dev. Ind. Pharm.* **1985**, *11* (2–3), 697–724.
- (54) Murdande, S. B.; Pikal, M. J.; Shanker, R. M.; Bogner, R. H. Solubility Advantage of Amorphous Pharmaceuticals: I. a Thermodynamic Analysis. *J. Pharm. Sci.* **2010**, *99* (3), 1254–1264.
- (55) Williams, H. D.; Trevaskis, N. L.; Charman, S. A.; Shanker, R. M.; Charman, W. N. Strategies to Address Low Drug Solubility in Discovery and Development. *Pharmacol. Rev.* **2013**, *65* (1), 315–499.
- (56) Hancock, B. C.; Zografi, G. Characteristics and Significance of the Amorphous State in Pharmaceutical Systems. *J. Pharm. Sci.* **1997**, *86* (1), 1–12.
- (57) Zarzycki, J. Glasses and the Vitreous State. *Cambridge Univ. Press* **1991**.
- (58) Angell, C. A. Structural Instability and Relaxation in Liquid and Glassy Phases near the Fragile Liquid Limit. *J. Non. Cryst. Solids* **1988**, *102* (1–3), 205–221.
- (59) Ediger, M. D.; Angell, C. A.; Nagel, S. R. Supercooled Liquids and Glasses. *J. Phys. Chem.* **1996**, *100* (31), 13200–13212.
- (60) Debenedetti, P. G.; Stillinger, F. H. Supercooled Liquids and the Glass Transition. *Nature* **2001**, *410* (6825), 259–267.
- (61) Sandler, S. I. *Chemical, Biochemical, and Engineering Thermodynamics: 5th Edition*; 2017.
- (62) Jain, N.; Yalkowsky, S. H. Estimation of the Aqueous Solubility I: Application to Organic Nonelectrolytes. *J. Pharm. Sci.* **2001**, *90* (2), 234–252.
- (63) Hoffman, J. D. Thermodynamic Driving Force in Nucleation and Growth Processes. *J. Chem. Phys.* **1958**, *29* (5), 1192–1193.
- (64) Bogner, R. H.; Murdande, S. B.; Pikal, M. J.; Shanker, R. M. Solubility Advantage of Amorphous Pharmaceuticals: II. Application of Quantitative Thermodynamic Relationships for Prediction of Solubility Enhancement in Structurally Diverse Insoluble Pharmaceuticals. *Pharm. Res.* **2010**, *27* (12), 2704–2714.
- (65) Mullin, J. W. *Crystallization: 4th Edition*; Elsevier Butterworth-Heinemann, 2001.
- (66) Mullin, J. W.; Söhnel, O. Expressions of Supersaturation in Crystallization Studies. *Chem. Eng. Sci.* **1977**, *32* (7), 683–686.

- (67) Erdemir, D.; Lee, A. Y.; Myerson, A. S. Nucleation of Crystals from Solution: Classical and Two-Step Models. *Acc. Chem. Res.* **2009**, *42* (5), 621–629.
- (68) Mayers, B.; Gates, B.; Yin, Y.; Xia, Y. Large-Scale Synthesis of Monodisperse Nanorods of Se/Te Alloys through a Homogeneous Nucleation and Solution Growth Process. *Adv. Mater.* **2001**, *13* (18), 1380–1384.
- (69) Chadwick, K.; Myerson, A.; Trout, B. Polymorphic Control by Heterogeneous Nucleation - A New Method for Selecting Crystalline Substrates. *CrystEngComm* **2011**, *13* (22), 6625.
- (70) Kashchiev, D.; Rosmalen, G. M. Van. Review: Nucleation in Solutions Revisited. *Cryst. Res. Technol.* **2003**, *38* (7–8), 555–574.
- (71) Kashchiev, D. *Nucleation: Basic Theory with Applications*; Butterworth Heinemann, 2000.
- (72) Vekilov, P. G. Nucleation. *Cryst. Growth Des.* **2010**, *10* (12), 5007–5019.
- (73) Brick, M. C.; Palmer, H. J.; Whitesides, T. H. Formation of Colloidal Dispersions of Organic Materials in Aqueous Media by Solvent Shifting. *Langmuir* **2003**, *19* (1), 6367–6380.
- (74) Ilevbare, G. a.; Taylor, L. S. Liquid–Liquid Phase Separation in Highly Supersaturated Aqueous Solutions of Poorly Water-Soluble Drugs: Implications for Solubility Enhancing Formulations. *Cryst. Growth Des.* **2013**, *13* (4), 1497–1509.
- (75) Raina, S. A.; Zhang, G. G. Z.; Alonzo, D. E.; Wu, J.; Zhu, D.; Catron, N. D.; Gao, Y. I.; Taylor, L. S. Enhancements and Limits in Drug Membrane Transport Using Supersaturated Solutions of Poorly Water Soluble Drugs. *J. Pharm. Sci.* **2014**, *103* (9), 2736–2748.
- (76) Hate, S. S.; Reutzel-Edens, S. M.; Taylor, L. S. Insight into Amorphous Solid Dispersion Performance by Coupled Dissolution and Membrane Mass Transfer Measurements. *Mol. Pharm.* **2019**, *16* (1), 448–461.
- (77) Moribe, K.; Pongpeerapat, A.; Tozuka, Y.; Yamamoto, K. Drug Nanoparticle Formation from Drug/HPMC/SDS Ternary Ground Mixtures. *Pharmazie* **2006**, *61* (2), 97–101.
- (78) Douroumis, D.; Fahr, A. Stable Carbamazepine Colloidal Systems Using the Cosolvent Technique. *Eur. J. Pharm. Sci.* **2007**, *30* (5), 367–374.
- (79) Ilevbare, G. A.; Liu, H.; Pereira, J.; Edgar, K. J.; Taylor, L. S. Influence of Additives on the Properties of Nanodroplets Formed in Highly Supersaturated Aqueous Solutions of Ritonavir. *Mol. Pharm.* **2013**, *10* (9), 3392–3403.
- (80) Watanabe, T.; Hasegawa, S.; Wakiyama, N.; Kusai, A.; Senna, M. Prediction of Apparent Equilibrium Solubility of Indomethacin Compounded with Silica by ¹³C Solid State NMR. *Int. J. Pharm.* **2002**, *248* (1–2), 123–129.

- (81) Xie, T.; Taylor, L. S. Dissolution Performance of High Drug Loading Celecoxib Amorphous Solid Dispersions Formulated with Polymer Combinations. *Pharm. Res.* **2016**, *33* (3), 739–750.
- (82) Guzmán, H. R.; Tawa, M.; Zhang, Z.; Ratanabanangkoon, P.; Shaw, P.; Gardner, C. R.; Chen, H.; Moreau, J. P.; Almarsson, Ö.; Remenar, J. F. Combined Use of Crystalline Salt Forms and Precipitation Inhibitors to Improve Oral Absorption of Celecoxib from Solid Oral Formulations. *J. Pharm. Sci.* **2007**, *96* (10), 2686–2702.
- (83) Williams, H. D.; Trevaskis, N. L.; Charman, S. A.; Shanker, R. M.; Charman, W. N.; Pouton, C. W.; Porter, C. J. H. Strategies to Address Low Drug Solubility in Discovery and Development. *Pharmacol. Rev.* **2013**, *65* (1), 315–499.
- (84) Loftsson, T.; Brewster, M. E. Pharmaceutical Applications of Cyclodextrins: Basic Science and Product Development. *J. Pharm. Pharmacol.* **2010**, *62* (11), 1607–1621.
- (85) Fahr, A.; Liu, X. Drug Delivery Strategies for Poorly Water-Soluble Drugs. *Expert Opin. Drug Deliv.* **2007**, *4* (4), 403–416.
- (86) Augustijns, P.; Wuyts, B.; Hens, B.; Annaert, P.; Butler, J.; Brouwers, J. A Review of Drug Solubility in Human Intestinal Fluids: Implications for the Prediction of Oral Absorption. *Eur. J. Pharm. Sci.* **2014**, *57* (1), 322–332.
- (87) Dressman, J. B.; Reppas, C. In Vitro-in Vivo Correlations for Lipophilic, Poorly Water-Soluble Drugs. *Eur. J. Pharm. Sci.* **2000**, *11* (Suppl. 2), S73–S80.
- (88) Nicolaides, E.; Galia, E.; Efthymiopoulos, C.; Dressman, J. B.; Reppas, C. Forecasting the In Vivo Performance of Four Low Solubility Drugs from Their In Vitro Dissolution Data. *Pharm. Res.* **1999**, *16* (12), 1876–1882.
- (89) Dressman, J. B.; Vertzoni, M.; Goumas, K.; Reppas, C. Estimating Drug Solubility in the Gastrointestinal Tract. *Adv. Drug Deliv. Rev.* **2007**, *59* (7), 591–602.
- (90) Taupitz, T.; Dressman, J. B.; Klein, S. New Formulation Approaches to Improve Solubility and Drug Release from Fixed Dose Combinations: Case Examples Pioglitazone/Glimepiride and Ezetimibe/Simvastatin. *Eur. J. Pharm. Biopharm.* **2013**, *84* (1), 208–218.
- (91) Foye, W. O.; Lemke, T. L.; Williams, D. A. *Foye's Principles of Medicinal Chemistry*, 7th ed.; Lippincott Williams & Wilkins: Philadelphia, 2012.
- (92) Diakidou, A.; Vertzonia, M.; Dressman, J.; Reppas, C. Estimation of Intragastric Drug Solubility in the Fed State: Comparison of Various Media with Data in Aspirates. *Biopharm. Drug Dispos.* **2009**, *30* (6), 318–325.
- (93) Kalantzi, L.; Goumas, K.; Kalioras, V.; Abrahamsson, B.; Dressman, J. B.; Reppas, C. Characterization of the Human Upper Gastrointestinal Contents under Conditions Simulating Bioavailability/Bioequivalence Studies. *Pharm. Res.* **2006**, *23* (1), 165–176.

- (94) Wanapun, D.; Kestur, U. S.; Kissick, D. J.; Simpson, G. J.; Taylor, L. S. Selective Detection and Quantitation of Organic Molecule Crystallization by Second Harmonic Generation Microscopy. *Anal. Chem.* **2010**, 82 (13), 5425–5432.
- (95) Kissick, D. J.; Wanapun, D.; Simpson, G. J. Second-Order Nonlinear Optical Imaging of Chiral Crystals. *Annu. Rev. Anal. Chem.* **2011**, 4 (1), 419–437.
- (96) Kestur, U. S.; Wanapun, D.; Toth, S. J.; Wegiel, L. A.; Simpson, G. J.; Taylor, L. S. Nonlinear Optical Imaging for Sensitive Detection of Crystals in Bulk Amorphous Powders. *J. Pharm. Sci.* **2012**, 101 (11), 4201–4213.
- (97) Schmitt, P. D.; Trasi, N. S.; Taylor, L. S.; Simpson, G. J. Finding the Needle in the Haystack: Characterization of Trace Crystallinity in a Commercial Formulation of Paclitaxel Protein-Bound Particles by Raman Spectroscopy Enabled by Second Harmonic Generation Microscopy. *Mol. Pharm.* **2015**, 12 (7), 2378–2383.
- (98) Bellur Atici, E.; Karlıla, B. Identification, Synthesis and Characterization of Process Related Desfluoro Impurity of Ezetimibe and HPLC Method Validations. *J. Pharm. Anal.* **2015**, 5 (6), 356–370.
- (99) Baťová, J.; Imramovský, A.; Hájíček, J.; Hejtmánková, L.; Hanusek, J. Kinetics and Mechanism of the Base-Catalyzed Rearrangement and Hydrolysis of Ezetimibe. *J. Pharm. Sci.* **2014**, 103 (8), 2240–2247.
- (100) Dixit, R. P.; Barhate, C. R.; Nagarsenker, M. S. Stability-Indicating HPTLC Method for Simultaneous Determination of Ezetimibe and Simvastatin. *Chromatographia* **2008**, 67 (1), 101–107.
- (101) Diakidou, A.; Vertzoni, M.; Dressman, J.; Reppas, C. Estimation of Intragastric Drug Solubility in the Fed State: Comparison of Various Media with Data in Aspirates. *Biopharm. Drug Dispos.* **2009**, 30 (6), 318–325.
- (102) Jackson, M. J.; Toth, S. J.; Kestur, U. S.; Huang, J.; Qian, F.; Hussain, M. A.; Simpson, G. J.; Taylor, L. S. Impact of Polymers on the Precipitation Behavior of Highly Supersaturated Aqueous Danazol Solutions. *Mol. Pharm.* **2014**, 11 (9), 3027–3038.
- (103) Clarysse, S.; Psachoulias, D.; Brouwers, J.; Tack, J.; Annaert, P.; Duchateau, G.; Reppas, C.; Augustijns, P. Postprandial Changes in Solubilizing Capacity of Human Intestinal Fluids for BCS Class II Drugs. *Pharm. Res.* **2009**, 26 (6), 1456–1466.
- (104) Raina, S. A.; Zhang, G. G. Z.; Alonzo, D. E.; Wu, J.; Zhu, D.; Catron, N. D.; Gao, Y.; Taylor, L. S. Enhancements and Limits in Drug Membrane Transport Using Supersaturated Solutions of Poorly Water Soluble Drugs. *J. Pharm. Sci.* **2014**, 103 (9), 2736–2748.
- (105) Van Eerdenbrugh, B.; Alonzo, D. E.; Taylor, L. S. Influence of Particle Size on the Ultraviolet Spectrum of Particulate-Containing Solutions: Implications for in-Situ Concentration Monitoring Using UV/Vis Fiber-Optic Probes. *Pharm. Res.* **2011**, 28 (7), 1643–1652.

- (106) Wang, D.; Ji, R.; Albrecht, A.; Schaaf, P. Ordered Arrays of Nanoporous Gold Nanoparticles. *Beilstein J. Nanotechnol.* **2012**, *3* (1), 651–657.
- (107) Lu, J.; Ormes, J. D.; Lowinger, M.; Xu, W.; Mitra, A.; Mann, A. K. P.; Litster, J. D.; Taylor, L. S. Impact of Endogenous Bile Salts on the Thermodynamics of Supersaturated Active Pharmaceutical Ingredient Solutions. *Cryst. Growth Des.* **2017**, *17* (3), 1264–1275.
- (108) Shin-Etsu. Shin-Etsu AQOAT® (Hypromellose Acetate Succinate) <http://www.metolose.jp/en/pharmaceutical/aqoat.html> (accessed Sep 6, 2019).
- (109) Friesen, D. T.; Shanker, R.; Crew, M.; Smithey, D. T.; Curatolo, W. J.; Nightingale, J. A. S. Hydroxypropyl Methylcellulose Acetate Succinate-Based Spray-Dried Dispersions: An Overview. *Mol. Pharm.* **2008**, *5* (6), 1003–1019.
- (110) Bevernage, J.; Forier, T.; Brouwers, J.; Tack, J.; Annaert, P.; Augustijns, P. Excipient-Mediated Supersaturation Stabilization in Human Intestinal Fluids. *Mol. Pharm.* **2011**, *8* (2), 564–570.
- (111) Mosquera-Giraldo, L. I.; Borca, C. H.; Meng, X.; Edgar, K. J.; Slipchenko, L. V.; Taylor, L. S. Mechanistic Design of Chemically Diverse Polymers with Applications in Oral Drug Delivery. *Biomacromolecules* **2016**, *17* (11), 3659–3671.
- (112) Schram, C. J.; Beaudoin, S. P.; Taylor, L. S. Polymer Inhibition of Crystal Growth by Surface Poisoning. *Cryst. Growth Des.* **2016**, *16* (4), 2094–2103.
- (113) Macheras, P. E.; Koupparis, M. a; Antimisiaris, S. G. Effect of Temperature and Fat Content on the Solubility of Hydrochlorothiazide and Chlorothiazide in Milk. *J. Pharm. Sci.* **1989**, *78* (11), 933–936.
- (114) Anby, M. U.; Williams, H. D.; McIntosh, M.; Benameur, H.; Edwards, G. A.; Pouton, C. W.; Porter, C. J. H. Lipid Digestion as a Trigger for Supersaturation: Evaluation of the Impact of Supersaturation Stabilization on the in Vitro and in Vivo Performance of Self-Emulsifying Drug Delivery Systems. *Mol. Pharm.* **2012**, *9* (7), 2063–2079.
- (115) Williams, H. D.; Trevaskis, N. L.; Yeap, Y. Y.; Anby, M. U.; Pouton, C. W.; Porter, C. J. H. Lipid-Based Formulations and Drug Supersaturation: Harnessing the Unique Benefits of the Lipid Digestion/Absorption Pathway. *Pharm. Res.* **2013**, *30* (12), 2976–2992.
- (116) Crum, M. F.; Trevaskis, N. L.; Williams, H. D.; Pouton, C. W.; Porter, C. J. H. A New in Vitro Lipid Digestion - In Vivo Absorption Model to Evaluate the Mechanisms of Drug Absorption from Lipid-Based Formulations. *Pharm. Res.* **2016**, *33* (4), 970–982.
- (117) Williams, H. D.; Nott, K. P.; Barrett, D. A.; Ward, R.; Hardy, I. J.; Melia, C. D. Drug Release from HPMC Matrices in Milk and Fat-Rich Emulsions. *J. Pharm. Sci.* **2011**, *100* (11), 4823–4835.

- (118) Pouton, C. W. Lipid Formulations for Oral Administration of Drugs: Non-Emulsifying, Self-Emulsifying and “self-Microemulsifying” Drug Delivery Systems. *Eur. J. Pharm. Sci.* **2000**, *11 Suppl 2*, S93–S98.
- (119) Pouton, C. W. Formulation of Poorly Water-Soluble Drugs for Oral Administration: Physicochemical and Physiological Issues and the Lipid Formulation Classification System. *Eur. J. Pharm. Sci.* **2006**, *29* (3–4), 278–287.
- (120) Porter, C. J. H.; Trevaskis, N. L.; Charman, W. N. Lipids and Lipid-Based Formulations : Optimizing the Oral Delivery of Lipophilic Drugs. *Nat. Rev.* **2007**, *6* (3), 231–248.
- (121) Lennernäs, H.; Abrahamsson, B. The Use of Biopharmaceutic Classification of Drugs in Drug Discovery and Development: Current Status and Future Extension. *J. Pharm. Pharmacol.* **2005**, *57* (3), 273–285.
- (122) Amidon, G. L.; Lennernas, H.; Shah, V. P.; Crison, J. R. A Theoretical Basis for a Biopharmaceutic Drug Classification: The Correlation of in Vitro Drug Product Dissolution and in Vivo Bioavailability. *Pharm. Res.* **1995**, *12* (3), 413–420.
- (123) Lipinski, C. A.; Lombardo, F.; Dominy, B. W.; Feeney, P. J. Experimental and Computational Approaches to Estimate Solubility and Permeability in Drug Discovery and Development Settings. *Adv. Drug Deliv. Rev.* **2001**, *46* (1–3), 3–26.
- (124) Stella, V. J.; Nti-addae, K. W. Prodrug Strategies to Overcome Poor Water Solubility. *Adv. Drug Deliv. Rev.* **2007**, *59*, 677–694.
- (125) Blagden, N.; de Matas, M.; Gavan, P. T.; York, P. Crystal Engineering of Active Pharmaceutical Ingredients to Improve Solubility and Dissolution Rates. *Adv. Drug Deliv. Rev.* **2007**, *59*, 617–630.
- (126) Qiao, N.; Li, M.; Schlindwein, W.; Malek, N.; Davies, A.; Trappitt, G. Pharmaceutical Cocrystals: An Overview. *Int. J. Pharm.* **2011**, *419* (1–2), 1–11.
- (127) Hancock, B. C.; Parks, M. What Is the True Solubility Advantage for Amorphous Pharmaceuticals? *Pharm. Res.* **2000**, *17* (4), 397–404.
- (128) Newman, A.; Knipp, G.; Zografi, G. Assessing the Performance of Amorphous Solid Dispersions. *J. Pharm. Sci.* **2012**, *101* (4), 1355–1377.
- (129) Megrab, N. A.; Williams, A. C.; Barry, B. W. Oestradiol Permeation through Human Skin and Silastic Membrane: Effects of Propylene Glycol and Supersaturation. *J. Control. Release* **1995**, *36* (3), 277–294.
- (130) Leveque, N.; Raghavan, S. L.; Lane, M. E.; Hadgraft, J. Use of a Molecular Form Technique for the Penetration of Supersaturated Solutions of Salicylic Acid across Silicone Membranes and Human Skin in Vitro. *Int. J. Pharm.* **2006**, *318* (1–2), 49–54.

- (131) Psachoulias, D.; Vertzoni, M.; Goumas, K.; Kalioras, V.; Beato, S.; Butler, J.; Reppas, C. Precipitation in and Supersaturation of Contents of the Upper Small Intestine After Administration of Two Weak Bases to Fasted Adults. *Pharm. Res.* **2011**, *28* (12), 3145–3158.
- (132) Sugar, A. M.; Liu, X. In Vitro and In Vivo Activities of SCH 56592 against Blastomyces Dermatitidis. *Antimicrob. Agents Chemother.* **1996**, *40* (5), 1314–1316.
- (133) Perfect, J. R.; Cox, G. M.; Dodge, R. K.; Schell, W. A. In Vitro and In Vivo Efficacies of the Azole SCH56592 against Cryptococcus Neoformans. *Antimicrob. Agents Chemother.* **1996**, *40* (8), 1910–1913.
- (134) Lutz, J. E.; Clemons, K. V; Aristizabal, B. H. Activity of the Triazole SCH 56592 against Disseminated Murine Coccidioidomycosis. *Antimicrob. Agents Chemother.* **1997**, *41* (7), 1558–1561.
- (135) Connolly, P.; Wheat, J.; Schnizlein-bick, C.; Durkin, M.; Kohler, S.; Smedema, M.; Goldberg, J.; Brizendine, E. Comparison of a New Triazole Antifungal Agent , Schering 56592 , with Itraconazole and Amphotericin B for Treatment of Histoplasmosis in Immunocompetent Mice. *Antimicrob. Agents Chemother.* **1999**, *43* (2), 322–328.
- (136) Sabatelli, F.; Patel, R.; Mann, P. A.; Mendrick, C. A.; Norris, C. C.; Hare, R.; Loebenberg, D.; Black, T. A.; Mcnicholas, P. M. In Vitro Activities of Posaconazole, Fluconazole, Itraconazole, Voriconazole, and Amphotericin B against a Large Collection of Clinically Important Molds and Yeasts. *Antimicrob. Agents Chemother.* **2006**, *50* (6), 2009–2015.
- (137) Macedo-silva, S. T. De; Urbina, J. A.; Souza, W. De; Cola, J. In Vitro Activity of the Antifungal Azoles Itraconazole and Posaconazole against Leishmania Amazonensis. *PLoS One* **2013**, *8* (12), e83247.
- (138) Döring, M.; Eikemeier, M.; Stanchi, K. M. C. Antifungal Prophylaxis with Posaconazole vs . Fluconazole or Itraconazole in Pediatric Patients with Neutropenia. *Eur. J. Clin. Microbiol. Infect. Dis.* **2015**, *34* (6), 1189–1200.
- (139) Benet, L. Z.; Broccatelli, F.; Oprea, T. I. BDDCS Applied to Over 900 Drugs. *AAPS J.* **2011**, *13* (4), 519–547.
- (140) Gubbins, P. O.; Krishna, G.; Sansone-parsons, A.; Penzak, S. R.; Dong, L.; Martinho, M.; Anaissie, E. J. Pharmacokinetics and Safety of Oral Posaconazole in Neutropenic Stem Cell Transplant Recipients. *Antimicrob. Agents Chemother.* **2006**, *50* (6), 1993–1999.
- (141) Lewis, R.; Hogan, H.; Howell, A.; Safdar, A. Progressive Fusariosis: Unpredictable Posaconazole Bioavailability, and Feasibility of Recombinant Interferon-Gamma plus Granulocyte Macrophage-Colony Stimulating Factor for Refractory Disseminated Infection. *Leuk. Lymphoma* **2008**, *49* (1), 163–165.

- (142) Dolton, M. J.; Ray, J. E.; Marriott, D.; McLachlan, A. J. Posaconazole Exposure-Response Relationship: Evaluating the Utility of Therapeutic Drug Monitoring. *Antimicrob. Agents Chemother.* **2012**, *56* (6), 2806–2813.
- (143) Lipp, H. Clinical Pharmacodynamics and Pharmacokinetics of the Antifungal Extended-Spectrum Triazole Posaconazole: An Overview. *Br. J. Clin. Pharmacol.* **2010**, *70* (4), 471–480.
- (144) Courtney, R.; Wexler, D.; Radwanski, E.; Lim, J.; Laughlin, M. Effect of Food on the Relative Bioavailability of Two Oral Formulations of Posaconazole in Healthy Adults. *Br. J. Clin. Pharmacol.* **2003**, *57* (2), 218–222.
- (145) Krishna, G.; Moton, A.; Ma, L.; Medlock, M. M.; Mcleod, J. Pharmacokinetics and Absorption of Posaconazole Oral Suspension under Various Gastric Conditions in Healthy Volunteers □. *Antimicrob. Agents Chemother.* **2015**, *53* (3), 958–966.
- (146) Hens, B.; Brouwers, J.; Corsetti, M.; Augustijns, P. Supersaturation and Precipitation of Posaconazole Upon Entry in the Upper Small Intestine in Humans. *J. Pharm. Sci.* **2016**, *105* (9), 2677–2684.
- (147) Fang, L. Y.; Harris, D.; Krishna, G.; Jr., A. E. M.; Prestipino, R. C.; Steinman, M.; Wan, J.; Waskin, H. A. Oral Pharmaceutical Compositions in a Solid Dispersion Comprising Preferably Posaconazole and HPMCAS - Merck Sharp and Dohme Corp. AU2014265059A1. AU2014265059A1, 2014.
- (148) Mathias, N. R.; Xu, Y.; Patel, D.; Grass, M.; Caldwell, B.; Jager, C.; Mullin, J.; Hansen, L.; Crison, J.; Saari, A.; Gesenberg, C.; Morrison, J.; Vig, B. Assessing the Risk of PH-Dependent Absorption for New Molecular Entities: A Novel in Vitro Dissolution Test, Physicochemical Analysis, and Risk Assessment Strategy. *Mol. Pharm.* **2013**, *10* (11), 4063–4073.
- (149) Mann, J.; Dressman, J.; Rosenblatt, K.; Ashworth, L.; Muenster, U.; Frank, K.; Hutchins, P.; Williams, J.; Klumpp, L.; Wielockx, K.; Berben, P.; Augustijns, P.; Holm, R.; Hofmann, M.; Patel, S.; Beato, S.; Ojala, K.; Tomaszewska, I.; Bruel, J.; Butler, J. Validation of Dissolution Testing with Biorelevant Media : An OrBiTo Study. *Mol. Pharm.* **2017**, *14* (12), 4192–4201.
- (150) Raina, S. A.; Alonzo, D. E.; Zhang, G. G. Z.; Gao, Y.; Taylor, L. S. Using Environment-Sensitive Fluorescent Probes to Characterize Liquid-Liquid Phase Separation in Supersaturated Solutions of Poorly Water Soluble Compounds. *Pharm. Res.* **2015**, *32* (11), 3660–3673.
- (151) Xie, T.; Gao, W.; Taylor, L. S. Impact of Eudragit EPO and Hydroxypropyl Methylcellulose on Drug Release Rate , Supersaturation , Precipitation Outcome and Redissolution Rate of Indomethacin Amorphous Solid Dispersions. *Int. J. Pharm.* **2017**, *531* (1), 313–323.
- (152) Merck Sharp & Dohme Corp. Product Information - NOXAFIL® (Posaconazole) - MODIFIED RELEASE 100 Mg TABLETS and 40 Mg/ML ORAL SUSPENSION, 2006.

- (153) Leung, S.; Poulakos, M. N.; Machin, J. Posaconazole: An Update of Its Clinical Use. *Pharm.* **2015**, *3* (4), 210–268.
- (154) Schneider, C. A.; Rasband, W. S.; Eliceiri, K. W. NIH Image to ImageJ : 25 Years of Image Analysis. *Nat. Methods* **2012**, *9* (7), 671–675.
- (155) Kourentas, A.; Vertzoni, M.; Barmpatsalou, V.; Augustijns, P.; Beato, S.; Butler, J.; Holm, R.; Ouwerkerk, N.; Rosenberg, J.; Tajiri, T.; Tannergren, C.; Symillides, M.; Reppas, C. The BioGIT System: A Valuable In Vitro Tool to Assess the Impact of Dose and Formulation on Early Exposure to Low Solubility Drugs After Oral Administration. *AAPS J.* **2018**, *20* (71), 1–12.
- (156) Lakowicz, J. R. *Principles of Fluorescence Spectroscopy*; Second Edition. New York : Kluwer Academic/Plenum, 1999.
- (157) Rodriguez-navarro, C.; Linares-fernandez, L.; Doehne, E.; Sebastian, E. Effects of Ferrocyanide Ions on NaCl Crystallization in Porous Stone. *J. Cryst. Growth* **2002**, *243* (3–4), 503–516.
- (158) Barbe, C. J.; Arendse, F.; Comte, P.; Jirousek, M.; Lenzmann, F.; Shklover, V.; Gra, M. Nanocrystalline Titanium Oxide Electrodes for Photovoltaic Applications. *J. Am. Ceram. Soc.* **1997**, *80* (12), 3157–3171.
- (159) Lafferre, L.; Garcia, E.; Hoff, C.; Luminy, C. De. Phase Transitions in Supersaturated Drug Solution. *Org. Process Res. Dev.* **2003**, *7* (6), 983–989.
- (160) Li, N.; Taylor, L. S. Tailoring Supersaturation from Amorphous Solid Dispersions. *J. Control. Release* **2018**, *279*, 114–125.
- (161) Davis, S. S.; Hardy, J. G.; Taylor, M. J.; Whalley, D. R. A Comparative Study of the Gastrointestinal Transit of a Pellet and Tablet Formulation. *Int. J. Pharm.* **1984**, *21* (2), 167–177.
- (162) Mojaverian, P.; Ferguson, R. K.; Vlasses, P. H.; Rocci, M. L.; Oren, A.; Fix, J. A.; Caldwell, L. J. Estimation of Gastric Residence Time of the Heidelberg Capsule in Humans: Effect of Varying Food Composition. *Gastroenterology* **1985**, *89* (2), 392–397.
- (163) Müllertz, A.; Ogbonna, A.; Ren, S. New Perspectives on Lipid and Surfactant Based Drug. *J. Pharm. Pharmacol.* **2010**, *62* (11), 1622–1636.
- (164) Davis, A. F.; Hadgraft, J. Effect of Supersaturation on Membrane Transport: Hydrocortisone Acetate. *Int. J. Pharm.* **1991**, *76* (1–2), 1–8.
- (165) Pellett, M. A.; Davis, A. F.; Hadgraft, J. Effect of Supersaturation on Membrane Transport: 2. Piroxicam. *Int. J. Pharm.* **1994**, *111* (1), 1–6.

- (166) Santos, P.; Watkinson, A. C.; Hadgraft, J.; Lane, M. E. Enhanced Permeation of Fentanyl from Supersaturated Solutions in a Model Membrane. *Int. J. Pharm.* **2011**, *407* (1–2), 72–77.
- (167) Umprakob, U. K.; Awakami, J. K.; Dachi, I. A. Permeation Enhancement of Ketoprofen Using a Supersaturated System with Antinucleant Polymers. *Biol. Pharm. Bull.* **2005**, *28* (9), 1684–1688.
- (168) Indulkar, A. S.; Gao, Y.; Raina, S. A.; Taylor, L. S. Exploiting the Phenomenon of Liquid-Liquid Phase Separation for Enhanced and Sustained Membrane Transport of a Poorly Water-Soluble Drug. *Mol. Pharm.* **2016**, *13* (6), 2059–2069.
- (169) Dietschy, J. M.; Sallee, V. L.; Wilson, F. A. Unstirred Water Layers and Absorption across the Intestinal Mucosa. *Gastroenterology* **1971**, *61* (6), 932–934.
- (170) Nielsen, P. E.; Avdeef, A. PAMPA — a Drug Absorption in Vitro Model 8. Apparent Filter Porosity and the Unstirred Water Layer. *Eur. J. Pharm. Sci.* **2004**, *22* (1), 33–41.
- (171) Korjamo, T.; Heikkinen, A. T.; Mönkkönen, J. Analysis of Unstirred Water Layer in In Vitro Permeability Experiments. *J. Pharm. Sci.* **2009**, *98* (12), 4469–4479.
- (172) Stewart, A. M.; Grass, M. E.; Mudie, D. M.; Morgen, M. M.; Friesen, D. T.; Vodak, D. T. Development of a Biorelevant, Material-Sparing Membrane Flux Test for Rapid Screening of Bioavailability-Enhancing Drug Product Formulations. *Mol. Pharm.* **2017**, *14* (6), 2032–2046.
- (173) Kesisoglou, F.; Wang, M.; Galipeau, K.; Harmon, P.; Okoh, G. Effect of Amorphous Nanoparticle Size on Bioavailability of Anacetrapib in Dogs. *J. Pharm. Sci.* **2019**, 1–9.
- (174) Mukerjee, P.; Cardinal, J. R. Solubilization as a Method for Studying Self-Association: Solubility of Naphthalene in the Bile Salt Sodium Cholate and the Complex Pattern of Its Aggregation. *J. Pharm. Sci.* **1976**, *65* (6), 882–886.
- (175) Mazer, N. A.; Carey, M. C.; Kwasnick, R. F.; Benedek, G. B. Quasielastic Light Scattering Studies of Aqueous Biliary Lipid Systems. Size, Shape, and Thermodynamics of Bile Salt Micelles. *Biochemistry* **1979**, *18* (14), 3064–3075.
- (176) Reis, S.; Moutinho, C. G.; Matos, C.; De Castro, B.; Gameiro, P.; Lima, J. L. F. C. Noninvasive Methods to Determine the Critical Micelle Concentration of Some Bile Acid Salts. *Anal. Biochem.* **2004**, *334* (1), 117–126.
- (177) Lu, J.; Ormes, J. D.; Lowinger, M.; Xu, W.; Mitra, A.; Mann, A. K. P.; Litster, J. D.; Taylor, L. S. Impact of Endogenous Bile Salts on the Thermodynamics of Supersaturated Active Pharmaceutical Ingredient Solutions. *Cryst. Growth Des.* **2017**, *17* (3), 1264–1275.
- (178) Higuchi; T. Physical Chemical Analysis of Percutaneous Absorption Process from Creams and Ointments. *J Soc Cosmet Chem* **1960**, *11*, 85–97.

- (179) Indulkar, A. S.; Box, K. J.; Taylor, R.; Ruiz, R.; Taylor, L. S. PH-Dependent Liquid–Liquid Phase Separation of Highly Supersaturated Solutions of Weakly Basic Drugs. *Mol. Pharm.* **2015**, *12*, 2365–2377.
- (180) Fang, L. Y.; Wan, J.; Harris, D. Oral Pharmaceutical Compositions in a Solid Dispersion Comprising Preferably Posaconazole and HPMCAS. US2011/0034478A1, 2011.
- (181) Elkhabaz, A.; Sarkar, S.; Dinh, J. K.; Simpson, G. J.; Taylor, L. S. Variation in Supersaturation and Phase Behavior of Ezetimibe Amorphous Solid Dispersions upon Dissolution in Different Biorelevant Media. *Mol. Pharm.* **2018**, *15* (1), 193–206.
- (182) Indulkar, A. S.; Mo, H.; Gao, Y.; Raina, S. A.; Zhang, G. G. Z.; Taylor, L. S. Impact of Micellar Surfactant on Supersaturation and Insight into Solubilization Mechanisms in Supersaturated Solutions of Atazanavir. *Pharm. Res.* **2017**, *34* (6), 1276–1925.
- (183) Elkhabaz, A.; Sarkar, S.; Simpson, G. J.; Taylor, L. S. Characterization of Phase Transformations for Amorphous Solid Dispersions of a Weak-Base upon Dissolution in Biorelevant Media. *Pharm. Res.* **2019**, Accepted.
- (184) Inagaki, I.; Adachi, M.; Ito, H.; Yasuda, M.; Tsurumi, H.; Deguchi, T.; Seishima, M. Atazanavir-Induced Urine Crystals Demonstrated by Infrared Spectroscopic Analysis. *Urol. Int.* **2015**, *94* (1), 121–124.
- (185) Daudon, M.; Frochot, V.; Bazin, D.; Jungers, P. Crystalluria Analysis Improves Significantly Etiologic Diagnosis and Therapeutic Monitoring of Nephrolithiasis. *Comptes Rendus Chim.* **2016**, *19* (11–12), 1514–1526.
- (186) Takano, R.; Takata, N.; Saito, R.; Furumoto, K.; Higo, S.; Hayashi, Y.; Machida, M.; Aso, Y. Quantitative Analysis of the Effect of Supersaturation on in Vivo Drug Absorption. *Mol. Pharm.* **2010**, *7* (5), 1431–1440.
- (187) Wilson, V.; Lou, X.; Osterling, D. J.; Stolarik, D. F.; Jenkins, G.; Gao, W.; Zhang, G. G. Z.; Taylor, L. S. Relationship between Amorphous Solid Dispersion in Vivo Absorption and in Vitro Dissolution: Phase Behavior during Dissolution, Speciation, and Membrane Mass Transport. *J. Control. Release* **2018**, *292*, 172–182.
- (188) Yalkowsky, S. H. *Solubility and Solubilization in Aqueous Media*; Oxford University Press: New York, 1999.
- (189) Poelma, F. G. J.; Breäs, R.; Tukker, J. J.; Crommelin, D. J. A. Intestinal Absorption of Drugs. The Influence of Mixed Micelles on the Disappearance Kinetics of Drugs from the Small Intestine of the Rat. *J. Pharm. Pharmacol.* **1991**, *43* (5), 317–324.
- (190) Katneni, K.; Charman, S. A.; Porter, C. J. H. Permeability Assessment of Poorly Water-Soluble Compounds under Solubilizing Conditions: The Reciprocal Permeability Approach. *J. Pharm. Sci.* **2006**, *95* (10), 2170–2185.

- (191) Miller, J. M.; Beig, A.; Krieg, B. J.; Carr, R. A.; Borchardt, T. B.; Amidon, G. E.; Amidon, G. L.; Dahan, A. The Solubility-Permeability Interplay: Mechanistic Modeling and Predictive Application of the Impact of Micellar Solubilization on Intestinal Permeation. *Mol. Pharm.* **2011**, *8* (5), 1848–1856.
- (192) Berben, P.; Mols, R.; Brouwers, J.; Tack, J.; Augustijns, P. Gastrointestinal Behavior of Itraconazole in Humans – Part 2: The Effect of Intraluminal Dilution on the Performance of a Cyclodextrin-Based Solution. *Int. J. Pharm.* **2017**, *526* (1–2), 235–243.
- (193) Shore, P. A.; Brodie, B. B.; Hogben, C. A. M. The Gastric Secretion of Drugs: A PH Partition Hypothesis. *J. Pharmacol. Exp. Ther.* **1957**, *119* (3), 361–369.
- (194) Crum, M. F.; Trevaskis, N. L.; Pouton, C. W.; Porter, C. J. H. Transient Supersaturation Supports Drug Absorption from Lipid- Based Formulations for Short Periods of Time, but Ongoing Solubilization Is Required for Longer Absorption Periods. *Mol. Pharm.* **2017**, *14* (2), 394–405.
- (195) Palmelund, H.; Madsen, C. M.; Plum, J.; Müllertz, A.; Rades, T. Studying the Propensity of Compounds to Supersaturate: A Practical and Broadly Applicable Approach. *J. Pharm. Sci.* **2016**, *105* (10), 3021–3029.
- (196) Blaabjerg, L. I.; Grohganz, H.; Lindenberg, E.; Löbmann, K.; Müllertz, A.; Rades, T. The Influence of Polymers on the Supersaturation Potential of Poor and Good Glass Formers. *Pharmaceutics* **2018**, *10* (4), 1–14.
- (197) Gao, P.; Akrami, A.; Alvarez, F.; Hu, J.; Li, L. A. N.; Ma, C.; Surapaneni, S. Characterization and Optimization of AMG 517 Supersaturatable Self-Emulsifying Drug Delivery System (S-SEDDS) for Improved Oral Absorption. *J. Pharm. Sci.* **2009**, *98* (2), 516–528.
- (198) Suys, E. J. A.; Chalmers, D. K.; Pouton, C. W.; Porter, C. J. H. Polymeric Precipitation Inhibitors Promote Fenofibrate Supersaturation and Enhance Drug Absorption from a Type IV Lipid-Based Formulation. *Mol. Pharm.* **2018**, *15* (6), 2355–2371.
- (199) Bevernage, J.; Forier, T.; Brouwers, J.; Tack, J.; Annaert, P.; Augustijns, P. Excipient-Mediated Supersaturation Stabilization in Human Intestinal Fluids. *Mol. Pharm.* **2011**, *8* (2), 564–570.
- (200) Rubbens, J.; Brouwers, J.; Tack, J.; Augustijns, P. Gastrointestinal Dissolution, Supersaturation and Precipitation of the Weak Base Indinavir in Healthy Volunteers. *Eur. J. Pharm. Biopharm.* **2016**, *109*, 122–129.
- (201) Ezzet, F.; Wexler, D.; Courtney, R.; Krishna, G.; Lim, J. Oral Bioavailability of Posaconazole in Fasted Healthy Subjects Dosage Recommendations. *Clin. Pharmacokinet.* **2005**, *44* (2), 211–220.

- (202) Söderlind, E.; Karlsson, E.; Carlsson, A.; Kong, R.; Lenz, A.; Lindborg, S.; Sheng, J. J. Simulating Fasted Human Intestinal Fluids: Understanding the Roles of Lecithin and Bile Acids. *Mol. Pharm.* **2010**, *7* (5), 1498–1507.
- (203) Hammad, M. A.; Mu, B. W. Increasing Drug Solubility by Means of Bile Salt Phosphatidylcholine-Based Mixed Micelles. *Eur. J. Pharm. Biopharm.* **1998**, *46* (3), 361–367.
- (204) Berben, P.; Bauer-brandl, A.; Brandl, M.; Faller, B.; Eide, G.; Jacobsen, A.; Brouwers, J.; Augustijns, P. Drug Permeability Profiling Using Cell-Free Permeation Tools: Overview and Applications. *Eur. J. Pharm. Sci.* **2018**, *119*, 219–233.
- (205) Persson, E. M.; Gustafsson, A.; Carlsson, A. S.; Nilsson, R. G.; Knutson, L.; Forsell, P.; Hanisch, G.; Lennerna, H. The Effects of Food on the Dissolution of Poorly Soluble Drugs in Human and in Model Small Intestinal Fluids. *Pharm. Res.* **2005**, *22* (12), 2141–2151.
- (206) Heikkilä, T.; Karjalainen, M.; Ojala, K.; Partola, K.; Lammert, F.; Augustijns, P.; Urtti, A.; Yliperttula, M.; Peltonen, L.; Hirvonen, J. Equilibrium Drug Solubility Measurements in 96-Well Plates Reveal Similar Drug Solubilities in Phosphate Buffer PH 6.8 and Human Intestinal Fluid. *Int. J. Pharm.* **2011**, *405* (1–2), 132–136.
- (207) Clarysse, S.; Tack, J.; Lammert, F.; Duchateau, G.; Reppas, C.; Augustijns, P. Postprandial Evolution in Composition and Characteristics of Human Duodenal Fluids in Different Nutritional States. *J. Pharm. Sci.* **2009**, *98* (3), 1177–1192.
- (208) Shegokar, R.; Müller, R. H. Nanocrystals: Industrially Feasible Multifunctional Formulation Technology for Poorly Soluble Actives. *Int. J. Pharm.* **2010**, *399* (1–2), 129–139.
- (209) Strickley, R. G. Solubilizing Excipients in Oral and Injectable Formulations. *Pharm. Res.* **2004**, *21* (2), 201–230.
- (210) Taylor, L. S.; Zhang, G. G. Z. Physical Chemistry of Supersaturated Solutions and Implications for Oral Absorption. *Adv. Drug Deliv. Rev.* **2016**, *101*, 122–142.
- (211) Ilevbare, G. A.; Liu, H.; Edgar, K. J.; Taylor, L. S. Maintaining Supersaturation in Aqueous Drug Solutions: Impact of Different Polymers on Induction Times. *Cryst. Growth Des.* **2013**, *13* (2), 740–751.
- (212) Ilevbare, G. A.; Liu, H.; Edgar, K. J.; Taylor, L. S. Impact of Polymers on Crystal Growth Rate of Structurally Diverse Compounds from Aqueous Solution. *Mol. Pharm.* **2013**, *10* (6), 2381–2393.
- (213) Ilevbare, G. A.; Liu, H.; Edgar, K. J.; Taylor, L. S. Effect of Binary Additive Combinations on Solution Crystal Growth of the Poorly Water-Soluble Drug, Ritonavir. *Cryst. Growth Des.* **2012**, *12* (12), 6050–6060.

- (214) Gutzow, I. S.; Schmelzer, J. W. P. Catalyzed Crystallization of Glass-Forming Melts. In *The Vitreous State: Thermodynamics, Structure, Rheology, and Crystallization*; Springer Berlin Heidelberg: Berlin, Heidelberg, 2013; pp 289–331.
- (215) Fuchs, A.; Dressman, J. B. Composition and Physicochemical Properties of Fasted-State Human Duodenal and Jejunal Fluid: A Critical Evaluation of the Available Data. *J. Pharm. Sci.* **2014**, *103* (11), 3398–3411.
- (216) Elkhabaz, A.; Moseson, D. E.; Brouwers, J.; Augustijns, P.; Taylor, L. S. Interplay of Supersaturation and Solubilization: Lack of Correlation between Concentration-Based Supersaturation Measurements and Membrane Transport Rates in Simulated and Aspirated Human Fluids. *Mol. Pharm.* **2019**.
- (217) Stappaerts, J.; Geboers, S.; Snoeys, J.; Brouwers, J.; Tack, J.; Annaert, P.; Augustijns, P. Rapid Conversion of the Ester Prodrug Abiraterone Acetate Results in Intestinal Supersaturation and Enhanced Absorption of Abiraterone: In Vitro, Rat in Situ and Human in Vivo Studies. *Eur. J. Pharm. Biopharm.* **2015**, *90*, 1–7.
- (218) Shi, Y.; Gao, P.; Gong, Y.; Ping, H. Application of a Biphasic Test for Characterization of In Vitro Drug Release of Immediate Release Formulations of Celecoxib and Its Relevance to In Vivo Absorption. *Mol. Pharm.* **2010**, *7* (5), 1458–1465.
- (219) Anby, M. U.; Williams, H. D.; McIntosh, M.; Benameur, H.; Edwards, G. A.; Pouton, C. W.; Porter, C. J. H. Lipid Digestion as a Trigger for Supersaturation: Evaluation of the Impact of Supersaturation Stabilization on the in Vitro and in Vivo Performance of Self-Emulsifying Drug Delivery Systems. *Mol. Pharm.* **2012**, *9* (7), 2063–2079.
- (220) Thomas, N.; Holm, R.; Müllertz, A.; Rades, T. In Vitro and in Vivo Performance of Novel Supersaturated Self-Nanoemulsifying Drug Delivery Systems (Super-SNEDDS). *J. Control. Release* **2012**, *160*, 25–32.
- (221) Gao, P.; Rush, B. D.; Pfund, W. P.; Huang, T.; Bauer, J. M.; Morozowich, W.; Kuo, M.; Hageman, M. J. Development of a Supersaturable SEDDS (S-SEDDS) Formulation of Paclitaxel with Improved Oral Bioavailability. *J. Pharm. Sci.* **2003**, *92* (12), 2386–2398.
- (222) Bevernage, J. A. N.; Brouwers, J.; Clarysse, S.; Vertzoni, M.; Tack, J. A. N.; Annaert, P.; Augustijns, P. Drug Supersaturation in Simulated and Human Intestinal Fluids Representing Different Nutritional States. *J. Pharm. Sci.* **2010**, *99* (11), 4525–4534.
- (223) Nielsen, A. E. *Kinetics of Precipitation*; Pergamon Press, 1964.
- (224) Fuchs, A.; Leigh, M.; Kloefer, B.; Dressman, J. B. Advances in the Design of Fasted State Simulating Intestinal Fluids: FaSSIF-V3. *Eur. J. Pharm. Biopharm.* **2015**, *94*, 229–240.
- (225) Shankland, W. The Equilibrium and Structure of Lecithin-Cholate Mixed Micelles. *Chem. Phys. Lipids* **1970**, *4* (2), 109–130.

- (226) Liu, H.; Taylor, L. S.; Edgar, K. J. The Role of Polymers in Oral Bioavailability Enhancement; a Review. *Polymer (Guildf)*. **2015**, *77*, 399–415.
- (227) Anwar, J.; Boateng, P. K.; Tamaki, R.; Odedra, S. Mode of Action and Design Rules for Additives That Modulate Crystal Nucleation. *Angew. Chemie - Int. Ed.* **2009**, *48* (9), 1596–1600.
- (228) Mullin, J. W. *Industrial Crystallization: 3rd Edition*; Elsevier Butterworth-Heinemann, 1993.
- (229) Sangwal, K. Kinetic Effects of Impurities on the Growth of Single Crystals from Solutions. *J. Cryst. Growth* **1999**, *203* (1), 197–212.
- (230) Kubota, N. Effect of Impurities on the Growth Kinetics of Crystals. *Cryst. Res. Technol.* **2001**, *36* (8–10), 749–769.
- (231) Kubota, N.; Mullin, J. W. A Kinetic Model for Crystal Growth from Aqueous Solution in the Presence of Impurity. *J. Cryst. Growth* **1995**, *152*, 203–208.
- (232) Holmberg, K.; Jönsson, B.; Kronberg, B.; Lindman, B. *Surfactants and Polymers in Aqueous Solution*; 2002.
- (233) Que, C.; Gao, Y.; Raina, S. A.; Zhang, G. G. Z.; Taylor, L. S. Paclitaxel Crystal Seeds with Different Intrinsic Properties and Their Impact on Dissolution of Paclitaxel-HPMCAS Amorphous Solid Dispersions. *Cryst. Growth Des.* **2018**, *18* (3), 1548–1559.

VITA

Ahmed Elkhabaz graduated from Suez Canal University in Egypt with a BSc degree in Pharmaceutical Sciences. Before joining Purdue, he received his MSc degree in Pharmaceutical Sciences from Utrecht University, the Netherlands. In the fall of 2014, Ahmed joined the Ph.D. program in the Department of Industrial and Physical Pharmacy at Purdue University, West Lafayette, Indiana. Upon completion of his Ph.D. in fall 2019, Ahmed joined Merck & Co., Inc., as a Senior Scientist in the Analytical Sciences group.